

Non-Equilibrium Transport in Surface Superlattices Realized by Cleaved-Edge Overgrowth

Dissertation
zur Erlangung des Doktorgrades
der Naturwissenschaften (Dr. rer. nat.)
der Fakultät für Physik
der Universität Regensburg

vorgelegt von
Thomas Feil
aus Ebermannsdorf
2005

Promotionsgesuch eingereicht am: 19.01.2006

Tag der mündlichen Prüfung: 23.02.2006

Die Arbeit wurde angeleitet von: Prof. Dr. W. Wegscheider

Prfungsausschuss:

Vorsitzender: Prof. Dr. M. Grifoni

1. Gutachter: Prof. Dr. W. Wegscheider

2. Gutachter: Prof. Dr. D. Weiss

weiterer Prüfer: Prof. Dr. K. F. Renk

“ . . . Denn dies ist die Wahrheit: ausgezogen bin ich aus dem Hause der Gelehrten, und die Tür habe ich noch hinter mir zugeworfen.

Zu lange saß meine Seele hungrig an ihrem Tische; nicht, gleich ihnen, bin ich auf das Erkennen abgerichtet wie auf das Nüsseknacken.

Freiheit liebe ich und die Luft über frischer Erde; lieber noch will ich auf Ochsenhäuten schlafen, als auf ihren Würden und Achtbarkeiten.

Ich bin zu heiß und verbrannt von eigenen Gedanken: oft will es mir den Atem nehmen. Da muß ich ins Freie und weg aus allen verstaubten Stuben.

Aber sie sitzen kühl in kühlen Schatten: sie wollen in allem nur Zuschauer sein und hüten sich, dort zu sitzen, wo die Sonne auf die Stufen brennt. . . .

Also sprach Zarathustra“

Friedrich Nietzsche, *Also sprach Zarathustra: Von den Gelehrten*

Contents

1	Introduction	9
2	The Semiconductor Superlattice	13
2.1	Overview	13
2.2	Minibands in superlattices	14
2.3	Energy scales and transport regimes	18
2.4	Semiclassical superlattice transport	20
2.5	The Esaki-Tsu Bloch oscillator	24
2.6	The dynamic superlattice conductivity	25
2.7	The Bloch oscillator	27
3	Surface superlattices	29
3.1	Overview	29
3.2	Technological realization	30
3.3	Basic electronic properties	31
3.4	Self-consistent device simulations	33
3.5	About minigaps	40
3.6	Device operation	41
4	Electric field instabilities	43
4.1	Overview	43
4.2	Origin of electric field instabilities	44
4.3	Instability regimes	44
4.4	Instabilities in surface superlattices	47
4.5	DC NDC in semiconductor devices	51
5	Transport in surface superlattice systems	53
5.1	Overview	53
5.2	Transport in long channel devices	54
5.3	The filling of the miniband	59
5.4	Transport in short channel devices	61
5.5	How to avoid electric field instabilities	63

5.6	The shunted surface superlattice	66
5.7	Properties of shunt-stabilized surface superlattices	75
5.8	A two-dimensional surface superlattice transport model	79
5.9	Surface superlattices without shunt	84
5.10	Conclusion	86
6	Transport in magnetic fields	89
6.1	Overview	89
6.2	Applying a magnetic field	90
6.3	Aligning the magnetic field parallel to the SL axis	92
6.3.1	Shunt transport in a magnetic field parallel to the superlattice axis	94
6.3.2	Surface superlattice transport in a magnetic field parallel to the superlattice axis	97
6.4	Aligning the magnetic field perpendicular to the SL axis	100
6.4.1	Shunt transport in a magnetic field perpendicular to the superlattice axis	104
6.4.2	Surface superlattice transport in a magnetic field perpendicular to the superlattice axis	105
6.5	Magnetic field perpendicular to the surface SL plane	109
6.6	Conclusion	111
7	Dynamic surface superlattice transport	113
7.1	Introduction	113
7.2	Superlattice transport in the presence of a static and dynamic electric field	114
7.3	DC current in the presence of an AC field	115
7.4	Gain and absorption in a SL structure	118
7.5	Measurement setups	121
7.6	GHz absorption in shunt-stabilized surface superlattices	124
7.7	THz absorption in shunt-stabilized surface superlattices	128
7.8	Gain considerations	131
7.9	Conclusion	133
8	Magnetotransport	135
8.1	Introduction	135
8.2	Semiclassical description	137
8.3	About contact geometries	145
8.4	Experimental data in the semiclassical regime	147
8.5	Weak localization	154
8.6	Quantum mechanical description	157
8.7	Some Loose Ends	171
8.8	Conclusions	174

<i>CONTENTS</i>	7
9 Summary	177
A Matlab program	181
B Folded phonons	183
Acknowledgments	201

Chapter 1

Introduction

This thesis is mainly concerned with the electric transport in surface superlattice structures under large bias. The origin of this topic goes back to the seminal work of Esaki and Tsu [ET70]. They suggested to fabricate so-called superlattice structures which consist of thin, alternately grown layers of two different semiconductor materials. The main idea behind this was to introduce a super crystal structure along the growth axis. Just like the normal crystal structure of solid matter leads to the formation of electronic bands, they also expected a band formation due to the artificially introduced super crystal structure. The lattice constant of a typical superlattice is much larger than that of natural crystals. This leads to a strongly reduced extension of the Brillouin zone in momentum space and to rather small energetic widths of the superlattice bands. Therefore, Esaki and Tsu referred to the new bands as minibands. The authors proposed that it should be possible to study bandstructure related non-linear transport effects in these structures at relatively small electric fields. Especially, the situation in which electrons are Bragg reflected at the Brillouin zone boundary should be observable for electric fields smaller than those leading to avalanche breakdown. Their first theoretical analysis showed that the transport characteristic of such a structure should exhibit a region of negative differential conductivity. In this region, an increasing bias leads to a decreasing current. The reason for this phenomenon is the rising number of electrons which reach the Brillouin zone boundary and start an oscillatory motion, rather than to drift along the superlattice. These oscillations are referred to as Bloch oscillations, a concept already introduced by Bloch [Blo28] and Zener [Zen34] in the context of transport in normal crystals. Esaki and Tsu predicted that the frequency of these oscillations falls into the region of about 1 to 10 THz. Therefore, they suggested a possible use of superlattices as solid state THz sources. The idea of the so-called Bloch oscillator was born.

The proposal by Esaki and Tsu was first followed up by a number of theoretical investigations [KSS72, Shi75, DK86]. These showed that a superlattice which is biased in the region of negative differential conductivity indeed exhibits gain for all frequencies below the Bloch frequency. Only in the late 1980s did the improvements in molecular beam epitaxy allow for the realization of high quality superlattice structures. This progress

initiated an enormous amount of experimental studies on superlattice structures in the following years, which included both optical and electrical measurements (see references in [Gra95, Wac02b, Leo03]). It was found that transport in superlattices has to be described by different means according to the superlattice parameters. The realization of a Bloch oscillator requires both relatively wide minibands and high current densities. Unfortunately, it became immediately clear that the negative differential conductivity in these structures leads to electric field instabilities [Gue71, BT77]. The latter phenomenon was already well understood, since it bears a strong similarity to the operation mode of a Gunn oscillator [Gun63, Gun64, Kro72, Kro66]. Thus, while THz gain was theoretically predicted for a homogeneously biased superlattice, the problem of electric field instabilities violated the fundamental requirement of homogeneity. And even 35 years after its earliest proposal, a Bloch oscillator has not been realized to date. So far, the stabilization of the electric field in a superlattice can only be achieved by a limited number of approaches. One way is to work with superlattices at very small products of carrier density n and sample lengths L [Hak67, SPM⁺89, SPWM90]. In small nL -product superlattices, the growth rate of electric field domains is so slow that the electric field can be very close to homogeneous. Currently, special small nL -product structures, so-called super-superlattices, are tested for their suitability as Bloch oscillators [SKLA04]. In a different approach [DGSA03], the electric field was predicted to be stabilized by the direct lateral attachment of a parallel transport channel. Electron accumulations which lead to electric field instabilities in superlattice structures can be eliminated in these systems since the electrons can flow off into the parallel transport channel.

In the work presented here, surface superlattice structures are studied. The term surface superlattice hereby refers to a two-dimensional electron system which experiences a superlattice potential along the main transport direction while movement along the perpendicular direction is free. Such structures can be fabricated with the Cleaved-Edge Overgrowth method [PWS⁺90]. This method offers great design flexibility. The main part of the presented discussion is concerned with high-field transport in surface superlattices and with the question whether such systems might be used to realize a Bloch oscillator. Such a tunable solid state THz emitter would be useful in a number of applications. Among these there are gas sensing, short-range communication, and imaging techniques. Starting point of the investigation is the work presented in [Deu01] which contains preliminary studies of non-equilibrium transport in surface superlattices.

The organization of the thesis is done in the following way. In chapter 2, the essential basics of electric transport in superlattice structures are discussed. Both the phenomenon of negative differential conductance due to Bloch oscillations and the concept of THz gain in superlattices are the main focus of the presentation. The following chapter 3 deals with the technological realization of the surface superlattice structures, their equilibrium electronic properties, and the principal device operation. The topic of electric field instabilities is introduced in chapter 4. Thereby a special focus will be given to the differences that arise when the three dimensional conventional superlattice is continuously reduced

in one lateral dimension so that a two-dimensional surface superlattice results. The major part of this thesis deals with the understanding of the high-electric field transport in surface superlattices. The discussion of the main results is presented in chapter 5 along a chronological line of improvements made on the surface superlattice design during the course of this thesis. It is shown that a near perfect surface superlattice-shunt system can be realized with the cleaved-edge overgrowth method. A claim for the direct observation of negative differential conductivity due to stable electrically excited Bloch oscillations at high electron densities is made for the transport through such structures. In chapters 6 and 7 this claim is tested by a comparison of the theoretical predictions for the transport through a homogeneous superlattice in magnetic and high-frequency fields with the corresponding experimental data. In chapter 7, also a detailed description of the gain mechanism in superlattice structures is presented and a potential Bloch oscillator application of shunted surface superlattices is discussed. The final chapter 8 deals with the linear response transport properties of surface superlattice structures. Special attention is drawn to the validation of earlier assumed bandstructure properties with the help of magnetotransport measurements. The presented results are in excellent agreement with a quantum-mechanical model and provide, for the first time, convincing evidence for the transition of the two-dimensional system into a one-dimensional state. This transition becomes most evident in a vanishing of the spin and cyclotron gaps of the system.

While all of the experiments discussed in the following chapters have been performed by the author himself, the interpretation of the corresponding results always includes the input from a larger number of people. A list of these 'helpers' can be found in the acknowledgments. The participation of a group of people in the most important part of the research process, the understanding of the observed physics, seems to require the use of 'we' instead of 'I' in the course of the text. Nevertheless, the author claims complete responsibility for any mistakes or other wrongdoings in the course of the discussion.

Every chapter of the thesis starts with a short introductory section in which an overview over the topic with (for the author) helpful literature citations is given. Since there are many thousands of publications dealing with superlattices, only a limited number of these (and maybe not always the most important) are cited during the discussions. Some chapters will end with a short conclusion which contains a summary of the results and deductions drawn from the presented experimental data.

Chapter 2

The Semiconductor Superlattice

2.1 Overview

In their seminal publication about the superlattice structure Esaki and Tsu suggested two different types of periodic modulation. The periodic potential can either be formed by alternating growth of two materials with different band gaps [Gra95] or by a periodic doping profile in the host material [Döh84]. Structures working according to the first approach are referred to as heterostructure superlattices. The others are called doping superlattices. Over the course of the last 35 years, thousands of papers have been published about many different aspects of superlattices.

Experimental work during the 1970s and the early 1980s was severely hampered by the relative low quality of the available superlattice structures [EC74]. This situation improved considerably once the development of molecular beam epitaxy allowed the realization of heterostructures with interfaces whose roughness was of the order of only 1 or 2 monolayers. When high-quality structures became available, the theoretical predictions about superlattices could be tested experimentally. The first major contribution was made by the resolution of the Wannier-Stark ladder through interband absorption experiments in nominally undoped superlattices [MARH88, VBB⁺88]. Soon, experimental studies followed which gave strong evidence for the existence of negative differential velocity in undoped superlattices [SPMM89, SPM⁺89, SPWM90]. These results supported the semiclassical concept of transport through minibands along the superlattice axis. In parallel, four-wave mixing experiments in which excitons were excited in biased, undoped superlattices by femtosecond laser pulses were performed ([FLS⁺92, WRS⁺93, LVL⁺97, LSL⁺98, Leo98] and extensive references in [Leo03]). The exciton time evolution was probed by a second femtosecond pulse at a variable delay time. It could be shown that the coherent exciton ensemble oscillates at the Bloch frequency. Besides the frequency also the amplitude and the emitted THz radiation of these excitonic Bloch oscillations could be detected. Much of the experimental work was carried out on undoped superlattice structures since the negative differential velocity in high-density superlattices leads to electric field instabilities [Gue71, BT77]. These instabilities destroy

the homogeneous electric field distribution which is the basis of most theoretical predictions. In extensive studies [HGS⁺96, SBH⁺98, SBG⁺98] on highly doped superlattices it was found that superlattices could be used as classical high-frequency oscillators. The operation principle of these structures is identical to that of the Gunn oscillator. While the inelastic relaxation in Gunn devices limits possible emission frequencies to a maximum of about 100 GHz, it was argued that this limit should be in the vicinity of 1 THz for superlattices. Nevertheless, to date classical superlattice oscillators have not reached frequencies significantly beyond 150 GHz.

A study of the photoconductivity of an undoped superlattice [UKW⁺96] confirmed the theoretically predicted THz gain mechanism [IRD93, WSG⁺97]. However, the achievable gain in undoped structures was shown [UKW⁺96] to be far too small to build electrically active Bloch oscillators. Thus, while many facets of the predicted superlattice physics could be confirmed experimentally, it is still unclear whether a THz Bloch oscillator can be realized. Since one of the main aims of this work is to check the suitability of surface superlattices for the Bloch oscillator concept, the following chapter introduces the essential basics of transport and gain in superlattices. For more detailed introductions to superlattice physics, the reader is referred to available reviews and books [Gra95, Wac02b, Leo03].

2.2 Minibands in superlattices

The term superlattice (SL) encompasses a wide variety of semiconductor heterostructures. Since all devices that were realized in the course of this work were grown in the GaAs/Al_xGa_{1-x}As material system, a SL shall henceforth be an alternating layer sequence with fixed thicknesses of two materials that form a type I heterojunction. The latter term means that the smaller bandgap of one material is completely enclosed in the bandgap of the other material [Dav98]. This situation is found in the GaAs/Al_xGa_{1-x}As system, in which GaAs is the smaller gap material. Figure 2.1 shows an illustration of the SL structure and the resulting potential landscape. The length of one period of the SL, consisting of one well and one barrier, is denoted as d and the well and barrier thicknesses are, respectively, given by w and b . For electrons with energies close to the GaAs conduction band, the Al_xGa_{1-x}As effectively forms a barrier.¹

The semiclassical transport description in solids is based on the bandstructure $E_n(k)$ of the underlying crystal structure [AM76, Chapter 12]. Therefore, our first concern is to find $E_n(k)$ for the SL system. If we assume a SL with very thick and high barriers, the eigenenergies and eigenfunctions are similar to those of isolated quantum wells with thickness w . When the barrier width b is then continuously reduced, the eigenstates in each well start to feel the presence of the neighboring wells. Eventually, all well states

¹Since only transport in the conduction band is studied, the lower half of figure 2.1 can be ignored although the conclusions drawn for electrons also apply to holes, albeit with additional complications introduced by a mixing of the heavy and light hole bands.

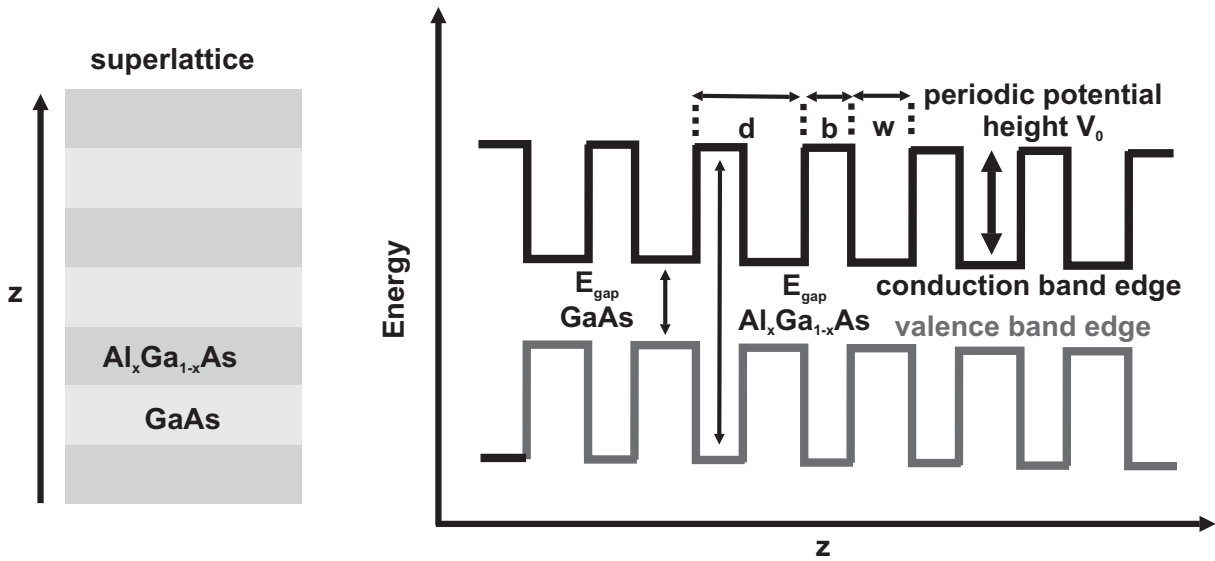


Figure 2.1: Schematic drawing of a superlattice and of its potential energy profile.

mix and their degeneracy is lifted. Such a description is very similar to the general ideas applied to the formation of electronic bands in normal crystals. In the latter case, isolated atoms are brought closer and closer together. The eigenstates of the system are the pure eigenstates of the atoms for a very large separation of the atoms. However, these sharp energy levels broaden into wide bands when the atoms are brought very close together.

The Kronig-Penney model [dLKP31], which was first used to calculate SL band structures [EC74], shows the same formation of energy bands from isolated quantum well states. The model is a generalization of the problem of a particle tunneling through a single barrier. Instead of one barrier, an infinite sequence of such barriers, separated by a fixed period d , is considered. In the SL system these barriers correspond to the regions of the material with the larger band gap (cf. figure 2.1). Thus, the barrier height for electrons is V_0 . The hamiltonian of the Kronig-Penney model consists of the kinetic energy² and the periodic potential profile $\hat{V}(z)$, as shown in figure 2.1,

$$\hat{H} = \frac{\hat{p}_z^2}{2m} + \hat{V}(z) . \quad (2.1)$$

For energies $E < V_0$, solutions within a well ($V(z) = 0$) are written as the superposition of left and right going plane waves $A_{\pm} \exp(\pm i k_w z)$ with energy $E = \frac{\hbar^2 k_w^2}{2m_w}$. The solutions inside a barrier are given by decaying wavefunctions $B_{\pm} \exp(\pm \kappa_b z)$ with energy $E = V_0 - \frac{\hbar^2 \kappa_b^2}{2m_b}$. A connection between solutions in different wells is established through Bloch's theorem

²The Kronig-Penney model was developed for free particles moving in a periodic potential. In case of the SL, the electrons are no longer free particles. Their properties are determined by the lattice potential of the underlying crystal structure. Therefore, the mass of the electrons is given by the GaAs effective mass in the wells of the SL and by the $\text{Al}_x\text{Ga}_{1-x}\text{As}$ effective mass in the barriers. The given hamiltonian is the one resulting from the effective-mass approximation [Dav98, Chapter 3.10].

which holds for periodic potentials. Similar to the eigenstates of a solid crystal, the eigenstates of energy $E_n(k) = \frac{\hbar^2 k^2}{2m}$ of the superlattice can then be labeled by a Bloch wavevector k , lying in the first Brillouin zone $|k| < \pi/d$, and a quantum number n which counts different energies for a fixed k . For a specific energy E , the values of k_w and κ_b are determined from their above definitions. Once k_w and κ_b are known, the corresponding k and n values can be determined from the condition

$$\cos(kd) = \cosh(\kappa_b b) \cos(k_w w) + \frac{1}{2} \left(\xi - \frac{1}{\xi} \right) \sinh(\kappa_b b) \sin(k_w w), \quad \xi = \frac{\kappa_b m_w}{k_w m_b} \quad (2.2)$$

which results from Bloch's theorem and from enforcing the boundary conditions that both the wavefunction and its derivative are continuous across a barrier.³ The limitation of the left side of expression (2.2) to values between -1 and 1 leads to the formation of allowed and forbidden energy ranges for $E_n(k)$. This can be seen when the right hand side of condition (2.2) is plotted as shown in figure 2.2. When the corresponding plot values lie in the range $[-1, 1]$, then there exist extended Bloch states at the given energies E with real Bloch wavevectors k . These Bloch states are solutions which propagate freely through the periodic potential. For absolute plot values larger than 1 , expression (2.2) results in a complex k -value, and there is no extended Bloch state at the corresponding energy. Thus, similar to a normal crystal, the artificial periodic potential leads to the formation of electronic bands $E_n(k)$ which are separated by forbidden energy gaps. The artificial potential leads to Brillouin zone boundaries lying at $\pm \frac{\pi}{d}$. Since d is considerably larger for the artificial layer sequence than in normal crystals, the k -space extension of the superlattice bands and their energetic widths are very small. Therefore, the bands are referred to as minibands. This name helps to distinguish them from the bands formed in the host crystal.

The alternative application of the tight-binding approach [AM76, chapter 10] to the electronic states of the individual quantum wells of the superlattice leads to a dispersion of the general form⁴

$$E(k) = \frac{\Delta}{2}(1 - \cos(kd)) \quad (2.3)$$

for the lowest lying miniband. In this expression Δ is the energetic width of this miniband. Δ can be determined from the Kronig-Penney model as the difference between the largest and smallest energy values of an allowed energy region. Although expression (2.3) follows from the assumption of small minibands, a comparison between the cosine dispersion and the numerical solution of the Kronig-Penney model, as depicted in figure 2.2, shows that it is also a very good approximation for wide minibands. Since the cosine approximation also possesses convenient mathematical properties, expression (2.3) is extensively used in the literature and will also be exclusively applied throughout this work.

The dispersion (2.2) is determined (and can be adjusted) both through the height of the barrier potential and the spatial extensions of wells and barriers. The width of the

³These boundary conditions result from the continuity equation of the particle probability density.

⁴The zero energy has been set to the bottom of the miniband.

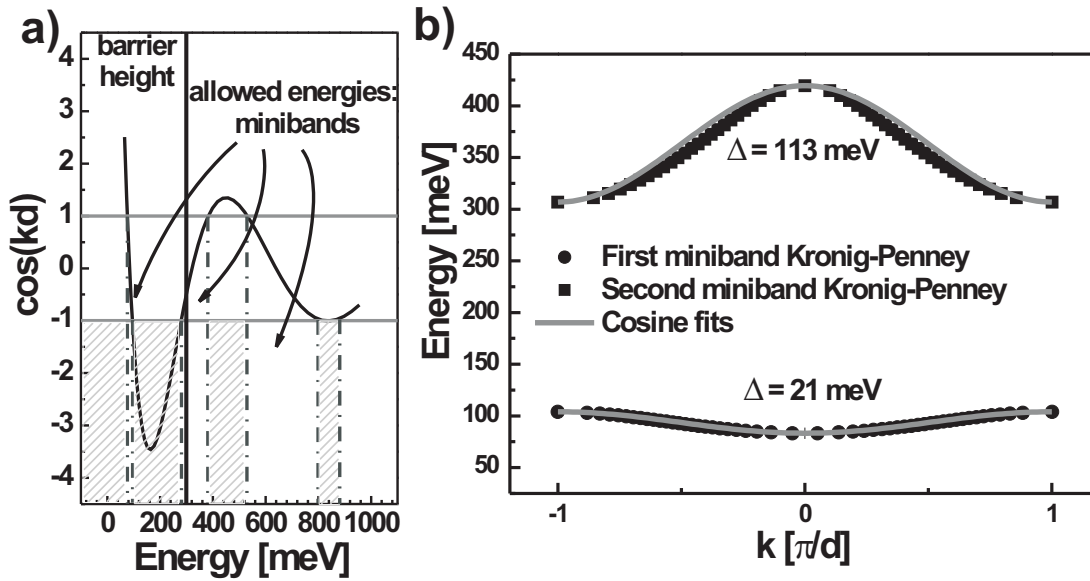


Figure 2.2: (a) Allowed and forbidden energy regions resulting from the Kronig-Penney model. Panel (b) compares a numerical solution of the Kronig-Penney model (scattered values) with the simple cosine dispersion (2.3).

lowest miniband of a typical SL can take on values between a few tenths of a meV and up to more than 100 meV. Small values result from high and thick barriers which effectively limit the coupling between the states in neighboring wells. Thin and small barriers on the other hand result in a large Δ . The width of the wells determines the energetic position of the coupling states inside the wells and influences thereby the effective barrier height. States at higher energies find the barriers to be less opaque than those at lower energies.

In an infinitely extended SL, all k -values corresponding to an energy value within an allowed energy region can be occupied. Typically, experimentally realized SLs have a limited number of about 20 – 100 periods. For these finite superlattices, there are only as many different k values as there are SL periods. These SLs are, in general, also treated within the semiclassical theory, even though this theory assumes a large (with respect to the period) macroscopic system size.

Once an electric field F is applied to the SL, the eigenstates of the system are given by the Wannier-Stark states [Wan60]. This is a set of eigenstates in which each member is centered in one of the SL wells (again one state per well) and extends over a number of SL periods. The number of wells across which a Wannier-Stark state extends depends on the strength of the applied electric field and decreases quickly for increasing electric field. The eigenenergies of the Wannier-Stark states are given by

$$E_n = neFd \quad n = 0, \pm 1, \pm 2, \dots, \quad (2.4)$$

where $e = -1.602 \times 10^{-19}$ As is the charge of an electron and n numbers the different SL wells. The spacing of the resulting equidistant energy ladder is given by eFd , an energy value which is equal to the potential drop of the electric field F over one SL period d . Some SL properties can be very conveniently explained within the concept of the equidistant Wannier-Stark energy ladder. Whenever the Wannier-Stark ladder is involved in a discussion in later chapters, only the facts that there is one state per well and that the eigenenergies form an equidistant energy ladder are made use of. More details about the Wannier-Stark states can be found in [Wan60] and in the reviews [Gra95, Wac02b, Leo03]. While the Wannier-Stark states are the true eigenstates of the biased SL, in the limit $eFd < \Delta$, transport can still be described by electrons being accelerated in the miniband structure of the unbiased SL.

2.3 Energy scales and transport regimes

Conduction in a superlattice is an example of transport in mesoscopic nanostructures and in principle requires a quantum mechanical description. At the same time, there exist alternative simpler approaches that offer several advantages to a complete quantum mechanical description. These theories also capture all the important details of the transport. Among their main advantages, they do not need a very detailed microscopic description of the transport properties and they can in large parts be treated analytically. In [Wac02b] a complete quantum approach to superlattice transport was presented and compared to the available alternative descriptions. It was found that the latter ones were in good agreement with the quantum calculations for a large range of superlattice parameters. The available alternatives are the miniband transport model [ET70], the sequential resonant tunneling approach [ML94, Wac98] and the Wannier-Stark-hopping transport model [TD75]. The suggested use of one or the other approach is governed by the ratios of three different energy scales:

1. The overlap integral T_1 between neighboring well states which is equal to one fourth of the miniband width, $\Delta/4$. The larger the overlap is, the wider the miniband width is, which in turn allows then the application of the semiclassical band transport equations.
2. The broadening $\Gamma = \hbar/\tau$ of the individual energy levels due to scattering processes. If the scattering time τ is so short that an electron cannot propagate coherently across a number of wells without being scattered, the transport along the superlattice is best described as sequential tunneling between the individual wells.
3. The voltage drop eFd across one period of the superlattice. This field dependent energy scale shifts the alignment of the Wannier-Stark states of the superlattice. Once its value dominates over Γ , the Wannier-Stark states, the true eigenstates of

the superlattice in an electric field, become resolved. In this situation transport is best described as hopping along the Wannier-Stark ladder.

Figure 2.3, taken from [Wac02b], summarizes how the interplay between these three different energy scales determines which theoretical approach should be chosen to model the transport in a certain SL structure.

If the relaxation times are long and the applied electric fields are not too large, the miniband transport regime is recovered from the full quantum mechanical description. The electron distribution occupies the Bloch states calculated from the Kronig-Penney model and the transport variables are calculated as distribution averages. Each individual Bloch state is accelerated according to the semiclassical transport equations.

If the miniband width is small and the scattering rate $1/\tau$ is short, then, transport cannot be described by extended Bloch states but rather by tunneling between the weakly

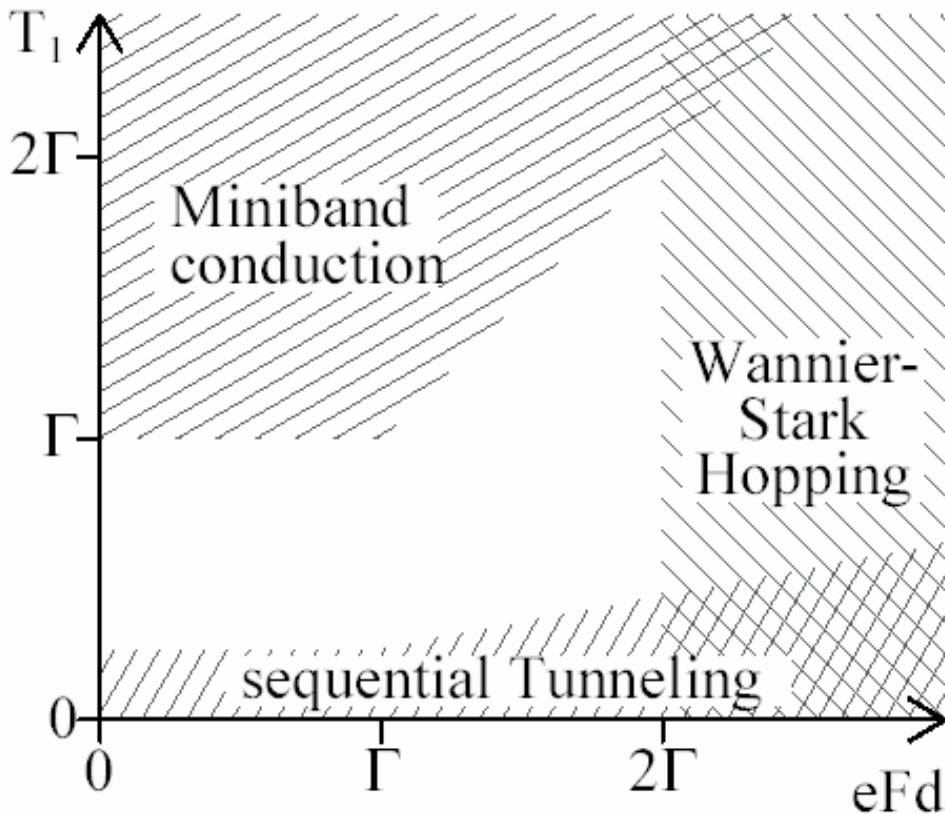


Figure 2.3: The figure (taken from [Wac02b]) shows the regions of validity of the different SL transport descriptions. $T_1 = \Delta/4$ is the overlap integral between neighbouring wells. The axis are scaled in units of the scattering induced broadening $\Gamma = \hbar/\tau$.

coupled localized states of the quantum wells. The current consists of electrons tunneling sequentially along the superlattice. In order to recover a linear transport regime for small applied electric fields, which is observed in experiments, it is important to include the broadening of the localized states due to scattering.

Once the applied electric field dominates the other energy scales, the current through the SL is carried by electrons hopping along the Wannier-Stark states.

Since the devices investigated in the later chapters exhibit rather long relaxation times, they are mainly described in the framework of miniband transport. This approach follows the standard semiclassical theory as applied to band transport in metals and semiconductors [AM76, chapter 12]. But due to the small k -space extension of the first Brillouin zone, the electron distribution starts to feel the non-linearities of the dispersion already for moderate electric fields. In principle, these non-linearities also occur in the conduction band of the host crystals. However, in these natural conduction bands the electric fields required to reach the regions of non-linear transport are so large that other mechanisms like Zener tunneling [Zen34] or intervalley transfer [Kro72] dominate the experimentally observed transport. This is the reason why Esaki and Tsu proposed the artificial SL structure in the first place.

2.4 Semiclassical superlattice transport

The first theoretical SL transport description was given by Esaki and Tsu [ET70]. They considered a single electron sitting at $k = 0$ at time $t = 0$ which is then accelerated along a cosine dispersion. Their simple one electron picture resulted in a velocity-field characteristic whose basic shape is, amazingly, reproduced by all the other more sophisticated transport descriptions applied to superlattices.

From the dispersion (2.2) a velocity

$$v(k) = \frac{1}{\hbar} \frac{\partial E}{\partial k} = \frac{\Delta d}{2\hbar} \sin(kd) \quad (2.5)$$

is found. Each k -state follows the semiclassical acceleration

$$\hbar \frac{dk}{dt} = eF . \quad (2.6)$$

The solution to this equation leads to a linearly increasing k value

$$\hbar k = eFt . \quad (2.7)$$

Due to the periodic SL potential, this results in a periodic motion of the electron both in k - and real space. This oscillatory motion is referred to as a Bloch oscillation. Figure 2.4(a) illustrates one period of such a Bloch oscillation in $k(t)$ -space. At $t = t_0$ the electron starts at the origin and due to the electric field its k -value and its velocity are increasing, $t = t_1$. At $t = t_2$ the velocity reaches a maximum and decreases then, $t = t_3$,

for increasing k until it vanishes right at the mini-Brillouin zone boundary. A further increase in k leads, after Bragg reflection, to a motion in the opposite direction, again first with an increasing velocity, $t = t_4$, followed by a deceleration, $t = t_5$, after going through a maximum. Therefore, if the motion of the electron remains unperturbed, there is no net current flow along the superlattice. A net current flow becomes possible once scattering is introduced into the system. Now, the electron can be backscattered to the origin (inelastic relaxation) after some movement along the dispersion as shown in figure 2.4(b). If scattering is strong, the electron will only move along the linear part of the velocity (2.5). It will acquire an average velocity along the superlattice which in turn leads to a net current flow. So the necessary condition for transport along the superlattice (or any other bandstructure) is scattering of the electrons. However, once the scattering time τ is fixed, only the magnitude of the electric field determines how far an electron travels along the dispersion before being scattered back. While transport is expected to increase with the electric field as long as the electron mainly stays in the linear regime of $v(k)$, it will saturate once the electron travels beyond the maximum velocity. Even more intriguing is the fact that when the electron reaches k -values beyond the Brillouin-zone boundary, the transport will even decrease with increasing electric field since the electron now also takes on negative velocities. If this behavior is translated into a current-voltage characteristic, the superlattice should exhibit a region in which the current *decreases* when the applied voltage *increases*. This uncommon phenomenon is referred to as negative differential conductivity (NDC). It was predicted by Esaki and Tsu as a superlattice property. Some years later, NDC was shown to exist in an Esaki-diode [Esa58].

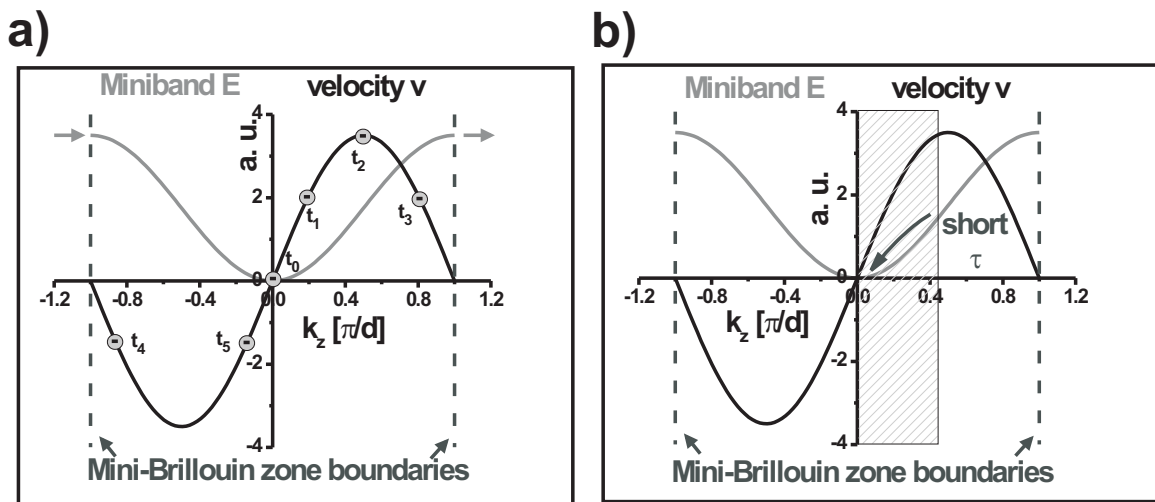


Figure 2.4: (a) Schematic representation of the oscillatory k -space motion of an electron without scattering. (b) Strong scattering effectively limits the k -space velocity to a small region close to the origin.

To find expressions for the velocity and current in a superlattice, we will follow a somewhat different approach [KSS72]. Instead of a single electron, a distribution $f(k, T, \mu)$ of N electrons filling the miniband according to the temperature T and the chemical potential μ is considered. When external fields are applied, the distribution shifts from its equilibrium position according to the Boltzmann equation in relaxation time approximation [AM76, Chapter 16],

$$\frac{\partial f(k, T, \mu)}{\partial t} + \frac{eF}{\hbar} \frac{\partial f(k, T, \mu)}{\partial k} = -\frac{1}{\tau} (f(k, T, \mu) - f_0(k, T, \mu)) . \quad (2.8)$$

$f(k, T, \mu)$ is the non-equilibrium distribution function which relaxes back to the equilibrium distribution $f_0(k, T, \mu)$ when the electric field F is turned off. The average drift velocity v_d of an electron along the superlattice is then given by the velocity average over the whole distribution

$$v_d = \frac{1}{N} \int_{-\pi/d}^{\pi/d} v(k) f(k, T, \mu) dk . \quad (2.9)$$

To gain further progress, both the non-equilibrium and equilibrium distribution are expanded in a Fourier series according to

$$f(k, T, \mu) = \sum_{n=-\infty}^{\infty} a_n(T, \mu) e^{inkd} \quad (2.10)$$

and

$$f_0(k, T, \mu) = \sum_{n=-\infty}^{\infty} a_n^0(T, \mu) e^{inkd} . \quad (2.11)$$

From the Boltzmann equation a relation between the expansion coefficients a_n and a_n^0 of the form⁵

$$a_n = \frac{a_n^0}{1 + \frac{eF\tau d}{\hbar} in} \quad (2.12)$$

is found. With this expression the drift velocity can be expressed as

$$v_d = \frac{1}{N} \int_{-\pi/d}^{\pi/d} \frac{\Delta d}{2\hbar} \sin(kd) \sum_{n=-\infty}^{\infty} \frac{a_n^0}{1 + \frac{eF\tau d}{\hbar} in} e^{inkd} dk . \quad (2.13)$$

Since the velocity has a sine form, only the terms with $n = \pm 1$ of the sum contribute to the integral. The final result for the drift velocity is given by

$$v_d = F(T, \mu) \frac{\Delta d}{2\hbar} \frac{\omega_B \tau}{1 + \omega_B^2 \tau^2} , \quad (2.14)$$

where $F(T, \mu)$ is the ratio a_1^0/a_0^0 between the first and zeroth order Fourier coefficient of the equilibrium distribution function and $\omega_B = eFd/\hbar$ is the Bloch frequency. The velocity-field characteristic (2.14) is plotted in figure 2.5(a). It shows the same behavior

⁵For clarity, we have dropped the dependence on temperature and chemical potential.

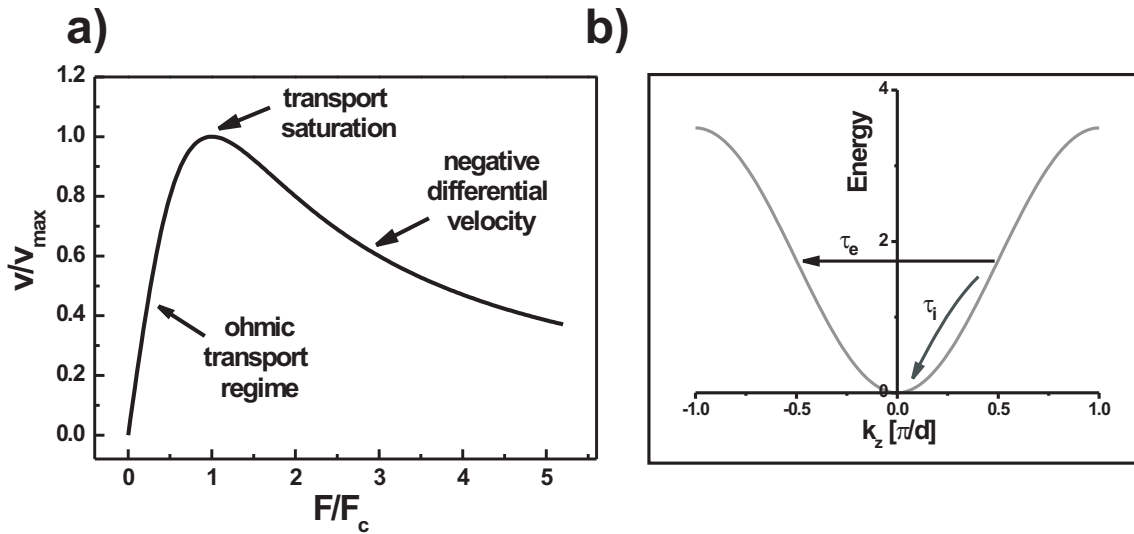


Figure 2.5: (a) Velocity-field characteristic for a cosine-shaped miniband. (b) The arrows indicate elastic (τ_e) and inelastic (τ_i) scattering processes in a one-dimensional superlattice structure.

as we inferred from the simple single electron picture. For small electric fields, transport is practically ohmic, whereas a velocity saturation followed by a region of negative differential velocity is observed for higher fields. In the latter region a large portion of the electrons performs Bloch oscillations, and, therefore, they do not contribute to the overall transport. This portion of Bloch oscillating electrons further increases with the electric field and would in the limit of diverging field encompass the whole distribution. From $j = env_d$ we find that the current-voltage characteristic follows the same shape as the velocity-field trace (assuming a homogeneous electric field distribution). From 2.14 the position of the current maximum, referred to as the NDC peak, is found at the critical field

$$F_c = \frac{\hbar}{ed\tau} . \quad (2.15)$$

This expression can be rewritten in the form $\omega_B(F_c)\tau = 1$.

So far, scattering has been introduced into the problem without any regard towards the nature of a scattering event. In the presented semiclassical description this has minor consequences since the relaxation time approximation ignores the detailed microscopic pictures of scattering processes. However, figure 2.5(b) indicates that elastic and inelastic scattering should be treated independently. While both processes destroy the coherent Bloch oscillation, only inelastic ones relax energy and scatter the electron back toward the origin as was assumed above.

The difference between elastic and inelastic scattering processes was first considered in [KSS72]. The authors replaced the simple relaxation time approximation in equation

(2.8) by dividing the distribution function into its symmetric and antisymmetric part. They could introduce independent relaxation time approximation terms for both parts since the total energy is the integral over the symmetric part of the distribution while the drift velocity is the sum over the antisymmetric part. Energy is relaxed only by inelastic scattering with a characteristic time τ_i . The velocity, proportional to the antisymmetric part of the distribution, depends both on elastic and inelastic scattering. Therefore, for this part of the distribution the elastic and inelastic scattering rates have to be added, resulting in the relaxation time $\tau = \frac{\tau_i \tau_e}{\tau_i + \tau_e}$. From this approach a velocity-field characteristic of the form

$$v_d = F(T, \mu) \delta^{1/2} \frac{\Delta d}{2\hbar} \frac{\omega_B \tau}{1 + \omega_B^2 \tau \tau_i}, \quad (2.16)$$

is derived [SS84, IDS91, WSG⁺97], where $\delta = \tau/\tau_i$. Except for the term $\delta^{1/2}$ this resembles the earlier result 2.14. However, for strong elastic scattering, $\tau \approx \tau_e$, the peak current becomes strongly reduced since $\delta \ll 1$. This essentially reflects the fact that elastic scattering does not relax energy but rather leads to a heating and, therefore, strong broadening of the electron distribution. This will be discussed in greater detail in chapter 5, where we will apply an even more realistic model to determine the transport parameters in surface SL samples. There, also the free direction(s) perpendicular to the superlattice axis are included, which have so far been ignored in the presented analysis.

2.5 The Esaki-Tsu Bloch oscillator

In their original proposal of the superlattice structure, Esaki and Tsu also estimated the frequency of the Bloch oscillations in a superlattice. For a typical scattering time of 0.3 ps and a SL period of 10 nm, one finds a critical field F_c of 2.2 kV/cm. For a field of $3F_c$, deep in the NDC region, for which a large portion of the electrons perform Bloch oscillations, a Bloch frequency ω_B of 10 THz is found. Since this corresponds to an oscillation frequency f_B of about 1.6 THz, Esaki and Tsu proposed to use the superlattice as a solid state THz source. They imagined that the oscillating electrons should emit an electromagnetic field at their oscillation frequency. In the following two paragraphs we will see that this simple picture of Bloch oscillations as a THz source cannot be upheld. Since the presence of an electromagnetic field strongly influences the superlattice transport, it is necessary not only to study the **static** transport in a superlattice but more importantly the **dynamic** conductivity. The latter determines the response of the superlattice to the presence of a high-frequency field. Nevertheless, it is interesting to note that so far the only experimentally measured THz emission from a superlattice [WRS⁺93, SHOC03] was in exact correspondence to the simple early oscillator picture. Electron-hole pairs were created in an undoped superlattice by interband excitations through a short laser pulse. The SL was biased in the NDC region. The electron-hole pairs performed Bloch oscillations similar to electrons in the superlattice and the radiation emitted from these oscillations was detected. The important difference to an electrically pumped superlattice is, however,

that the electron-hole pairs were excited coherently through a laser pulse, which in turn caused them to Bloch oscillate coherently. If Bloch oscillations are excited only by a static electric field, they have no phase coherence. It can therefore not be deduced from this experiment that a SL Bloch oscillator would emit at the Bloch frequency.

2.6 The dynamic superlattice conductivity

In order to understand the gain properties of a biased superlattice, it is necessary to study its dynamic conductivity $\sigma(\omega)$. This was first undertaken by Ktitorov and co-workers [KSS72]. They extended the formalism which was used in section 2.4 to the situation where an additional time-varying electromagnetic field is present. Working in the limit of small amplitude of the alternating field, which allowed the linearization of the Boltzmann equation, they found a high-frequency conductivity of the form

$$\sigma(\omega) = \sigma_0 \frac{1 - \omega_B \tau_e \tau_i - i\omega \tau_i}{(\omega_B^2 - \omega^2) \tau_e \tau_i + 1 - i\omega(\tau_e + \tau_i)} \quad (2.17)$$

with

$$\sigma_0 = \frac{F(T, \mu) \frac{ne^2\tau}{m}}{1 + \omega_B^2 \tau_e \tau_i} = \frac{\sigma_{00}}{1 + \omega_B^2 \tau_e \tau_i} . \quad (2.18)$$

Here, τ_i and τ_e again stand, respectively, for the inelastic and elastic relaxation times and σ_{00} is the Drude conductivity. A long-wavelength electromagnetic wave which is proportional to $\exp(-\alpha x)$ has a propagation constant whose conductivity dependent part α is determined by [AD00]

$$\alpha = \frac{\sigma(\omega)}{\sqrt{\epsilon \epsilon_0} c} . \quad (2.19)$$

Thereby, ϵ is the dielectric number, ϵ_0 the dielectric constant and c the vacuum speed of light. From this, we find that the sign of the real part of the dynamic conductivity determines whether the wave is attenuated or whether it grows. The former situation corresponds to a positive sign and the latter to a negative when the wave travels along the positive x -axis. The real part of expression 2.17 is plotted in figure 2.6(a) for the cases of $\omega_B \sqrt{\tau_i \tau_e} < 1$ and $\omega_B \sqrt{\tau_i \tau_e} > 1$. In the first case, the dynamic conductivity takes on only positive values. In this regime the biased superlattice acts purely as an attenuator for the alternating electric field. But for electric fields which fulfill the opposite limit of $\omega_B \sqrt{\tau_i \tau_e} > 1$, the real part of the dynamic conductivity remains negative for all frequencies up to the Bloch frequency. In this region, the biased superlattice represents an active gain medium for frequencies up to the THz range. The optimum gain is found in the resonance feature close to the Bloch frequency. Therefore, the emission frequency of a Bloch oscillator will always be smaller than the Bloch frequency. This is in contrast to the simple Esaki-Tsu picture.

It was mentioned at the beginning of the discussion that the results of Ktitorov *et al.* are only valid in the limit of small alternating field strength. Moreover, they

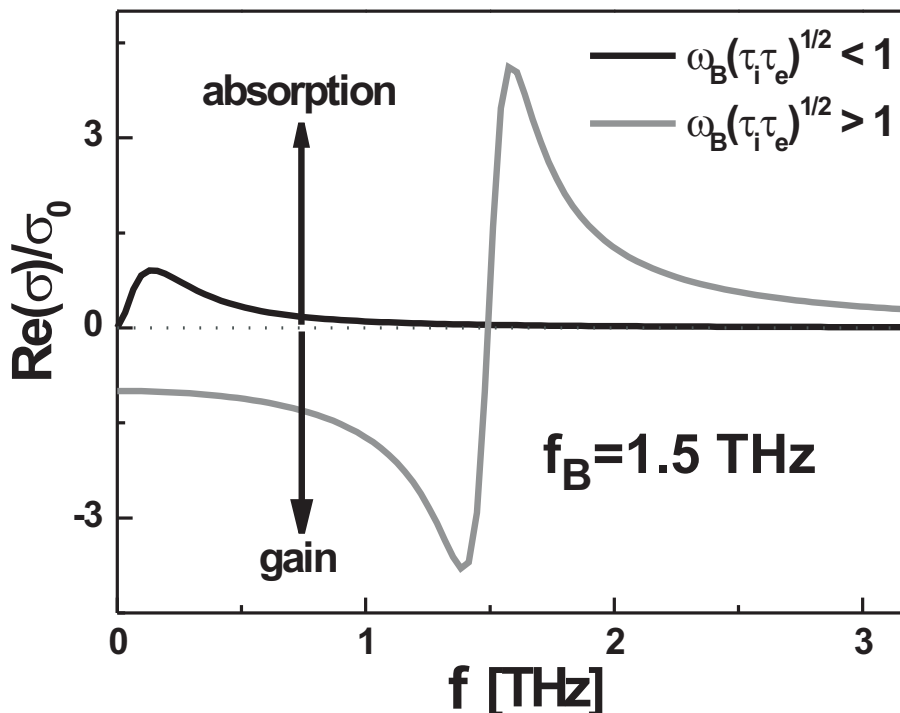


Figure 2.6: The figure shows the real part of the dynamic conductivity $\sigma(\omega)$ of a superlattice calculated according to equation (2.17) in the limits of a small ($\omega_B\sqrt{\tau_i\tau_e} < 1$) and large ($\omega_B\sqrt{\tau_i\tau_e} > 1$) applied static electric field.

were also assuming an electric bias that produces a Wannier-Stark splitting well below the width of the miniband. In the last couple of years, also in connection with the development of quantum cascade lasers in the far infrared region, new theoretical approaches were developed that extend the validity of expression (2.17) to a much larger range of parameters. Kroemer [Kro03] extended the Ktitorov result to the regime of high electric fields, providing at the same time a semiclassical picture of the origin of the amplification. We will return to this in more detail in chapter 7, where the dynamic DC transport in surface SL structures is investigated. In [SDR03] the one-dimensional results by Kroemer were confirmed by three-dimensional Monte-Carlo-simulations. Willenberg *et al.* [WDF03] applied the density matrix formalism in order to calculate general gain curves for intersubband transitions. Their approach is a generalization to the work of Kazarinov and Suris [KS72] whose predictions led to the development of quantum cascade laser structures. For high temperatures, Willenberg *et al.* find excellent agreement between their quantum mechanical results for gain in a superlattice structure and the semiclassical solution of the Boltzmann equation. For lower temperatures they find even higher maximum gain. A good agreement between semiclassical and quantum-mechanical gain calculations was also found by Wacker [Wac02a] who applied

the non-equilibrium Green's functions formalism to the problem of a biased superlattice. Experimental evidence for the calculated shape of the gain curve was given by Shimada *et al.* [SHOC03] who derived the high-frequency conductivity from the THz emission of time-domain THz spectroscopy measurements. They found excellent agreement between their results and the semiclassical predictions. Savvidis *et al.* [SKLA04] also found that the change in THz transmission through their super-SL structure, when it was biased during a THz pulse, coincided closely with a semiclassical calculation.

2.7 The Bloch oscillator

From the last section we can conclude that by a Bloch oscillator we mean a super-critically biased ($F > F_c$), doped superlattice structure which exhibits gain for all frequencies below the Bloch frequency. In order to turn this into an active coherent oscillator, the structure must be combined with an appropriate waveguide for the THz region. Then, the emission frequency will be determined both by the gain characteristic and the properties of the waveguide. The superlattice oscillator is in principle a widely tunable device since the maximum gain lies close to the Bloch frequency which can simply be shifted by the magnitude of the applied DC electric field. Whenever the term Bloch oscillator is mentioned in the following sections, we always have a device in mind which corresponds to this definition.

The discussion in the preceding section showed that a biased doped superlattice is expected to exhibit gain in the THz frequency range. The question that needs clarification is, why there exists no Bloch oscillator to date. The single dominant reason for this can be traced back to the instability of the situation in which a large bias is applied to a device exhibiting NDC, as it occurs in superlattices. All the forgoing discussions assumed a homogeneous electric field distribution along the superlattice structure, even in the NDC region. However, this situation could so far only be realized experimentally in a few systems through the application of a strong THz field. For biased doped superlattices with realistic field distributions no gain has been predicted in the limit of small THz fields, a property which is necessary for the turning on of an active oscillator.

But before this problem is addressed in detail in chapter 4, an introduction into the technological realization and the electronic properties of surface superlattice structures is given.

Chapter 3

Surface superlattices realized by Cleaved-Edge Overgrowth

3.1 Overview

Modulated two-dimensional electron systems have almost exclusively been realized by the application of lithographic processes. However, even with electron beam lithography the modulation period cannot be pushed significantly below 50 nm and the resulting modulation strengths are too small to force the formation of energetically separated minibands.

In 1990 Pfeiffer *et al.* [PWS⁺90] realized a two-dimensional electron system directly on the (110) cleavage plane of a [001] oriented GaAs substrate. The applied method came to be known as the Cleaved-Edge Overgrowth (CEO) method. With the same approach Stormer *et al.* [SPB⁺91] fabricated an atomically precise, short-period modulated two-dimensional electron system, i.e. a surface superlattice. However, since the applied modulation doping led to a Fermi energy far below the top of the miniband, magnetotransport measurements only showed the formation of a two-dimensional electron system. Magnetotransport in surface SLs is discussed in detail in chapter 8. In [MRT⁺00] the same technique was applied to realize a surface SL structure. In addition to the modulation doping, the device was equipped with an aluminum gate in order to vary the electron density in the two-dimensional channel. They also observed purely two-dimensional behavior.

The first non-equilibrium transport studies on CEO surface SLs were reported by [KZT⁺95], who used liquid phase epitaxy for the overgrowth step. High quality CEO surface SLs with wide range tunable densities were first realized by Deutschmann [DWR⁺00, DLW⁺00]. The work of this thesis is based on similar samples and their structure will be discussed in detail in this chapter and in chapter 5.

The quality of conventional SLs depends mainly on the MBE growth. For high quality surface SL structures this requirement is not only expected for growth along the typical [001] direction, but also for growth along the perpendicular [110] direction. The MBE machines used for the sample growth during the time period of this work continuously produced two-dimensional electron systems with mobilities beyond 10^7 cm²/Vs and $3 \times$

10^6 cm²/Vs for the [001] and [110] directions, respectively.

The following sections give a detailed account of how the surface SL structures of this work were realized and how their equilibrium electronic properties were calculated. The band structure calculations are performed with a self-consistent Schrödinger-Poisson solver. Results similar to the presented ones have also been found in a perturbation calculation approach [GVB⁺03, GBE⁺02]. The last section gives a short discussion about the standard measurement technique.

3.2 Technological realization

The term surface superlattice refers in this work to a two-dimensional electron system that has a strong, short-periodic modulation in its immediate vicinity. All presented structures are realized through growth on the cleaved surface of an undoped conventional superlattice. Figure 3.1 shows a cut through the sample in a plane spanned by the two subsequent growth directions. The initial MBE growth is performed on a standard semi-insulating [001]-oriented GaAs substrate. The growth is started with a thin layer of GaAs followed by a transition SL, since the alternation between the two materials of this SL leads to a smoothing of the growth surface. Both layer sequences are not shown in figure 3.1 as they have no influence on the transport properties of the surface SLs. Alternatively, it is possible to work on n+-doped GaAs substrates. In this case the lower doped n+-layer of figure 3.1 is immediately grown on top of the wafer. The lower n+-contact is followed by the GaAs/Al_xGa_{1-x}As SL structure which acts as the modulation potential for the two-dimensional electron system. The first growth step ends with another n+-GaAs layer on top of the SL. The two n+-layers are used to contact the surface SL.

After the first growth step, the sample is removed from the MBE machine and is thinned to a thickness of about 100μm by chemical polishing, which is necessary in order to achieve an atomically precise cleave. The wafer is then cut into small rectangular pieces which are marked with a small scratch along the [1-10] direction. The scratch predefines the line along which the piece of wafer is cleaved before the second growth step. Mounted standing on a special holder, the pieces are put back into the MBE chamber, where they are cleaved and immediately overgrown. This second growth step starts with an optional GaAs quantum well which is referred to as the cleaved-edge well (CEW) throughout this work. This well is followed by an Al_xGa_{1-x}As barrier which essentially acts as a non-conducting dielectric barrier between the two-dimensional electron system and the n+-doped GaAs layer which completes the second growth step.

The wafer pieces are then taken from the machine and a mesa is etched to reveal the buried n+-GaAs layer. Multiple samples are cleaved from each wafer piece and ohmic contacts are applied to the three n+-layers. The ohmic contacts are made from annealed indium. The sample is finally mounted on a small piece of circuit board, gold wires are attached and everything is soldered to a standard IC socket. The individual steps of the

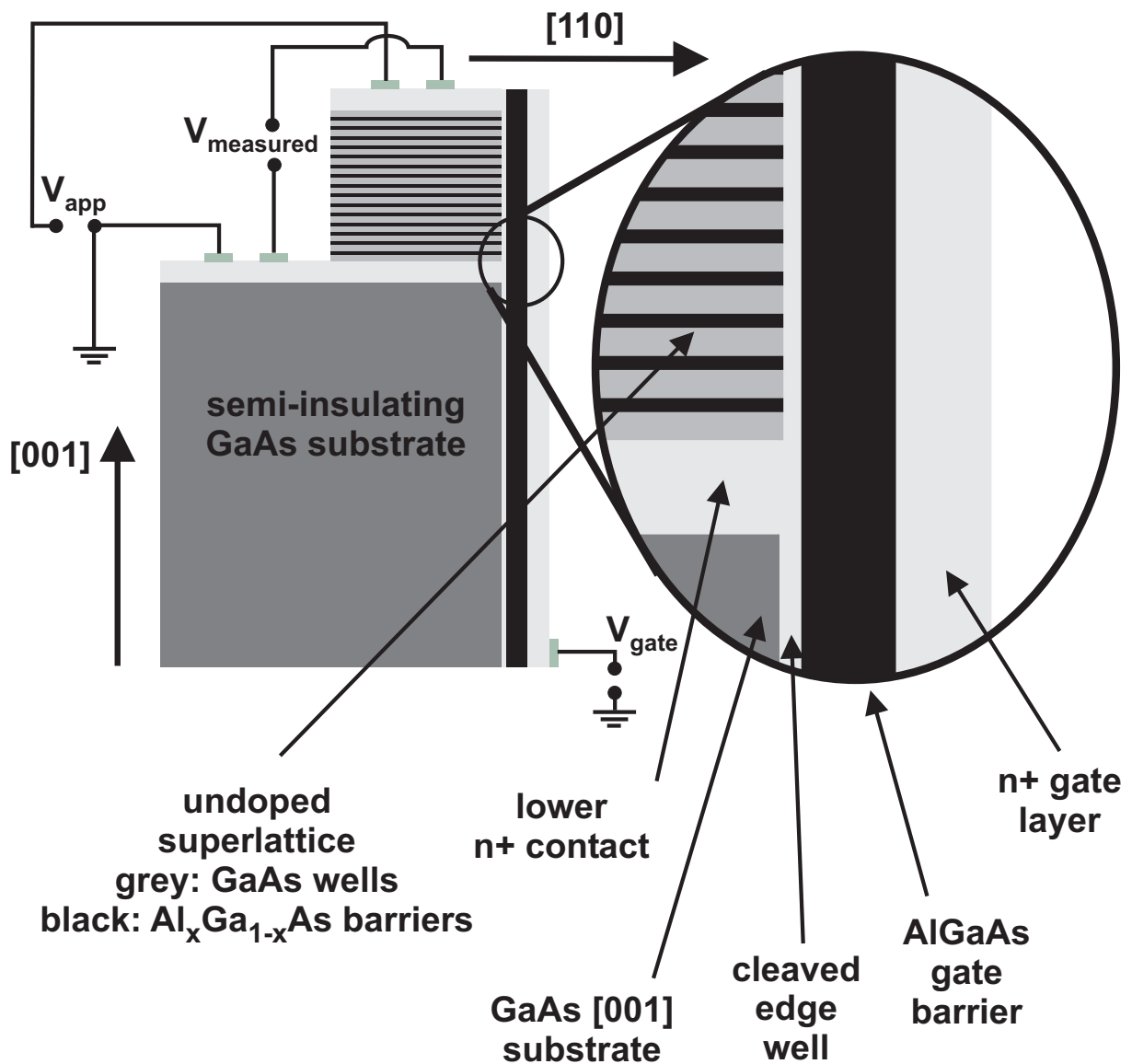


Figure 3.1: Schematic drawing of a surface superlattice structure.

realization of a surface SL are summarized in figure 3.2.

3.3 Basic electronic properties

Without additional bias, the structure described in the last section is electrically inert. The surface superlattice needs to be switched on since there is no doping in the CEW of the second growth step. The opening of the two-dimensional channel is achieved by applying a positive electric bias to the n+-layer of the second growth step. This part will from now on be referred to as the gate. The gate potential can be defined with respect to one of the other two n+-contacts attached to the undoped SL. The gate bias leads to a bending of the conduction band at the interface between the CEW and the dielectric

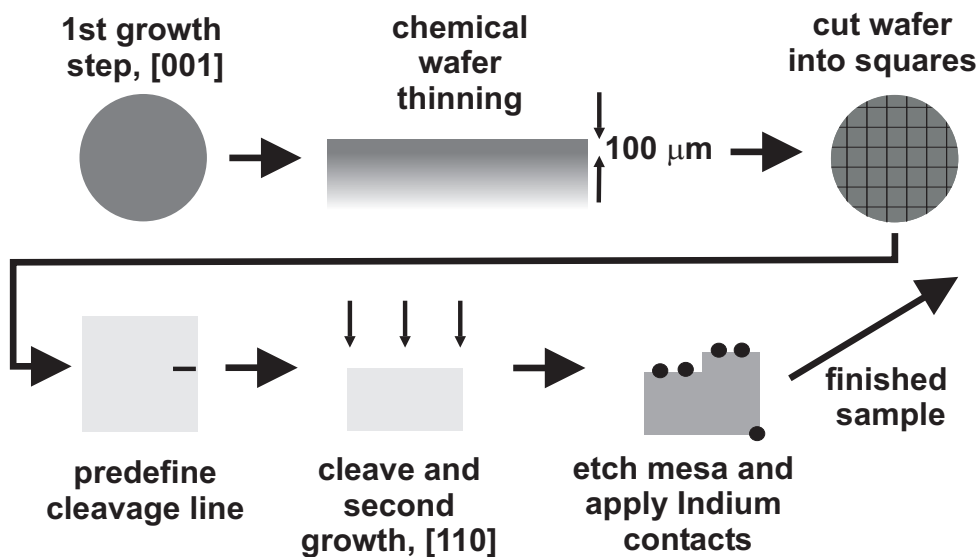


Figure 3.2: Preparation steps for the realization of a surface superlattice.

gate barrier. At a critical voltage, electrons start to flow into the interface region and a two-dimensional electron layer is formed through which transport can be studied by the application of an additional bias between the two SL contacts. All applied voltages are defined with respect to the same ground potential (cf. figure 3.1). The situation is similar to the working principle of a field effect transistor [Sze81, Chapter 8], although the contacts applied to the two-dimensional channel are quite different in the two structures.

Just as in the case of transport through a conventional SL, the band structure has to be known in order to describe the transport through the sample. Unfortunately, the effective potential experienced by the electrons at the interface between SL and gate barrier is more complicated than in the original SL problem. The increased complexity results from the two-dimensional confinement both due to the SL potential and the triangular gate induced potential. Neither the localized states within one quantum well as needed for a tight binding calculation, nor possible quasi-free states as input for a Kronig-Penney problem like approach can easily be deduced. Additionally, the electric charge of the electrons in the two-dimensional channel strongly influences the total potential. Therefore, it becomes necessary to self-consistently solve the Schrödinger and Poisson equations.

The input parameters for this calculation are the grown material sequences, the doping profile of the layers, and the boundary conditions of the device, including any applied bias. The Schrödinger and Poisson equations are then solved recursively until stable solutions for both equations are found. The calculation usually yields the quantized electronic states in the system together with the corresponding wave functions and gives the electron density distribution inside the simulation area. Already in an arbitrary one-dimensional problem the numerical solution process becomes quite intricate and complex. In two dimensions the situation becomes even worse. Fortunately, the simulation of nanostructures has become an active field itself in solid state physics and has yielded a number

of non-commercially available simulation tools. All device simulations shown throughout this work were performed with the program `nextnano3`,¹ developed at the Walter Schottky Institut in the framework of *Sonderforschungsbereich 348*. For details concerning the internal structure of the simulation tool we refer the reader to *www.nextnano.de*.

3.4 Self-consistent device simulations

Before we embark on the summarization of the device parameters of the studied surface SLs, it seems advisable to study one specific simulation in more detail. The input for such a simulation consists of the active region of a device as sketched in figure 3.1. For the undoped superlattice we choose, in accordance with actual devices, wells of 12 nm and barriers of 3 nm width. The doping density in the n+-layers and the gate contact is $5 \times 10^{17} \text{ cm}^{-3}$, a value also taken from measurements. The width of the CEW is 10 nm and the number of superlattice periods was limited to 25. Although real structures have sometimes more than 100 periods, the results do not change significantly for larger number of periods and a smaller simulation region helps to speed up the anyhow lengthy simulations. The doped layers are included in the calculation in order to study how the surface SL is connected to its contacts. A positive gate voltage is applied, but there is no bias across the undoped superlattice structure. Simulations with an applied SD-bias were also attempted, however, `nextnano3` did not yield reliable results in this situation, if any.² The calculated equilibrium band structure will later be used as input for a semiclassical transport description in surface superlattices.

The current in this structures is carried by electrons occupying the conduction band between the doped regions. Figure 3.3(a) shows the calculated shape of the conduction band edge. The Fermi energy which divides the occupied from the empty states lies at $E = 0 \text{ eV}$, and all areas shown in a dark gray color³ lie below this value. The doped contact layers on the outside of the structure along the [001] direction naturally show a dark gray color.

Between them the superlattice conduction band shows the regular discontinuous steps of the GaAs/Al_{0.3}Ga_{0.7}As heterojunctions. For both wells and barriers the band edge lies above the Fermi energy which reflects the fact that the SL region is undoped. Later, it will be seen that this is not strictly true since there is some unintentional doping. The level of this doping is, however, rather small and results in a very small current density.

In the [110] direction it is found that the applied gate bias bends the conduction band downwards. The band edge in the CEW is pulled below the Fermi energy and electrons

¹An other simulation tool called Aquila [Rot99] was initially also used and showed results in good agreement with `nextnano3`. Due to problems with non-periodic boundary conditions its use was discontinued.

²Newer versions of the program show major improvements for two-dimensional simulations, so this problem might now be tractable. Nevertheless, for devices as introduced in the next chapter, the simulations would require an unacceptable running time.

³except for the top of the barriers in the SL.

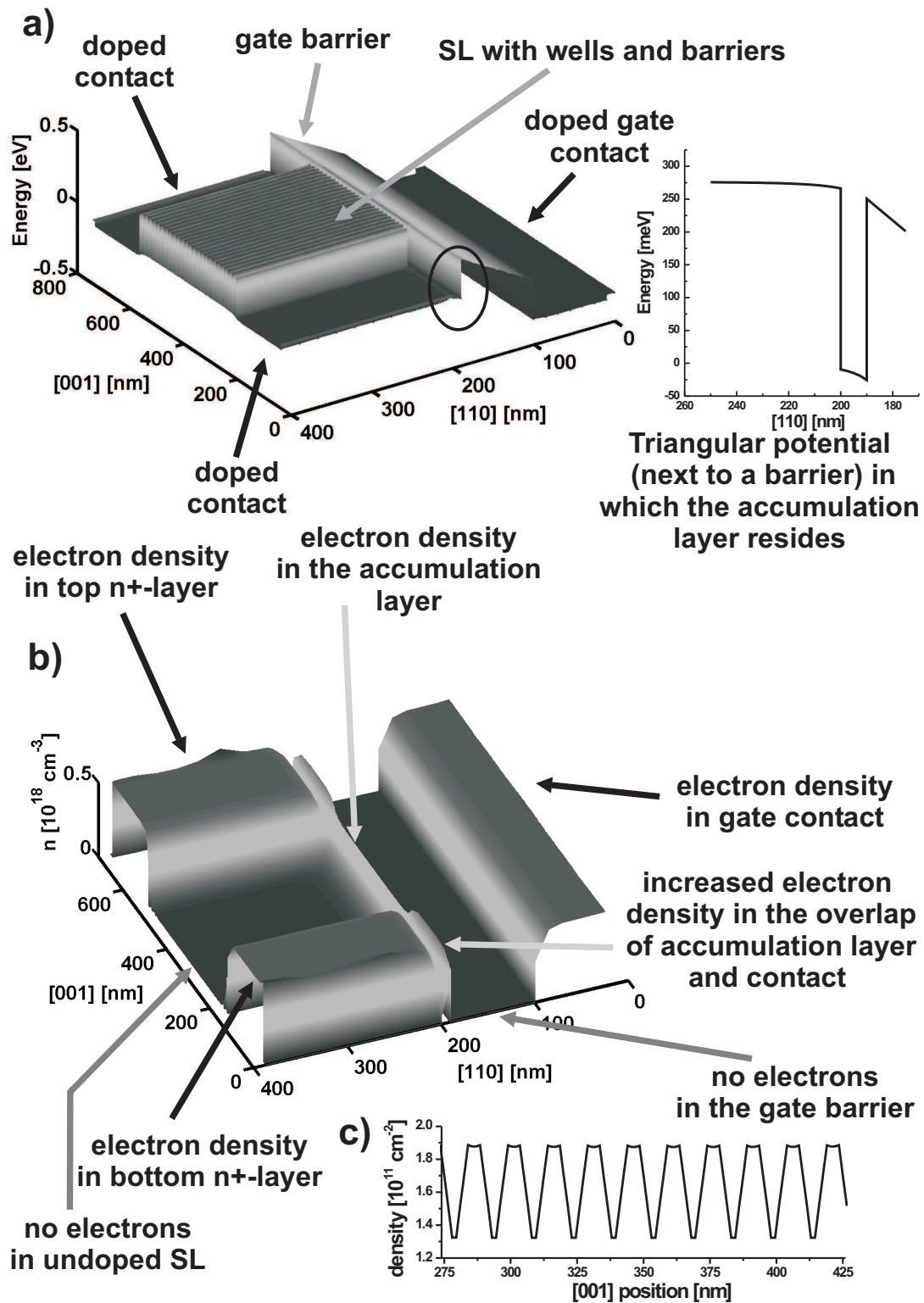


Figure 3.3: (a) Bandstructure and (b) density resulting from a two-dimensional device simulation. Graph (c) shows part of the integrated density of the two-dimensional channel.

from the contacts flow in and form a conducting layer (cf. right part of figure 3.3(a)). The band discontinuity of the gate barrier prevents these carriers from escaping into the gate contact. The Fermi energy of the gate contact is offset from $E = 0$ eV by 0.3 eV due to the gate voltage.

Figure 3.3(b) shows the electron density resulting from the same quantum mechanical calculation. It nicely reveals how the electrons build up an accumulation layer inside the CEW. This charge accumulation is not restricted to the undoped superlattice region, but is also found in the doped contact layers. In this side region an even larger electron sheet density is found in the CEW. These electron rich areas ensure that the doped layers act as low resistance ohmic contacts for the two-dimensional channel. A two-dimensional density inside the accumulation layer can be calculated by integration of the density n along the [110] direction. The corresponding result, depicted in figure 3.3(c), shows a strong periodic modulation. The electrons show an increased probability of being found in the region next to a SL well. For all semiclassical calculations we work with the average charge density in the channel.

The band structure $E_n(k)$, the starting point for all semiclassical calculations, can be deduced from the eigenvalues and wavefunctions of the quantum mechanical states in the accumulation layer. Figure 3.4(a) shows the obtained energies. Only eigenvalues for extended states are considered.⁴ The energies are sorted by increasing value and are plotted against their respective numbers. We see that the states deviate from the free electron parabola, and forbidden energy regions originate. This result is very similar to the miniband and minigap formation in conventional SLs. This analogy is based on a visual comparison since the energies are plotted versus eigenvalue number, whereas the SL dispersion relates the energy to the Bloch wavevector k . However, since only the energies for extended states are plotted, each of these states corresponds to one Bloch wavevector k . And since we know from conventional superlattices that the gaps occur at the miniband Brillouin zone boundary, the individual minibands can be shifted back into the first minizone. In this process, one has to distinguish between a shift of the lowest energy to the origin and a translation by a reciprocal lattice vector of length $2\pi/d$. The decision is based on whether the minibands originate from the ground and excited states of the SL potential (as in conventional SLs) or from the ground and excited states of the gate induced confinement.

When the modulation potential in [001] direction is so strong that no mixing of the SL well states occurs, then, the overlapping confinements of the superlattice wells and the triangular well produce isolated quantum wire states in the accumulation region. These states can easily be distinguished by their number of nodes in the [110] direction. The n th state of the triangular well has $n - 1$ nodes [Dav98]. For weaker SL modulation strength, the states in the SL wells mix and form minibands. This occurs independently

⁴The simulations also produce eigenenergies with localized wavefunctions. These states are artificially produced by the calculation due to the boundary conditions on the quantum region which covers only the small part of the accumulation layer and not the whole device. These states are ignored.

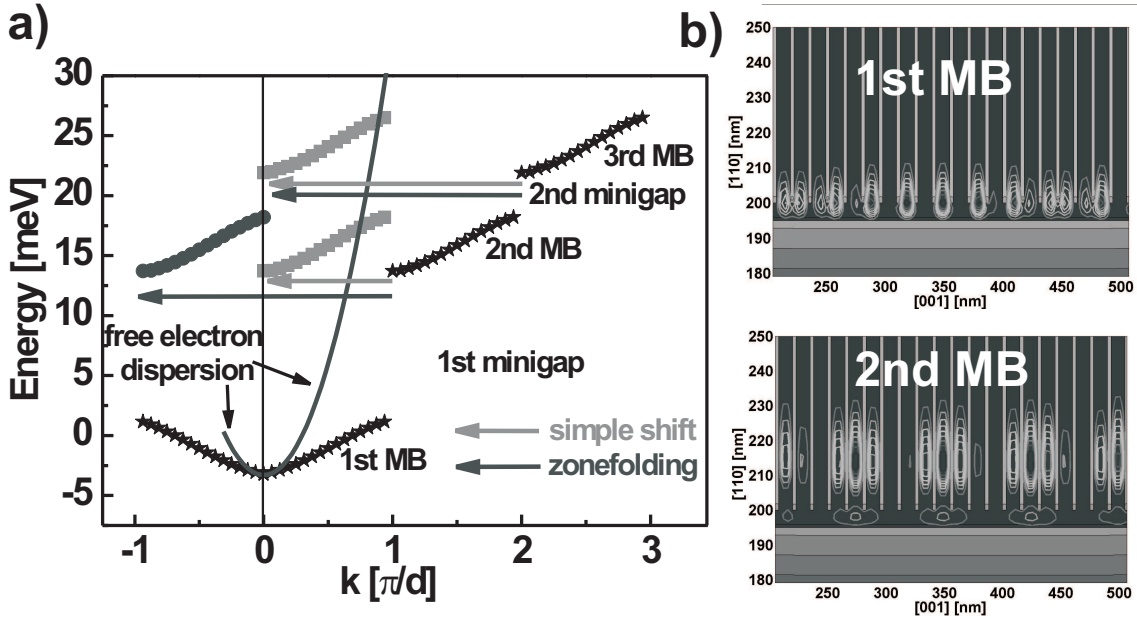


Figure 3.4: (a) Energy eigenvalues of a two-dimensional device simulation. (b) Wavefunctions, each belonging to one individual eigenenergy of the lowest (upper plot) and first excited (lower plot) miniband.

for each state of the triangular well. Thereby, the number of nodes in the $[110]$ direction will not change. Thus, the minibands can be distinguished by the number of nodes in the second growth direction. In figure 3.4(b) two wavefunctions of states lying in the first and second miniband are plotted. We see that the state of the first miniband has no node along the $[110]$ direction. But the state of the second miniband possesses one node. Therefore, the lowest miniband is formed from the ground state of the triangular well, whereas the second miniband results from the first excited state of the triangular confinement potential. The states of the third miniband possess two nodes (not shown). Thus the shown minibands originate from the ground and excited states of the gate induced confinement. No excited state of the SL confinement potential participates in the formation of the calculated minibands. This means that all shown minibands have to be shifted back to the origin. A translation by a reciprocal lattice vector would apply only to a miniband formed from an excited state of the SL confinement potential. However, such minibands are found at very large energies since the SL confinement is much stronger than that of the triangular well. The number of states which would need to be computed in order to find them is beyond the abilities of the simulation program. One more thing to note about the excited minibands is that, due to their excited nature, the probability distribution of their eigenstates is shifted into the undoped superlattice region. Thus, electrons in these minibands experience a stronger modulation than those in the lowest miniband. On one hand this results in a weaker coupling with smaller resulting miniband

widths. On the other hand, any intraband relaxation due to the superlattice potential is much stronger for these electrons.

The energy gaps of the surface superlattices are much smaller than those found for conventional superlattices with identical parameters. Thus, one could infer that electrons can much more easily escape to excited minibands once a strong electric field is applied. But this is not necessarily true. The reason for this is that the different minibands result from the overlap of states that belong to different energy eigenvalues in the gate induced triangular confinement. In the ideal case, these different eigenstates are orthogonal to each other, and thus the wavefunctions of different minibands can be expected to have very small spatial overlap. This in turn makes a transition of electrons from one miniband to the other very unlikely. We will see in later sections that the transport characteristics indeed show no such transition between minibands.

For a fixed SL potential, the simulation results depend mainly on two device parameters:

1. Thickness of the CEW:

Figure 3.5 shows the eigenenergies of surface superlattices as described above for CEW widths of 0 nm, 5 nm, 10 nm and 20 nm. The applied gate bias was the same in all four cases, resulting in almost identical densities. For each lowest miniband a cosine fit with a dispersion as given in equation (2.2) is also plotted.

There is a number of distinct features that change with the CEW width. The miniband width strongly increases as the CEW becomes thicker. This is readily understood since a thicker well leads to a reduced strength of the modulation potential, which in turn leads to a stronger coupling between the quantum wire states, reflected in wider minibands. In the limit of an extremely thick CEW, the dispersion is expected to resemble the GaAs band structure without any gaps since the modulation strength vanishes. This return to the pure GaAs behavior is also clearly seen in figure 3.5 by the shift of the inflection point of the miniband towards the mini-Brillouin zone boundary. The position of this point is given by the k -value where the effective mass $m(k) = \hbar^2 \left(\frac{\partial^2 E}{\partial k^2} \right)^{-1}$ changes its sign from positive to negative. Such a point exists since the dispersion has to be flat at the zone boundary (cf. discussion in [AM76, Chapter 9]). For the strongest modulation (0 nm CEW) this point lies at $\pm\pi/2d$. In this case, the cosine fit is close to perfect. But even for the 10 nm CEW the cosine fit is still not too bad. A wider CEW also reduces the extension of the forbidden energy ranges. This is again due to the reduced influence of the modulation potential. Thus, in our structures the CEW width introduces a new design parameter which allows to tune bandwidth and gaps in opposite directions.

2. Gate voltage:

The value of the applied gate voltage has a profound influence on the band structure. A larger gate bias results in a steeper triangular potential confinement. This leads

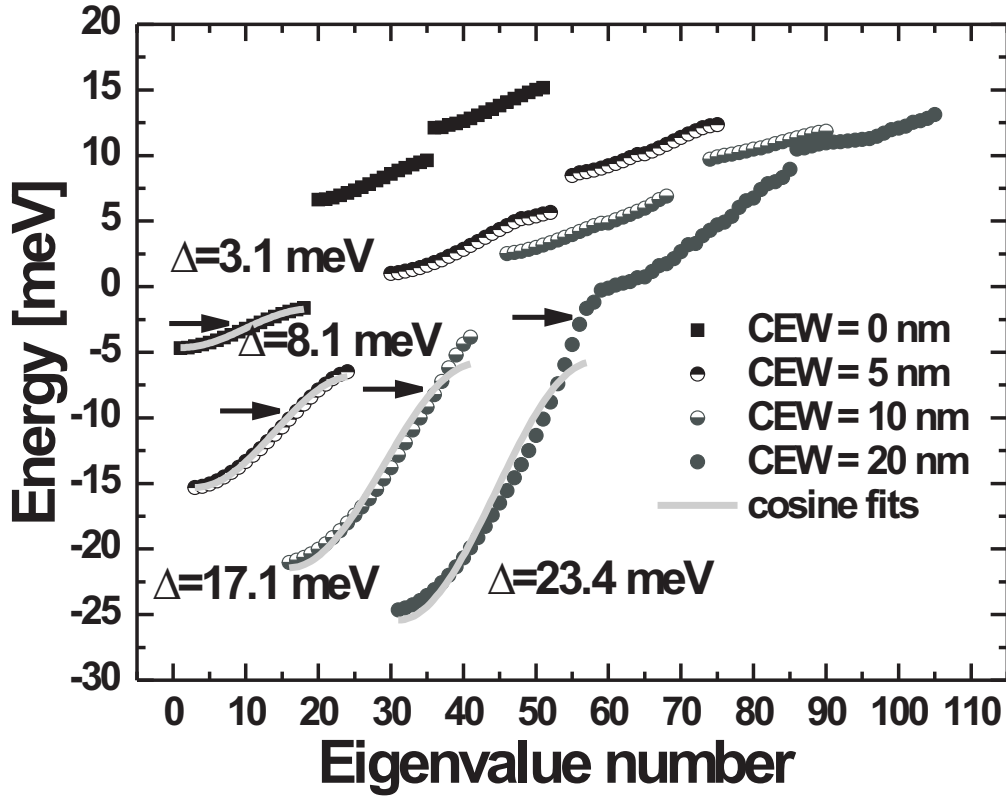


Figure 3.5: Calculated miniband structures of surface superlattices with identical superlattice structure, but different cleaved-edge well (CEW) thicknesses. The gray lines show fits with the cosine approximation. For clarity the data for different CEW-samples have been offset laterally. The position of the inflection point in the lowest minibands is marked by a horizontal arrow.

on one hand to an increasing electron density in the accumulation layer and is accompanied by a shift of the center of the electron wavefunctions towards the gate barrier. Thus, the effective strength of the modulation potential decreases which contributes in the case of a finite CEW width to an increasing miniband width. On the other hand, the steeper triangular potential leads to a larger energetic separation of the confined states. As a result, the minigaps between the minibands become wider. Since the ground state of the triangular confinement increases in energy when the potential becomes steeper, the effective height of the SL modulation potential is also reduced. This contributes to an increased miniband width. All these effects are summarized in figure 3.6, where all plotted energy values are given with respect to a common zero energy value ($E = 0$ meV).

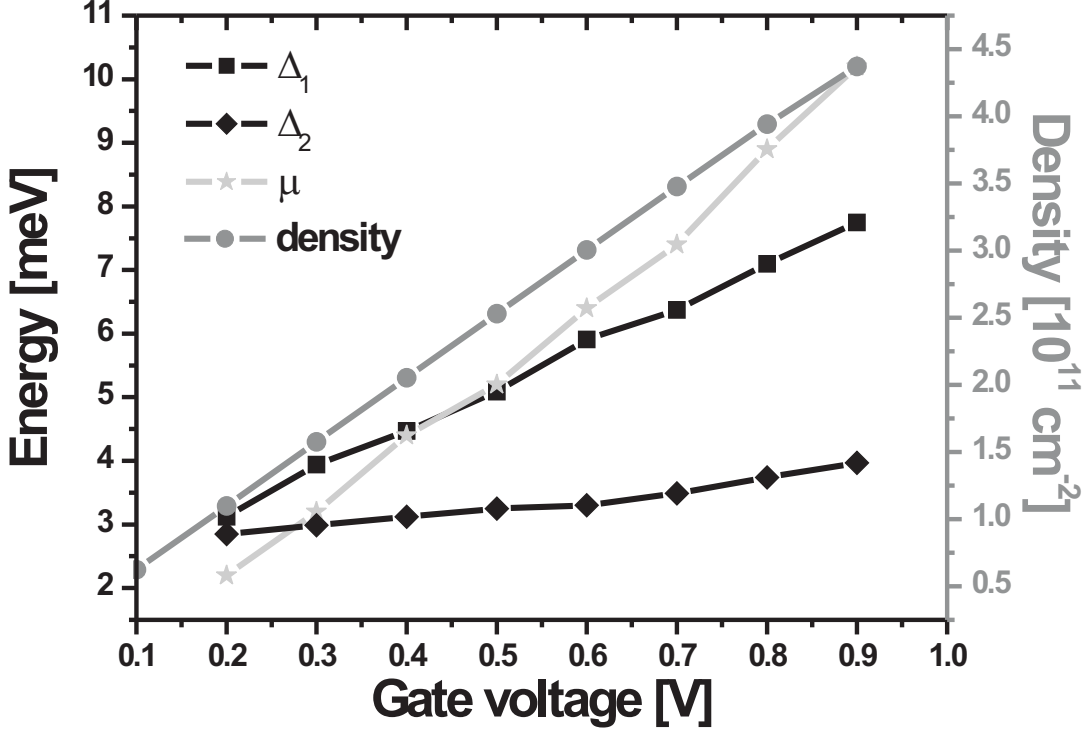


Figure 3.6: Calculation of the widths of the lowest two minibands (Δ_1, Δ_2), the chemical potential μ , and the density of a 5 nm cleaved-edge well structure for increasing applied gate bias.

The same figure also shows the chemical potential at $T = 4.2$ K. It was calculated using the relationship between density n and chemical potential μ

$$n = \frac{1}{2\pi^2} \int_{-\infty}^{+\infty} \int_{-\pi/d}^{+\pi/d} f(k_{[001]}, k_{[1\bar{1}0]}, \mu, T) dk_{[001]} dk_{[1\bar{1}0]} \quad (3.1)$$

where $f(k_{[001]}, k_{[1\bar{1}0]}, \mu, T)$ is the Fermi-Dirac distribution

$$f(k_{[001]}, k_{[1\bar{1}0]}, \mu, T) = \frac{1}{e^{\frac{E(k_{[001]}, k_{[1\bar{1}0]}) - \mu}{k_B T}} + 1} \quad (3.2)$$

The energy expression entering the Fermi-Dirac distribution is given by

$$E(k_{[001]}, k_{[1\bar{1}0]}) = \frac{\hbar k_{[1\bar{1}0]}^2}{2m} + \frac{\Delta}{2} (1 - \cos(k_{[001]}d)) \quad (3.3)$$

In the last expressions we considered not only the $[001]$ direction along which the transport takes place, but also the perpendicular free direction $[1\bar{1}0]$. Since the problem is symmetric about this axis, there is no net current transport along $[1\bar{1}0]$. However, in order to find the chemical potential, the complete problem has to be addressed.

3.5 About minigaps

The discussion about SL transport has so far been exclusively one-dimensional. But in the case of conventional SLs there are two free perpendicular directions and in the case of a surface SL there is one free direction. Due to these additional degrees of motion there are always electronic states at the Fermi energy, even when the latter is shifted into the first minigap. In this sense the minigap is not a true gap. The situation is shown in figure 3.7.

For all further discussions the [001] direction is identified with the x -axis and likewise the [110] and $[1\bar{1}0]$ directions with the z - and y -axis, respectively. In the situation where only an electric field along the superlattice axis is applied, the free direction comes into play only when considering the electron distribution in the miniband. This will become especially important when the average electron temperature of the distribution is calculated in chapter 5. The expression for the drift velocity which is derived there is quite different from the one given in chapter 2 from purely one-dimensional considerations.

The additional free direction becomes even more important when a magnetic field is applied perpendicular to the accumulation layer. Then, the transport problem becomes fully two-dimensional, and it will strongly depend on the states in the free direction. Within the semiclassical model the real-space motion of an electron can be directly linked

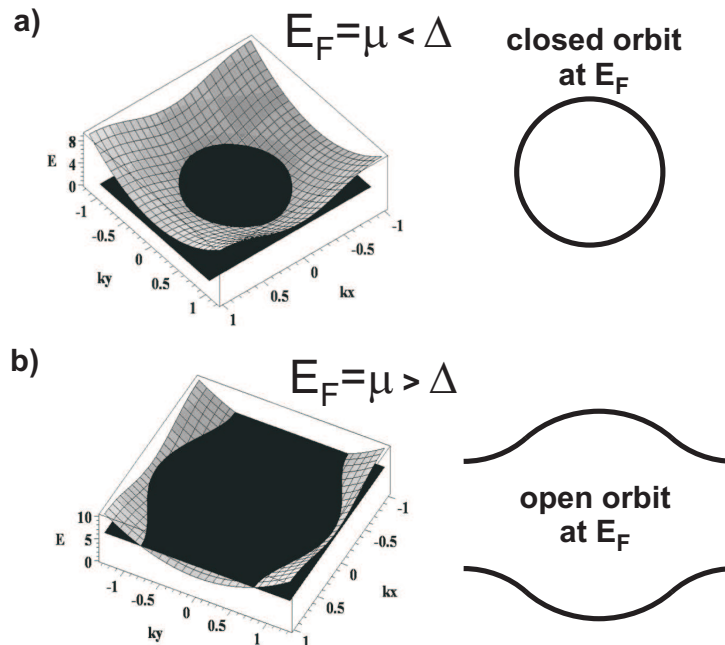


Figure 3.7: Two-dimensional band structure of a surface superlattice. The Fermi level is shown by the black plane for the situation of being smaller (a) and larger (b) than the miniband width. The corresponding Fermi contours are shown on the right.

to its k -space trajectory [AM76, chapter 12]. As figure 3.7 shows, this trajectory will strongly depend on the value of the chemical potential. If the latter resides inside the first ($V_{\text{Gate}} \leq 0.5$ V in figure 3.6) or second miniband, the electrons at the Fermi level⁵ $E_F = \mu$ can perform a rotational motion along a closed trajectory. But as soon as the chemical potential moves inside the first minigap ($V_{\text{Gate}} > 0.5$ V in figure 3.6), a closed orbit is no longer possible. Thus, we can expect a strong change in the transport properties when this transition from open to closed orbits occurs. This situation is discussed in detail in chapter 8. The results found there provide an experimental justification for the calculated band structures of this chapter.

3.6 Device operation

The simplest experimental approach for the determination of the transport properties of a SL structure is the measurement of the current-voltage characteristic. The setup for such a measurement, applied to the surface SLs of this work, is shown in figure 3.8. Each of the two n+-layers of the first growth step is contacted with two separate metal contacts. The pads 1 and 4, which are farthest from the two-dimensional electron system, are used to apply a DC bias across the sample structure. In this circuit loop also the total current I_{SD} flowing through the system is measured. In order to exclude the voltage drops across the metal-semiconductor junctions across pads 1 and 4, the voltage on the

⁵At low temperatures, the difference between the chemical potential and the Fermi energy is negligible.

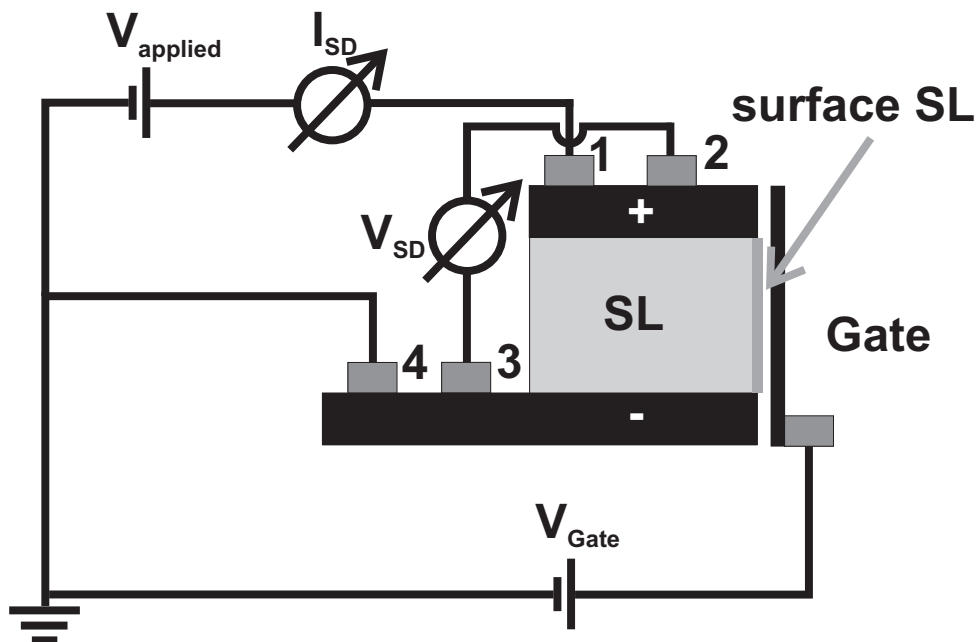


Figure 3.8: Schematic drawing of the electric circuit for a standard current-voltage characteristic measurement.

sample, referred to as the source-drain voltage V_{SD} , is independently determined using pads 2 and 3. Although this approach equals the usual four-point measurement scheme, there is one important drawback to these structures: the determined four-point voltage is not applied directly to the surface superlattice but rather to some specific points of the n+-layers. There is no direct access to the voltage applied to the surface superlattice only. By measuring the resistivities of the n+-layers and the length of the path between pads 2 and 3, the series resistance included in the voltage drop across pads 2 and 3 can be determined. Then the voltage drop across the series resistance can be subtracted from V_{SD} to arrive at the bare voltage drop across the two-dimensional system. Nevertheless, we will see in the upcoming chapters that such a simple approach is no longer possible under somewhat more complicated circumstances.

The two-dimensional electron system of the surface SL structure is created by applying a positive bias to the side gate. This part of the design bears great similarities to that of a metal-oxide-semiconductor field-effect transistor (MOSFET). In analogy to this device, we will call the grounded contact the source and the one where the voltage across the two-dimensional channel is applied the drain. A MOSFET, which is an integral part of nowadays electronics [Sze81, Chapter 8], has for small applied drain bias a linear transport characteristic. The two-dimensional channel essentially represents a resistor whose value depends on the applied gate bias. However, in addition to driving a current through the conducting channel, the drain bias also reduces the effective channel width at the drain end of the device. The reduced effective gate voltage leads to a shift in the Fermi energy so that the channel starts to deplete. At this point the transport characteristic saturates and becomes sublinear. Once the applied drain bias reaches a value at which the channel is completely depleted, the current flow beyond this pinch-off point stays constant since the current driving voltage is pinned at the channel pinch-off value. A further increase in voltage only moves the pinch-off point closer to the source contact [Sze81, Chapter 8.2.2]. Since the surface superlattice, too, possesses a gate induced channel, we can expect the device to show similar behavior once the channel pinch-off is reached. Though, due to the different contact geometries and the superlattice present in our device, it is unclear what the device characteristic will look like beyond saturation.

However, before a study of the transport characteristics of surface superlattices is attempted, it is essential to deal with the aforementioned topic of electric field instabilities. Superlattice transport is very strongly influenced by this phenomenon and its appearance or non-appearance introduces certain limitations on the current-voltage characteristics of SL devices. Therefore, the next chapter deals with negative differential velocity and its consequences for the transport in a SL structure.

Chapter 4

Density fluctuations and electric field instabilities in semiconductor devices exhibiting negative differential velocity

4.1 Overview

The terminology of electric field instabilities refer to the situation where the electric field applied to a homogeneous medium splits up into regions of different values due to internal microscopic processes. In the case of superlattices this occurs due to the electron localization by the electric field. This localization leads to a negative differential drift velocity (NDV) when the electric field becomes larger than a critical value F_c . However, the concept of electric field instabilities applies universally to devices which exhibit NDV. Whenever such a device is biased in the negative slope region of the NDV characteristic, it becomes unstable. A small fluctuation in the carrier density leads to a growth of this fluctuation. Eventually, regions of large carrier accumulations are developed inside the sample. The situation stabilizes as soon as the electric fields in the different domains reach values for which the velocity-field trace has positive slope. However, diffusion also balances the accumulation of carriers, and since the electrons overall keep on moving through the device, the contacts also play a major role in the determination of the actual transport properties.

Before studies [Ign80, IS84, IPS85, IS87, ML94] about electric field instabilities in SLs were undertaken, the topic had already been discussed in great detail for Gunn devices [Kro66, Kro68, Hak67]. In these structures, NDV results when large electric fields transfer electrons from the Γ -valley to the L -valley.¹ In the latter the electrons have a much lower mobility than in the former which increasingly decreases the drift velocity when more and

¹The described process applies to GaAs. For other materials different valleys can be involved, although the physics stays the same.

more electrons are transferred. Transport experiments [SPM⁺89, SPWM90] with SLs over a wide parameter range have shown that the results for Gunn devices can also be applied to SL structures.

In the following discussion, we first introduce the concept of electric field instabilities and explain then what differences between conventional and surface SLs can be expected. In the calculation of the onset of instabilities in surface SL structures an important contribution from Bernhard Rieder, who derived the closed form expression, is gratefully acknowledged. In [Kum68] a somewhat similar argument has been presented for Gunn devices.

4.2 Origin of electric field instabilities

Let us at first try to understand how field instabilities originate in a bulk device that has a velocity-field characteristic whose derivative is negative between the fields F_c and F_2 as shown in the right part of figure 4.1(a). Assume that the voltage at the device is increased instantaneously to a value such that the electric field inside lies just beyond the negative differential velocity (NDV) peak. If a fluctuation in the density along the device occurs in this condition, the Poisson equation leads to an electric field distribution where the field inside the fluctuation is somewhat higher than in the outside region (cf. figure 4.1(b)). This leads, according to the NDV relation, to a drift velocity distribution as shown in figure 4.1(c). In the region of enhanced electric field the electrons move slower than in the rest of the device. As a consequence, an increased number of electrons flows towards the instability and less flow out. The fluctuation grows instead of being smoothed out. The latter usually happens in devices without NDV. But in a NDV device the electric fields inside and outside the fluctuation drift further apart. The drift ends, when the large and small electric fields reach values at which both the derivative of the velocity-field characteristic is positive (Points $F_<$ and $F_>$ in figure 4.1(a)) and the drift velocity is equal. At this point the instability has become stable and can move through the device (cf. figure 4.1(d)). Such a traveling dipole domain is the working principle of a microwave emitting Gunn oscillator [Kro72].

4.3 Instability regimes

The conclusion from the above section is that NDV automatically leads to an instability of the electric field. In real devices the situation is more complicated. One important factor comes from the finite extension of the structure. It has contacts attached that in turn make it subject to specific boundary conditions. If the device length L is smaller than the extension of the dipole domain or the length scale across which the dipole domain is formed, the traveling dipole domain mode breaks down. The same is true if the electron density n in the system is not large enough to form a fully grown domain. Then, the

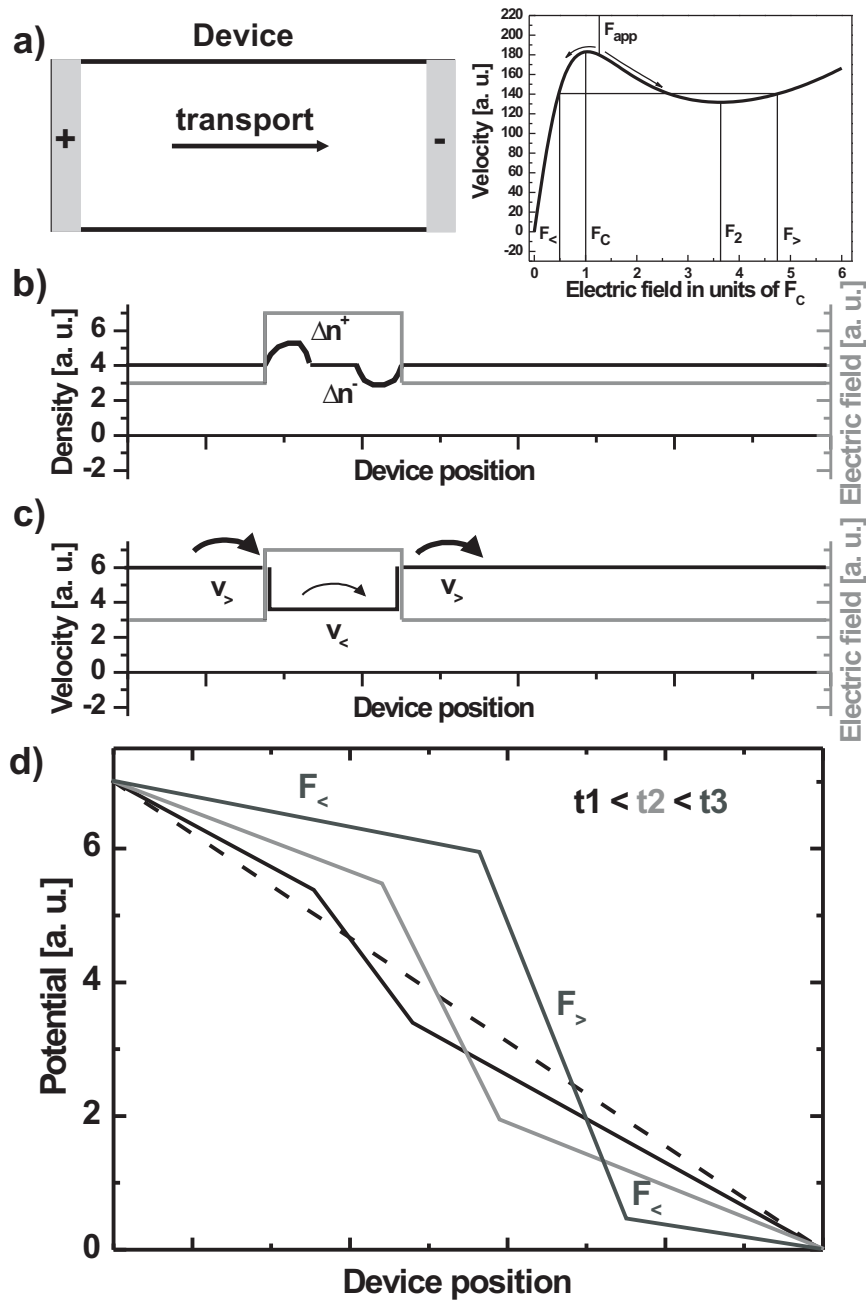


Figure 4.1: (a) Schematic drawing of a semiconductor device with a velocity-field characteristic (shown on the right side) that has a negative slope in the electric field range between F_C and F_2 . (b), (c) Schematic plot of the density and velocity distribution along the device when a small fluctuation is present. (d) Evolution of the potential distribution inside the device for three different times. The dashed line shows the homogeneous drop of the potential across the device before the fluctuation occurs. At t_3 the slopes of the potential inside and outside the fluctuation have taken on the limiting values of $F_<$ and $F_>$. The resulting fluctuation no longer changes in form and is referred to as a fully grown electric field domain.

traveling dipole domain again becomes an invalid description.

In the course of the investigation of transport in Gunn diodes it was found that there are three specific transport regimes that can be distinguished [Hak67, Kro66] according to their so called ' nL -product' value.²

1. If the sample properties fall into the region $nL^2 < 2 \times 10^7 \text{ cm}^{-1}$, then the growth of space charge fluctuations is completely suppressed. The resulting static electric field distribution is strongly non-uniform and DC³ NDC is not observed in transport measurements.
2. For the conditions $nL^2 > 2 \times 10^7 \text{ cm}^{-1}$ and $nL < 2 - 5 \times 10^{11} \text{ cm}^{-2}$ space charge fluctuations can grow, but no fully grown domain is established. In this regime, the electric field can be assumed to be close to homogeneous [Hak67] and it is possible to use the device as an amplifier for frequencies in the GHz regime⁴ [Hak67]. Again, no DC NDC occurs.
3. Once the device reaches the regime $nL > 2 - 5 \times 10^{11} \text{ cm}^{-2}$, transport is dominated by the traveling dipole domain mode. The devices first investigated by Gunn [Gun63], [Gun64] show this transport behavior. The current-voltage characteristics in this regime show DC NDC, however, mostly in form of discontinuous jumps.

In the following, regime number 2 is called the intermediate or space charge wave growth regime. Devices in the third transport regime are referred to as operating in the traveling dipole domain mode.

The above given results have been found during the investigation of the electron transfer effect in semiconductors. The different mobilities in the participating conduction band valleys lead to a drift velocity-electric field characteristic with negative slope. In chapter 2 we saw that the nonlinearity of the superlattice dispersion also leads to NDV. Therefore, it can be expected that the transport in SLs bears strong similarities to the one in Gunn oscillators, as long as the physical origin of the NDV is not concerned directly. In the late 1980s and early 1990s Sibille *et al.* [SPMM89, SPM⁺89, SPWM90] performed experiments on superlattices with a wide variety of different parameters. They found that the results for Gunn devices also hold true in superlattices. The critical density-length product for the observation of DC NDC was experimentally determined to be of the order of 10^{12} cm^{-2} [SPM⁺89], which is very close to the value given above. They could also show that the NDV was caused by the non-linearity of the miniband dispersion [SPWM90],

²In section 4.4 it is shown in some detail from what considerations these different regimes originate.

³The specification of the term 'DC NDC' stresses that the discussions in this chapter assume only the presence of a static electric field.

⁴This AC field amplification is a pure transit time phenomenon where the AC field interacts with a space charge that traverses the sample with the velocity v_d . It has no connection to the gain mechanism described in chapter 2 and chapter 7.

and they could operate the superlattice as an amplifier⁵ in the intermediate nL -product regime [SPM⁺89].

Superlattice transport can therefore be divided into the three regimes given above. For extremely short and almost undoped SLs the electric field inside the device is static and strongly inhomogeneous. In such a device the Bloch oscillator arguments of chapter 2 become obsolete. This can also be said for SLs working in the regime of traveling dipole domains. Here, the system also operates far from the homogeneous field distribution that is the foundation of the Bloch oscillator. Doped SLs with typical parameters fall into this category. Since the dipole domains, just as in a Gunn diode, lead to an oscillating current, active oscillators can be made from these SLs [KHP⁺97], [SBH⁺98]. Their upper operating frequency limit is estimated to go up to 1 THz.⁶ Only the intermediate transport regime offers an almost homogeneous field distribution while avoiding the growth of dominating dipole domains. Unfortunately, for sufficient device lengths, the doping density in the superlattice has to be reduced drastically in order to reach this quasi-stable situation. As a result, these devices show very low current densities and provide very low gain according to the discussion in chapter 2.

Nevertheless, Savvidis *et al.* [SKLA04] try to realize an active oscillator by operating a superlattice structure in the intermediate transport regime. They reduce the sample length for medium doping densities down to 10 to 15 SL periods and then connect many of these extremely short sections to a super-superlattice. However, it remains to be seen whether this leads to enough gain to overcome the device losses. Another, density independent suggestion for domain free superlattice transport was made by Daniel *et al.* [DGSA03]. They performed transport simulations on superlattices that are shunted by conducting sidewall layers. Their results showed that the shunt can stabilize the field distribution inside the SL up to a lateral thickness of a few microns. We show in the next section that such a setup can actually be realized in the surface SL system.

However, the main reason for the investigation of surface SLs was that a reduction of the dimensionality of the SL system has a profound influence on the Poisson equation when electric field instabilities are modeled. This difference was expected to lead to a much greater stability against domain growth in such a two-dimensional system. Both an algebraic and a numerical analysis of the problem show that this is indeed true, and this topic is discussed in detail in the following section.

4.4 Instabilities in surface superlattices

The principal difference between a charge carrier density fluctuation in a conventional superlattice and one realized by CEO is shown in figure 4.2. In the 3D system there are

⁵The basis for this amplification is again a transit time effect and is in no way connected to the Bloch gain discussed in chapter 2.

⁶So far, all realized active oscillators show frequencies below about 150 GHz which seems to be an upper limit.

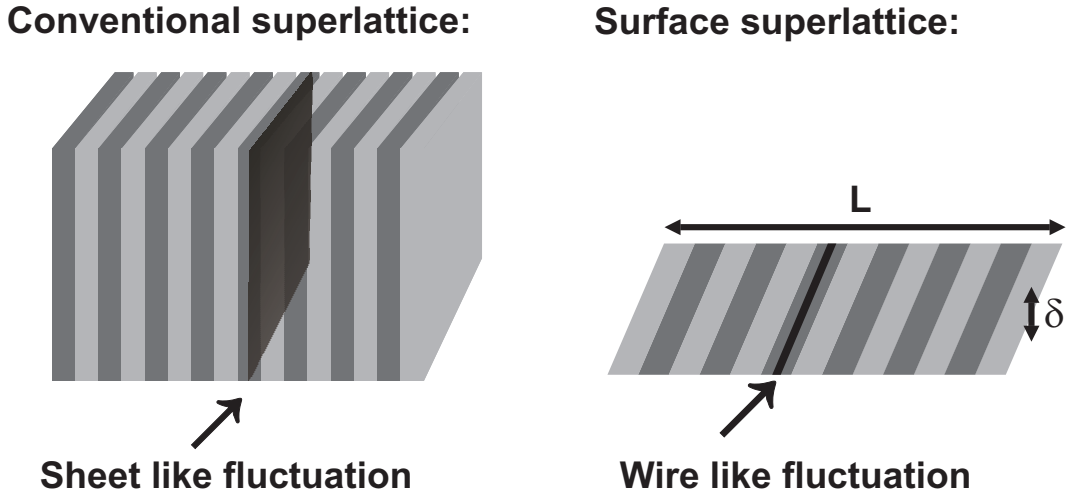


Figure 4.2: The left part of this figure shows an electron accumulation area (shaded region) in a conventional SL. Since it quickly spreads out along the two directions of free electron motion, it resembles a charged plate. The same reasoning leads to a charged wire form for a fluctuation in a surface SL as shown in the right part of the figure.

two free directions perpendicular to the superlattice axis along which the electrons can move with a mobility much higher than along the superlattice. Therefore, a fluctuation in the carrier distribution spreads out fairly quickly along these directions and the fluctuation will resemble a charged plate for other electrons away from the fluctuation (cf. left part of figure 4.2). There is only one such free direction in the 2D case and consequently the fluctuation looks like a charged wire (cf. right part of figure 4.2). When we solve the Poisson equation for these fluctuations, we can expect the electric field of a plate capacitor for the 3D case and that of a charged wire for the 2D system. The former is simply constant perpendicular to the charged plate whereas the latter one drops off inversely with the distance from the wire. It is this reduction in electric field which leads to a slower build up of the charge carrier accumulations in surface SLs and results in the fact that the 2D system is stable up to larger nL -products compared to conventional SLs.

To put this into more quantitative terms, the drift-diffusion model is used to solve for the short-term stability of the system after introducing a fluctuation around a stationary state characterized by $j_0 = en_0v_d(F_0)$. Here n_0 is the equilibrium carrier density, v_d the average drift-velocity at the applied external field F_0 , and j_0 is the resulting current density. To this stationary state a fluctuation in form of a space charge wave proportional to $e^{ikz-i\omega t}$ is added. Accordingly, small oscillatory terms have to be added to all stationary quantities: $F = F_0 + \eta$, $n = n_0 + \nu$ and $j = j_0 + \chi$, assuming $\eta, \nu, \chi \sim e^{ikz-i\omega t}$. Hereby, k and $\omega(k)$ are the properties of the space charge fluctuation and the value of ω determines the temporal evolution of the fluctuation. In order to determine ω , the new system

parameters must be inserted into the drift-diffusion (D is the diffusion constant) and continuity equations,⁷

$$j = env - eD\nabla n \quad (4.1)$$

$$\frac{\partial n}{\partial t} = -\frac{1}{e}\nabla \cdot j. \quad (4.2)$$

From these we find

$$i\omega\nu = ik(\nu v_d(F_0) + n_0 \frac{\partial v_d}{\partial F}(F_0)\eta - ikD\nu) \quad . \quad (4.3)$$

Then, once the Poisson equation

$$\nabla \cdot F = -\frac{en}{\epsilon\epsilon_0} \quad (4.4)$$

has been solved for η , we can extract the time evolution of the fluctuation from the dispersion $\omega(k)$. In order to arrive at a closed form expression for the electric field η , it is assumed that the charged wire of the 2D system actually resembles a charged plate with infinite extension in the free direction and a thickness equal to the 2DEG width $\delta = 2\xi$ (cf. right part of figure 4.2) in the confinement direction. This should give a realistic picture of the situation since an electron which is far from the fluctuation simply sees a charged wire whereas an electron located very near ($< \xi$) the fluctuation sees a charged plate just as in the 3D situation. This can also be viewed as going from 3D to 2D by shrinking one of the free directions from infinite extension down to the width δ of the 2DEG. In this geometry the Poisson equation results in

$$ik\eta = \frac{e}{\epsilon\epsilon_0}\nu - \frac{e}{\pi\epsilon\epsilon_0} \int_0^L \nu e^{-ik(z-z')} \frac{\xi}{\xi^2 + (z-z')^2} dz'. \quad (4.5)$$

Here L is again the length of the sample. The fact that the surface superlattice is very thin, $\xi \ll L$, allows an extension of the integral limit to infinity. Then, with

$$\int_{-\infty}^{+\infty} \frac{\cos(kz)}{\xi^2 + z^2} dz = \frac{\pi}{2\xi} e^{-\xi k}, \quad (4.6)$$

the dispersion $\omega(k)$ of the fluctuation is found according to

$$\omega = kv_d(F_0) - i \left(Dk^2 + \frac{\sigma_0}{\epsilon\epsilon_0} (1 - e^{-\xi k}) \right). \quad (4.7)$$

Here σ_0 is the (negative) differential conductivity at F_0 . Although the result for ω was calculated after a linearization of the drift-diffusion equations, the results are expected to describe the behavior for small fluctuations rather well. Since the fluctuation has a dependence of the form $\Delta n \sim e^{-i\omega t}$, equation (4.7) states that the imaginary part of ω

⁷The presented calculation is purely one-dimensional. The difference between conventional and surface SLs enters only through a different Poisson equation. In the numerical investigations mentioned below, the complete two-dimensional problem was solved.

can become positive when both NDC is given, meaning $\sigma_0 < 0$, and diffusion is weak. A positive imaginary part of ω leads to a temporal growth of the fluctuation.

In the limit $\xi \rightarrow \infty$, the exponential factor in expression (4.7) vanishes and the result for a 3D system is recovered. This is quite reasonable since we rebuild a conventional superlattice if the surface SL is continuously made thicker. Neglecting the exponential term in equation (4.7), the condition for growth of the fluctuation can be written as

$$n_0 L^2 > \frac{4\pi^2 \epsilon \epsilon_0 D}{e |\mu_0|} \quad (4.8)$$

where μ_0 is the differential mobility given by $\mu_0 = \frac{\partial v_d}{\partial F_0}$ and we have assumed that $\lambda = \frac{2\pi}{k}$ is bound by the device length L . The right hand side of the growth condition equates to $4\pi^2 \epsilon \epsilon_0 k_B T_e / e^2 = 8 \times 10^6 \text{ cm}^{-1}$, when the diffusion constant is given by the Einstein relation $D = \mu k_B T_e / e$ at an electronic temperature of 300 K. This value is close to the condition that was stated in the introductory discussion of the results found for the Gunn effect in [Hak67] and [Kro66].

It is easy to see that the exponential term in (4.7) leads to a weaker condition for space charge wave growth. For small ξ we can expand the exponential factor $\exp(-\xi k)$ and with the assumption of a maximum wavevector $k = \frac{2\pi}{L}$, limited by the length L of the sample, we find

$$\omega = k v_d(F_0) - i \left(D k^2 + \frac{\sigma_0}{\epsilon \epsilon_0} \frac{\delta \pi}{L} \right). \quad (4.9)$$

This shows that the term responsible for the growth of fluctuations in a 2D system is smaller by a factor of $\frac{\delta \pi}{L}$ compared to a 3D system. With a typical 2DEG thickness of 10 nm and a typical superlattice length of about 1 μm , the growth rate is about 50 times smaller in the 2D system.

During the derivation of this result we assumed that the initial fluctuation has a wire-like form in the 2D system. However, a real fluctuation will develop on a local scale. Due to the system having a high mobility direction perpendicular to the superlattice axis this local fluctuation spreads out quickly into the wire form. But initially the field leading to the growth of the density fluctuation is even smaller than in the wire geometry. This means that the nL -product at which fluctuation growth occurs is even higher than just calculated. In order to quantify this, we performed a numerical two-dimensional drift-diffusion simulation. From this, it was found that a 2D system is stable against space charge wave growth for nL -products about two orders of magnitude larger than in a comparable 3D system, under the assumption of a typical 2DEG thickness of 10 nm.

The boundary between space charge growth and dipole domain mode transport is determined by the condition that the fluctuation traverses the sample in a time L/v_d that is shorter than the characteristic growth time $1/\omega$ [Hak67]. From equation (4.7) it is found that all conventional SLs with nL -products fulfilling the condition

$$n_0 L < \frac{2\pi \epsilon \epsilon_0 |v_d|}{e |\mu_0|} \quad (4.10)$$

are outside the traveling dipole domain mode. The right side of this condition gives a value of about $1 \times 10^{12} \text{ cm}^{-2}$ for typical parameters. This is again close to what was stated earlier as a result found for Gunn devices. For the surface SL we can expect this value to be also increased by the ratio $\frac{L}{\pi\delta}$ since the fluctuations in those devices have an accordingly smaller growth rate. Therefore, the quasi-stable regime of space charge wave growth lasts up to much higher nL -products in surface SLs. The typical transition density into the dipole domain mode regime is about $2 \times 10^{16} \text{ cm}^{-3}$ for conventional SLs. With the additional factor, surface SLs might be expected to stay in the intermediate regime for densities up to $2 \times 10^{18} \text{ cm}^{-3}$. It is also quite interesting to notice that an increase in the sample length seems to be directly accounted for by the additional 2D factor $L/\pi\delta$.

4.5 DC NDC in semiconductor devices

At this point it seems important to point out again that although diffusion can balance the formation of domains, *it is impossible to observe DC NDC with a homogeneous electric field distribution*. To see this, imagine a homogeneous electric field along the device. This would lead to a transport characteristic that shows NDC, according to the relation $j = env_d$. Now imagine that a voltage beyond the NDC peak is applied to the device. Then, analogous to our argument in the beginning of the discussion, a density fluctuation would again lead to a small difference in the electric fields inside and outside of the fluctuation. This in turn would result in a current distribution where more electrons flow into the fluctuation than are leaving it. Thus, the fluctuation would again grow and our argument would evolve in the same direction as before. But now there is a huge difference. Unlike before, the transport characteristic which shows NDC already includes the process of diffusion. Thus we can no longer argue that diffusion prevents the build up of domains. And although the growth of the fluctuation can be small and the electric field can be close to homogeneous, there is no DC NDC observable.

We can conclude from this that it is impossible to observe DC NDC in a bare device with homogeneous field distribution. This situation would simply not be stable as was already pointed out by Shockley in 1954 [Sho54]. In a situation where diffusion is strong and no fully grown domains are formed, it is important to include the boundary conditions in any theoretical calculation. The whole system will then show no DC NDC. For very small nL products the electric field distribution will be static and extremely inhomogeneous. If space charge growth is possible, but no fully grown domains exist, there occurs still no DC NDC but the field distribution can be close to homogeneity.

These arguments are of course limited to situations in which drift and diffusion govern the transport. In situations where transport is for example due to electrons tunneling across barriers, it is possible to observe stable DC NDC (see e.g. [Sze81, Chapter 9] for tunneling devices or [Dav98, Chapter 5] for resonant tunneling structures).

Chapter 5

Transport in surface superlattice systems

5.1 Overview

The work presented in this chapter describes the successive development of an improved surface SL design. The transport properties of a number of different sample structures are discussed. Thereby, it is attempted to shed some light on the manifold observations that can be made when studying transport in surface SLs.

Up to now there has only been a very limited amount of work concerning itself with non-equilibrium transport in short-period modulated two-dimensional electron systems. The first study we are aware of was performed on a GaAs HEMT structure [BF87b, BF87a]. The gate that was used to establish the two-dimensional electron system was two-dimensionally patterned in a periodic grid and led to a periodic modulation of the electron density. The reported transport characteristics show regions of negative differential conductivity (NDC). However, no conclusive connection to Bloch oscillations could be established. The first high electric field measurements on GaAs based CEO structures were published in [KZT⁺95]. In these structures, the second growth step was deposited by liquid phase epitaxy. The two-dimensional electron system was established by modulation doping. Again, NDC was seen in the current-voltage characteristics. However, also no conclusive claim towards the existence of Bloch oscillations could be made. In [DWR⁺00, Deu01] the first gated CEO samples were investigated with respect to their non-equilibrium transport properties. Since these samples are the starting point of the discussion in the next section, the detailed results are presented and explained there. While NDC is again observed, it turns out that it is not connected to Bloch oscillations, but rather to the gate structure.

Based on this first design, continuous changes have been made to the sample structure. The investigation of the different realized devices has led to important conclusions for the understanding of the general transport properties of surface SLs. One important step has been the reduction of the superlattice length. While the presented arguments for

this change are conclusive, important insights have also been gained by THz absorption experiments performed at the Free Electron Laser facilities at UCSB.¹ However, in order to tighten the discussion, those results are omitted. Nevertheless, the performance of this experiment has still been an important step for the evolution of the project.

All presented measurements were recorded at a temperature of 4.2 K.

5.2 Transport in long channel devices

An introduction to the realization of CEO based surface SL structures was given in chapter 3. The combination of two growth steps allows the fabrication of two-dimensional electron systems with, in principle, arbitrary one-dimensional modulation. The two-step process also introduces a wide parameter space within which the individual sample properties can be varied. Therefore, we start our investigations with a sample structure that has previously been studied [DWR⁺00, Deu01] and which has shown dramatic effects due to the introduction of a superlattice in the first growth step.

The exact layer sequence of the active region of this structure is shown in figure 5.1(a).² A 1 μm thick doped contact layer with a doping density of about $1 \times 10^{18} \text{ cm}^{-3}$ forms the basis on which a 100 nm wide undoped GaAs buffer layer followed by an undoped superlattice with 12 nm thick GaAs wells and 3 nm wide $\text{Al}_{0.32}\text{Ga}_{0.68}\text{As}$ barriers was deposited. The number of SL periods was 100, giving a total SL length of 1.5 μm . On top of the SL a final barrier, for symmetry reasons, followed by another 100 nm wide GaAs buffer layer were deposited, and the structure was then capped by a second doped contact layer with properties identical to the lower one. The introduction of GaAs buffer layers between the superlattice and its contacts is quite common. At the SL boundaries the artificially introduced symmetry is broken and the concept of minibands can no longer be used for the description of electron transport in these regions. Since even the lowest miniband has a positive energy offset with respect to the conduction band edge of GaAs, the formation of an effective injection barrier can be expected at the SL boundaries. This has indeed been observed for a wide range of samples [SPM⁺89, SPWM90] and, therefore, different kinds of contact-buffer-SL designs have been developed with which the transport properties at the SL boundaries could be adjusted to the experimental requirements. These designs include the use of aluminum in the contact layers [PMF⁺04], the introduction of so-called transition SLs [SBH⁺98], which are short SL sections of varying period that slowly raise the conduction band to the value of the lowest miniband, or even the deposition of In monolayers in the wells of the SL [PSE⁺02] which leads to an effective lowering of the miniband position. Also, in order to exclude electron spill over effects between contact and SL, undoped GaAs buffer layers were inserted between the

¹Similar experiments on the final sample design are presented in chapter 7.

²Before the lower contact layer is deposited, a GaAs buffer layer and a GaAs/ $\text{Al}_{0.32}\text{Ga}_{0.68}\text{As}$ SL are grown in order to achieve a high quality surface for the active structure. Since these additional parts are electrically inert, we ignore them.

a) first growth step		time	total	
		Å	time	
			[s]	
			[s]	
102	As11beepSiPoCaPo	0.00	15.00	3199.63
103	As11Ga8Si10SiPoCaPo	10000.00	3607.50	6807.14
104	As11Ga8CaPo	1000.00	360.75	7167.89
105	As11CaPo	0.00	10.00	7177.89
106*	As11Ga8Al7CaPo	31.13	7.64	7185.53
107*	As11Ga8CaPo	118.86	42.88	7228.41
108*	As11CaPo	0.00	10.00	7238.41
	repeated 100 times	149.99	60.52	13229.93
406	As11Ga8CaPo	881.00	317.82	13547.75
407	As11beepSiPoCaPo	0.00	15.00	13562.75
408	As11Ga8Si10SiPoCaPo	10000.00	3607.50	17170.26
409	As11Si10SiPoCaPo	0.00	60.00	17230.26
410	As11Ga8Si10SiPoCaPo	50.00	18.04	17248.29
b) second growth step				
1	As11Al7Ga4CaPo	1000.00	407.50	407.50
2	As11Ga4CaPo	150.00	88.13	495.63
3	As11beepSiPoCaPo	0.00	15.00	510.63
4	As11Ga4Si10SiPoCaPo	2000.00	1175.09	1685.72
5	As11Si10SiPoCaPo	0.00	40.00	1725.72
6	As11Ga4Si10SiPoCaPo	50.00	29.38	1755.09

Figure 5.1: The figure shows excerpts from the growth protocols of the first and second growth step of a surface superlattice structure.

two regions. Thus, the introduction of such a buffer layer in the first growth step of the surface SL structure seems quite natural. However, we shall see that this GaAs buffer layer plays a more crucial role in the surface SL samples than in conventional SLs.

In the second growth step (cf. figure 5.1(b)) the structure is overgrown with a 100 nm wide $\text{Al}_{0.32}\text{Ga}_{0.68}\text{As}$ barrier, protected with 15 nm of GaAs, and a 205 nm wide highly doped GaAs layer which acts as the gate electrode.

A Kronig-Penney model calculation predicts widths of 3 meV and 13 meV, respectively, for the lowest and first excited minibands. The offset of the lowest miniband with respect to the GaAs conduction band edge is 25 meV and the width of the first minigap is 72 meV. For the surface SL without CEW the miniband width, calculated from simulations as described in chapter 3, is found to also be about 3 meV and can be assumed constant with respect to the electron density in the two-dimensional channel.

The results of the measurement of the current-voltage characteristics of such a sample are shown in figure 5.2(a) for a number of applied gate voltages. For zero gate bias there is no significant current flow up to a SD-bias of about 0.8 V. Beyond this voltage, the current starts to rise strongly. At a SD-bias of 1 V the current suddenly drops down showing a region of strong negative differential conductance. For even larger voltages the current increases exponentially. From this we can infer that the first growth step does not carry any significant current in the low voltage regime so that the transport for gate biases in the accumulation regime is solely due to the induced two-dimensional electron system.

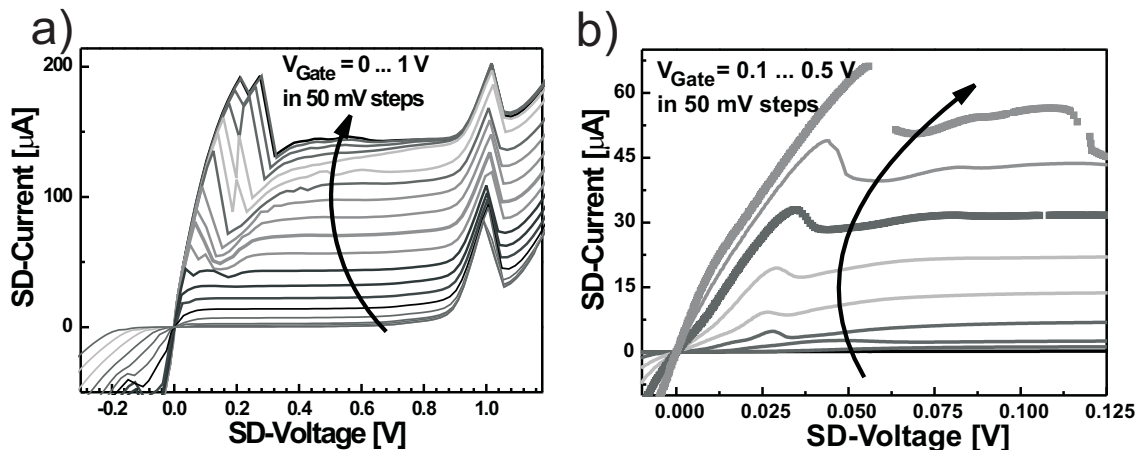


Figure 5.2: (a) Current-voltage characteristics of a surface SL for many different gate voltages. (b) Magnification of the low SD-bias and low gate bias region of panel (a).

However, the NDC observed at around 1 V must be attributed to the channel across the undoped SL since it is seen even when the surface SL is not present. It is interesting to note that the reverse bias trace for zero gate bias shows considerable current flow already at about -200 mV applied SD-bias. This current cannot flow across the gate which is leakage free up to much higher voltages in both directions. Therefore, the transport also occurs across the undoped SL of the first growth step. This is most surprising since this part of our structure is completely symmetric. The strong difference in transport behavior, which is observed in all samples grown for this investigation, must therefore be attributed to the differences in sample structure introduced by the MBE growth itself. One such difference is the orientation of the GaAs/ $\text{Al}_{0.32}\text{Ga}_{0.68}\text{As}$ interfaces. It is known [PWSB89] that GaAs grows very smoothly on $\text{Al}_{0.32}\text{Ga}_{0.68}\text{As}$, while the interface in opposite deposition order possesses a higher roughness. Nevertheless, it seems unlikely that this could lead to such large discrepancies in the break-through of the bulk SL since the electrons have to cross both interfaces no matter what direction the SD-bias is applied. Another asymmetry introduced by the MBE growth is the positioning of the doping material in the structure. The SL is grown on top of the lower doped contact so that it is quite likely that there will be some diffusion of Si atoms into the undoped GaAs buffer layer. In contrast, the interface between the upper buffer layer and contact is sharper since there the contact is grown on top of the buffer, making diffusion of Si into the buffer during growth quite unlikely. Again this effect seems not very dramatic since the diffusion length of Si into the lower GaAs buffer is expected to decrease exponentially on a length scale of some nanometers. However, we must be aware that now the asymmetry is not introduced in the SL region itself but at the boundaries of the SL. Thus, it might not be the SL that is responsible for the different behavior with respect to the transport direction, but rather

the electron injection into the SL that controls this behavior. The combination of all these effects must be the reason for the observed asymmetry.

Once the gate voltage exceeds about 200 mV, strong current flow can be observed in the positive low SD-bias regime which is carried by the accumulation layer, induced by the applied gate bias. In the gate bias range $200 \text{ mV} < V_{\text{Gate}} < 450 \text{ mV}$ a region of relatively weak NDC is observed before the current essentially stays constant until the bulk SL starts to leak. In the higher gate bias regime beyond 450 mV the traces show increasingly stronger NDC with a series of smaller features that continuously persist up to higher SD-bias. Since the NDC is not found in reference samples without SL [DWR⁺00, Deu01], it was marked down as a SL effect and was attributed to the onset of Bloch oscillations as described in chapter 2.4. One attractive feature of this explanation can be seen in figure 5.2(b), where the surface superlattice I-V-traces in the gate bias range below 500 mV are enlarged. For both the traces of 400 mV and 500 mV gate voltage the unconnected experimental current-voltage points are shown. Whereas the 400 mV curve is still completely smooth, the 500 mV one shows a clear jump at about 57 mV SD-bias which is characteristic for instabilities as discussed in the preceding chapter. That would mean that a transition from stable to unstable SL transport occurs as we increase the channel density. But this is exactly what is theoretically predicted, since more electrons means a larger nL -product and therefore a crossover into the instability regime. As intriguing as this explanation sounds, it cannot be true. The reason for this was explained at the end of the last chapter. *In general, it is impossible to observe stable DC NDC in a drift-diffusion transport regime.* This brings us directly to the conclusion

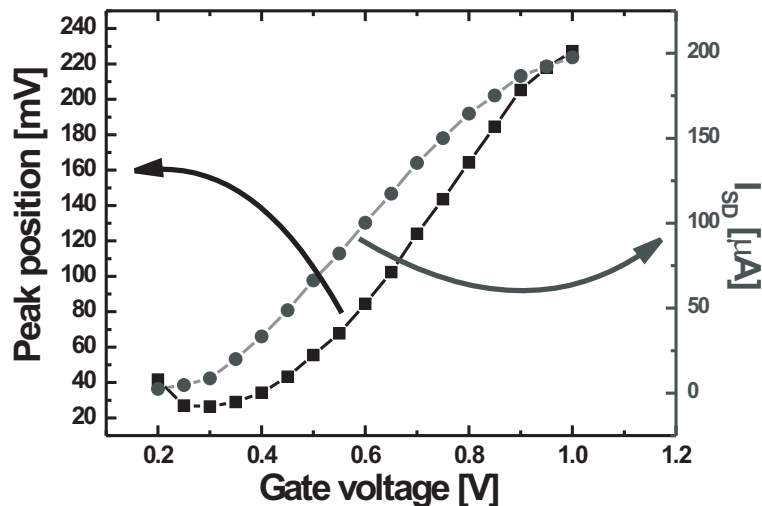


Figure 5.3: SD-bias position and the corresponding current value of the first NDC peak of the current-voltage traces of figure 5.2(a) plotted versus the applied gate voltage.

that the NDC observed in these samples is most probably due to some tunneling effect. This does not, however, tell us whether this tunneling occurs inside the SL or if it is rather a boundary effect.

When the position and the current value of the first occurring NDC peak are plotted versus the applied gate bias, as shown in figure 5.3, it is found that both the peak position and peak current increase almost linearly over a wide range of gate biases. This behavior is not quite similar to the changes in the pinch-off point of a MOSFET structure [Sze81, Chapter 8.2.2]. However, a pinch-off effect would provide a satisfactory explanation for some features observed in the transport characteristics. Most notably, it could explain the current plateau observed for all gate biases. Moreover, the fact that the additional small features which follow the initial NDC peak extend to higher SD-bias for larger gate voltages also suggests a pinch-off problem since the pinch-off point strongly depends on the ratio between both voltages.

Further insight can be gained when we study the I-V-characteristics of a sample structure that possesses identical sample parameters as given at the beginning of the section with the only difference being that the GaAs buffer layers now have a thickness of 500 nm instead of 100 nm. The corresponding I-V-characteristics given in figure 5.4(a) show no NDC for small gate biases, and for larger densities, although present, the NDC is much less pronounced than in figure 5.2(a). Since we did not change the SL properties but rather the injection region into the surface superlattice, it can be concluded that the NDC observed in these samples is very likely due to tunneling processes occurring at the edge of the SLs. This is also in agreement with the fact that samples in which the SL is replaced by $\text{Al}_x\text{Ga}_{1-x}\text{As}$ with an identical aluminum fraction show no NDC at all, but rather perfect

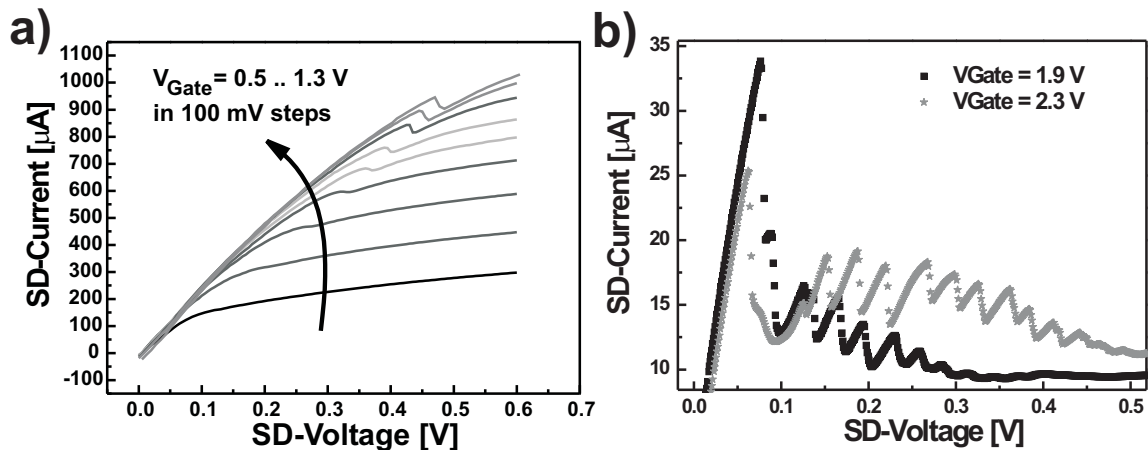


Figure 5.4: (a) Current-voltage characteristics of a surface superlattice with 500 nm wide intrinsic buffer layers. (b) Current-voltage traces that exhibit many equidistant NDC jumps.

transistor behavior. The most likely explanation therefore is that at a certain pinch-off point the electric field at the drain edge of our structure becomes inhomogeneous, forming a tunneling junction at its end, across which a large part of the total voltage is dropped. For further increasing bias, the current is now limited by the tunneling junction instead of the superlattice. The additional features occurring for higher channel densities correspond then to resonant tunneling processes involving inelastic scattering events or in case of very large gate voltages the resonant tunneling over a small number of superlattice cells. The possible involvement of a growing number of SL cells in the tunneling process seems to be confirmed by I-V-traces taken for a sample which allowed the application of comparably large gate voltages. Such I-V-traces are given in figure 5.4(b). After the initial, very steep NDC a series of further, almost equidistant instabilities is observed. Such a behavior is well known from the studies of instabilities in superlattices that are operated in the resonant tunneling regime [Wac98]. There, the superlattice is divided into two parts of constant electric fields. In one part the current is carried along the broadened ground states of the individual wells, whereas in the other part the electrons tunnel resonantly between the ground- and first excited states of neighboring wells. When in this situation the SD-bias is increased, the current increases until the SD-voltage is large enough such that one of the ground state to ground state junctions switches to the ground state to first excited state tunneling process. Such continuous switching with increasing SD-bias leads to characteristic, equidistant current jumps which are similar to the ones observed in figure 5.4(b). Thus, our explanation of the measured NDC in terms of a tunneling process at the edge of the superlattice finds further support.

Besides these striking current jumps, figure 5.4(b) shows another surprising feature. For small SD-biases the current carried by the two-dimensional system is smaller for the high-density configuration, whereas in the high SD-bias regime the larger number of electrons also lead to a larger transport. The explanation for this crossover behavior actually gives proof to the existence of the miniband structure in our device and is the topic of the next section.

5.3 The filling of the miniband

The magnitude of the current transport through a conventional doped semiconductor crystal is usually expected to continuously increase when the electron density grows. The drift velocity is dominantly determined by the applied electric field strength. In our surface superlattice structures with rather small miniband widths and high densities the situation is different. Recalling the surface SL drift velocity

$$v_D = F(T, \mu) \frac{\Delta d}{2\hbar} \frac{\omega_B \tau}{1 + \omega_B^2 \tau^2} \quad (5.1)$$

from chapter 2.4, we see that the electron density enters into the expression through the magnitude of the chemical potential in the factor $F(T, \mu)$. Here, $F(T, \mu)$ is the ratio

between the first and the zeroth order Fourier coefficient of the Fermi-Dirac-distribution (FDD) in the miniband. Since the sheet electron density in the active region is given by the same zeroth order Fourier coefficient, the total current carried by the miniband

$$I = en_{2D}v_d b , \quad (5.2)$$

where b is the width of the two-dimensional channel, is proportional to the first order Fourier coefficient of the FDD. In figure 5.5(a) the density, the velocity and the current carried by the miniband are plotted for increasing chemical potential. As the density increases, the drift velocity decreases steadily. This leads to an initially increasing current which takes on a maximum value for a chemical potential somewhat below the top of the miniband. Beyond this maximum the current decreases even though the electron density still grows. This behavior is simply a reflection of the well known fact [AM76, chapter 12] that a filled band, and that includes SL minibands, does not carry any current. Therefore, once the miniband is filled, only those electrons beyond the top of the miniband effectively contribute to the transport. As the chemical potential moves further and further beyond the upper edge of the miniband the density of states in the system becomes more and more one-dimensional (this will be discussed in greater detail in chapter 8). And this in turn leads to a continuously decreasing current when the chemical potential shifts beyond the top of the miniband, as shown in figure 5.5(a). The latter statement is of course only correct as long as no excited minibands are occupied. In figure 5.5(b) the current through a surface superlattice at a fixed, small SD-bias is plotted versus the gate voltage. The sample is structurally equivalent to those described in the preceding section. However, for this particular device a breakthrough of the gate structure occurs only for, compared to other structures, very large gate voltages. The plotted traces show a gate voltage dependence

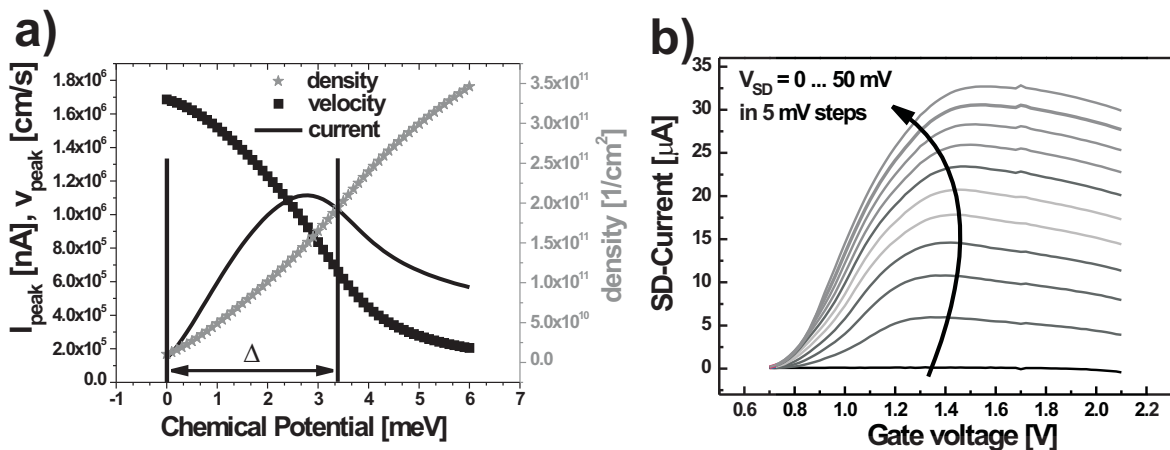


Figure 5.5: (a) Theoretical calculation of the density, the peak velocity and peak current of a surface SL in dependence on the chemical potential. (b) Gate voltage dependent current at small SD-biases.

that agrees with the theoretically expected behavior. The current first increases, reaches a maximum, and eventually decreases for very large gate biases. From figure 5.5(a) we find that the density at the peak should be about $1.6 \times 10^{11} \text{ cm}^{-2}$. Unfortunately, the mobility in the two-dimensional electron system is not good enough to observe Shubnikov-de Haas oscillations which could be used to extract this value experimentally. A comparison with gate voltages applied to samples in which this is possible suggests an electron density of the order of about $2 \times 10^{11} \text{ cm}^{-2}$, which is in agreement with theory. This correspondence between theory and experiment is the first experimental evidence of the formation of the surface SL structure.

Despite this proof of the surface SL structure at low SD-biases, the large SD-bias region is still dominated by pinch-off effects introduced through the gate. Therefore, it is desirable to work with structures in which non-linear SL transport occurs at low SD-biases. Such devices can be realized by a reduction of the gate channel length. In these samples, high electric fields can be achieved at small SD-biases.

5.4 Transport in short channel devices

For the first short channel devices, the number of SL periods was reduced from 100-200 down to 25 periods with unchanged well and barrier thicknesses of respectively 12 nm and 3 nm. Furthermore, the undoped GaAs buffer was reduced to a length of 75 nm. The combination of these changes leads to a much earlier breakthrough of the first growth step as seen in figure 5.6(a). There is already considerable current flow for SD-biases beyond about 150 mV. Figure 5.6(a) actually shows the I-V-characteristic of the bulk SL part of the sample for two different situations. One trace was taken for zero applied gate bias, after the sample was overgrown with the $\text{Al}_{0.32}\text{Ga}_{0.68}\text{As}$ barrier and the doped GaAs layer (no CEW). The corresponding cleaved-edge is shown in figure 5.6(b). The other one was measured after the second growth step was again removed by breaking it off with a very fine tungsten carbide tip. The removal of the gate structure is clearly visible in figure 5.6(c). The equivalence of the transport through the undoped bulk SL for zero applied gate bias and without any overgrowth is very important for the following discussion.

Once the gate voltage is increased so that an accumulation layer is formed, an additional current flow through the two-dimensional electron system is observed. However, as the traces in figure 5.7(a) show, there is a strong difference in shape as compared to the long channel devices discussed in section 5.2. The abrupt and strong NDC which we found to correspond to a pinch-off effect combined with resonant tunneling at the edge of the SL is no longer present. Only the traces for the highest gate voltages show NDC, but also much less pronounced than in the thicker SL samples. Nevertheless, there still seems to be a plateau-like behavior for most applied gate biases. However, the traces in figure 5.7(a) do not only include the transport through the two-dimensional channel but also through the bulk SL which opens up in the high SD-bias regime. So in order to find the

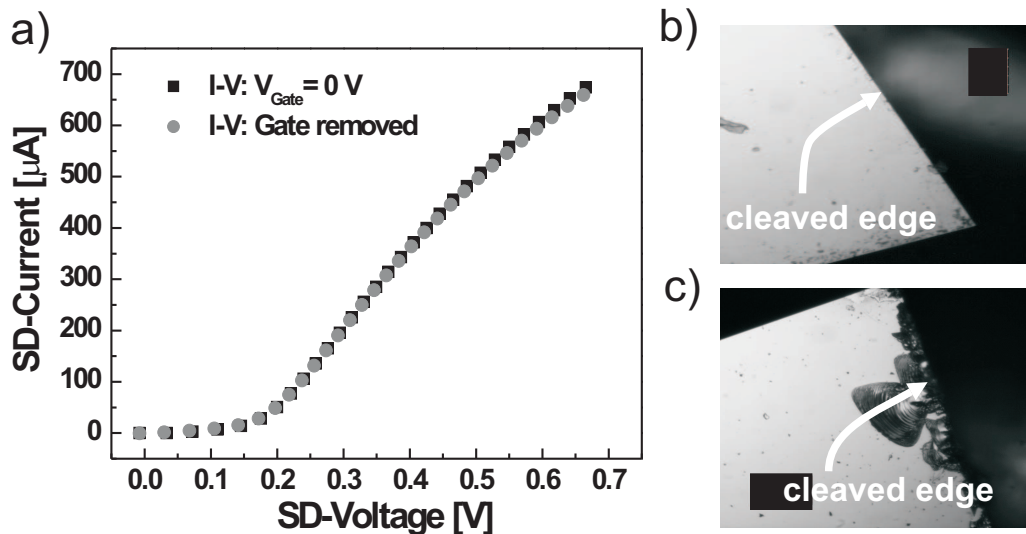


Figure 5.6: (a) Comparison of the bulk superlattice transport characteristics measured for zero gate voltage and with the gate mechanically removed. (b), (c) Cleaved-edge of the sample before and after the gate was scratched away.

current carried by the surface SL, we must subtract the transport contribution through the bulk SL. But as discussed in the preceding argument, this current is equal to the I - V -trace for zero applied gate voltage. Thus we can directly correct for this parallel transport and find the current through the surface SL only, as shown in figure 5.7(b). And although this still does not exactly resemble the theoretically expected transport characteristics as calculated in chapter 2.4, the overall shape is now much closer. For small SD-biases the current increases linearly, showing ohmic transport. When the SD-voltage is further increased, the transport saturates and reaches a maximum before it continuously decreases. Despite these similarities, there appear also some marked differences. Most notably, the current is almost completely quenched for SD-biases only twice as large as the one at the NDC peak. And in the NDC region, the characteristics possess a number of shoulders which are absent in the theoretical description.

A favorable explanation for this behavior would be to assume that the NDC is caused by Bloch oscillations in the surface SL while the quick quenching of the SD-current is again caused by a pinch-off of the conduction channel. This time, such a pinch-off could lead to a rapidly increasing electric field over a larger part of the SL which would quickly cause a very strong Stark localization of the electrons and consequently a vanishing of the overall transport.

In order to find experimental support for this interpretation, the influence of the gate must be further diminished. And since a further decrease in the number of SL periods would be the cause for concern about whether the resulting structure could still be called

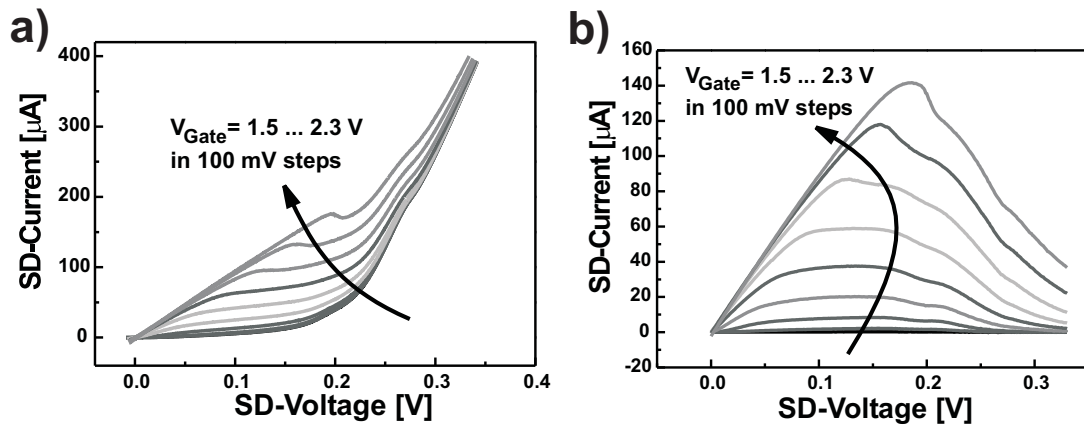


Figure 5.7: (a) Transport through a surface SL structure with strongly leaking bulk SL. (b) Current-voltage characteristics of the same surface SL after the transport has been corrected for the bulk SL leakage current.

a SL, pushing the pinch-off to higher SD-bias can only be achieved by increasing the gate barrier thickness. Just as a reduction in the channel length, this leads to a decrease in the effective ratio between SD-bias and gate bias, which determines the onset position of pinch-off. However, before such improved samples are investigated, there is another remarkable observation to make about the traces shown in figure 5.7(b). Due to the parallel transport through the bulk SL, most of the traces in figure 5.7(a) which show the combined transport through both bulk and two-dimensional transport channel do not exhibit any negative differential conductivity. Nevertheless, NDC is present as soon as we correct for the bulk SL transport. This indicates that, although NDC cannot be observed directly in the drift-diffusion transport through a superlattice structure,³ the addition of a parallel transport channel circumvents this limitation. At the time of these experimental observations there appeared a theoretical paper [DGSA03] suggesting such a combination of a SL with a parallel shunt. Therefore, before continuing our discussion about the short channel devices, we will briefly take a look at the predictions for the addition of a side shunt to a SL structure.

5.5 How to avoid electric field instabilities

In chapter 4 it was discussed that the formation of charge carrier domains prevents the observation of stable DC NDC. It was also stated that for the realization of a Bloch oscillator it is necessary to have a homogeneous electric field across the SL structure. However, such a homogeneous field distribution leads in turn to DC NDC. Thus, there seems to be an inherently unsolvable problem regarding the requirements for a Bloch oscillator. We need a homogeneous electric field, but it is not possible to realize it since it leads to DC

³This was discussed in some detail in the preceding chapter.

NDC, which is subject to electric field instabilities. In order to escape this situation, it becomes necessary to either relax the requirement of a completely homogeneous electric field, in such a way that DC NDC does not inevitably result, or to work with a homogeneous field while at the same time extending the system in such a way that no DC NDC results. Conventional SLs that fulfill the intermediate nL -product criterion (cf. chapter 4.3), which is for a $1 \mu\text{m}$ device given by $10^{11} \text{ cm}^{-2} < nL < 10^{12} \text{ cm}^{-2}$, are possible candidates for Bloch oscillators. The field distribution will be very close to homogeneous while at the same time no DC NDC occurs. The main problem with such devices is the fact that the nL -criterion fixes the maximum possible carrier densities in the range from $10^{15} \text{ cm}^{-3} < n < 10^{16} \text{ cm}^{-3}$. If these rather small values are inserted in expression (2.17) for the dynamic conductivity, the resulting gain values are very small and would hardly overcome unavoidable waveguide losses. The calculations of chapter 4 showed that surface SLs that fall into the intermediate nL -product range can have much larger densities. Due to the correspondingly larger gains, such surface SLs are very promising for a potential Bloch oscillator application.

Savvidis *et al.* [SKLA04] suggested a different approach that allows to work with conventional SLs that have somewhat larger densities. They proposed to strongly decrease the length of the superlattice so that the density can take on reasonably large values at a fixed nL -product. This should lead to reasonable gain in the structure. A short superlattice consists then of only about 10 to 15 periods.⁴ Since doped layers are put right next to the periodic structure, boundary effects like level misalignments and electron spill over play a crucial role for such devices. In order to realize structures with reasonable thicknesses, Savvidis *et al.* combined many of these short sections with highly doped layers in between. The resulting device, referred to as a super-SL structure, showed a THz transmission change under applied bias which is in accordance with the shape of the theory in chapter 2, assuming that about 75 percent of the structure are under perfect homogeneous alignment. Nevertheless, it is still unclear whether the resulting gain will be large enough to build an active oscillator.

Besides working with SLs that possess low nL -products, another suggestion of how to avoid field instabilities has been given by Daniel and co-workers [DGSA03]. They theoretically tested how density fluctuations evolve in the combination of a superlattice and a side shunt resistor. The latter is an extension of the system which can help to keep the total conductivity positive so that the electric field can be constant while no DC NDC occurs. Their principal ideas are graphically shown in figure 5.8(a) and (b). On the sides of the superlattice a doped layer acting as a parallel micro shunt resistor is attached. In order for this approach to succeed, it is important that the shunt is grown directly on the side of the superlattice since the theory requires direct lateral transport between the SL and the shunt.⁵

⁴This raises the interesting question of how many periods one needs to get a superlattice.

⁵It is not possible to merely connect the SL electrically in parallel with a resistor. In this case the dynamics in the SL are unchanged and instabilities cannot be avoided.

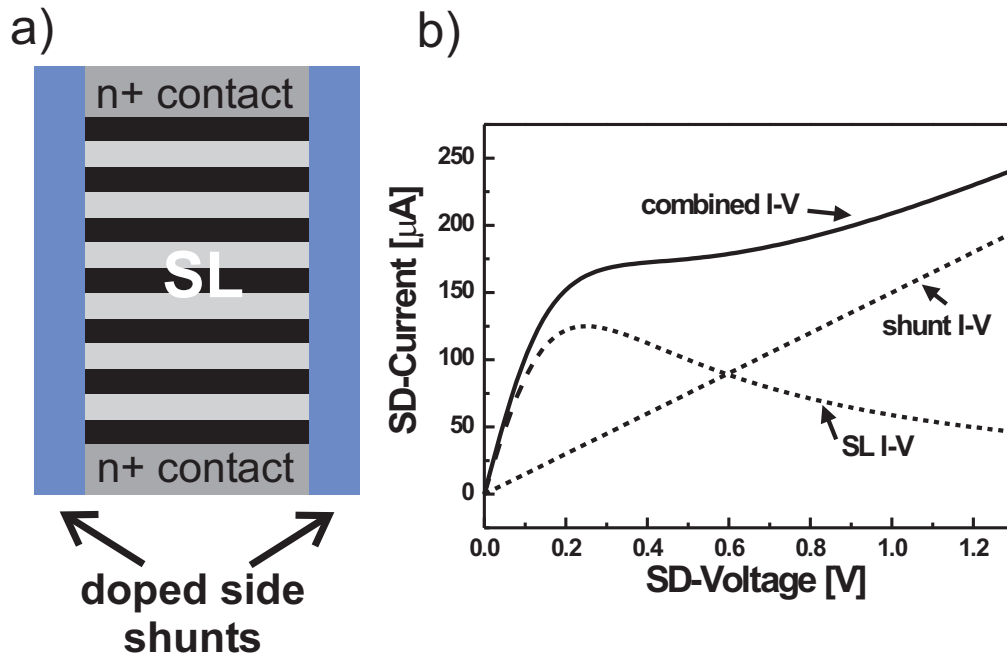


Figure 5.8: (a) Schematic drawing of a SL with doped side wall layers. (b) Individual and combined theoretical transport characteristics of a SL-shunt system.

The simulations in [DGSA03] show that if lateral transport between the micro shunt and the SL is possible, charge accumulations inside the SL can flow off into the micro shunt, thereby avoiding electric field instabilities. With this picture in mind it becomes immediately clear that the lateral extensions and resistivities of both the SL and the micro shunt are crucial parameters. The further the electrons have to travel between SL and shunt and the higher the resistance on their lateral route is, the less likely a stabilizing effect will occur. Also, with higher vertical resistance of the micro shunt, a smaller amount of charge can be conducted away from inside the SL and electric field stabilization will become poorer. The effective stabilization by the micro shunt can best be expressed in terms of a healing length. This scale determines how far into the SL the shunt can keep the electric field distribution homogeneous.⁶

The not too surprising result is that for a sufficiently small lateral extension of the SL structure, the formation of electric field instabilities is completely suppressed for all possible SD-biases. The healing length is then larger than the lateral size of the SL region. Therefore, if we had to design an ideal SL-shunt structure, we would choose a very narrow active SL size and would assume an atomically perfect interface between SL and shunt. But when this ideal structure is compared to the short channel surface SL discussed in the last section, a near perfect agreement is found. The lateral extension of the active high-density SL is only about 10 – 20 nm and due to the application of the CEO method

⁶The actual situation is somewhat more complicated, but the description is sufficient with regard to the discussion of the samples presented in this work.

an atomically precise interface is achieved. From this observation it can be concluded that our interpretation of the results shown in figure 5.7(b), with the NDC being due to Bloch oscillations in the surface SL, is strongly supported by the theoretical results that have just been discussed. The leakage current across the undoped bulk SL effectively shunts the surface superlattice transport, and keeps thereby both the electric field constant and the total differential conductivity positive. Though, we must point out that the electric field distribution across our shunt is not completely homogeneous, but only very nearly so.

From this point on, the discussion will entirely deal with SL-shunt systems where the shunt is always represented by an intermediate nL -product-SL and the active region is a high-density surface superlattice. While the next section is concerned with their static transport properties, it is discussed in chapter 7 how a shunt affects the high-frequency properties of a SL structure. From this point on, all shown transport characteristics of surface SLs have already been corrected for the zero gate voltage current carried by the shunt at equal SD-bias.

5.6 The shunted surface superlattice

At the end of the discussion about short gate length surface SL structures it was found that although NDC due to the SL seems present, pinch-off still strongly influences the overall shape of the I-V-characteristic, especially for high electric fields. A reduction of the channel length below 25 SL periods is impractical. Therefore, new samples with an increased gate barrier of thickness 500 nm (100 nm for former devices) were realized. This linear scaling of the gate bias is expected to keep the density along the surface SL closer to homogeneous while the SD-bias is increased.

Other structural changes include the removal of the intrinsic GaAs buffer layer and the addition of a CEW of finite width. The exclusion of the buffer layer is motivated in chapter 8 which deals with linear response transport in surface SLs. Moreover, structures with finite CEWs possess higher mobilities which is of important consequence in these small miniband surface SLs.

The I-V-characteristics measured for such a surface SL are shown in figure 5.9(a) for a variety of gate biases. The resulting traces are very close to those expected for a SL with a homogeneous electric field distribution. There is a linear transport regime for small SD-bias. Then, the transport saturates, reaches a maximum and eventually decreases in the high SD-bias region. The influence of the gate seems only present for gate voltages of 1.5 V, 2 V and 2.5 V. For the first two gate biases the current still drops very quickly towards zero, while the third gate bias shows a kink at a SD-bias of about 370 mV. This kink indicates that the NDC beyond 370 mV is due to pinch-off, while the NDC at lower SD-biases is due to the SL. For gate voltages beyond 2.5 V no pinch-off effect seems present in the shown SD-bias interval. The overall current saturation observed for these

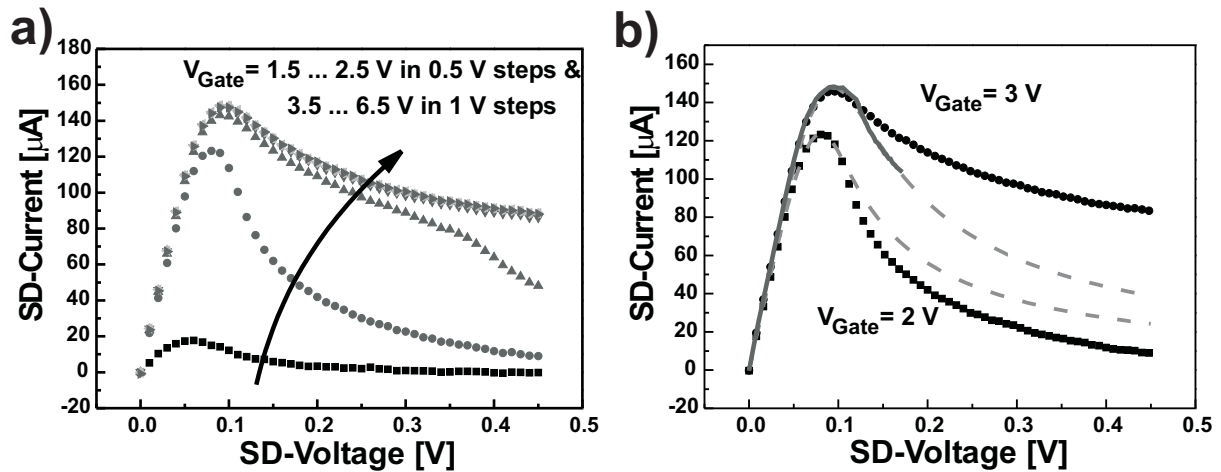


Figure 5.9: (a) Current-voltage characteristics of a surface SL with a 500 nm thick gate barrier. (b) Comparison of two traces (black symbols) of panel (a) with theoretically calculated transport characteristics (gray dashed lines). A linear rescaling of the SD-bias axis beyond the NDC peak for the 3 V gate voltage trace (full dark gray line) leads to a good agreement between experiment and theory.

latter traces must be attributed to the filling of the miniband, as discussed in section 5.3, since Shubnikov-de Haas measurements show a linear increase in density when the gate bias is raised.

Nevertheless, if we calculate the transport characteristics from the simple Esaki-Tsu model according to equation (2.14), including a series resistance for the doped contact layers and adjusting the peak current to the experimental data, a comparison between experiment and theory still shows major differences as seen in figure 5.9(b). While for a gate bias of 2 V the experimental current drop is much stronger than the one expected from theory, the 3 V gate voltage trace shows a much slower current decrease compared to the Esaki-Tsu model. As mentioned before, the small gate bias behavior can be explained by a pinch-off effect introduced through the gate. But the differences for gate voltages larger than 2.5 V cannot be accounted for in this way. They rather go back to the device geometry. The measurement setup for the transport characteristics shown throughout this chapter was discussed briefly in section 3.6. As mentioned there, one drawback of the device design is the position of the voltage probes which measure the SD-bias. They are not located directly at the surface SL, but on the contact layers. As long as the current flow is restricted to the surface SL the inclusion of a series resistance can account for the voltage differences introduced by the unfavorably positioned voltage probes. But the parallel current flow through the shunt makes the situation more complicated. A linear rescaling of the SD-bias for the 3 V gate voltage trace in the range between 120 mV and 250 mV by a factor of 0.7 gives an indication of how the device geometry has to be taken into account for shunted devices. After the rescaling, the experimental data agrees very

well with the theoretical prediction, as seen in figure 5.9(b). From this it can be deduced that the shunt current can lead to a considerable drop of voltage between the position of the SD-voltage probe and the edges of the surface SL.

To clarify the problem in more detail, let us investigate the current and voltage distribution of the device shown in figure 5.10. Just as in the surface SL structures we are dealing with a bulk SL which has two contact layers on each side. To make things simpler, let us assume that the total current flows into the top contact at the left upper corner and exits from the lower contact also at the left corner. As the current spreads through both SL and contact, the voltage along the upper contact becomes increasingly smaller. For a more quantitative description let us assume a voltage V_0 is applied, leading to a total current flow of I_0 . Due to the finite resistance of the contact layer, the voltage across the SL at position $x + \Delta x$ has dropped to a value $V(x + \Delta x) = V(x) - 2\Delta V$ compared to its value $V(x)$ at position x . At the same time, a current of magnitude ΔI has spread away through the bulk SL. If ρ_c and ρ_{SL} are, respectively, the sheet resistivity of the contact and the resistivity of the bulk SL, then the voltage and current distributions inside the

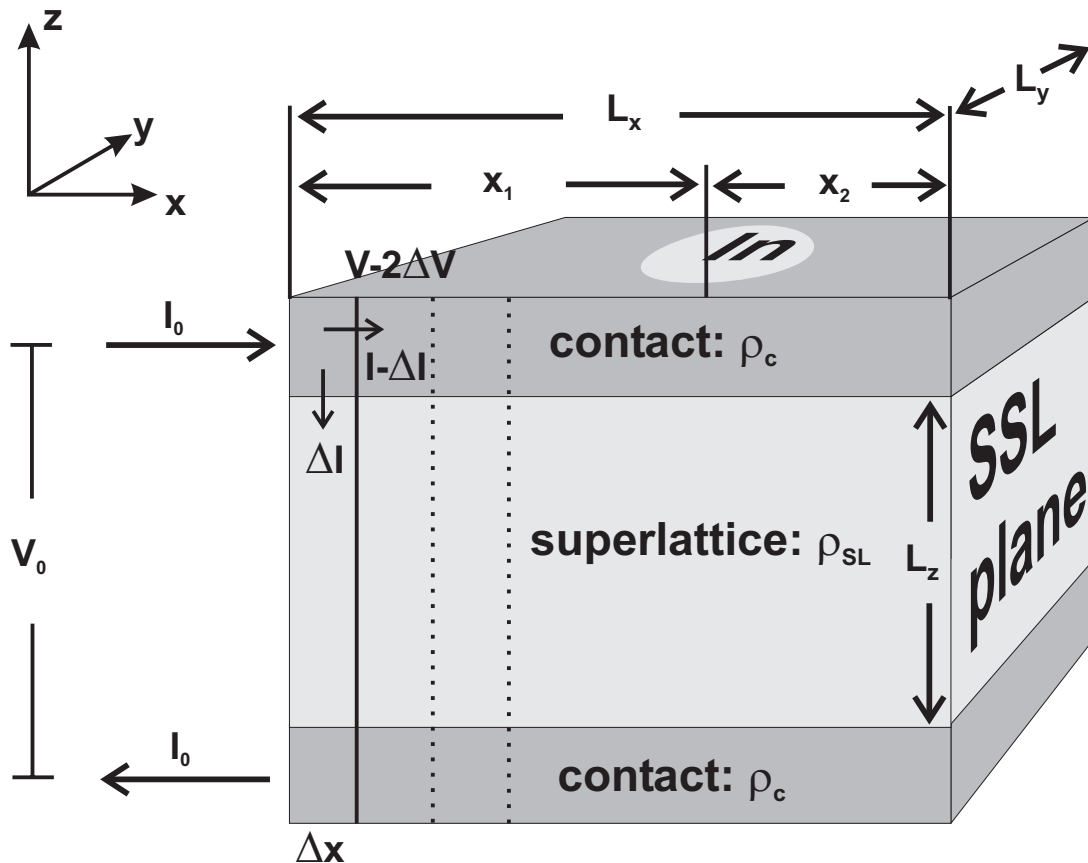


Figure 5.10: Model device for studying the voltage and current distributions in a shunted surface SL sample.

sample are described by the differential equations⁷

$$\frac{dV(x)}{dx} = -\frac{2\rho_c}{L_y}I(x) \quad (5.3)$$

$$\frac{dI(x)}{dx} = -\frac{L_y}{\rho_{SL}L_z}V(x). \quad (5.4)$$

The general solution for this problem is given by

$$V(x) = C_1 e^{\sqrt{\frac{2\rho_c}{L_z\rho_{SL}}}x} + C_2 e^{-\sqrt{\frac{2\rho_c}{L_z\rho_{SL}}}x} \quad (5.5)$$

$$I(x) = \frac{L_y}{\sqrt{2\rho_c\rho_{SL}L_z}} \left(C_1 e^{\sqrt{\frac{2\rho_c}{L_z\rho_{SL}}}x} + C_2 e^{-\sqrt{\frac{2\rho_c}{L_z\rho_{SL}}}x} \right). \quad (5.6)$$

Since the voltage continuously drops from V_0 when x increases from 0 to L_x , C_1 must be zero and C_2 is equal to V_0 from the starting condition at $x = 0$. The solution for the idealized structure therefore reads,

$$V(x) = V_0 e^{-\sqrt{\frac{2\rho_c}{L_z\rho_{SL}}}x} \quad (5.7)$$

$$I(x) = \frac{L_y V_0}{\sqrt{2\rho_c\rho_{SL}L_z}} e^{-\sqrt{\frac{2\rho_c}{L_z\rho_{SL}}}x}. \quad (5.8)$$

This means that the voltage applied at the left side of the structure decreases exponentially due to the transport through the bulk SL and can have a substantially smaller value at the right end $x_1 + x_2$ than at the position x_1 where the indium contact for the SD-bias measurement is. Thereby the magnitude of the difference between the voltages at x_1 and x_2 is determined by the value of $\sqrt{2\rho_c/L_z\rho_{SL}}$, which is the decay rate of the exponential factor. A direct measurement gives a sheet resistivity of about 120 Ω for the contacts and from its current-voltage characteristic a resistance of 400 Ω is deduced for the SL. With $L_x = 1 \times 10^{-3}$ m, $L_y = 0.5 \times 10^{-3}$ m, and $L_z = 1 \times 10^{-6}$ m the exponential factor takes on a value of about 0.58 for a distance of about 0.5 mm between SD-voltage probe and surface SL. This number is comparable to the value used before to rescale the SD-bias in order to find agreement between theory and experiment.

The thing to keep in mind for the realization of shunted surface SLs, which are not contacted directly at the active region, is to design them in such a way that the factor $\sqrt{2\rho_c/L_z\rho_{SL}}$ becomes very small. This can be achieved by high doping densities in the contact layers (small ρ_c), by a comparatively large resistivity ρ_{SL} of the shunt, and by a large number of SL periods (large L_z). In order to account for this result, later structures, which are discussed shortly, were grown with thicker contact layers in order to reduce the sheet resistivity ρ_c .

Before these final surface SL versions are investigated, let us take a look at the properties of another structure which consists of an undoped bulk SL with 60 periods of 12 nm

⁷In principle, ρ_{SL} depends on the voltage $V(x)$. However, for large parts of the concerned bias range the bulk SL transport characteristic is linear, exhibiting a constant ρ_{SL} .

wide wells and 5 nm thick barriers. Both its contact layers follow immediately next to the SL and the second growth step consists of a 5 nm wide CEW followed by a gate structure with a 500 nm thick barrier. The current-voltage characteristics of this structure are plotted in figure 5.11(a) for a number of gate biases. While the traces for gate voltages of 1.5 V, 2 V and 2.5 V show a very good agreement with the Esaki-Tsu theory represented by the black lines, the trace for a gate bias of 3 V shows a kink that we came to associate with pinch-off. Even more intriguing, the data for even higher gate voltages do not show NDC at all, but the corresponding characteristics rather increase strongly after a short plateau at the position where the NDC is expected. From this we can draw the following conclusions. Although the data in the small gate bias regime is close to the theoretical expectation, the NDC part seems to still be in part influenced by gate-induced pinch-off effects. And in the high gate bias regime it seems as if a second transport channel has opened up. At this point one might be inclined to start to worry about exciting electrons to higher minibands. The minigaps in surface SLs are after all smaller than in conventional SLs. However, as the black lines in figure 5.11(a) show, the high gate bias traces can be very accurately fitted⁸ assuming an ohmic resistance transport channel in parallel to the surface SL. Once the transport traces are corrected for this additional contribution, the almost perfect current-voltage characteristics of a SL with homogeneous field alignment as plotted in figure 5.11(b) result. The 2.5 V gate bias trace seems to behave exceptionally as compared to the other traces. This can clearly be attributed to the fact that this characteristic falls into the crossover regime between additional ohmic transport and gate induced pinch-off. The two effects essentially offset each other. However, this compensation makes it rather likely that there is some additional parallel current flow

⁸The corresponding fit functions consist of the sum of an Esaki-Tsu trace, which includes a series resistance, and a linear term $a * x + b$.

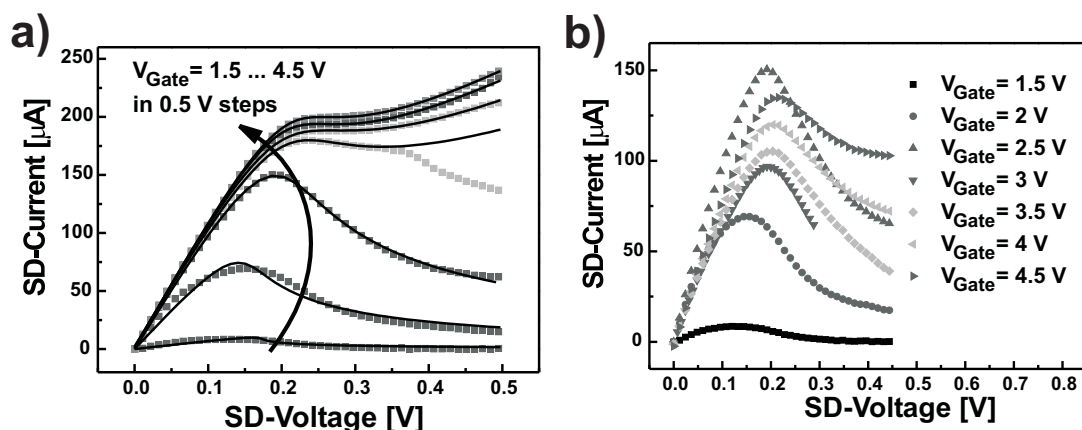


Figure 5.11: (a) Current-voltage characteristics of a surface superlattice which shows no NDC for large applied gate biases. (b) Same data as in graph (a), however, the high gate bias traces have been corrected for an additional linear current contribution.

at the NDC peak position. Therefore, the NDC peak height of this trace is somewhat overestimated.

But where does the parallel ohmic current flow originate from? The answer is contained in the observations that the additional current increases linearly with the applied SD-bias and that the current-voltage characteristic of the shunt is also linear over large SD-bias regions. Having stated this, it seems quite natural to conclude that the additional parallel transport is carried by the shunt, which is a parallel channel that is present by design. In order to understand this in more detail, let us assume that the current carried by the surface SL introduces an additional voltage drop ΔV_{SSL} between $x = 0$ and $x = x_1$ in figure 5.10. x_1 marks the position of the indium contact at which the SD-bias is measured. In the high SD-bias regime, where the surface SL current has already dropped considerably and can therefore be taken as nearly constant, the induced additional voltage drop is given by

$$\Delta V_{SSL} = I_{SSL} \frac{\rho_c}{L_y} x_1 . \quad (5.9)$$

This in turn then requires that the applied voltage V_0 is increased by the same amount in order for the measured SD-bias to be equal in the cases of the surface SL transport channel being off and on. Nevertheless, this voltage shift cannot be responsible for the additional ohmic transport channel. This can be deduced from the observation that an additional constant voltage shift means that we compare shunt characteristics which are laterally shifted by the small value of ΔV_{SSL} . But since the two traces are still parallel, the additionally caused current flow would be constant.

However, we have neglected that the increased applied total bias also leads to an increased total current flow across the shunt. This additional shunt current introduces an increased voltage drop between $x = 0$ and $x = x_1$, which is given by

$$V_{SL} = \int_0^{x_1} I_{SL}(x) \frac{\rho_c}{L_y} dx \quad (5.10)$$

where the shunt current I_{SL} is given by equation (5.8). The integral on the right side can be evaluated and the voltage drop can be expressed as

$$V_{SL} = V_0 \left[1 - \exp \left(\sqrt{\frac{\rho_c}{2\rho_{SL}L_z}} x_1 \right) \right] . \quad (5.11)$$

This result states, that the voltage drop V_{SL} is actually proportional to the applied bias V_0 itself. Since the shunt trace becomes sublinear in the high bias regime, ΔV_{SL} , which is the difference between V_{SL} with the surface SL being on or off, will depend on V_0 and can even become proportional to it. Thus, while the constant voltage drop ΔV_{SSL} could only lead to an additional constant parallel current, the additional shunt current flow can lead to an ohmic parallel transport channel just as observed in the experiment. The difference in total current for equal SD-bias in the cases of surface SL channel on and off can then be expressed as

$$\Delta I = I_0(V^{(1)} + \Delta V_{SSL} + \Delta V_{SL}) - I_0(V^{(1)}) , \quad (5.12)$$

where $V^{(1)}$ is the total bias V_0 in the case of the surface SL channel being off. Assuming a linear relationship between current and voltage for the shunt, which is realistic for large parts of the shunt characteristic, the latter equation leads to

$$\Delta I = I_{SSL} + \frac{V^{(1)} + \Delta V_{SL}}{R_{SL}} - \frac{V^{(1)}}{R_{SL}} \quad (5.13)$$

$$= I_{SSL} + \gamma V_0, \quad (5.14)$$

where γ is a constant factor. Thus, it is the shunt which provides the parallel ohmic transport and it appears in the measurement due to the shortcomings of the placing of the voltage probes. But we shall see in the following that a fitting procedure including this parallel transport allows for a separation of the different current contributions. This fitting procedure is applied to the transport characteristic depending on the SD-bias. However, since all structures to which this approach is applied have parameters so that the exponential factors in all equations of this chapter can be well approximated by their linear expansions, the SD-bias V_{SD} and the total bias V_0 are connected by a linear relation. Therefore, all conclusions drawn for the voltage V_0 remain valid for V_{SL} , albeit with a rescaled factor γ .

Despite this explanation for the additional observed current transport in the shunted surface SL structures, one might still worry about a possible excitation of electrons into higher lying minibands. However, such an excitation cannot account for the observed transport characteristics. If the saturation of the high gate voltage transport characteristics shown in figure 5.11(a) were indeed due to a transfer effect between different minibands, then the excited minibands would have to have smaller mobilities.⁹ However, there are a number of samples without a CEW in which the same effects (NDC and saturation) have been observed during the course of this work. For samples without CEW, the energetic widths of at least the three lowest lying minibands are equal. From this fact equal band structures and mobilities result and, therefore, a transfer effect is not expected in these structures. Moreover, the NDC peak positions of all samples in this chapter lie at Stark splittings (the potential drop over one SL period) which are much smaller than the widths of the minigaps between the two lowest minibands. The reason why the NDC occurs already for such small electric fields is the high mobility of the two-dimensional electron system.

Based on the understanding developed for the last two described sample structures, one further design was realized with which most of the measurements presented in the following chapters were performed. It consists of a SL with, respectively, 12 nm and 3 nm wide wells and barriers. The number of periods is 66, giving a total channel length of nearly 1 μm , and the contacts are immediately set next to the SL without any buffer layers. The width of the gate barrier was chosen to be either 500 nm or 2 μm . The 2 μm design was realized in order to reach large ratios of gate voltage to SD-bias even for small

⁹This situation occurs in Gunn devices.

channel densities. Different samples with CEW widths of 1.6 nm, 5 nm, 10 nm, and 20 nm were realized. Structures without CEW did not show the formation of a two-dimensional transport channel. The measured current-voltage characteristics of these structures are shown in figure 5.12. Structures with CEW widths of 1.6 nm, 5 nm and 10 nm have a 2 μm thick gate barrier. The device with the 20 nm CEW has a 500 nm thick gate barrier. Several noteworthy features are observed in these figures. For the sample with the 1.6 nm CEW jumps in the current-voltage characteristic are visible. Beyond these jumps, however, the traces do follow the SL behavior quite nicely. The reason for the initial abrupt jump is the turning on of the shunt transport. The shunt characteristic shown in the same plot reveals that there is only considerable current flow through the shunt beyond about 100 mV. For smaller SD-biases, the system behaves as if there was no shunt and, as we shall see in the next section, this results in a stronger increase of the total transport through the surface SL than when a shunt is present. Thus, the initial jumps in figure 5.12(a) mark those voltages at which the shunt carries enough current to stabilize the electric field distribution along the surface SL. The traces therefore directly show the crossover between shunted and unshunted surface SL transport. The reason for the additional second jump in the traces at $V_{\text{Gate}} = 14$ V and 15 V is discussed for the 5 nm CEW samples which also shows these jumps at large gate biases. The high SD-bias parts of the traces of the 1.6 nm CEW sample do look noisier than those of the other structures. This goes back to the fact that this structure has the smallest minibands and thus carries the least current. For small surface SL current, the noise in the measurement increases naturally since the surface SL current is measured as the difference between much larger transport values which each include the shunt.

In figure 5.12(b), in which the data of the 5 nm CEW sample is plotted, each of the high gate bias characteristics exhibits one current jump. A study of the current through the combined SL-shunt system, as shown in figure 5.13(a), reveals that these jumps are caused when the voltage drop for the combined system shows an abrupt horizontal shift. When the smoothly rising shunt current is subtracted from the trace with the horizontal jump, the jumps seen in the surface SL transport traces are produced. It is currently not clear what the cause of these horizontal voltage jumps in the characteristics of the combined SL-shunt system is. The shift towards higher SD-bias with increasing gate voltage indicates that the ratio between both values is important. This suggests an influence from the gate even though no pinch-off is observed for traces at smaller gate voltages. Since the current jumps also occur in regions with relatively low NDC and do not show hysteresis, they are not connected to the concept of charge domain instabilities. The current jumps rather seem to appear due to a boundary effect between two-dimensional channel and bulk SL. Apparently, the correct way to handle them is to cancel the shift in SD-bias for the combined system and to then do the subtraction of the shunt current. As shown in figure 5.13(b), this restores the surface SL current to the shape which is observed for smaller gate biases and which agrees quite well with the Esaki-Tsu theory. Just as for the 1.6 nm CEW sample, also the 5 nm CEW structure shows a small double peak before

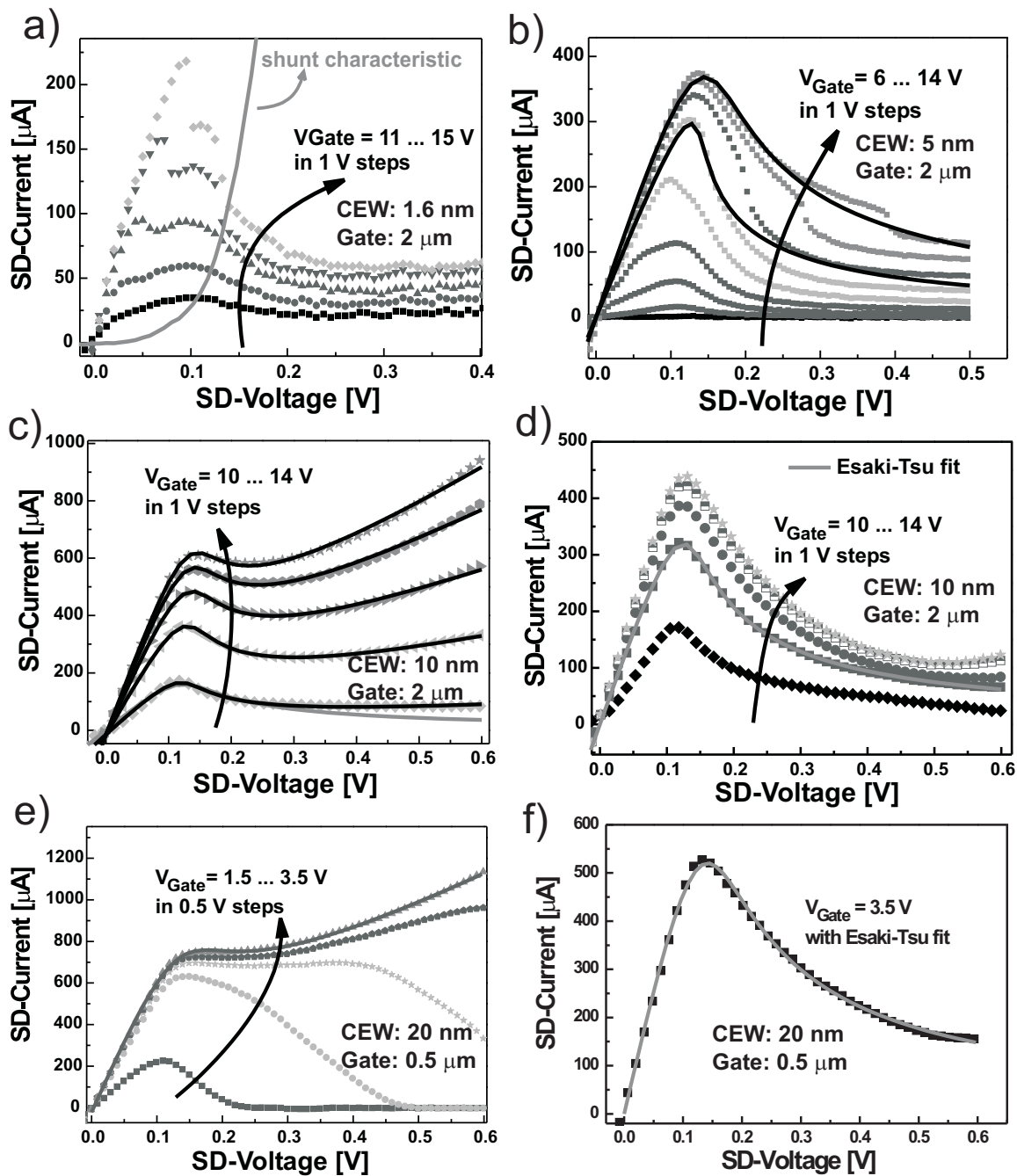


Figure 5.12: (a), (b), (c) Current-voltage characteristics of surface SLs with identical parameters, except that the cleaved-edge well (CEW) is 1.6 nm in (a), 5 nm in (b), and 10 nm in (c). In (d) the traces of (c), corrected for a parallel linear transport channel, are plotted. (e), (f) Same as (c) and (d), however, for a sample with a 20 nm CEW. The black and gray lines are theoretical fits with either the simple Esaki-Tsu model (b),(d),(f) or with the Esaki-Tsu model plus an ohmic transport channel (c),(e).

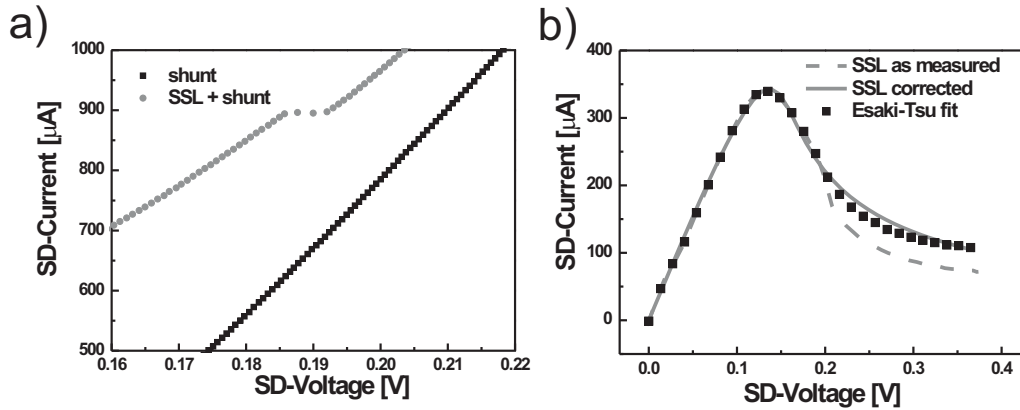


Figure 5.13: (a) Part of the combined current-voltage characteristic of a shunted surface SL structure with a 5 nm wide cleaved-edge well. (b) Resulting surface SL transport characteristic once the lateral jump in figure (a) has been accounted for.

the onset of NDC for small gate bias traces. This is again attributed to a small current overshoot before the shunt transport sets in.

The samples with 10 nm and 20 nm thick CEW show a very pronounced parallel ohmic transport contribution. This is on one hand due to the fact that both samples carry more current than the samples with thinner CEW. The higher surface SL current increases the growth rate of the additional ohmic shunt contribution. On the other hand, however, the strength of the ohmic transport through the shunt, which is not canceled with the zero gate voltage trace, also depends on the individual sample properties. Some 5 nm CEW samples have shown almost as much additional transport as the 10 nm and 20 nm CEW samples in figure 5.12. Once corrected for additional transport, the traces in figure 5.12(d) and (f) show a near perfect SL behavior. The fact that the corrected high gate bias transport characteristics of the 10 nm CEW sample show a current increase at the high SD-bias end goes back to an imperfect fitting of the data. This can be both caused by non-linearities of the shunt characteristic and a possible deviation of the SSL characteristic from the Esaki-Tsu behavior, when the bandstructure deviates increasingly from the cosine form with increasing CEW width.

5.7 Properties of shunt-stabilized surface superlattices

Up to now, the discussion was mainly focused on the development of surface superlattices and the interpretation of the observed transport in comparison to an ideal superlattice. The samples introduced at the end of the last section are the ones which are investigated for the remainder of this work. Therefore, it is advisable to take a closer look at their

transport properties.

In chapter 2 it was found that the semiclassical expression for the drift velocity of a SL system, which is directly proportional to the current, can be written as

$$v_d = F(T, \mu) \frac{\Delta d}{2\hbar} \frac{\omega_B \tau}{1 + \omega_B^2 \tau^2} . \quad (5.15)$$

In this expression the Bloch frequency is given by $\omega_B = \frac{eFd}{\hbar}$, τ is the relaxation time of the system, and $F(T, \mu)$ is a coefficient which depends on the actual distribution of the electrons in the miniband. The electric field position F_c at which expression (5.15) takes on its maximum value and to which the current peak of the measurement can be compared is determined by the condition

$$\omega_B \tau = 1 \quad \text{which is similar to} \quad F_c = \frac{\hbar}{ed\tau} . \quad (5.16)$$

The time τ in this simple picture characterizes the rate at which the non-equilibrium electron distribution relaxes back to equilibrium once the external electric field is turned off. This simple single relaxation time approximation is very crude, since elastic and inelastic scattering processes have profoundly different influences on the transport through the superlattice. A more sophisticated approach is studied in the next section. Nevertheless, equation (5.16) gives us a rough estimate of the characteristic transport time scales in surface SLs. Figure 5.14(a) and (b) show respectively the current peak position and height for structures with different CEW values. The gate voltage values for the sample with 20 nm CEW was scaled by a factor of 4 to make up for the same factor in gate barrier thickness. The peak positions are corrected for a series resistance of about 150 Ω , a value which results both from the aforementioned fitting procedure and, as we shall see, also from the linear response measurements presented in chapter 8. The evolution of the peak height with increasing gate voltage is different than discussed in section 5.3, where we found that the peak current should first increase and then decrease again. However, this is only true if the miniband width stays constant as the density rises. But as we found in chapter 3.4, for a finite CEW width the miniband width increases linearly with the electron density and therefore also the peak current should increase (cf. equation (5.15)). A combination of the decrease in the distribution factor describing the miniband filling and of the increase in miniband width fits very well with the observed slow saturation of the peak current. Also, we need to be aware of the fact that the highest achievable densities ($V_{\text{Gate}} = 19$ V) are only about 66 % of the densities realized with the 100 nm thick gate barriers. This is most likely caused by imperfections introduced at the upper end of the cleavage plane (the top corner on the right side in figure 3.1) during the second growth processes. These imperfections seem to play a more important role when a thicker gate barrier is grown and lead to a smaller electric breakdown field, resulting in smaller achievable electron densities. Finally, as we shall see in the next section, the current peak height is determined not only by the SL parameters but also by the scattering rates. And

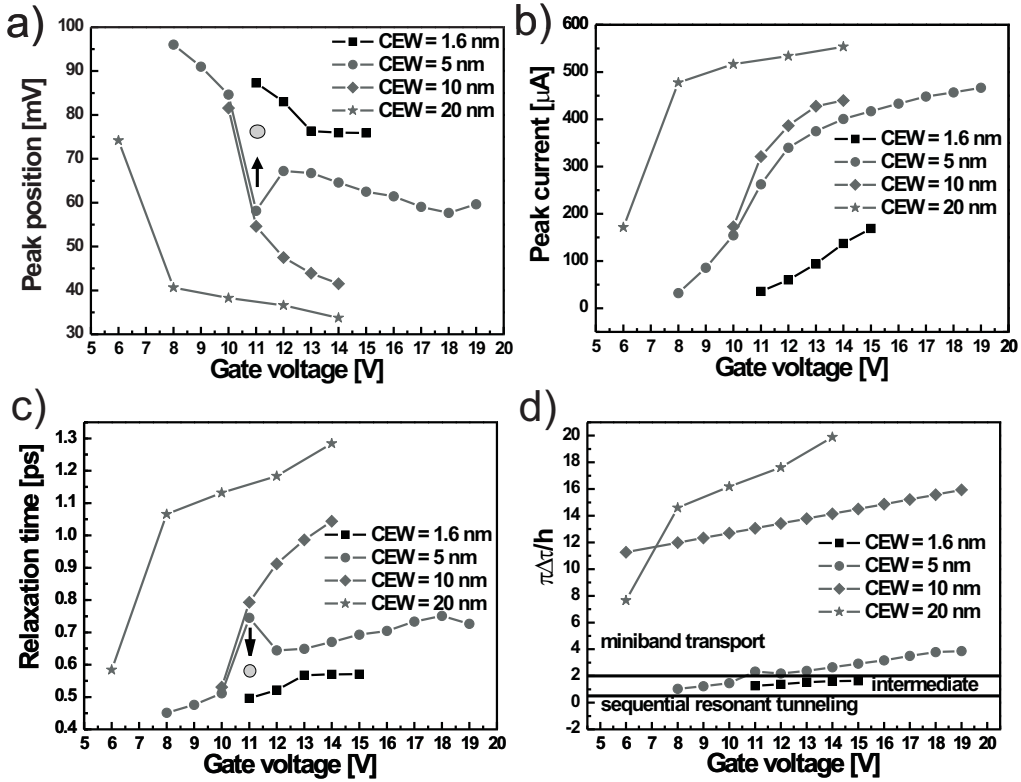


Figure 5.14: (a), (b) NDC peak position and peak height for different surface SL systems plotted versus the applied gate bias. (c), (d) Relaxation times and the transport regimes deduced from the data in (a) and (b). The transport regimes are found by comparing the ratio of one fourth of the miniband width $\Delta/2$ and the scattering induced broadening \hbar/τ to the calculations reported in [Wac02b]. The gray circle in panels (a) and (c) indicates that the extracted values at $V_{\text{Gate}} = 11$ V appear to be exceptional. The reason for this is, probably, that the current jump which occurs in the traces at higher gate voltages happens here right in the vicinity of the NDC peak.

since these usually depend also on the electron density, a complete theoretical description of the evolution of the peak current with increasing density is quite intricate. For the sample in section 5.3 the situation was simpler since the miniband width could be assumed constant and the scattering rates should have also depended less strongly on the electron density, as the two-dimensional system always resided completely in the undoped bulk SL.

In figure 5.14(c) the relaxation times, calculated according to expression (5.16) from the NDC peak positions, are plotted. With increasing CEW width the relaxation times become longer, which can be understood once we look at the dominant scattering mechanisms in the system. In conventional high density SLs the dominant elastic scattering

processes result from interactions with impurities and interface roughness. Since the electrons in our structure are induced by a gate rather than doping, we are only concerned with interface roughness. Even in doped SLs the latter seems to be the dominant source of elastic scattering [DB90, MPP⁺94, WBR⁺99]. Among inelastic events longitudinal optic (LO) phonons are usually most important. However, the miniband widths in the studied structures are too small to emit LO phonons and at the temperature of 4.2 K no LO phonons are present which could be absorbed. Therefore, acoustic phonon scattering is the only source for energy relaxation in the presented surface SL structures. Due to a zone-folding of the acoustic branches in SL structures (cf. appendix B), these processes can also become more effective at small wavevectors k . But through the insertion of a CEW, both the scattering from interface roughness and from possible backfolded acoustic phonons are expected to be weakened. The electronic system simply resides less and less inside the bulk SL where both processes originate. Thus, it seems quite reasonable that an increase in the CEW width or an increase in the electron density, which also shifts the electrons closer to the gate barrier, leads to longer relaxation times.

In order to determine the correct transport description for the investigated structures, the scattering-induced broadening of the SL states must be compared to the miniband width, as described in detail in chapter 2. Figure 5.14(d) shows the resulting values and classifies them according to the theoretical work done in [Wac02b], assuming zero SD-bias. All structures except the 1.6 nm CEW one lie very close or clearly in the regime of miniband transport. Thus, the comparison with the Esaki-Tsu model is justified and it can be concluded that, if we can proof a homogeneous field across the structure, we have for the first time electrically excited stable Bloch oscillations in a high density SL.

The results presented in the next section show that the scattering rates which determine the onset of Bloch oscillations in the studied surface SL devices are even longer than the ones determined from the NDC peak positions. The reason for this is that the electronic system heats up strongly under the influence of a large electric field. The peak position is then no longer completely determined by the scattering rates in the system, but also by the effective electronic temperature in the electron distribution. A more advanced theoretical description is necessary to model the transport in this situation. Such an advanced description is given in terms of a fully two-dimensional model in the following section. The model will on one hand give us a much better understanding about the involved transport processes. On the other hand, it allows us to extract important system parameters. A comparison of the model to the experiment will yield three central values: the elastic and inelastic scattering rates τ_e and τ_i and also the effective electron temperature T_e which characterizes the average energy in the electron distribution. These three parameters are crucial because they are necessary to calculate the gain in the surface SL structure according to equation 2.17. Thereby it is very important to go beyond a simple one-dimensional model in order to acquire more realistic values.

5.8 A two-dimensional surface superlattice transport model

As just mentioned, a fully two-dimensional transport study in surface SLs is undertaken in the following. The model we apply has previously been used for conventional SLs [MPP⁺94]. The study in [MPP⁺94] involved wide miniband structures in which the chemical potential lay far below the bottom of the first miniband. This situation allows the use of the Maxwell-Boltzmann distribution function for the description of the electronic system. However, in the high-density surface SLs measured at low lattice temperatures the chemical potential lies inside the miniband or even beyond the top of the miniband. In this case we must work with the Fermi-Dirac distribution function.

The main difference between a one-dimensional and a two-dimensional transport model is that the phase space for scattering is in the one-dimensional case much smaller than when the free direction k_y is also considered. Especially for elastic processes not only scattering between the states at $\pm k$ is possible. Instead, all k_x and k_y values are involved which lead to the same energy.

In the two-dimensional model the total energy of an electron at (k_x, k_y) is given by

$$E(k_x, k_y) = \frac{\hbar^2 k_y^2}{2m} + \frac{\Delta}{2} (1 - \cos(k_x d)) , \quad (5.17)$$

where m is the effective mass along the free surface SL direction and Δ, d are the usual SL parameters. According to the semiclassical acceleration theorem a k -state velocity

$$v_x(k_x) = \frac{\Delta d}{2\hbar} \sin(k_x d) \quad (5.18)$$

along the superlattice axis is derived from the dispersion (5.17). Since we will stay within the semiclassical picture, the governing transport equation is the Boltzmann equation. In contrast to the equation used in chapter 2.4, we now explicitly distinguish between elastic and inelastic scattering processes,

$$\frac{\partial f(k_x, k_y, T, \mu)}{\partial t} + \frac{eF}{\hbar} \frac{\partial f(k_x, k_y, T, \mu)}{\partial k_x} = - \frac{f(k_x, k_y, T, \mu) - f_0(k_x, k_y, T_L, \mu)}{\tau_i} - \frac{f(k_x, k_y, T, \mu) - f_0(k_x, k_y, T_e, \mu)}{\tau_e} . \quad (5.19)$$

The relaxation time approximation consists now of two terms. The first one describes the inelastic processes, which relax the non-equilibrium distribution $f(k_x, k_y, T, \mu)$ back to the equilibrium distribution $f_0(k_x, k_y, T_L, \mu)$ at the lattice temperature T_L when the electric field is turned off and elastic relaxation is neglected.¹⁰ The second term represents the relaxation due to elastic scattering. When the electric field is turned off and inelastic processes are neglected,¹¹ this term brings the system back to the equilibrium distribution

¹⁰Mathematically this corresponds to the assumption of $\tau_e \rightarrow \infty$.

¹¹This corresponds to the mathematical assumption of $\tau_i \rightarrow \infty$.

$f_0(k_x, k_y, T_e, \mu)$. However, since no energy can be dissipated, the effective temperature T_e of the distribution is higher than the lattice temperature.

As we have now introduced a further parameter in T_e , it is necessary to give a defining equation for it. This is done through the requirement that the total energy of the non-equilibrium distribution has to be equal to the energy of an equilibrium distribution at the effective temperature T_e ,

$$\int_{-\infty}^{+\infty} dk_y \int_{-\frac{\pi}{d}}^{+\frac{\pi}{d}} dk_x E(k_x, k_y) f(k_x, k_y, T, \mu) = \int_{-\infty}^{+\infty} dk_y \int_{-\frac{\pi}{d}}^{+\frac{\pi}{d}} dk_x E(k_x, k_y) f_0(k_x, k_y, T_e, \mu) . \quad (5.20)$$

Once T_e has been determined from it, the drift velocity of the system can be calculated according to

$$v_d = \frac{1}{N} \int_{-\infty}^{+\infty} dk_y \int_{-\frac{\pi}{d}}^{+\frac{\pi}{d}} dk_x v_x(k_x) f(k_x, k_y, T, \mu) . \quad (5.21)$$

Applying the above equations to a system described by a Maxwell-Boltzmann distribution is straight forward. Once the Fermi-Dirac distribution is worked with, however, a more careful approach is necessary. A change in temperature will always be accompanied by a change in the chemical potential since the density is fixed by the gate voltage. Therefore, equation (5.20) cannot be solved straight forward, but we also have, at the same time, to fulfill the condition

$$n = \int_{-\infty}^{\infty} dk_y \int_{-\frac{\pi}{d}}^{+\frac{\pi}{d}} dk f_0(k_x, k_y, T_e, \mu) . \quad (5.22)$$

This means that the particle conservation and the definition for T_e have to be solved simultaneously, which is done in a self-consistent approach. For every applied electric field, starting from the situation at lattice temperature, the conditions (5.20) and (5.22) are solved self-consistently before the drift velocity is calculated.

For a numerical evaluation of the model, equations (5.20) and (5.21) can be rewritten in the form

$$FD_1(T_L) = FD_1(T_e) \left[1 + \left(\frac{F}{F_1} \right)^2 \right] + \frac{2}{\Delta} (G_0(T_L) - G_0(T_e)) \left[1 + \left(\frac{F}{F_0} \right)^2 \right] \quad (5.23)$$

$$v_D = \left[1 + \frac{\tau}{\tau_e} \left(\frac{2(G_0(T_L) - G_0(T_e))}{\Delta FD_1(T_L)} \right) \right] \frac{e\tau\Delta d^2}{2\hbar^2} FD_1(T_L) \left[\frac{1}{1 + (F/F_1)^2} \right] \quad (5.24)$$

where $F_0 = \hbar/ed\tau$, $F_1 = \hbar/ed\sqrt{\tau\tau_i}$, and $\tau = \tau_i\tau_e/(\tau_i + \tau_e)$. The quantities G_0 , FD_1 and

the density n can be expressed as integrals involving Fermi-Dirac integrals,

$$G_0(T) = k_B T \frac{\int_{-\pi}^{\pi} dx F_{\frac{1}{2}} \left(\frac{\mu}{k_B T} - \frac{\Delta}{2k_B T} (1 - \cos(x)) \right)}{\int_{-\pi}^{\pi} dx F_{-\frac{1}{2}} \left(\frac{\mu}{k_B T} - \frac{\Delta}{2k_B T} (1 - \cos(x)) \right)}, \quad (5.25)$$

$$FD_1(T) = \frac{\int_{-\pi}^{\pi} dx \cos(x) F_{-\frac{1}{2}} \left(\frac{\mu}{k_B T} - \frac{\Delta}{2k_B T} (1 - \cos(x)) \right)}{\int_{-\pi}^{\pi} dx F_{-\frac{1}{2}} \left(\frac{\mu}{k_B T} - \frac{\Delta}{2k_B T} (1 - \cos(x)) \right)}, \quad (5.26)$$

$$n = \sqrt{\frac{2mk_B T}{\hbar^2 d^2}} \frac{1}{2\pi^2} \int_{-\pi}^{\pi} dx F_{-\frac{1}{2}} \left(\frac{\mu}{k_B T} - \frac{\Delta}{2k_B T} (1 - \cos(x)) \right). \quad (5.27)$$

Thereby, the Fermi-Dirac integral $F_q(\eta)$ is defined by

$$F_q(\eta) = \int_{-\infty}^{\infty} \frac{y^q}{\exp(y - \eta)} dy. \quad (5.28)$$

The numerical evaluation of Fermi-Dirac integrals where q is an integer can be performed effortlessly [AHSMM83]. For half-integer q a second term appears in the series expansion of the integral which converges extremely slowly [AHSMM83]. Therefore, a very precise numerical calculation of the expression (5.28) can be very demanding and time consuming. However, in our calculations we only require the precision of a few percent. This can be achieved by using closed form approximations for the integral (5.28) [AHSMM83].

The independent parameters of our model are the elastic and inelastic relaxation times. In order to compare the theoretical calculations to the experimental data, both scattering times were varied until an agreement of the NDC peak position and peak height was achieved. The two conditions determine the two unknowns completely.

In figure 5.15(a) - (c) the results of the theoretical model for a number of different relaxation time pairs are shown.

1. For an infinitely long elastic scattering time¹² the result resembles the Esaki-Tsu prediction with the inclusion of a finite number of electrons being distributed in the miniband. Both for $\tau_i = 1$ ps and $\tau_i = 100$ fs the same peak current is reached. However, the onset of NDC and of Bloch oscillations, which are determined in these cases by τ_i , require different electric fields which correspondingly also differ by about an order of magnitude. The electronic temperatures do not increase too strongly since all scattering events are inelastic and allow for an effective dissipation of energy. This in turn leads to minor changes in the chemical potential. Except for a rescaling of the electric field axis both cases are equivalent.
2. Once elastic and inelastic relaxation are of equal importance, the situation changes. The electronic temperature rises to higher values, indicating that elastic scattering

¹²1 ms is at least 9 orders of magnitude longer than the chosen τ_i . Thus the result is very close to the limit $\tau_e \rightarrow \infty$.

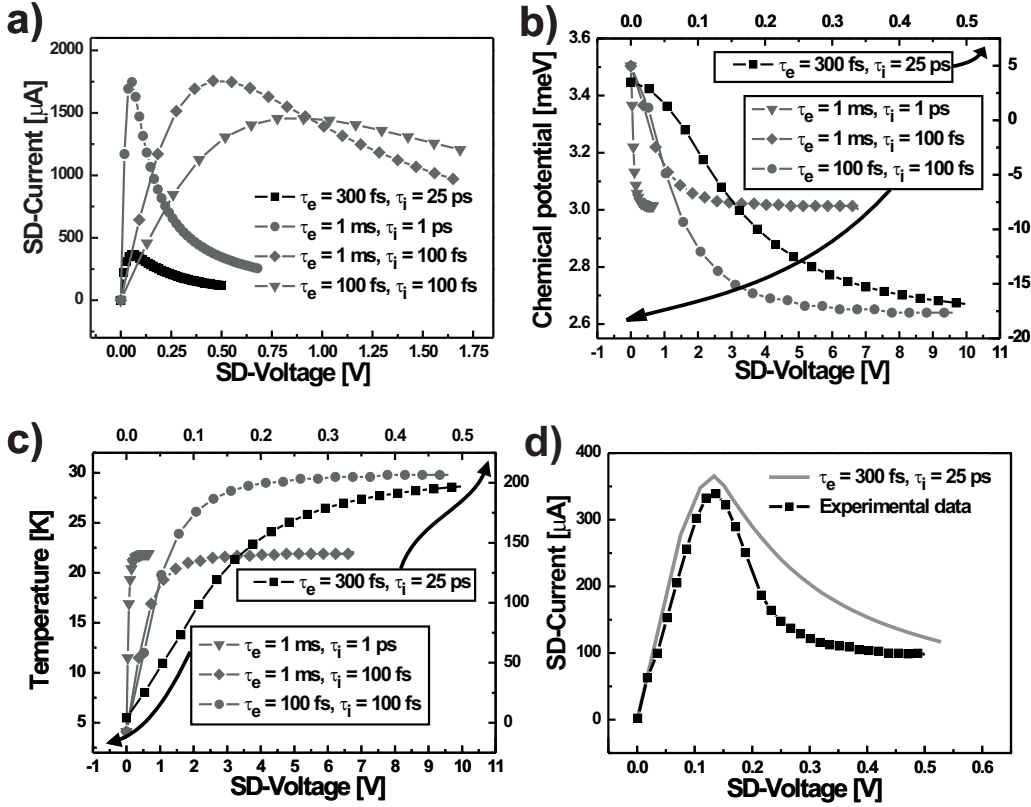


Figure 5.15: (a) - (c) Theoretical results for the transport characteristics, the chemical potential, and the effective electron temperature T_e from the two-dimensional model described in the text. (d) Comparison of the experimental data with a theoretical transport characteristic which has been calculated with the aim of similar NDC peak properties.

heats up the carrier distribution. At the same time, this causes a larger shift in the chemical potential and the peak current also drops. In the one-dimensional model the peak current is proportional to $\sqrt{\tau/\tau_i}$ (cf. equation (2.16)). This factor produces a current reduction similar to the one that is observed in the two-dimensional model.

3. When elastic scattering becomes the dominant process, the changes observed in case 2 grow increasingly stronger. In the shown situation with $\tau_i = 25 \text{ ps}$ and $\tau_e = 300 \text{ fs}$ a strong heating of the carrier distribution is observed and, correspondingly, the chemical potential becomes strongly negative. The system can then in the high T_e region also be described by a Maxwell-Boltzmann distribution. Accordingly, the peak current decreases strongly.

The scattering values of case 3 were chosen such that the theoretical peak position and height are in close agreement with the experimental data. A direct comparison is shown in figure 5.15(d). Due to the strong increase in T_e , the position of the NDC peak does not

directly correspond to the relaxation time $\sqrt{\tau\tau_i} \approx 2.7ps$, but is rather found at an electric field which gives a τ of about 1 ps. This means that the transport in all the presented samples is best described by miniband conduction, since the parameter plotted in figure 5.14(d) increases by at least a factor of 2 for all devices. The difference in shape between theory and experiment can be attributed to different reasons. An important one is that the relaxation rates are assumed to be energy independent. It would be more realistic to implement a detailed description of the scattering processes, or at least to allow for energy dependent scattering rates. However, while such approaches are beyond the scope of this work, the rather simple approximations with fixed scattering rates have also often turned out to be very close to the results of more sophisticated calculations.

Additionally, the main concern for the implementation of the above theory was not to get an exact correspondence between theory and experiment, but rather the determination of a parameter set τ_i, τ_e, T_e that is as realistic as possible. These values determine the magnitude of the dynamic conductivity which is directly proportional to the gain in the surface SL. Therefore, if we want to determine realistic gain values, it is necessary to apply a transport model that captures the important details. One of these is the possibility that an electron transfers energy from the applied DC field into a motion perpendicular to the electric field direction. It is this process that leads to the strong heating of the carrier distribution. Figure 5.16 shows how the energy transfer occurs. An electron starts at $k = 0$ and is accelerated by the applied electric field along the superlattice axis. Its k_x -value increases. When the electron is scattered elastically (white arrow marked with an "e"), the final states are made up of all k -space values that possess the same energy as the initial state. Many of these states have a larger momentum k_y . Therefore, a part of the energy acquired in the electric field along the superlattice is transferred into the perpendicular direction. Since between two scattering events k_y does not change while k_x varies according to the applied electric field, the electron stays on the traces indicated in light gray. Now, it is easy to see that the more dominant elastic processes are, the stronger the energy transfer is. The electron undergoes many elastic scattering events before it finally dissipates some of its energy. Therefore, it can reach states with very large k_y value. And this in turn increases the energy in the distribution, which is equivalent to a strong heating.¹³ A higher temperature means a flatter distribution function, which leads to smaller current and gain values.

Before we turn our attention to the study of surface SL transport in external fields, a short discussion of the surface SL transport for samples without a shunt seems necessary. So far, we switched from the unshunted to the shunted system quite naturally. The reduction of the channel length led to a parallel transport contribution across the undoped bulk SL. However, there are also samples similar to those discussed at length in the last two sections which do not possess a parallel shunt channel. Their properties and the

¹³The application of an electric field to the SL system always leads to a heating of the carrier distribution. But for dominant elastic scattering, the electronic temperatures are much larger than in the case of strong inelastic relaxation.

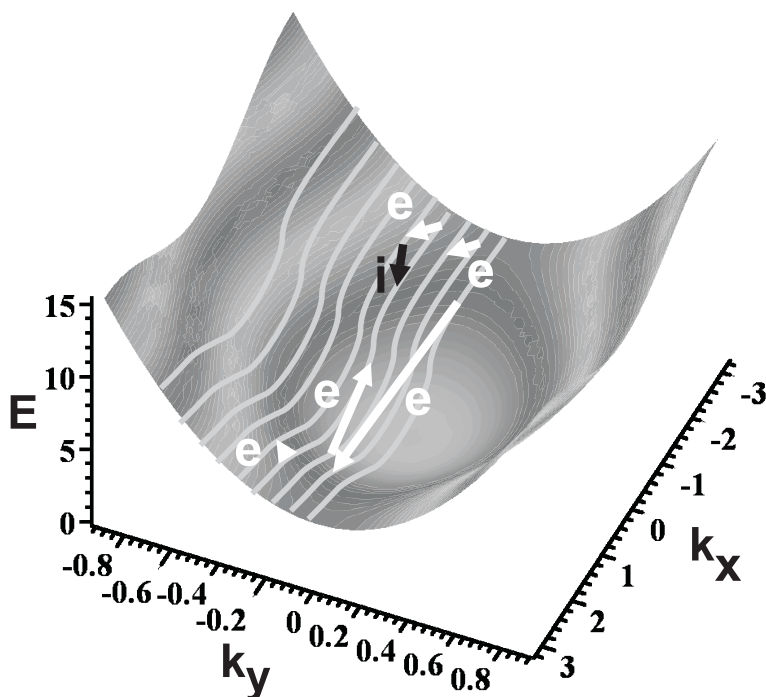


Figure 5.16: The figure illustrates how dominant elastic (white arrows) scattering can transfer energy taken from the electric field along the x -direction into the motion perpendicular to the SL axis. The light gray lines show the electron trajectories in between scattering events. The black arrow shows an inelastic scattering event.

conclusions drawn from them, especially in correspondence to the 2D stability discussion of chapter 4.4, is the topic of the next section.

5.9 Surface superlattices without shunt

One of the initial motivations for the study of surface SL structures was the reduced dimensionality of the structure. As shown in chapter 4, this geometry change should allow the realization of high-density surface SLs operating outside the traveling dipole domain mode. With the development of the SL-shunt system this argument became obsolete, since there the shunt stabilizes the electric field distribution at every density. Due to the asymmetry of the shunt characteristics it is, however, possible to investigate samples which possess parallel transport along one bulk SL direction, while no shunt current flows in opposite source-drain geometry. The resulting current-voltage characteristics of samples with CEW widths of 1.6 nm, 5 nm and 10 nm, identical to those of figure 5.14 but without immediate shunt current, are shown in figure 5.17(a) – (c). A significant shunt current is only found to flow beyond SD-voltages of about 400 mV. For small SD-biases the system is unshunted. Both for the 1.6 nm and the 5 nm CEW samples clear

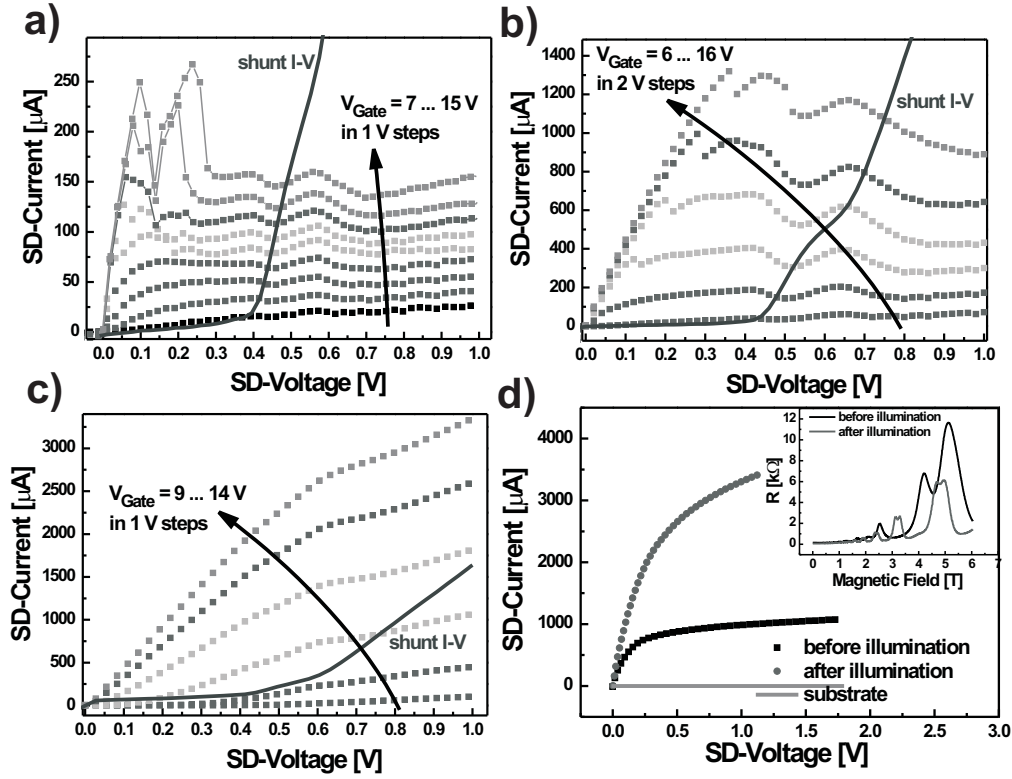


Figure 5.17: (a) - (c) Current-voltage characteristics of surface SLs that do not possess a shunt in the SD-bias region below 400 mV ((a) 1.6 nm CEW, (b) 5 nm CEW, (c) 10 nm CEW). (d) Transport characteristic of a surface SL (5 nm CEW), where the two-dimensional channel was induced by modulation doping. The inset shows magneto-transport measurements before and after illumination of the modulation doped sample structure.

instabilities can be observed in the unshunted region of the high gate bias traces. These characteristics also show a total current flow which is significantly larger than in samples that have parallel transport. As soon as the shunt turns on, the current seems to drop to a different transport characteristic which again resembles that of a homogeneous SL, showing a current peak followed by a region of NDC. A possible interpretation would be to assume that a large part of the voltage is dropped at the boundary between contact and SL so that the stable surface SL trace only starts at a voltage of about 450 mV. This would, however, suggest that the instability related NDC seen in the unshunted parts of the traces is possibly induced by a boundary pinch-off effect similar to the one discussed at the very beginning of this chapter. Such a conclusion is further supported by the fact that the 10 nm CEW sample shows no instabilities up to the point where the parallel transport sets in. Nevertheless, the large current in the unshunted voltage regions of this sample could shift instabilities into the shunted transport region.

A decision about possible instabilities can be made when we look at a 5 nm CEW sample¹⁴ in which the two-dimensional electron system was induced by modulation doping. Without the gate, there is no equipotential layer on the side of the SL and, therefore, all problems concerned with gate induced density inhomogeneities are remedied. The I-V characteristics of such a sample are shown in figure 5.17(d). The corresponding densities of $2 \times 10^{11} \text{ cm}^{-2}$ (before illumination) and $2.4 \times 10^{11} \text{ cm}^{-2}$ (after illumination)¹⁵ were determined from the Shubnikov-de Haas oscillations shown in the inset of figure 5.17(d). Neither instabilities nor NDC are observed in the data, and no parallel transport occurs in the studied SD-bias regime. This suggests that the nL -product is subcritical as to avoid NDC which would inevitably cause instabilities. The Shubnikov-de Haas data results in corresponding bulk densities of the order of $5 \times 10^{17} \text{ cm}^{-3}$. This value is well within the limits calculated in chapter 4 where we assumed a high effective electron temperature as also found in the last section.

Why the current increases so strongly after illumination, although the density increases only by 20 percent, is unclear. A possible explanation would be a strong increase in the mobility, which is supported by the appearance of a resistance maximum at filling factor 3 in the illuminated magnetoresistance trace shown in the inset of figure 5.17(d). A parallel channel due to the modulation doping is not expected for a thin spacer of 150 Å at these densities.

Thus, there is some support suggesting that the electric field along a surface SL is even without shunt only slightly inhomogeneous. Instabilities observed in gated structures might only be brought about by small density inhomogeneities introduced through the equipotential gate at the side of the SL. This offers the intriguing possibility to use a surface SL with or without shunt for the realization of a Bloch oscillator.¹⁶

5.10 Conclusion

A number of important facts can be deduced from the discussion in this chapter. The evolution of the peak currents observed in a number of samples indicates the correct miniband filling expected for surface SLs. Moreover, the observed instability-free negative differential conductance, which leads to current-voltage traces in close agreement with theory, also lets us conclude that minibands are formed in short-period modulated two-dimensional electron systems. Also, the electrons perform Bloch oscillations instead of being excited to the close lying minibands of the excited states of the triangular confinement.

When a gate structure is used to establish the two-dimensional transport channel, then it is necessary that the condition $V_{gate} \gg V_{SD}$ is met. Otherwise, pinch-off effects

¹⁴The sample actually possesses 500 nm thick intrinsic buffer layers. Since we have removed the gate, however, the additional channel length is of minor importance.

¹⁵The magnetoresistance traces show double peaks which is attributed to different densities in the intrinsic buffer layers and the SL section of the two-dimensional channel.

¹⁶This would be an invaluable advantage in the design process for such a system.

will mask the real superlattice transport behavior. Small current jumps, whose positions are shifted strongly to higher SD-bias with increasing gate voltage, can be introduced by the gate, even though the former condition is met. However, they are not connected to the concept of superlattice instabilities.

The great flexibility offered by the cleaved-edge overgrowth method allows the realization of shunt stabilized surface SLs. The parallel transport helps to keep the electric field homogeneous even in the region of negative differential conductance. From the observed data we derive the claim that we could for the first time electrically excite stable Bloch oscillations in a high-density superlattice structure. This claim is crosschecked in the following two chapters where surface SL transport in the additional presence of a magnetic and a high-frequency field is studied.

Finally, surface SLs without shunt show no negative differential conductance at high carrier densities. This supports the result found in chapter 4 that two-dimensional surface SLs are subject to electric field instabilities only at much higher carrier densities than conventional SLs. This observation suggests one possible approach towards the realization of a Bloch oscillator from surface SL structures.

Chapter 6

Surface superlattice transport in an external magnetic field

6.1 Overview

Studying the transport through a nanostructure in the presence of an external magnetic field has often helped to gain a better general understanding of the system properties.

In superlattices there are two distinguished magnetic field directions: parallel or perpendicular to the SL axis. Initially, one would not expect strong changes in the transport behavior when magnetic field and current are in parallel. However, such a magnetic field can localize the electrons into quantized Landau tubes. The resulting transport channels become essentially one-dimensional and carry much less current [MHEM01, PMF⁺04]. Moreover, for strong electric fields so called Stark-cyclotron resonances can occur [Pol81, Fer91, SN96, SN97, PMF⁺04] when the cyclotron energy is equal to the Stark ladder splitting. This effect will allow us to check the assumptions made about the shunt in the last section.

A magnetic field perpendicular to the SL axis can have different effects depending on the SL parameters. If the SL is operated in the sequential resonant tunneling regime, the conservation of perpendicular momentum during the tunneling process forces a shift in the NDC peak position which is quadratic in the magnetic field [MGvKP93]. This is in contrast to miniband transport which predicts a linear position dependence [ASP⁺93, ML95]. This difference in behavior provides us with a direct means to experimentally verify the miniband transport assumption of the last chapter. As we shall see, the electrons in a miniband are subject to a magnetic field induced confinement, and the strength of this confinement with respect to the electric field induced localization can cause both positive or negative magnetoresistance [Mov87, ML95, PSE⁺92].

The main aim of this chapter is to compare the experimental transport data in the presence of an external magnetic field to the theoretical predictions of the semiclassical model we have so far worked with. Depending on how good or bad this comparison turns out to be, we can either confirm the proposed SL-shunt system of the last chapter or try

to come up with an alternative explanation.

A magnetic field applied perpendicular to the surface SL axis can either lie in the plane of the two-dimensional electron system or be perpendicular to it. In the latter case the mobility of the electron system is so large that the electrons will condense in Landau levels. This situation cannot be described with the semiclassical transport picture. Therefore, only a short qualitative discussion of the data for this situation is given. In contrast, the large effective mass for the motion perpendicular to the two-dimensional electron system prevents a quantization of the eigenenergies when the magnetic field lies in the plane of the surface SL. In this situation the semiclassical model is expected to work fine even for very large magnetic fields.

The sample structures used in the experiments described below are shunted surface SLs of the final design as described in chapter 3. The SL consists of 66 periods with 12 nm wide wells and 3 nm thick barriers without any intrinsic buffer layers. Structures with CEW widths of 5 nm and 10 nm are investigated. The gate barrier thickness is 2 μm . Again, all presented measurements were recorded at a temperature of 4.2 K.

6.2 Applying a magnetic field

In a conventional SL structure there are two distinguished directions for the application of a magnetic field B . One is along the SL growth axis with the magnetic field perpendicular to the individual SL layers. Since the SL is fully symmetric with respect to any rotation around the SL growth axis, the second distinguished magnetic field alignment is parallel to the SL layers. The two cases influence the transport properties in very different ways. When current and magnetic field are parallel, there is no $\vec{F} \times \vec{B}$ -drift of the electronic system. However, if the mobility inside a SL well is high enough, the electrons condense in quantized Landau levels. As we shall see, this strongly changes the transport along the SL axis. A magnetic field aligned perpendicular to the SL axis results in the electrons experiencing the Lorentz-force $q\vec{v} \times \vec{B}$ in addition to the acceleration due to the static electric field. While the Lorentz-force strongly changes the transport along the SL axis, the effect of the Hall voltage on the SL transport can be neglected [ML95].

The principle influence of a magnetic field on the transport in a surface SL is the same as just described for a conventional SL. However, there are not only two, but three different distinguished axes along which the magnetic field can be aligned. Figure 6.1 shows a schematic drawing of the possible scenarios. While the x -axis points along the SL axis, the z -axis defines the orientation of the second growth step and the y -axis lies along the single free electron direction. Unlike in a conventional SL the electrons do not only feel a confining potential along the SL axis but also due to the voltage applied at the gate electrode. Thus, the rotational symmetry around the SL axis is broken. With the addition of the gate induced confinement the electron system becomes two-dimensional. The electrons essentially move only along the free y -axis and the periodically modulated x -

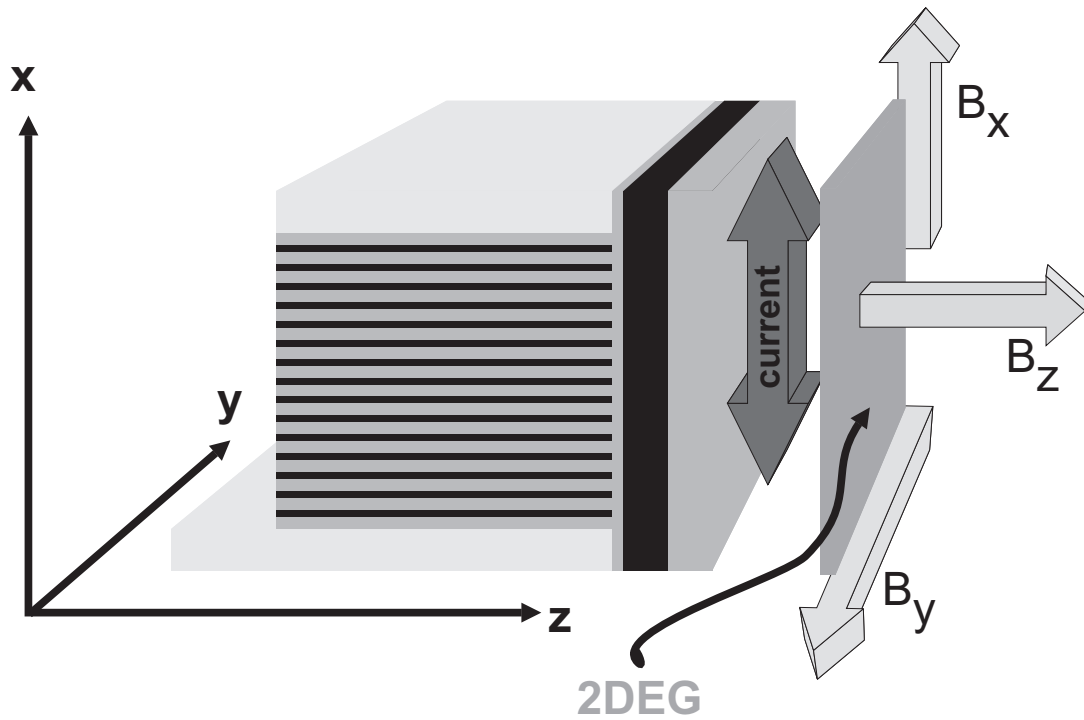


Figure 6.1: The figure shows the distinguished magnetic field directions defined by the surface superlattice structure.

axis. Thus, one would initially assume that only a magnetic field alignment perpendicular to the two-dimensional system would have a significant impact on the transport properties. However, as we shall see, the confinement induced by the gate is still weak enough so that a magnetic field in the plane of the two-dimensional system can result in marked transport changes.

In the following sections we will discuss in respective order the application of fields

$$B_x = B \begin{pmatrix} 1 \\ 0 \\ 0 \end{pmatrix}, \quad B_y = B \begin{pmatrix} 0 \\ 1 \\ 0 \end{pmatrix}, \quad B_z = B \begin{pmatrix} 0 \\ 0 \\ 1 \end{pmatrix}, \quad (6.1)$$

which are defined with respect to the geometry depicted in figure 6.1. For B_x and B_y , the transport changes are explained in the framework of the semiclassical model we have worked with so far. This model cannot be applied to the B_z case since the electron mobility in the two perpendicular directions is so high that the electron system condenses into Landau levels. In this situation, the additional SL potential is treated as a perturbation [Mov87].

6.3 Aligning the magnetic field parallel to the superlattice axis

Depending on the SL parameters, the presence of a magnetic field parallel to the SL axis can result in distinct changes of the transport properties. Since our SL structures possess both small miniband widths and long relaxation times, a magnetic field induces two main transport changes.

The application of the magnetic field leads to the Landau quantization [Dat03, Chapter 1.5] of the electrons in the SL layers. The resulting set of equidistant ladder states individually forms minibands by interaction with the corresponding states in neighboring wells. This leads to a ladder of minibands as shown in figure 6.2(a), which are separated by the cyclotron energy $E_C = \hbar\omega_C$, with $\omega_C = eB/m$. Hereby, m is the effective mass for in plane movement of the electrons. If the cyclotron energy is smaller than the miniband width, then electrons can be scattered elastically between minibands belonging to different Landau levels. Therefore, electrons can reach high energy values as shown in figure 6.2(a) from which they can relax inelastically down to lower minibands. Once the cyclotron energy exceeds the miniband width, however, no scattering between minibands of different Landau levels is possible at low temperatures, restricting inelastic processes to intraminiband relaxation. However, as we have seen, it is mainly by means of inelastic processes that electrons are driven along the SL axis. Since a large cyclotron energy leads to a

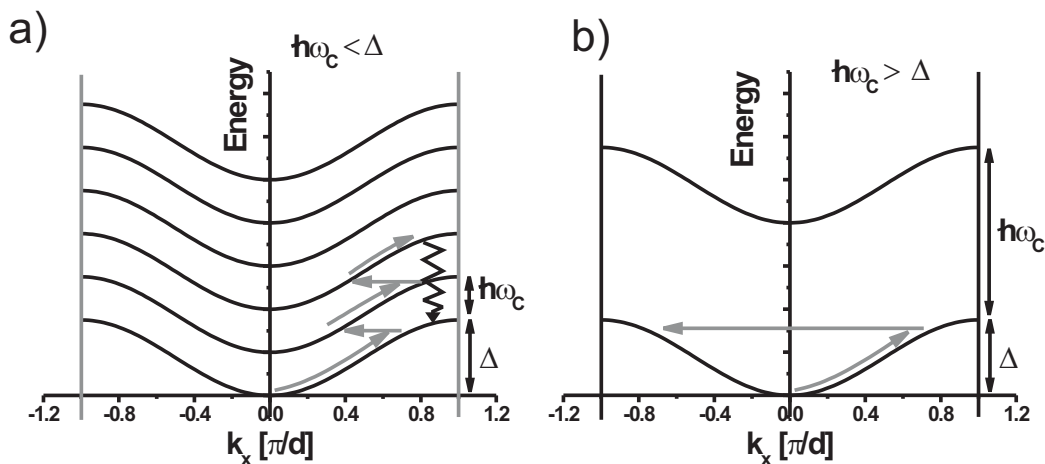


Figure 6.2: (a) Set of minibands which result when a magnetic field along the superlattice axis leads to Landau quantization in the superlattice planes. For the small magnetic field situation shown, the arrows indicate that an electron can reach large energy values by elastic scattering between the minibands before it relaxes back down to lower energies. (b) Same as in graph (a), however, now the magnetic field is so strong that elastic scattering between the minibands is no longer possible.

limitation of these scattering events, a current suppression for increasing magnetic field is predicted [MHM01, PMF⁺04].

When the SL sample also possesses very long relaxation times, the application of modest electric fields already leads to a resolution of the Wannier-Stark ladder states. The electronic energy levels are then quantized along the SL with an equidistant energy separation eFd proportional to the applied electric field F . If, at the same time, a strong magnetic field parallel to the electric field is present, the electrons are also localized within the individual SL layers due to the Landau quantization. Therefore, in the situation of combined parallel electric and magnetic fields, the electronic states become totally quantized with the energy states given according to

$$E_{\nu,n} = \nu eFd + \hbar\omega_C \left(n + \frac{1}{2} \right) \quad \nu = 0, \pm 1, \pm 2, \dots \quad n = 0, 1, 2, \dots \quad , \quad (6.2)$$

where ν is the number of the individual SL quantum well and n the Landau level index. Therefore, as shown in figure 6.3, in each SL well an equidistant ladder of energy states is formed. If there is no energetic alignment of energy levels in neighboring wells, then as shown in figure 6.3(a), the electrons move along the SL by hopping between the lowest states ($\nu = i, n = 0$) of the quantum wells. This is somewhat reminiscent of the situation of Wannier-Stark hopping without magnetic field.¹ However, whenever quantized states in neighboring wells lie at equal energies, electrons can be scattered elastically by interface roughness or quasi-elastically by acoustic phonons between them ($\Delta n \neq 0$). Such

¹When the magnetic field is present, the dispersions along the two directions of free electron motion collapse into a quantized state. This results in a dramatically reduced current.

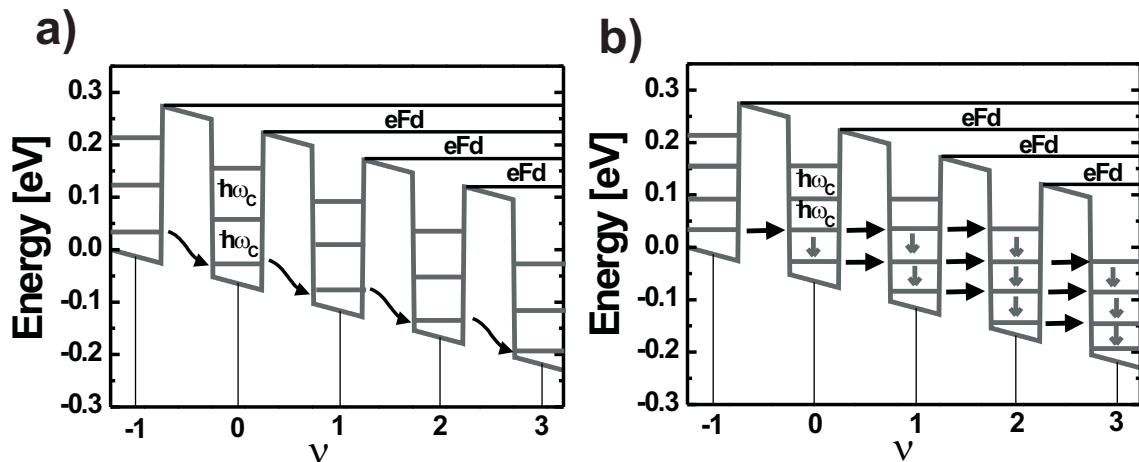


Figure 6.3: (a) Totally quantized states resulting from the combined application of strong magnetic and electric fields. (b) Same as in (a), however, in the depicted situation the Stark-Landau-levels in neighboring wells are aligned. This situation is referred to as a Stark-cyclotron resonance.

processes followed by inelastic relaxation open up additional transport paths through the SL, leading to a current increase. Since the Wannier-Stark states extend over a number of SL periods, additional transport paths open up whenever quantized states in any of the SL wells lie at equal energies. Generally, these additional paths lead to current resonances in the transport characteristics which are called Stark-cyclotron resonances (SCR) [Pol81, Fer91, SN96, SN97]. When an electric field sweep is performed for a fixed magnetic field strength, a sequence of SCRs should appear whenever the condition

$$\nu eFd = \hbar\omega_C \left(n + \frac{1}{2} \right) \quad \nu = 0, \pm 1, \pm 2, \dots \quad n = 0, 1, 2, \dots \quad (6.3)$$

is fulfilled. Since the electric field localizes the Wannier-Stark states across a small number of SL periods, those resonances that involve the hopping across a large number of periods ($|\nu| \gg 1$) quickly become insignificant.

Strong current resonances, referred to as Stark-cyclotron-phonon resonances, are also expected for resonant alignments including longitudinal optical (LO) phonons [Pol81, Fer91, SN96, SN97]. The corresponding resonance condition is given by

$$\nu eFd = \hbar\omega_C \left(n + \frac{1}{2} \right) + \hbar\omega_{LO} \quad \nu = 0, \pm 1, \pm 2, \dots \quad n = 0, 1, 2, \dots \quad , \quad (6.4)$$

where $\hbar\omega_{LO}$ is the LO phonon energy. Since the latter energy is about 36 meV in GaAs, whereas the typical measurement range ends at a Stark-splitting of about 16 meV, such resonances would only be observable for $\nu \geq 3$. As the extension of the Wannier-Stark states decreases with increasing bias, it is not clear whether these resonances will be observable in the experiments.

The foregoing discussion did not explicitly distinguish between SLs and surface SLs. The concept of the SCRs and the current suppression by the magnetic field parallel to the SL axis do, in principle, remain valid for surface SLs. However, the gate induced confinement is so strong that Landau quantization does not occur for the available magnetic field strengths. Therefore, SCRs are not expected to appear in the transport characteristics of surface SLs.

Before we, however, discuss the transport through the surface SL, let us take a look at the magnetic field induced changes in the shunt transport. This is rather important since the shunt is itself a SL and we have to take care to attribute any observed feature correctly to the shunt or the surface SL.

6.3.1 Shunt transport in a magnetic field parallel to the superlattice axis

Figure 6.4 shows the current-voltage characteristics of the shunt for magnetic field values ranging from 0 to 13 T. Two characteristic changes are observed when the magnetic field strength is increased:

- The total transport along the shunt strongly decreases.
- A number of resonance features are visible in the transport traces.

These observations seemingly correspond one to one to the theoretical predictions discussed in the last section. On one hand, the Landau quantization introduces a limitation on inelastic scattering processes, leading to a reduced current flow. On the other hand, for (ν, n) pairs that fulfill condition (6.3), resonant current features appear. Test samples without second growth step do show exactly similar data, rejecting any connection to the presence of the overgrown layers. In order to establish a possible correlation between the observed features and SCRs, we foremost have to determine their positions. This can be done in a number of ways. In figure 6.5(a) the positions of the features extracted from the first and second derivatives of the current-voltage traces are plotted. In contrast, figure

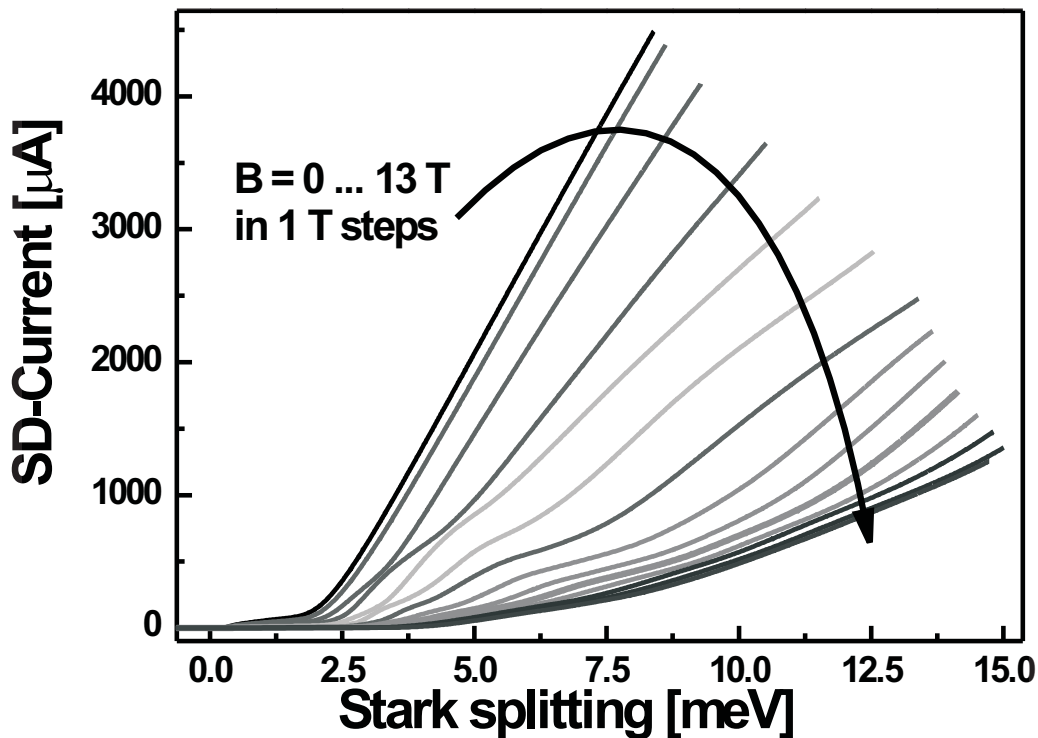


Figure 6.4: Current-voltage characteristics of the shunt SL when a magnetic field is applied parallel to the transport direction.

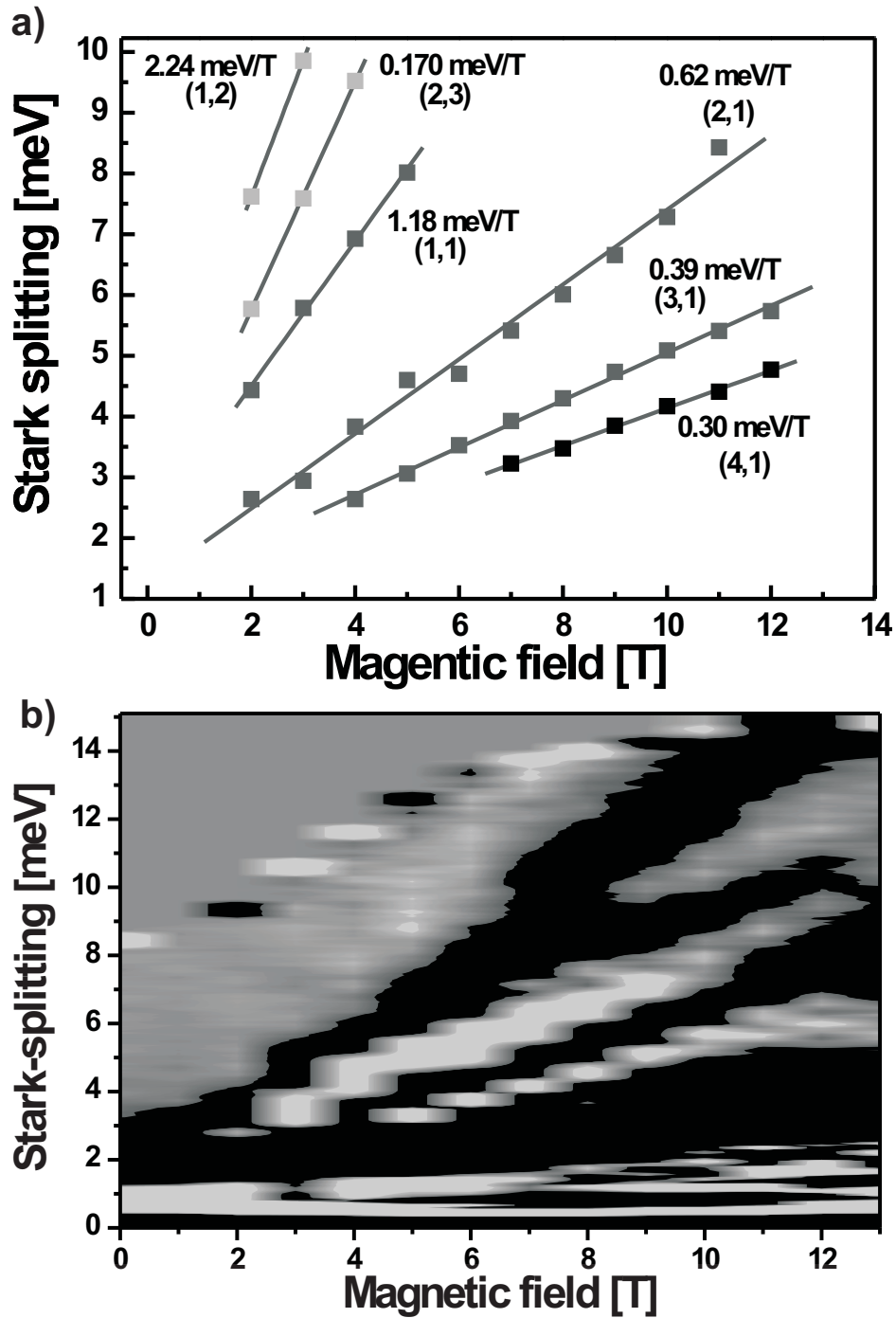


Figure 6.5: (a) Positions of the Stark-cyclotron resonances extracted from the data of figure 6.4. Both the slopes of the individual lines and the corresponding (ν, n) values are shown. (b) Gray-scale plot of the resistance calculated from the same data. Black (light gray) is a resistance minimum (maximum) indicating a current maximum (minimum).

6.5(b) shows a gray-scale plot of the function

$$\alpha(B, F) = -\frac{\partial^2 R(B, F)}{\partial F^2} \bigg/ \frac{\partial R(B, F)}{\partial F}, \quad (6.5)$$

where $R(B, F)$ is the resistance V_{SD}/I_{SD} , which unlike the current increases in the high SD-bias regime with increasing magnetic field. The function α possesses extrema whenever the first derivative of R crosses through or comes close to zero, while the second derivative determines the sign of this extrema. A negative sign indicates a maximum and a positive sign a minimum. While the gray-scale plot presents a nice overview, a comparison of the extracted slopes² with those found directly from the derivatives of the current traces is quantitatively difficult. One reason for this is the sample geometry. In order to allow for at least a four point measurement at the n+-contact layers, the current is injected at a fixed position. From this point it spreads out laterally. The further a specific point on the n+-contact layer is away from the injection point, the smaller is the voltage across the SL at this location. Thus, the SCR occurs only for a certain percentage of the bulk SL at the same SD-bias. This leads to very broad current resonances. These in turn lead then to rather wide areas of large or small values for α such that the gray-scale plot is rather imprecise for the determination of the exact positions of its extrema.

Nevertheless, the gray-scale plot clearly shows a linear dependence of the resonance condition on the magnetic field strength. The slopes given in figure 6.5(a) can unambiguously be assigned with values (ν, n) , also shown in the graph, for the possible Stark-cyclotron resonances. A comparison of the slope of the (1, 1) transition with expression (6.3) leads, with an effective mass³ of $0.07m_e$, to the conclusion that about 75 percent of the bulk SL are aligned homogeneously. Due to a possible magnetic field misalignment, which would both reduce the magnetic field and further increase the effective mass, this number is a lower limit. Furthermore, electrons spilling over from the unbuffered contact layers into the first periods of the SL may reduce the effective length of the SL across which the voltage is dropped. However, there must be a small inhomogeneity in the electric field over a very short section of the SL since otherwise NDC would occur in the nominally undoped shunt.

6.3.2 Surface superlattice transport in a magnetic field parallel to the superlattice axis

While the observation of the SCRs in the bulk SL confirms that the electric field alignment in the shunt is very close to homogeneity, it also poses a problem for the determination of the transport characteristics of the surface SL. In the discussion of the voltage and current distributions in the shunted surface SL structure we found that the surface SL

²Minima in α directly correspond to *maxima* in the current.

³Due to the confinement of the SL potential the effective mass is a little larger than in pure GaAs [WMN⁺92].

transport also changes the current flow in the bulk SL at similar SD-voltages. These current changes naturally go along with changed voltage distributions. Therefore, the SCRs of the bulk SL occur at different voltage positions when the two-dimensional channel is turned on. This, however, artificially introduces current resonances into the surface SL current-voltage characteristics, as seen in figure 6.6, when a simple subtraction of the zero gate voltage trace is performed. And even though the observed peaks do shift with gate voltage and also for different CEW widths while the shunt resonances remain unchanged, a careful analysis shows that the minima between two peaks remain fixed at positions that correspond to the maxima of the subtracted traces. Moreover, the strengths of the extrema in figure 6.6 changes in exactly the same way as those of the current resonances in the shunt. Thus, the features seen in figure 6.6 are artificially introduced by the subtraction of the shunt transport. Now, a possible approach to remedy the situation might be the realignment of identical features in the traces with and without gate bias. However, the change in the voltage distribution of the device leads not only to a shift of the resonance, but also changes the shape of the resonance. Therefore, even after a

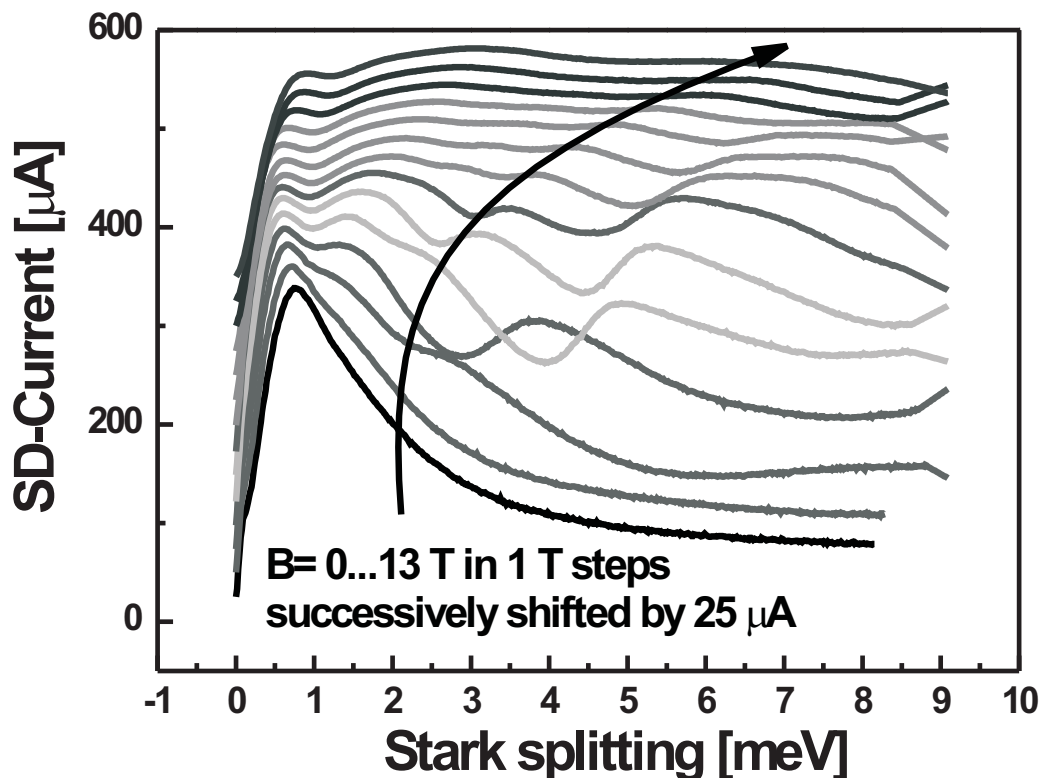


Figure 6.6: Current-voltage characteristics for a surface superlattice when a magnetic field along the transport direction is applied. The traces result when the zero gate voltage characteristic is directly subtracted from the total transport through the shunted surface SL system. The apparent resonances are artificially introduced since this subtraction does not fully cancel the features observed in figure 6.4.

correct realignment, artificial features remain in the surface SL transport characteristics. This makes it extremely difficult to get a clear idea of the magnetic field induced changes in the surface SL transport.

Moreover, the parallel alignment of the electric and magnetic fields strongly quenches the shunt current (cf. figure 6.4). When the conductivity of the shunt decreases below a certain minimum value, the surface SL will become unshunted. This probably contributes to the current plateaus which appear in figure 6.6 for large magnetic fields.

In figure 6.7(a) the absolute value of the surface SL current at SD-biases of ± 10 mV and the shunt current at a Stark splitting of 2.5 meV are plotted versus the parameter $\hbar\omega_c/\Delta$. In [PMF⁺04] it was found that the current in the presence of a parallel magnetic field approximately follows a universal curve when plotted versus $\hbar\omega_c/\Delta$. This curve was calculated in [PMF⁺04] with the help of a nonequilibrium Green's function approach. Values according to this result are also given in figure 6.7(a) both for the surface SL and the shunt. The shunt data is consistent with the predicted universal behavior. A comparison of the surface SL data with this theory shows no agreement. There is a major shift in the parameter $\hbar\omega_c/\Delta$ between both data sets. The universal behavior discussed in [PMF⁺04] is attributed to the formation of quasi-one-dimensional transport channels when a large magnetic field leads to a strong Landau quantization in the SL layers. Due to the strong triangular confinement potential Landau quantization does not occur in the surface SL. Making use of results found in the next section, we can calculate an effective mass of about $0.6m_e$ for the lateral cyclotron motion in the triangular well. This suggests a rescaling of the $\hbar\omega_c/\Delta$ -axis in figure 6.7(a) by a factor of about 9. However, the rescaling does not lead to a better agreement between experiment and theory as figure 6.7(b) shows.

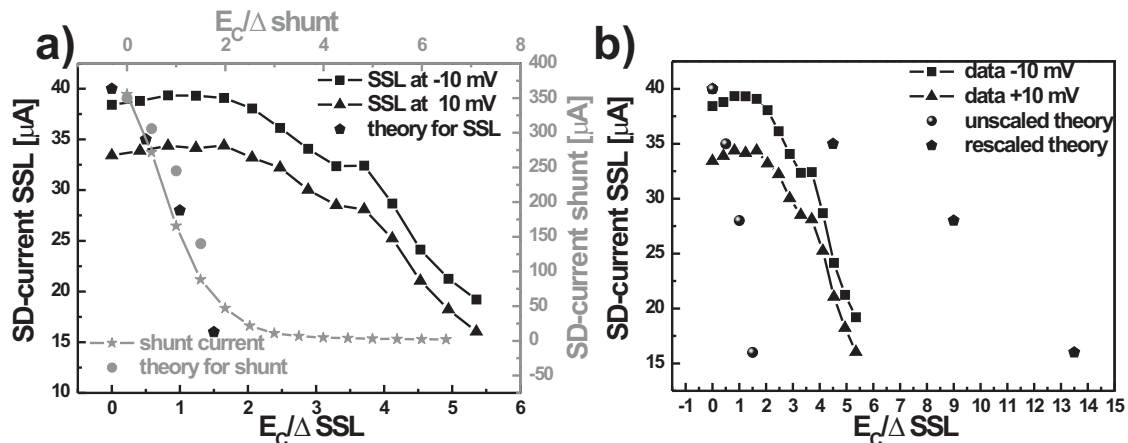


Figure 6.7: (a) Comparison of the current flow through shunt and surface superlattice at fixed SD-biases with a supposedly universal theoretical prediction ($E_c = \hbar\omega_c$). The magnetic field alignment is parallel to the superlattice axis. (b) Same as in graph (a), however, only data of the surface superlattice is shown. The two theoretical traces are calculated under the assumption of two different effective cyclotron masses.

It rather suggests that the miniband width might also show some B -field dependence and that the reduced dimensionality of the surface SL might introduce an additional geometry factor in the universal curve.

It is interesting to note that the experimental surface SL data in figure 6.7 shows some structure in form of a kink and a flat maximum. Such features are also present in the theoretical data [PMF⁺04, figure 4] when a small broadening of about 0.5 meV of the miniband states is assumed. A smooth current decrease is found only for strong energetic broadening. The features in figure 6.7 are in agreement with the quite general observation that the relaxation times in surface SLs are much longer than in conventional SL structures.

6.4 Aligning the magnetic field perpendicular to the superlattice axis

A free electron in crossed electric and magnetic fields drifts perpendicular to both field directions. The application of a magnetic field perpendicular to the electric one also leads to a finite $\vec{F} \times \vec{B}$ -drift of the electrons in the SL structure. When the mobility in the plane perpendicular to the magnetic field is not high enough so that separate Landau levels are formed, the semiclassical transport model can again be applied in order to study the effects of the magnetic field on the drift velocity and current along the SL axis.

The major change introduced by the magnetic field is a coupling of the electron movements along and perpendicular to the SL axis. The semiclassical acceleration theorem now contains the sum of the electrostatic force and the Lorentz-force,

$$\hbar \dot{\vec{k}} = e\vec{F} + e(\vec{v} \times \vec{B}). \quad (6.6)$$

With⁴

$$\vec{F} = F \begin{pmatrix} 1 \\ 0 \\ 0 \end{pmatrix}, \quad \vec{B} = B \begin{pmatrix} 0 \\ 0 \\ 1 \end{pmatrix} \quad (6.7)$$

and

$$v_{x,y} = \frac{1}{\hbar} \frac{\partial E}{\partial k_{x,y}}, \quad (6.8)$$

the time evolution of the momenta k_x and k_y is governed by the expressions [HHHS94]

$$\frac{\partial k_x}{\partial t} = \frac{eF}{\hbar} + \frac{eB}{m_{\parallel}} k_y(t), \quad (6.9)$$

$$\frac{\partial k_y}{\partial t} = -\frac{eB}{m_{\perp} d} \sin(k_x(t)d), \quad (6.10)$$

⁴The current discussion concerns conventional SLs. Therefore, the situations $B = B_y$ and $B = B_z$ are identical.

where m_{\parallel} is the effective mass of the movement in the SL planes and $m_{\perp} = 2\hbar^2/\Delta d^2$ is the zone center effective mass along the SL axis. The equations clearly show the coupling between k_x and k_y introduced by the magnetic field. Due to this coupling, the difficulty of solving the corresponding Boltzmann-equation increases considerably. In order to avoid this, the drift velocity is usually calculated with the approach introduced by Esaki and Tsu [ET70]. According to their work, the average drift velocity of an electron along the superlattice axis is given by [HHHS94]

$$v_d = \frac{\hbar}{\tau m_{\perp} d} \int_0^{\infty} e^{-\frac{t}{\tau}} \sin(k_x(t)d) dt . \quad (6.11)$$

The combined effects of all scattering events are described with the single relaxation time τ . Expression (6.11) leads, for zero magnetic field, to the same velocity-field dependence as the Boltzmann-equation description, except for any distribution factors.

A numerical integration⁵ of equations (6.9)⁶ and (6.10) and a subsequent evaluation of the integral (6.11) for a set of different magnetic and electric fields leads to current-voltage characteristics⁷ of the form shown as in figures 6.8(a) and (b). In both figures the electric field is given in dimensionless units of $F_c = \hbar/ed\tau$. While the peak current actually increases for magnetic fields smaller than 0.6 T, a strong peak current suppression is observed for very large fields. Simultaneously, the NDC peak position is continuously

⁵The actual computation was done with ready to use functions of the numerical computation tool Matlab. The short programs are given in appendix A.

⁶Here, it is assumed that m_{\parallel} equals the effective mass in GaAs.

⁷Actually, the calculations only yield the drift velocity-electric field characteristics. However, assuming a homogeneous electric field across the SL, the current-voltage characteristics have to look the same.

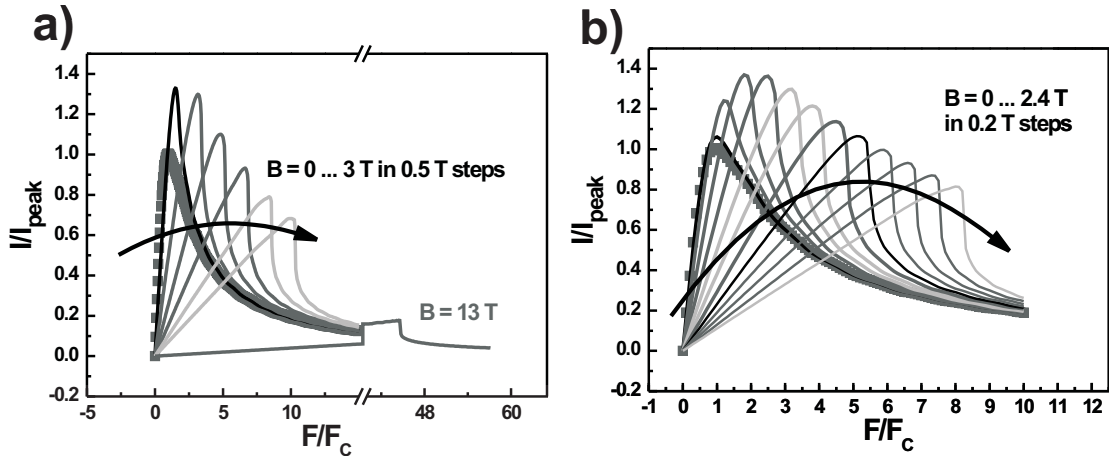


Figure 6.8: (a) Theoretical current-voltage characteristics for different magnetic fields applied perpendicular to the transport direction. In (b) the small electric field region is magnified and additional magnetic fields are considered.

shifted to higher electric fields. A distinct threshold electric field F_{th} can be defined when a transport characteristic for $B > 0$ is compared to the $B = 0$ case. For all electric fields smaller than F_{th} a positive magnetoresistance is observed and for all electric fields larger than F_{th} a negative magnetoresistance occurs. In the limit $B \rightarrow 0$ the threshold field F_{th} is given by [HHHS94]

$$F_{th} = \frac{F_C}{2} . \quad (6.12)$$

The latter condition allows us to extract the scattering time τ from the crossover point at small magnetic field values.

The origin of the trace crossings of figure 6.8(a) and (b) can be understood in terms of the so-called free flight trajectories. The following discussion is based on the ideas

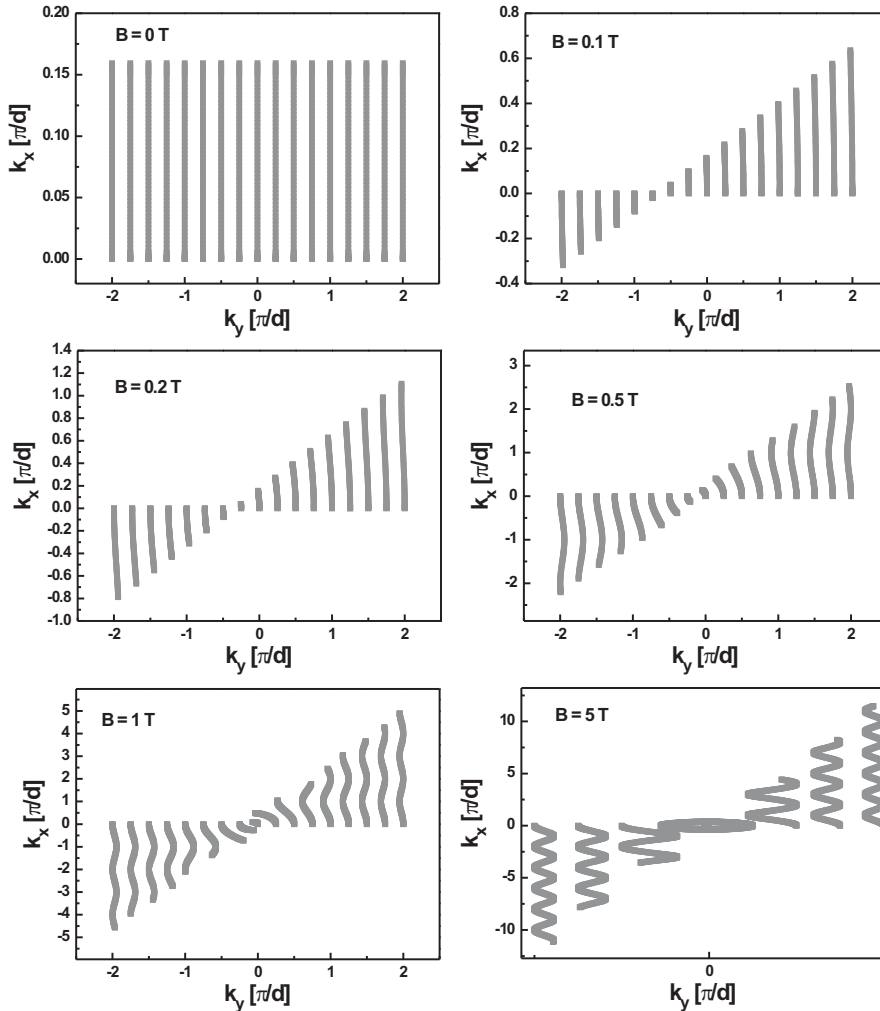


Figure 6.9: Free flight trajectories of electrons that start at $k_x = 0$ and at different k_y values for an electric field ($F = 0.5F_C$) in the linear superlattice transport regime.

presented in [PSE⁺92]. In figure 6.9 the free flight trajectories described by equations (6.9) and (6.10) are plotted for electrons starting at $k_x = 0$ with different k_y values. Free flight refers to the time interval $[0, \tau]$. Both k_x and k_y are normalized to $\frac{\pi}{d}$, while F is given in units of the critical field $F_C = \hbar/ed\tau$. For zero magnetic field and a small electric field $F = 0.5F_C$, at which the SL is still ohmic, the free flight trajectories extend straight along the k_x direction, however, they do not come close to the Brillouin zone boundary. Small magnetic fields divert these trajectories in the k_y direction (cf. figure 6.9(b)-(e)). For a strong magnetic field of 5 T, the trajectories near the origin are closed (cf. figure 6.9(f)). This closing of the free flight trajectories is interpreted as an increased

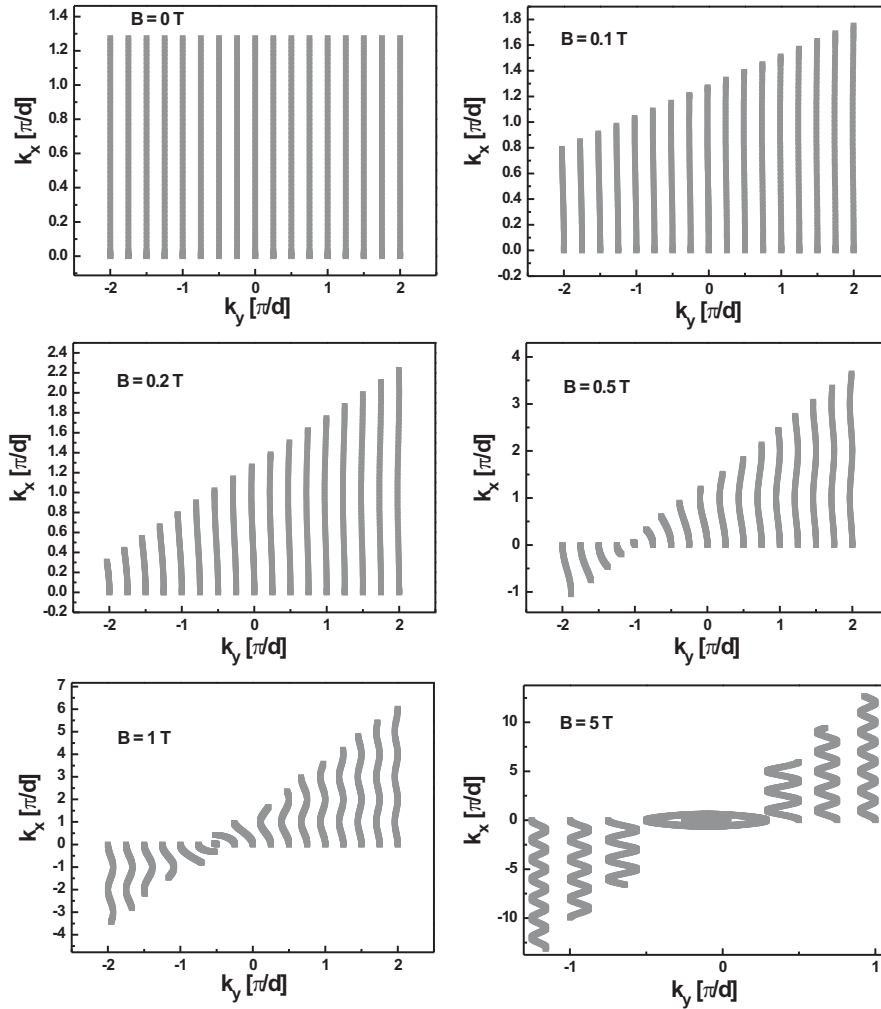


Figure 6.10: Free flight trajectories of electrons that start at $k_x = 0$ and at different k_y values for an electric field ($F = 4F_C$) in the negative differential conductance transport regime of a superlattice.

localization compared to the one induced by the interplay of scattering and electric field. Thus, the average drift velocity of an electron decreases and a positive magnetoresistance is observed as seen in the characteristics of figures 6.8(a) and (b).

In the case of a large electric field of $4F_C$ and equal τ , the changes in the free flight trajectories due to the magnetic field are similar to the ones described above. The corresponding plots are shown in figure 6.10. For zero magnetic field, the trajectories now extend much further along the k_x direction, indicating that the NDC regime has been reached. Figures 6.9 and 6.10 look similar, except for the fact that it takes higher magnetic fields to reach the same stage of twisting for the free flight trajectories. However, now a reduced extension of the trajectory along the k_x -direction does not lead to a smaller drift velocity. Instead, the extension of the Bloch oscillation cycle is reduced. This weakening of the Bloch oscillation mode leads to a larger drift velocity. This result is evident in form of an increased current (negative magnetoresistance) in the numerical solutions in figure 6.8(a) and (b).

The conclusions drawn from this discussion agree very well with the numerical calculations. In the small SD-bias regime a positive magnetoresistance is expected when the magnetic field is increased. For every B -value, there exists a threshold electric field (where the trajectories change from closed to open) beyond which a negative magnetoresistance region is entered. Moreover, the position of the NDC peak is continuously shifted towards higher biases since the magnetic field increasingly limits the k_x -extension of the electron trajectories.

6.4.1 Shunt transport in a magnetic field perpendicular to the superlattice axis

Most of the features just discussed should be observable in the shunt characteristics. The corresponding experimental data for structures with a 5 nm CEW and a 10 nm CEW are shown in figure 6.11 for zero gate bias. The characteristics are independent of the magnetic field alignment within the plane of the SL layers, as expected from the rotational symmetry around the SL axis of the shunt. For each $B > 0$ there exists a threshold field F_{th} which separates a region of positive magnetoresistance at small bias from a region of negative magnetoresistance at large bias when compared to the $B = 0$ trace. Numerical simulations show that the current-voltage characteristic of a low-density SL at a fixed B -value should eventually cross all transport characteristics taken for smaller magnetic fields. However, the exact positions of these crossings depend on the SL characteristics and their determination requires additional numerical calculations beyond this work. Thus, these additional crossings either occur only for Stark-splittings beyond 14 meV or are artificially shifted beyond this value when higher electric fields are necessary to inject carriers into the SL for increasing magnetic field. The latter is indicated by the transport onset being seemingly shifted to somewhat larger SD-biases. However, the current-voltage characteristics do change in a continuous way so that we

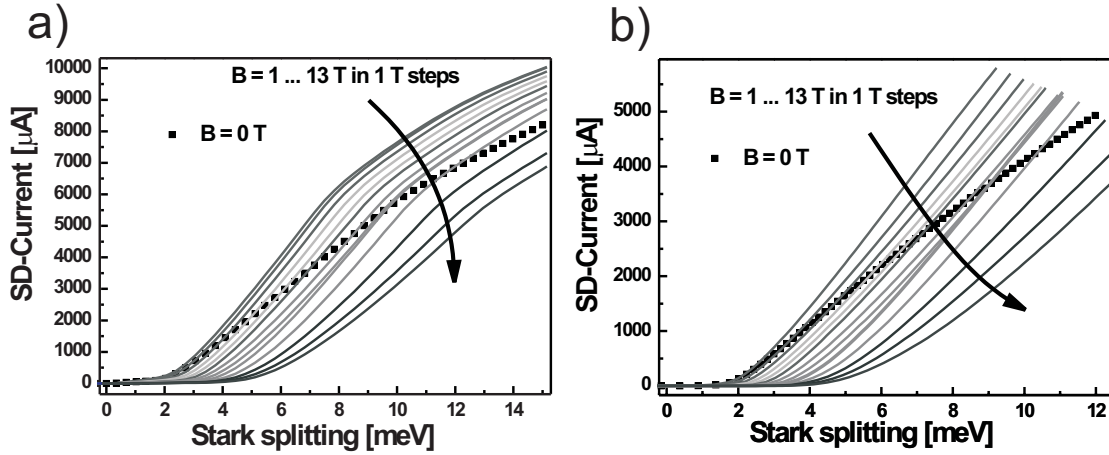


Figure 6.11: Shunt current-voltage characteristics for a magnetic field applied perpendicular to the transport direction. The traces in (a) for a sample with 5 nm wide cleaved-edge well are (in the same bias range) identical to those in (b) for a sample with 10 nm cleaved-edge well.

have to worry less about observing changes in the surface SL transport traces that are essentially changes in the shunt characteristics as was the case for the SCRs.

6.4.2 Surface superlattice transport in a magnetic field perpendicular to the superlattice axis

The transport characteristics of a surface SL with a 5 nm CEW are shown in figure 6.12(a) and (b) for densities of $1.7 \times 10^{11} \text{ cm}^{-2}$ and $3 \times 10^{11} \text{ cm}^{-2}$, respectively. The observed magnetic field-induced changes are precisely as expected, except for the $B = 0$ traces which exhibit a too large peak current. Otherwise, the peak current initially increases until about 6 T, and then decreases again for higher B -fields. Simultaneously, the peak position is continuously shifted to larger Stark splittings. The shoulder appearing in some of the transport characteristics is again due to a slight current overshoot before the shunt transport sets in (cf. chapter 5.6).

Similar observations are made for the traces of the 10 nm CEW sample shown in figure 6.12(c) at a density of $2 \times 10^{11} \text{ cm}^{-2}$. But the decrease in peak current observed beyond about 10 T is not very pronounced and the $B = 13 \text{ T}$ value actually increases again. This indicates that additional transport through the shunt is present, as was discussed for the 10 nm and 20 nm CEW samples in chapter 5.6. The same reason is responsible for shifting the magnetic field at which the absolute current peak is observed to higher values. For a more detailed evaluation, the peak positions and peak currents of all three samples are plotted versus the applied magnetic fields in figure 6.12(d)-(f). The $B = 0$ anomaly is clearly visible for all samples. Its origin is currently not understood. Since high density

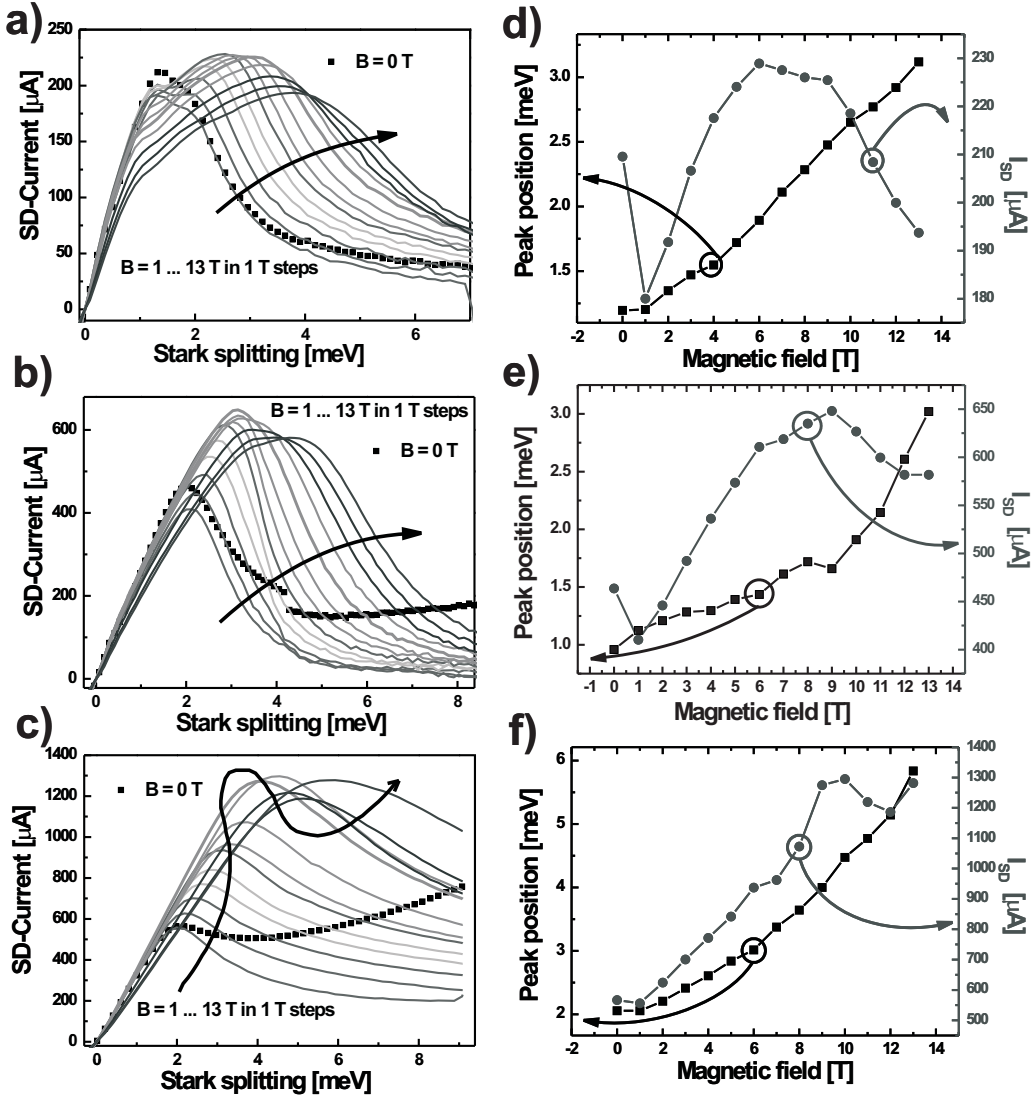


Figure 6.12: Current-voltage characteristics of a surface superlattice with a 5 nm cleaved-edge well in the presence of a perpendicular magnetic field at a density of $1.7 \times 10^{11} \text{ cm}^{-2}$ (a) and $3 \times 10^{11} \text{ cm}^{-2}$ (b) and for a 10 nm cleaved-edge well sample (c) at a density of $2 \times 10^{11} \text{ cm}^{-2}$. (d), (e), (f) Negative differential conductance peak position (corrected for a 150Ω series resistance) and peak height in dependence on the magnetic field strength for the data (a) - (c), respectively.

transport characteristics are increasingly subject to additional shunt transport which is difficult to correct for in this situation, the following discussion focuses on the 5 nm CEW sample at a density of $1.7 \times 10^{11} \text{ cm}^{-2}$.

By inspection the peak position in figure 6.12(d) changes roughly linear with the magnetic field beyond about 4 T. This agrees with the applied semiclassical model which predicts a change from open to closed orbits at critical magnetic fields [ASP⁺93, ML95]

$$B_C = F_C \sqrt{\frac{m_{||}}{2\Delta}}. \quad (6.13)$$

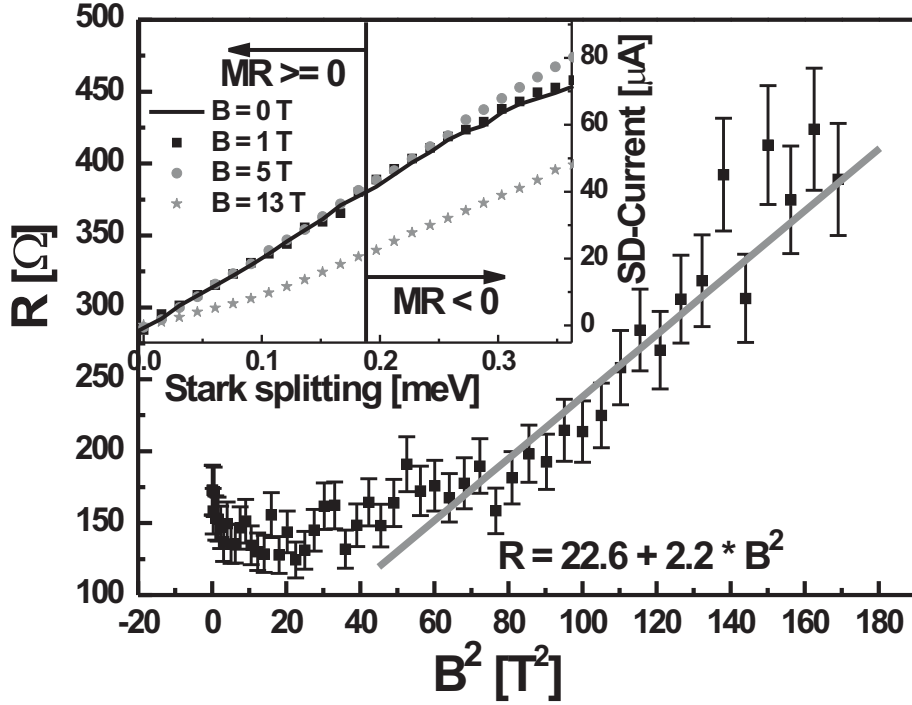


Figure 6.13: Resistance $R = V/I$ of the data in figure 6.12(a) plotted against B^2 for a SD-bias of 5 meV. A linear fit is performed in the high B regime. The inset shows a magnification of the small SD-bias regime of figure 6.12(a), indicating the regions with positive and negative magnetoresistance in the limit $B \rightarrow 0$.

From this expression a slope of $10^3 d\sqrt{2\Delta/m_{\parallel}}$ meV/T is predicted. A comparison of this value with a linear fit to the data of figure 6.12(d) gives a mass m_{\parallel} equal to $7.2 m_e$. The mass m_{\parallel} characterizes the electron motion perpendicular to the two-dimensional transport channel. For a perfect two-dimensional electron system, no such movement is possible. The electrons are completely confined in the layer. This complete quantization means that the dispersion for these electrons is flat perpendicular to the layer. This flat dispersion corresponds to an infinite electron mass in the perpendicular direction. Therefore, the huge value for m_{\parallel} seems quite reasonable for the surface SL structure, which is not quite a perfect two-dimensional electron system.

Once m_{\parallel} is known, additional information about the transport properties can be found. Equation (6.11) possesses in the limit $|F/F_C| \ll |B/B_0|$ of small electric fields [HHHS94] the analytic solution

$$v_d = \frac{\mu F}{1 + \left(\frac{B}{B_0}\right)^2}, \quad (6.14)$$

where B_0 is given by $B_0 = \sqrt{m_{\parallel}m_{\perp}}/e\tau$. In this small electric field limit, the electric field and the current are, respectively, directly proportional to the SD-bias and the drift velocity. Therefore, drift velocity and electric field can be replaced by current and voltage in expression (6.14). The resulting equation can then be rewritten as

$$\frac{R}{R_0} = 1 + \left(\frac{B}{B_0}\right)^2, \quad (6.15)$$

where $R = V/I$ and R_0 is the resistance for $B \rightarrow 0$. Since the limit $B \rightarrow 0$ violates the condition $|F/F_C| \ll |B/B_0|$, B_0 and R_0 can experimentally only be deduced from a linear extrapolation of the high B -field data to $B = 0$. In figure 6.13 this is shown for a small SD-bias of 5 meV for the 5 nm CEW sample at a density of $1.7 \times 10^{11} \text{ cm}^{-2}$. The dependence of the resistance on the square of the magnetic field becomes linear beyond about 8 T. Fitting this region linearly leads to an R_0 value of about 22.6Ω and a B_0 field of about 3.2 T. With $m_{\parallel} = 7.2 m_e$, this B_0 -value results in a scattering time of about 1.5 ps. However, since the series resistance is not exactly known, the fit procedure rather suggests a τ -range of 1.2 ps – 2.3 ps. These numbers are a little longer than the 0.8 ps directly extracted from the position of the NDC peak for zero magnetic field. From the two-dimensional transport model, presented in chapter 5.15, an elastic scattering time τ_e of about 300 fs and an inelastic scattering time of about $\tau_i = 25$ ps was found. Those numbers lead to a characteristic time scale of $\sqrt{\tau_i\tau} \approx 2.5$ ps, where $\tau = \frac{\tau_i\tau_e}{\tau_i + \tau_e}$, for the onset of Bloch oscillations. The reason for the difference between the τ determined from the peak position and that from the experiment lies in the dependence of the NDC peak position on the effective electron temperature. The 2.5 ps are close to the values extracted from the magnetic field measurements. Also, if we determine the scattering time from the threshold field that separates positive and negative magnetoresistance in the limit $B \rightarrow 0$

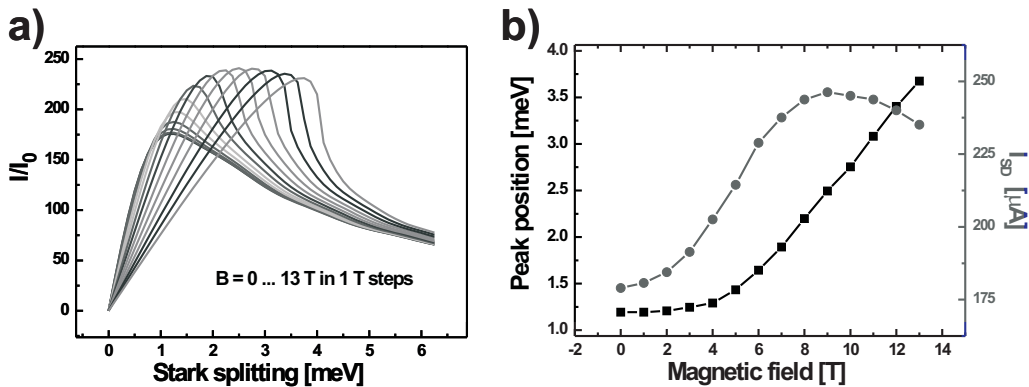


Figure 6.14: (a) Calculated current-voltage characteristics for comparison with the data in figure 6.12(b). (b) Position and height of the negative differential conductance peak extracted from the calculation in graph (a).

from the inset of figure 6.13, we find a value of about 2 ps.

Figure 6.14(a) again shows current-voltage characteristics calculated with the Esaki-Tsu model for a magnetic field perpendicular to the SL axis. However, this time we use $m_{\parallel} = 7.2 m_e$ and $\tau = 0.8$ ps. The latter value is chosen since it leads to the experimental NDC position at $B = 0$. Although a larger τ is responsible for the onset of Bloch oscillations, this value must be used for a comparison with the experiment. Essentially, this defines an effective scattering time which incorporates an increased effective electron temperature. Figure 6.14(b) shows that now both the peak height and the peak position, which have been scaled to the experimental value at $B = 0$, come *quantitatively* very close to the experimental data of figure 6.12(d). This suggests that the SSL transport can indeed be modeled by the applied semiclassical theory and that electrons inside the surface SL do perform stable electrically excited Bloch oscillations.

6.5 Aligning the magnetic field perpendicular to the surface superlattice plane

When a magnetic field perpendicular to the plane of the two-dimensional electron system is applied, in principle, the same situation as discussed in the last section arises. As mentioned there, the shunt characteristics are similar as long as the magnetic field and the electric field are perpendicular. However, there is an important difference when the surface SL transport is concerned. The gate induced confinement leads, as shown in the last section, to an extremely large effective mass for the lateral cyclotron motion. This large mass results in a very small mobility and prevents Landau quantization. This situation changes dramatically when the magnetic field is no longer inside the plane of the two-dimensional transport channel but perpendicular to it. It is shown in chapter 8 that the surface SLs studied here show Shubnikov-de Haas oscillations at magnetic fields well below 1 T. This means that a transport description is needed which is valid in the limit of strong Landau quantization. The semiclassical model can no longer be applied in this situation. Since the mobility in conventional SLs is much lower than the mobility in the plane of the surface SL, the regime of strong Landau quantization cannot be reached in these devices, and we are not aware of a detailed theoretical description for this transport regime. Therefore, we only discuss the experimental findings and relate them to the precious few theoretical predictions [Mov87] stated for the limit of a very large perpendicular magnetic field.

The experimental data for a 5 nm CEW sample at densities of $1.7 \times 10^{11} \text{ cm}^{-2}$ and $3 \times 10^{11} \text{ cm}^{-2}$ are shown, respectively, in figure 6.15(a) and (b). In graphs (c) and (d) of the same figure the magnetic field induced change of the NDC peak current and peak position is plotted. While the position dependence beyond 3–4 T is again linear, the peak current shows no maximum as predicted in the semiclassical theory but rather decreases strongly and continuously. Since the peak position changes linearly, one could assume

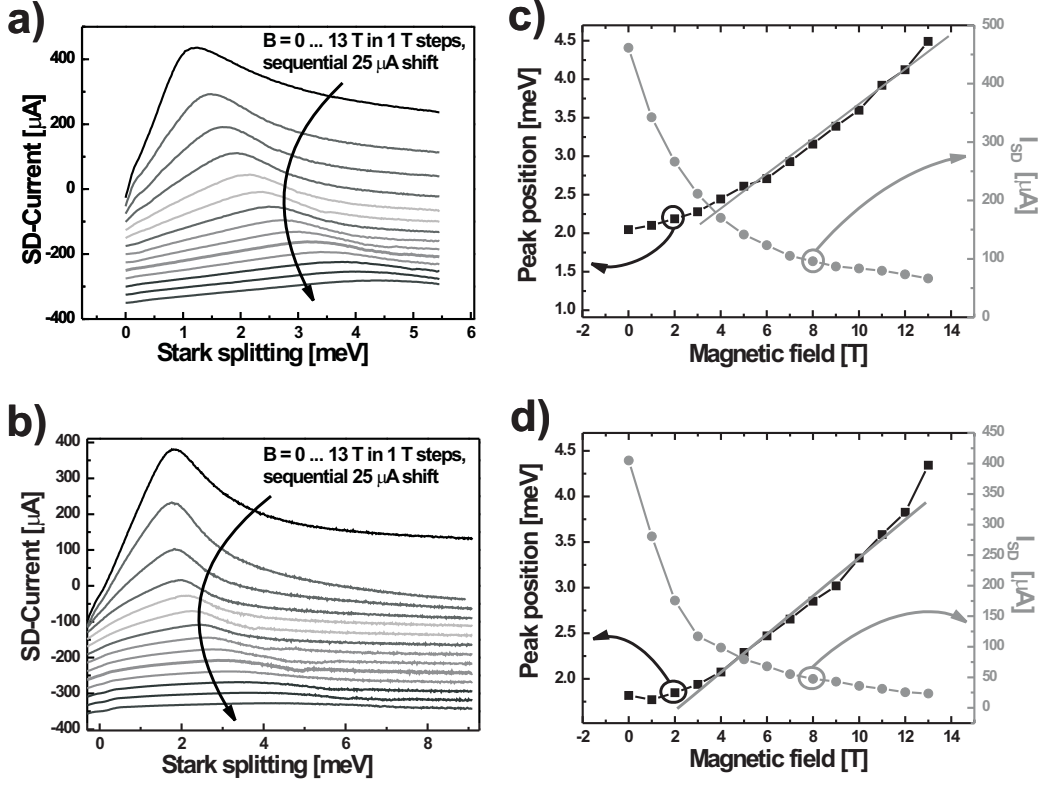


Figure 6.15: Current-voltage characteristics of a surface superlattice with a 5 nm cleaved-edge well when a magnetic field is applied perpendicular to the two-dimensional electron system. (a) $n = 3 \times 10^{11} \text{ cm}^{-2}$, (b) $n = 1.7 \times 10^{11} \text{ cm}^{-2}$. In (c) and (d) the position and height of the negative differential conductance peaks in (a) and (b) are plotted. The gray straight lines are linear fits to the peak position.

that the magnetic length introduces a scale with which the electric field has to compete for inducing the localization leading to NDC. Then, in imitation of the discussion in the previous section, if we normalize the peak positions $V_p(B)$ to the value at $B = 1 \text{ T}$, a length of about 12 nm is found for L_0 assuming a relation of the form

$$\frac{V_p(B)}{V_p(B = 1 \text{ T})} = \frac{L_0^2}{a_0^2}, \quad (6.16)$$

where $a_0 = \sqrt{\hbar/eB}$ is the magnetic length. L_0 is of the order of the period length of the structure and corresponds to a magnetic field value of about 4 T.

One theoretical prediction found in the literature [Mov87] states that the drift velocity is dominated by a factor $\exp(-\tilde{L}_0^2/2a_0^2)$ in the limit $a_0 \rightarrow 0$. Hereby, \tilde{L} denotes a minimum jump distance of the order of the barrier width of the SL. And, indeed, if we plot the dependence of the current on the magnetic field for a fixed Stark splitting, as shown in figures 6.16(a) and (b) for the above low and high density data, a good fit is found when

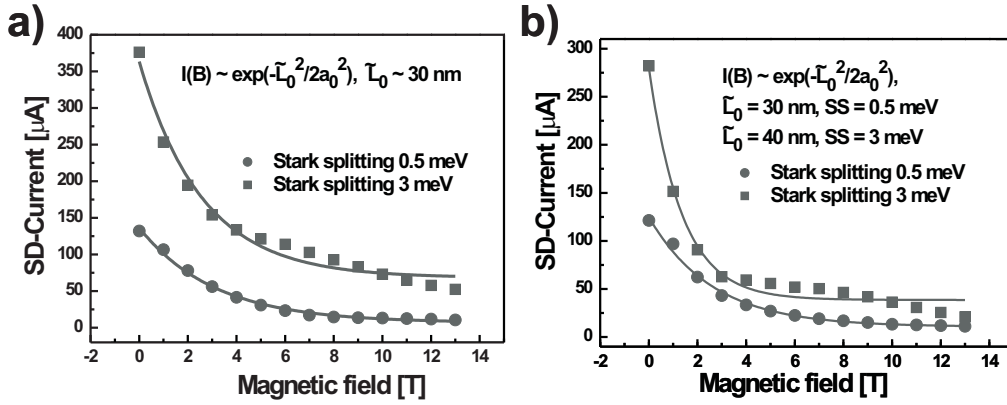


Figure 6.16: (a), (b) Current values (symbols) extracted from the data in figure 6.15(a) and (b), each at two fixed SD-bias positions. The gray lines are fits to the data assuming an exponential decay of the form written in the figures.

an exponential decay is assumed. The deduced value for \tilde{L}_0 is about 30 nm which is more than twice as large as the L_0 value and much larger than the barrier width. Such an exponential decay is also found for the peak current itself.

However, for the lack of a more detailed theory, the development of which is beyond the scope of this work, we will leave the discussion of surface SL transport in magnetic fields at this point.

6.6 Conclusion

The magnetic field dependent investigations in this chapter were started with the aim to validate or invalidate the SL-shunt system which was proposed in the preceding chapter. The data presented for different magnetic field alignments allows us to draw a number of conclusions.

When the magnetic field is aligned along the transport direction, then the electrons in the individual wells of the shunt are Landau quantized and the current-voltage characteristics show Stark-cyclotron resonances. From the position dependence of these current peaks we found that the electric field in the shunt is homogeneous across at least 75 percent of the structure. The reasons for a less than 100 percent perfect alignment are electron spill over from the contact layers, a magnetic field misalignment, and a small inhomogeneity which must be present so that no negative differential conductance is observed.

A magnetic field perpendicular to the transport direction causes the shunt characteristics to show a theoretically predicted trace crossing without exhibiting negative differential conductance. When the magnetic field is also in the plane of the two-dimensional electron

system, the surface superlattice transport is in excellent agreement with the predictions of the semiclassical model. A very large effective mass in the direction perpendicular to the electric and magnetic field is found. The large effective mass is deduced experimentally and directly reflects the two-dimensional confinement which assumes an infinite effective mass in the perpendicular direction. It also explains why no Stark-cyclotron resonances are found for the surface superlattice. Finally, the linear shift of the negative differential conductance peak with the magnetic field excludes the notion that sequential resonant tunneling transport might dominate in the surface superlattice.

The application of a magnetic field perpendicular to the two-dimensional electron system leads due to the large electron mobility to strong Landau quantization. The current generally shows an exponential decrease when the magnetic field is increased and the negative differential conductivity peak is found to shift linearly to higher SD-biases. However, the author is not aware of a detailed theory to which these results could be compared.

Thus, by studying the transport through a shunted surface superlattice in an external magnetic field, we could show that the assumption of a homogeneously aligned shunt is correct and that the surface superlattice again shows excellent agreement with the semiclassical picture based on stable electronically excited Bloch oscillations in a miniband structure.

Chapter 7

Superlattice transport in the presence of an external high-frequency field

7.1 Introduction

In this chapter we study how the irradiation of a shunted surface superlattice with an external high-frequency field changes its transport properties. Generally, a possible application of a superlattice structure for the realization of a Bloch oscillator can be deduced from the interaction with an external radiation field. The easiest experimentally accessible quantity in this situation is the DC current. It turns out that from this data the gain in a superlattice can be deduced [Wac02b, UKW⁺96]. Beyond a DC current measurement, the gain properties of superlattice structures have also been estimated from the transmission of a high-frequency field through a super-superlattice [SKLA04] and even from the study of Bloch oscillations in time domain spectroscopy [SHOC03]. Most of these experiments have again only been successful for superlattices with low nL -products. While electric field instabilities can be overcome to a certain degree by the THz field [Unt00], highly doped superlattices show none of the expected features in their negative differential resistance regions [WSG⁺97].

Theoretically, the problem of a superlattice under external irradiation has been studied widely with many different semiclassical [Kro03, SDR03, ACM⁺98, DZI98, IS83, BI77, IR76, API⁺05] and quantum mechanical [KS71, Wac02b, WDF03] approaches. Those investigations predict a number of interesting effects, many of which have indeed been shown to exist experimentally [UKW⁺96, KZA⁺95]. Among these properties are photon assisted transport, absolute negative resistance, frequency multiplication and chaotic transport behavior. A small number of reviews [BT86, Wac02b, Unt00, PA04] concerning irradiated superlattices or other heterostructures is available.

In the following sections first a theoretical discussion of the problem is given, which explains some of the effects just mentioned. This is followed by a short overview of the

experimental setups applied in the measurements. In the last sections the absorption data for surface superlattices is investigated and we try to draw some conclusions towards a possible application for a Bloch oscillator. Again, all presented measurements were recorded at a temperature of 4.2 K.

7.2 Superlattice transport in the presence of a static and dynamic electric field

In the preceding chapters a time scale of the order of 1 ps was found for the onset of NDC induced by Bloch oscillating electrons in the surface SL. According to $\omega_B\tau = 1$ this corresponds to a frequency f_B of about 160 GHz. Thus, when we study SL transport in the presence of a time-dependent electric field, it can be expected that the response greatly depends on the ratio between these two frequencies. It turns out that the external field represents a new time and energy scale which can significantly change the transport properties once it exceeds the scattering rates and becomes of the order of the Stark splitting. A frequency $\Omega = 2\pi$ THz corresponds to an energy of about 4.14 meV.

In the following calculations it is assumed that both a static electric field F and a time-dependent field F_Ω are applied to a SL system. Then, for a harmonic field F_Ω , the total electric field is given by

$$F_T(t) = F + F_\Omega \cos(\Omega t) , \quad (7.1)$$

and the semiclassical acceleration theorem reads

$$\hbar\dot{k} = eF + eF_\Omega \cos(\Omega t) . \quad (7.2)$$

The external field now introduces a term with explicit time dependence in the Boltzmann-equation. This complicates the situation tremendously. Nevertheless, in single relaxation time approximation a solution for an electric field F_a of arbitrary time dependence can be found [IR76] and the drift velocity is given by

$$v_d(t) = \frac{\Delta d}{2\hbar\tau} \int_{-\infty}^t e^{-\frac{t-\hat{t}}{\tau}} \sin\left(\int_{\hat{t}}^t \frac{eF_a(\hat{t})d\hat{t}}{\hbar}\right) d\hat{t} . \quad (7.3)$$

Neglecting aperiodic phenomena, the drift velocity is of the form

$$v_d(t) = v_0 + \sum_{n=1}^{\infty} (v_n^s \cos(n\Omega t) + v_n^a \sin(n\Omega t)) , \quad (7.4)$$

where the superscripts s and a characterize the v_n as belonging to the symmetric and anti-symmetric cosine and sine terms. When the field (7.1) is inserted into the general

solution (7.3), the $v_n^{s,a}$ are given by [Wac02b, Chapter 6]

$$v_0 = \sum_{k=-\infty}^{\infty} J_k(\nu)^2 v_{DC} (\hbar\omega_B + k\hbar\Omega) \quad (7.5)$$

$$v_n^s = \sum_{k=-\infty}^{\infty} J_k(\nu) (J_{k+n}(\nu) + J_{k-n}(\nu)) v_{DC} (\hbar\omega_B + k\hbar\Omega) \quad (7.6)$$

$$v_n^a = \sum_{k=-\infty}^{\infty} J_k(\nu) (J_{k+n}(\nu) + J_{k-n}(\nu)) \frac{\hbar}{eFd\tau} v_{DC} (\hbar\omega_B + k\hbar\Omega) . \quad (7.7)$$

Hereby, the J_k are Bessel functions, ν is defined as $eF_\Omega d/\hbar\Omega$ and the DC velocity v_{DC} is given by the static solution (cf. equation (2.14))

$$v_{DC} = \frac{I_1(\Delta/2k_B T)}{I_0(\Delta/2k_B T)} \frac{\Delta d}{2\hbar} \frac{\tau edF/\hbar}{1 + (\tau edF/\hbar)^2} . \quad (7.8)$$

Of all the terms making up the drift velocity (7.4) the most interesting ones are v_0 and v_1^s . v_0 is directly proportional to the DC current measured in the presence of the dynamic electric field and is the most easily accessible quantity in an experiment. v_1^s indicates the strength of absorption or amplification of F_Ω and its value is essential for the design of an active oscillator.

7.3 DC current in the presence of an AC field

The important parameter in the study of the DC current, driven by the combined static and dynamic electric fields, is ν which appears in the argument of the Bessel functions. It is defined by the ratio between the AC Stark splitting $eF_\Omega d$ and the photon energy $\hbar\Omega$. For a fixed frequency, ν increases when the power of the external radiation field rises.

In figure 7.1 the DC transport through a SL in the presence of a high-frequency field as calculated from equation (7.5) is plotted for increasing ν . Graph (a) shows the limit $\Omega \ll 1/\tau$ and panel (b) depicts the $\Omega \gg 1/\tau$ case. In the low-frequency limit, an irradiation of the SL with increasing power leads to a strong suppression of the NDC peak at its original position and to a shift of the peak to higher static fields F .

A better understanding of the origin of these changes can be developed if expression (7.3) is evaluated under the assumption $\Omega\tau \ll 1$. Then v_0 has the form [TF85, WSG⁺97]

$$v_0 = \frac{1}{T'} \int_0^{T'} \frac{\Delta d}{2\hbar} \frac{\omega_B(t)\tau}{1 + (\omega_B(t)\tau)^2} dt , \quad (7.9)$$

where the integral is taken over one period T' of the external field and the time dependent Bloch frequency $\omega_B(t) = \omega_B + \nu\Omega \cos(\Omega t)$ has been introduced. The meaning of expression (7.9) is readily understood. In the limit $\Omega\tau \ll 1$, the system always follows the total applied field instantaneously. Thus, the DC current flowing along the SL is just the

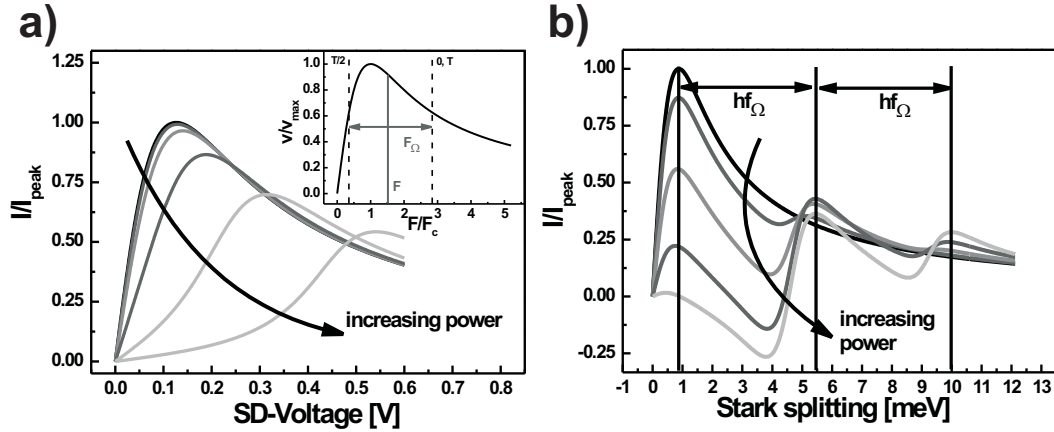


Figure 7.1: (a) Calculation of the current-voltage characteristics of a superlattice in the presence of a low-frequency radiation field ($\Omega \ll 1/\tau$) of increasing power. The inset shows the electric field range over which the total current is averaged in order to find the response to the external field. (b) Same as in (a), however, in the limit of a radiation field frequency much faster than the scattering rates ($\Omega \gg 1/\tau$).

average of the time-dependent current flowing during the time interval $(0, T')$. However, the current at time t is simply given by the DC current for the total field F_T . The situation is shown in the inset of figure 7.1(a). The electric field takes on values between $F - F_\Omega$ and $F + F_\Omega$. The resulting DC transport is therefore the average of all currents in this interval. Hereby, an increase in power means an increase in the averaging interval.

While the current changes induced by an external dynamic field at low-frequency can be explained classically, the problem becomes much more involved in the high-frequency limit $\Omega\tau \gg 1$ (cf. figure 7.1(b)). The suppression of the DC current is not only much stronger for similar ν , but the current can actually become negative for a positive bias. This means that once the power of the exciting field reaches a threshold value, the SL should show absolute negative resistance. Moreover, in the high bias regime additional current peaks appear which are shifted with respect to the static NDC peak by multiples of the photon energy $\hbar\Omega$.

In the Wannier-Stark ladder picture the effects described above can be explained in terms of photon absorption and emission processes. Figure 7.2 shows the energetic positions of the Wannier-Stark states of a SL when a field F is applied along the SL axis. The energy difference between states centered in different wells is given by the Stark splitting eFd . Transport occurs by electrons hopping along these ladder states when the external high-frequency field is absent. In the presence of the dynamic electric field the ratio between the Stark splitting and the photon energy $\hbar\Omega$ determines additional contributions from transitions between the ladder states that involve photon absorption or emission. If the photon energy is smaller than the ladder spacing, then emission of

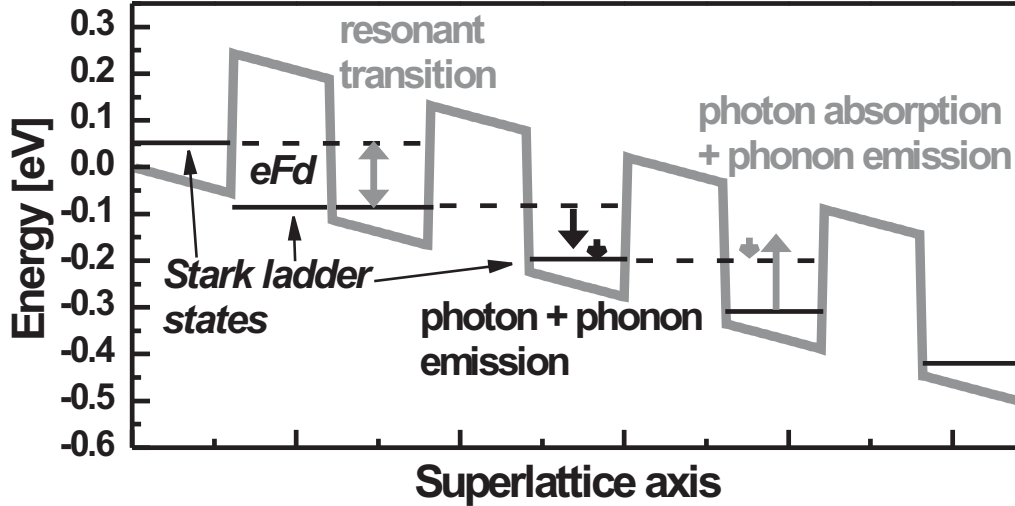


Figure 7.2: The figure illustrates the different dominant processes that occur when an external high-frequency field interacts with the biased superlattice. If the Stark splitting is larger than the energy of the external field (center), then electrons are dominantly driven down the Stark ladder. For an opposite ratio (right), electrons are taken up the Stark ladder against the static applied field. When both energies are equal (left), photon absorption and emission occur with identical probabilities.

a photon can occur when it is followed by one or more inelastic processes so that the energy difference to the lower ladder state is bridged (cf. center process in figure 7.2). Photon absorption is also possible when one or more phonons are absorbed during the absorption process. However, the latter process requires the presence of phonons and is therefore less likely than its counterpart. As long as the Stark splitting is larger than the photon energy, the field F_{Ω} drives electrons *down* the Stark ladder and thus the current is increased. In the opposite case, when the Stark splitting is smaller than the $\hbar\Omega$, photon absorption processes involve the emission of phonons (cf. right process in figure 7.2) while photon emission requires the presence of phonons. In this situation, the external field drives electrons *up* the ladder in the direction opposite to the static applied field F . This leads to a reduced current flow along the SL. Absolute negative resistance will occur in the extreme case in which the high-frequency field dominates the total transport.

When Stark splitting and photon energy are equal, absorption and emission occur without the involvement of phonons (cf. left process in figure 7.2) and are, due to the equal occupation of the individual Wannier-Stark ladder rungs, equally likely to take place. This means that no change in current flow is expected when the photon energy $\hbar\Omega$

and the Stark splitting have the same value. The changes in the transport through a SL, shown in figure 7.1(b), induced by a high-frequency field in the limit $\Omega\tau \gg 1$ can now be directly related to the above discussion. Since an external field of energy $\hbar\Omega = 4.8$ meV was applied, a transition from transport suppression to increase is expected as the Stark splitting is continuously widened. And indeed at a Stark splitting of about 4.8 meV the static and dynamic transport characteristics cross, indicating that in the lower bias region absorption processes dominate while for higher Stark splittings electrons are driven down the ladder.

The discussion about the absorption and emission of photons is not only valid for one photon processes but applies also to multiple photon processes. Therefore, additional crossing points are observed (cf. figure 7.1(b)). They are consecutively shifted by the photon energy. Looking at equation (7.5) we find that the current along the superlattice consists of an infinite sum of DC current-voltage characteristics. Each term in this sum represents the absorption or emission process that involves k photons and leads to a NDC peak that is shifted by $k\hbar\Omega$ with respect to the static peak. The power of the radiation field in the argument of the Bessel function determines how likely this process is. The observation of these shifted current peaks is one of the main goals of absorption experiments with SLs.

As we shall see, the changes in the DC current as described above are closely related to the gain and absorption properties of a SL. It is noted here that the theoretical calculation of the dynamic DC transport was performed in the miniband transport regime whereas an interpretation of the results was given in terms of the Wannier-Stark hopping picture. However, it was shown [Wac02b] that the presence of a high-frequency field leads to identical effects in all the different transport descriptions. The next section, in which the gain properties of a SL are discussed, also contains a semiclassical description of the effects that were here attributed to the imbalance of photon emission and absorption processes.

7.4 Gain and absorption in a SL structure

While the coefficient v_0 in equation (7.5) represents the direct current measured under irradiation, the coefficient v_1^s determines the current which is directly coupled to the external high-frequency field. Generally, if a long-wavelength (compared to the mean free path) electromagnetic wave E_0 inside a medium gives rise to a corresponding current density j_0 , then the wave itself experiences a conductivity-dependent change in phase¹ and amplitude of the form [AD00]

$$E_0 \sim \exp\left(\frac{-\sigma(\Omega)}{\sqrt{\epsilon\epsilon_0}c}x\right), \quad (7.10)$$

¹Generally, σ is a complex quantity.

where σ is given by

$$\sigma(\Omega) = \frac{\partial j_0(\Omega)}{\partial F_\Omega} . \quad (7.11)$$

Thus, it is the dynamic conductivity $\sigma(\Omega)$ which determines absorption and gain in a SL. When the condition $\sigma(\Omega) > 0$ holds, then the exponential factor in expression (7.10) decreases the wave amplitude. The medium absorbs the electro-magnetic radiation. However, in the opposite limit $\sigma(\Omega) < 0$ the external field increases in strength inside the medium. The medium exhibits gain and amplifies the external radiation.

Figure 7.3(a) illustrates why devices exhibiting negative differential conductivity might be possible gain media.² Once the device is biased in the NDC region, an additional high-frequency field leads to a smaller current when the static and dynamic field point in the same direction. On the other hand, when both fields are aligned in opposition the total current increases. Thus, the high-frequency field and the resulting current are in opposite phase, which leads to a differentially negative dynamic conductivity according to equation (7.11). From this discussion it also becomes clear that gain can only be expected when the device is biased in the NDC region.

In order to approximate v_1^s , it is assumed that F_Ω is not too strong so that multi-photon processes can be neglected. It is then possible to replace the relevant Bessel functions by $J_0(\nu) \approx 1$, $J_{\pm 1}(\nu) \approx \pm \frac{\nu}{2}$, and $J_{\pm k}(\nu) \approx 0$ for $|k| > 1$. In this limit v_1^s takes on the form

$$v_1^s = \left(v_{DC}(\hbar\omega_B + \hbar\Omega) - v_{DC}(\hbar\omega_B - \hbar\Omega) \right) \frac{eF_\Omega d}{2\hbar\Omega} = \sigma(\omega)F_\Omega . \quad (7.12)$$

²The following gain description is only valid as long as the external frequency is not faster than the processes that determine the corresponding current-voltage characteristic.

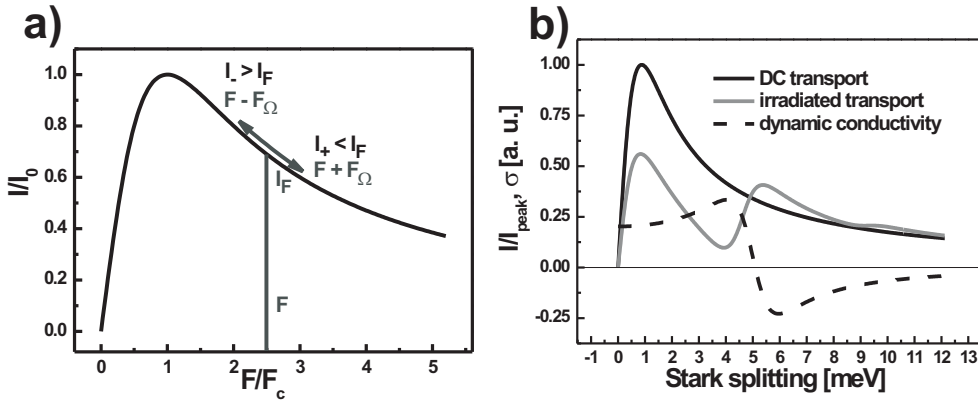


Figure 7.3: (a) Changes in current and total electric field when a high-frequency electric field is added to a static electric field that biases a device in a region of negative differential conductivity. (b) Comparison of the DC transport (v_0) in the presence of a high-frequency field to the dynamic conductivity (real part of $\partial v_1^s / \partial F_\Omega$).

Figure 7.3(b) compares the current contributions proportional to v_0 and v_1^s for identical parameters τ and Ω . A one to one correspondence between current suppression and absorption on one hand and current increase and gain on the other hand is found. The gain in a SL structure can be understood in terms of the same photon absorption and emission processes that determine the DC current response. When the Stark splitting is smaller than the photon energy, absorption processes decrease the current and attenuate the electro-magnetic radiation field. Once the Stark splitting exceeds the photon energy, photon emission processes increase the current along the SL and amplify the electro-magnetic radiation field. Although this is somewhat reminiscent of the laser principle, the origin for the gain is completely different. In a laser the gain is based on *occupation inversion between the laser transition levels*. In the SL structure, however, there is no occupation inversion. Here the gain is induced by an *asymmetry of the scattering processes involving phonon emission and absorption*. Those with emission dominate and make it more likely for electrons to go up ($eFd < \hbar\Omega$, absorption) or down ($eFd > \hbar\Omega$, gain) the Wannier-Stark ladder.

So far we have explained the changes induced by a high-frequency field in the Wannier-Stark transport picture. Recently, in [Kro03] a semiclassical approach was developed which leads to identical results. In the following the ingredients of this theory are briefly sketched.

The most important assumption underlying this approach again concerns the nature of the scattering events. It is assumed that the scattering probability from the upper half of the miniband to the lower half is higher than the other way around. It should be maximum near the top of the miniband. Based on this very reasonable argument, the electron distribution is split into two parts which pass the top of the miniband at different times. One part goes through the top part of the miniband when the total electric field is largest. Thus, these electrons spend less time there and experience less inelastic scattering than the other distribution part which passes the top of the miniband when the total field is smallest. This difference in the effectiveness of inelastic relaxation leads to an imbalance between the two distribution parts. Essentially, the theory shows that electron bunches in k -space originate with a frequency identical to that of the high-frequency field. The important point now is that these electron bunches oscillate in k -space at the Bloch frequency. Thus, when the Bloch and the electric field frequencies are different, the electron bunches pick up a phase difference in consecutive rounds through the Brillouin zone. It is the sign of this phase shift which determines whether the dynamic conductivity is positive or negative. In the limit of small amplitude F_Ω , the result of this model is very similar to the one that was derived above. However, the bunching approach gives a similar result for large external field strength, showing that the gain in a SL structure survives in this limit. The validity of the bunching concept was also supported by three-dimensional Monte-Carlo simulations [SDR03]. Since such calculations are, however, beyond the scope of this work, we will calculate the gain in our surface SL structures with the help of equation (2.17) which is similar to the expression derived in this section but

distinguishes also between elastic and inelastic processes. In [WDF03] it was shown that this semiclassical expression agrees quite well with a full, three dimensional quantum-mechanical approach if reasonable effective values for τ_e , τ_i , and T_e are used. For the surface SL structures these numbers were derived in chapter 5.8.

Before a discussion of the dynamic transport in surface SL structures is presented, a short overview of the utilized experimental setups is given.

7.5 Measurement of the DC transport in the presence of an external high-frequency field

There are two experimental difficulties that must be dealt with when a measurement of the DC current in the presence of an external high-frequency field is attempted.

The frequencies of interest are in the GHz to THz range. The corresponding wavelengths are between 100 μm and 10 mm and are much larger than the active region of about 1 μm . Thus we have to worry about how the AC field is coupled to our structure.

The second problem is that substantial powers are required to observe the features described in the last section. In the GHz regime there do exist solid state devices that provide high-power fields in a continuous wave mode. In the THz range, such high-power fields can be generated with the help of free-electron lasers (FEL) or CO₂-laser pumped gas lasers. However, the resulting fields are only pulsed and have a time length between 100 ns (gas laser) and a few μs (FEL). Under pulsed conditions, the DC current can no longer be measured with the setup described in chapter 3.6. An additional complication lies in the requirement that the experiments are performed at liquid helium temperatures.

Two different experimental setups have been utilized in the GHz frequency regime. Since available radiation sources for this frequency range do work in continuous wave mode, the measurement setup of chapter 3.6 (cf. figure 3.8) can still be applied in order to measure the current-voltage characteristics. However, the AC field must be coupled to the device while the current-voltage traces are recorded. Therefore, the electro-magnetic wave has to be guided into the liquid helium reservoir. For frequencies below 10 GHz this can be done with the help of special coaxial cables, whereas the use of rectangular waveguides is required for frequencies in the upper GHz regime. The coupling of the electro-magnetic wave to the sample at the end of the coaxial cable is straight forward. However, at the input, one has to take care to separate DC and AC bias from the corresponding sources. This is generally achieved with the help of a so-called Bias-T. This passive device connects two inputs into one output. One input contains a capacitor which allows the high-frequency voltage to pass unhindered. The DC power, which is coupled in from the second input, cannot pass the capacitor. Likewise the DC bias arm contains an inductance which stops the AC power from reaching the DC source.

In an ideal situation, the coaxial line would be connected to the sample through a matching circuit in order to minimize the reflection of the AC field. However, since the

electric properties of the shunted surface SL structures vary over large ranges, since the matching circuit would have to be designed for liquid helium temperatures, and since the sample contacts also play an important role in the matching between sample and transmission line, no such matching was employed in the experiments. This resulted most probably in a smaller maximum power delivered to the active device. However, the amount of power that did couple to the device was still large enough to produce significant results.

In the high GHz regime (10 – 100 GHz) losses in coaxial cables become so large that their use is no longer advisable. Electromagnetic waves at these frequencies were guided to the sample along standardized rectangular waveguides. The sample was mounted at the end of the waveguide. A short gold wire was glued to one of the top contacts of the sample, and the waveguide short, closing off the waveguide, was adjusted³ so that the distance between antenna and short was one fourth of the waveguide wavelength. Figure 7.4 shows a schematic drawing of the end part of the waveguide structure.

For measurements at THz frequencies the sample was mounted inside a cryostat with transparent windows. In order to achieve an efficient coupling, samples are often mounted in the center of some kind of antenna or lens. But since the size of the surface SL structures is rather large, the THz radiation was focused directly onto the sample. The wires connected to the sample most probably already served as antennas.

The measurement setup utilized for THz absorption experiments is shown in figure 7.5(a). The THz pulse, generated by the FEL or gas laser, first passes a beam splitter at which a small part of the pulse is separated and focused onto a reference detector with the help of an off-axis paraboloid. The main part of the pulse is guided to the cryostat window at which it is again focused with an off-axis paraboloid onto the sample inside the cryostat. Part (b) of figure 7.5 shows the electrical circuit. The sample is connected

³The adjustment was performed by a length measurement of the distance between antenna and waveguide short outside the cryostat with the help of a microscope.

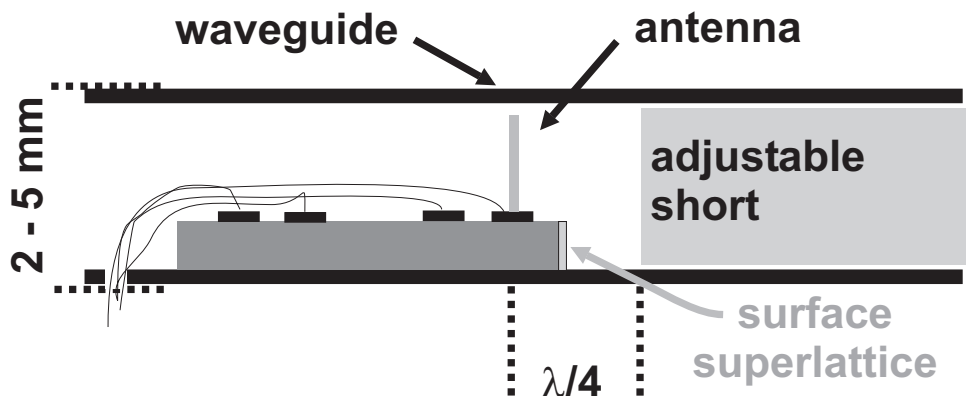


Figure 7.4: Schematic drawing of the waveguide section in which the high-frequency field is coupled to the surface SL.

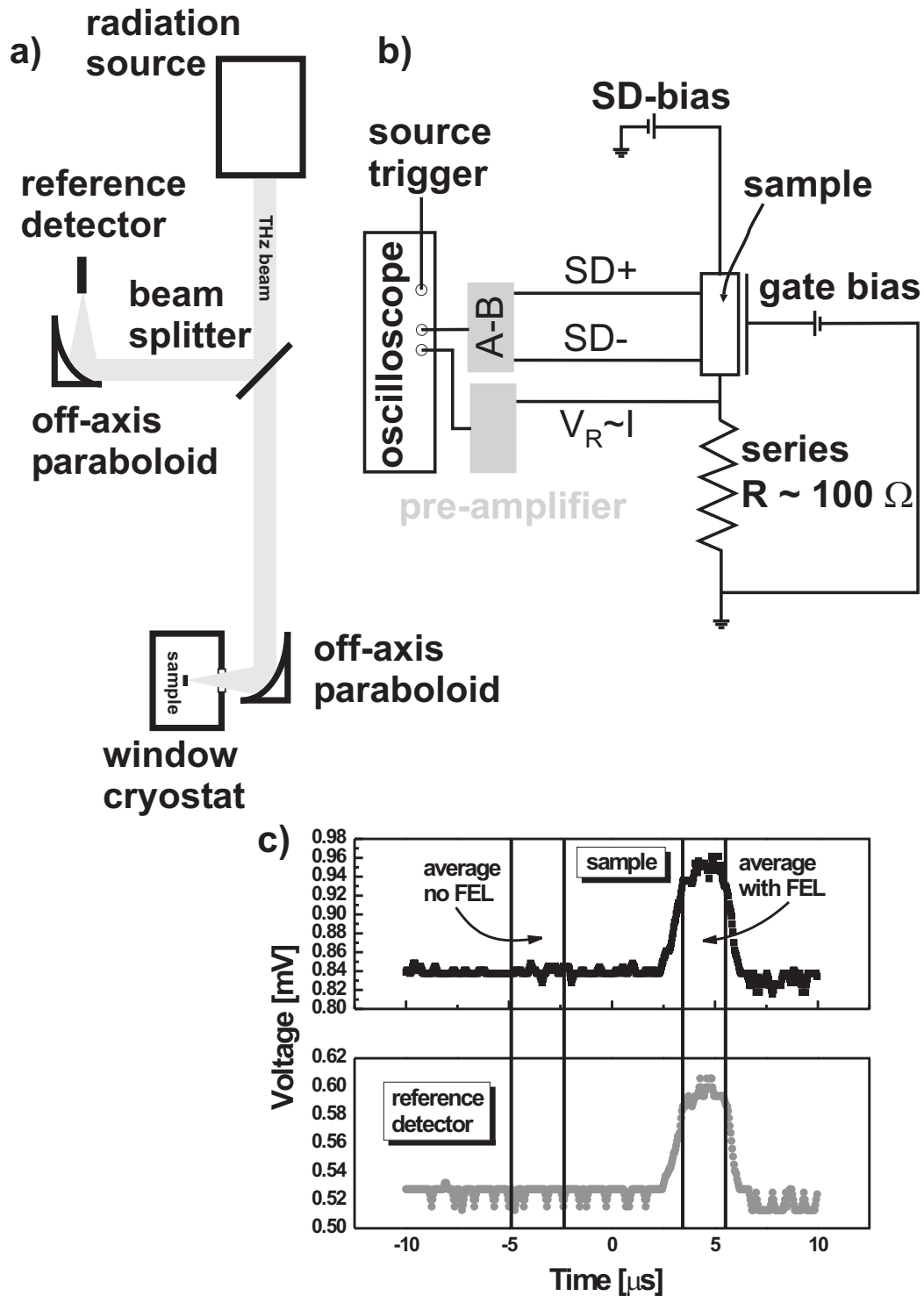


Figure 7.5: (a) Optical setup used to guide the THz field to the sample which is cooled to liquid helium temperature. (b) Schematic representation of the electrical setup for the THz absorption measurements. Graph (c) shows how the current and voltage data can be extracted by averaging over intervals during which the THz pulse is off or on.

in series with a small resistor of about 100Ω . The constant electric field results from an external voltage applied between one upper and lower contact of the sample. The SD-voltage is now recorded with an oscilloscope. During the THz pulse the current flow in the sample is increased and this leads to a change in the SD-bias value. The total current through the shunted surface SL is determined from the voltage drop over the series resistor at the second oscilloscope channel. Figure 7.5(c) shows how for every oscilloscope trace values before and during the THz pulse can be measured by averaging over intervals in which the THz pulse is off or on. In order to be able to find the DC current response with this approach, the THz pulses need to be much longer than the average time scale of the relaxation processes in the sample. The transport through the device is only then in a steady state during the presence of the pulse. With a characteristic time scale of about 1 ps for the scattering processes in the surface SL, the pulse lengths of 100 ns for the gas laser and up to 5 μ s for the THz laser are quite sufficient. Fluctuations in the individual THz pulses can be eliminated by normalizing the measured values with respect to the reference signal. However, since the surface SL current results from the difference between two larger signals the residual noise is still significant. Averaging over many measurements further increases the accuracy. Nevertheless, since the noise is proportional to $1/\sqrt{n}$ where n is the number of independent measurements, the low repetition rates of 0.25 to 1 Hz of the excitation sources represent a strong limitation. Even more so since the radiation sources do tend to drift and need realignment or other readjusting after a couple of hours, at the latest.

7.6 GHz absorption in shunt-stabilized surface superlattices

During the development process of the shunted surface SL system, absorption experiments were performed on a number of different sample structures. In the following, however, we will solely focus on the shunted surface SL structures.

Figure 7.6 shows the irradiated current-voltage characteristics of a surface SL with 12 nm wide wells, 5 nm thick barriers, and a gate barrier thickness of 500 nm. The excitation source was a Gunn oscillator operating at 65 GHz with a maximum output power of 17 dBm (50 mW).⁴ The different power levels were achieved by inserting a tunable attenuator between the Gunn oscillator and the rectangular waveguide. The main changes introduced by the GHz radiation is a clear suppression of the NDC peak at its original position and a shift of the peak to higher SD-bias. For comparison, equation (7.5) was evaluated for this sample with the parameters $\tau = 1$ ps, $f_{\Omega} = 65$ GHz, and with the peak current set to the experimental value. A power increase of 1 dBm between different traces was used. Since it is extremely difficult to estimate how much power is absorbed by the

⁴The logarithmic dBm units relate to the Watt scale according to $P(\text{dBm}) = 10 \log \left(\frac{P(\text{mW})}{1 \text{ mW}} \right)$.

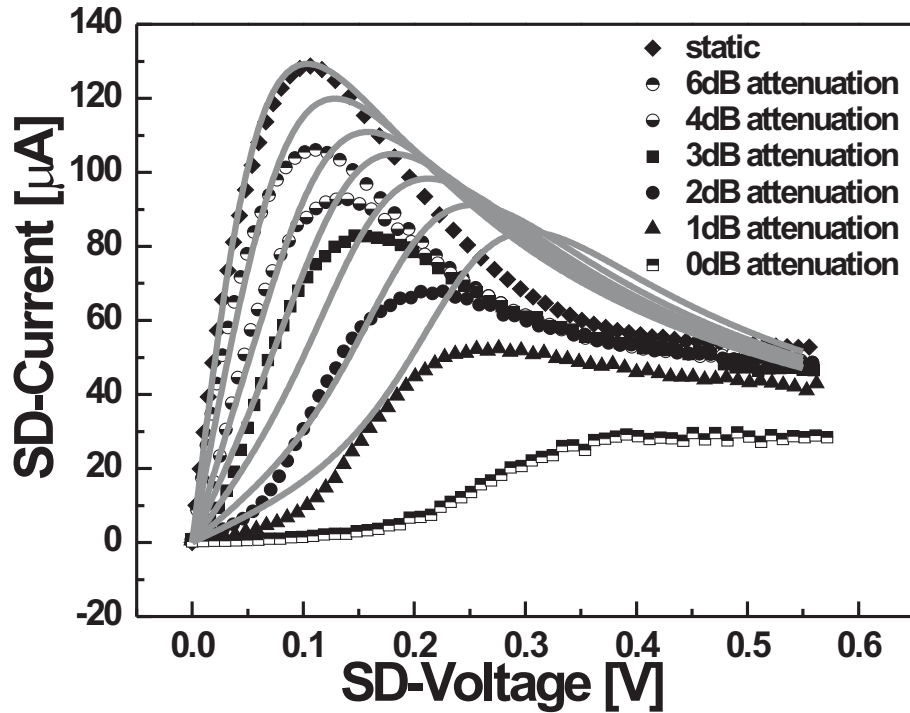


Figure 7.6: DC transport characteristics of a surface SL structure excited at 65 GHz for increasing input power. The given attenuation has to be subtracted from the maximum output power of 17 dBm of the Gunn oscillator that excites the system. The gray lines are plotted from the evaluation of expression (7.5). The power difference between two theoretical traces is 1 dBm and the lowest $\nu > 0$ was chosen so that the experimental and theoretical NDC peak positions cover about the same SD-bias changes.

surface SL, the lowest ν -value was chosen so that the experimental and theoretical NDC peak positions cover about the same SD-bias changes. From observation, the qualitative behavior is similar for the experimental and theoretical traces. Nevertheless, the theoretical data shows a crossing of the dynamic NDC peak over the static DC characteristic. Also, the theoretically predicted peak shift is not as large as the one recorded in the experiment. The fact that the dynamic DC characteristics are always smaller than the static transport trace could be explained by an additional heating of the electron distribution by the high-frequency field. Simultaneously, the increased experimental SD-voltage shift might be caused by the resistance reduction in the shunt induced by the high-frequency field. According to the discussion in chapter 5.6 the smaller shunt resistance requires a rescaling of the SD-bias down to smaller values. However, since the external AC field leads to very strong transport changes in the shunt, it is very difficult to make a more

quantitative comparison between theory and measurement for the data shown in figure 7.6.

The frequency of 65 GHz was chosen for the absorption experiment according to a scattering time of 1 ps. The latter time scale was determined from the series resistance corrected DC current-voltage characteristics. However, since the two-dimensional transport model of section 5.15 yielded a characteristic time of about 2.5 ps for the onset of Bloch oscillations, the limit $\Omega\tau \ll 1$ is not clearly reached at 65 GHz. Therefore, absorption measurements with an improved surface SL structure were performed at an external field frequency of 5 GHz. The studied device possesses 12 nm wide wells, 3 nm thick barriers, a 2000 nm gate barrier, and a 5 nm wide CEW. The data in figure 7.7(a) and (c) shows the current-voltage characteristics in the presence of the 5 GHz field for positive and negative SD-voltages. Due to the strongly increasing shunt current (cf. figure 7.7(f)) the noise in the data is very strong, especially at high SD-biases. Therefore, the traces have been smoothed by averaging over 5 nearest neighbors, and some traces are only shown for limited bias ranges. The observed transport changes in the positive voltage region are similar to those of the 65 GHz experiment: a current suppression with a simultaneous shift of the NDC peak towards larger SD-bias. In figure 7.7(b) a direct averaging of the experimental DC transport characteristic according to equation (7.9) is plotted. The averaged data looks just like the theoretically calculated one in figure 7.6. Again, the experimental data exhibits continuously smaller current values when compared to the theoretically expected values. However, the exaggerated SD-bias shift is not present this time. The latter fact is an indication that the designed reduction in the sheet resistivity of the contact layers can somewhat compensate the AC field induced resistance reduction in the shunt (cf. page 69).

Figures 7.7(c) and (d) show the same transport data as (a) and (b) for negative SD-biases. Interestingly, the current minimum at -6.5 meV is smoothed down similar to the NDC peak in the positive direction, while the maximum at 8 meV shows no continuous change. However, the latter observation could be caused through changes in the shunt transport induced by the AC field. Overall, the changes on the negative bias side are much weaker.

Figure 7.7(e) compares the series resistance corrected NDC peak positions and heights at positive SD-biases with those found from the DC averaged data. Thereby, the 60 data points average was set arbitrarily to 20 dBm, and the other traces were then adjusted by identifying the lateral averaging interval with the corresponding AC electric field amplitude F_Ω . Again, while qualitatively a similar behavior is found, a quantitative discussion is extremely difficult.

Thus, while a conclusive quantitative discussion of the GHz absorption experiments is lacking, the observed data is qualitatively close to the theoretical predictions for a SL with a homogeneous electric field distribution.

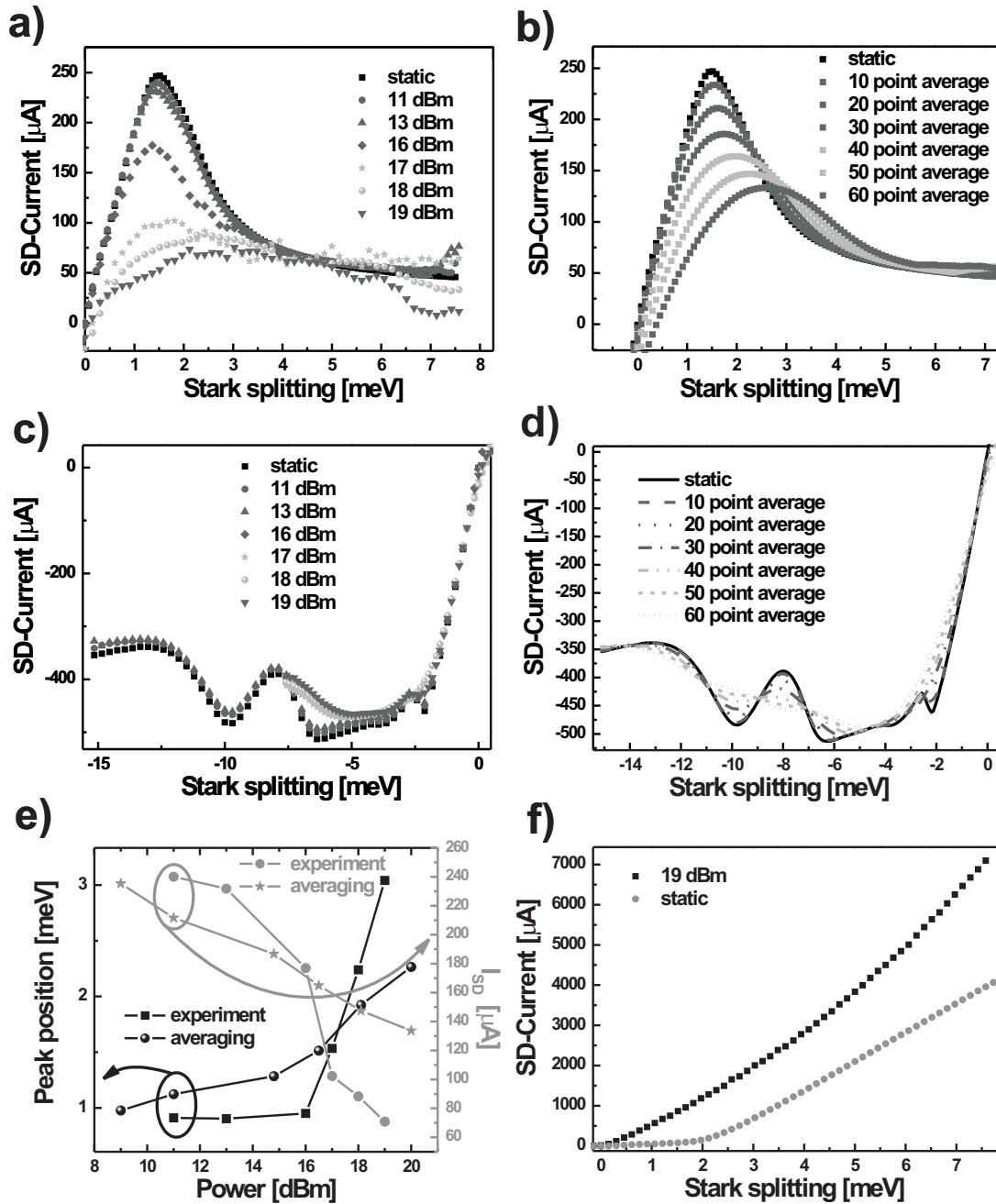


Figure 7.7: (a) Current-voltage characteristics of a surface superlattice irradiated with a high-frequency field at 5 GHz for different radiation field powers. (b) Transport characteristics derived from the static one by averaging over increasing voltage intervals. Panel (c) and (d) show the same as (a) and (b), however, in the negative SD-bias range. (e) A comparison of the position and height dependence of the negative differential resistance peaks in graphs (a) and (b) is shown. (f) Static and high-power irradiated current-voltage characteristics of the shunt.

7.7 THz absorption in shunt-stabilized surface superlattices

Absorption experiments at THz frequencies were both performed with pulsed FIR gas lasers at the University of Regensburg and with the FEL at the University of California at Santa Barbara. In figures 7.8(a)-(c) typical results for the gas laser experiments are shown. The plotted quantity is the DC current that is induced by the THz field. This current must be added to the static (only a static electric field is present) DC current in order to find the total DC current through the surface SL. The utilized sample is identical to the device used for the 5 GHz absorption experiments. For Stark splittings smaller than 3 meV the THz field drives more DC current through the shunt than through the combined shunt-surface SL system. Therefore, the total DC current through the surface SL is suppressed. However, for Stark splittings larger than 3 meV there is no difference observable whether the gate is turned on or off. This indicates that there is no AC field induced change in the surface SL transport at these SD-biases. A similar situation is found in the data of figure 7.8(d) which shows the results of an absorption measurement for a 25 period SL sample with a 5 nm CEW, in which the device was excited with the FEL at 1.5 THz. The presence of the THz field (dynamic DC I-V) again leads to a suppression of the total DC current in the small SD-bias regime.⁵ But for Stark-splittings larger than about 10 meV the static and dynamic total DC current are again identical.

It is possible that the increase in the effective electron temperature beyond about 3 meV, discussed in section 5.15, leads to photon assisted transport peaks that are so small that they cannot be resolved in the measurement shown in figures 7.8(a) and (c).⁶ However, the frequency independence of the 3 meV crossover point (cf. figure 7.8(c)) might suggest a different explanation. Hereby, the high-power trace (P_4) at a wavelength of 280 μm must probably be ignored, since the much higher power also introduces a much larger noise into the measurement.

In principle, the suppression of the NDC peak in the small SD-bias regime is consistent with the theoretical predictions (cf. figure 7.1(b)). If the largest suppression happened directly at the NDC peak position it would suggest an important difference to what was observed in the GHz absorption experiments. This can be understood when v_0 is expanded in the limit of quasi-static and dynamic irradiation (cf. equations (7.5) and (7.9)). This approach leads to the expressions

$$v_0 = J_0(\nu)^2 v_{DC}(\hbar\omega_B), \quad (7.13)$$

$$v_0 = v_{DC} + \frac{F_\Omega^2}{4} \frac{\partial^2 v_{DC}}{\partial F^2}, \quad (7.14)$$

for the high and low-frequency limits, respectively. In the dynamic absorption problem

⁵The difference of the two traces leads to a negative THz induced DC current for the surface SL, similar to the one shown in figure 7.8(b).

⁶A similar argument can be made for the data in figure 7.8(d).

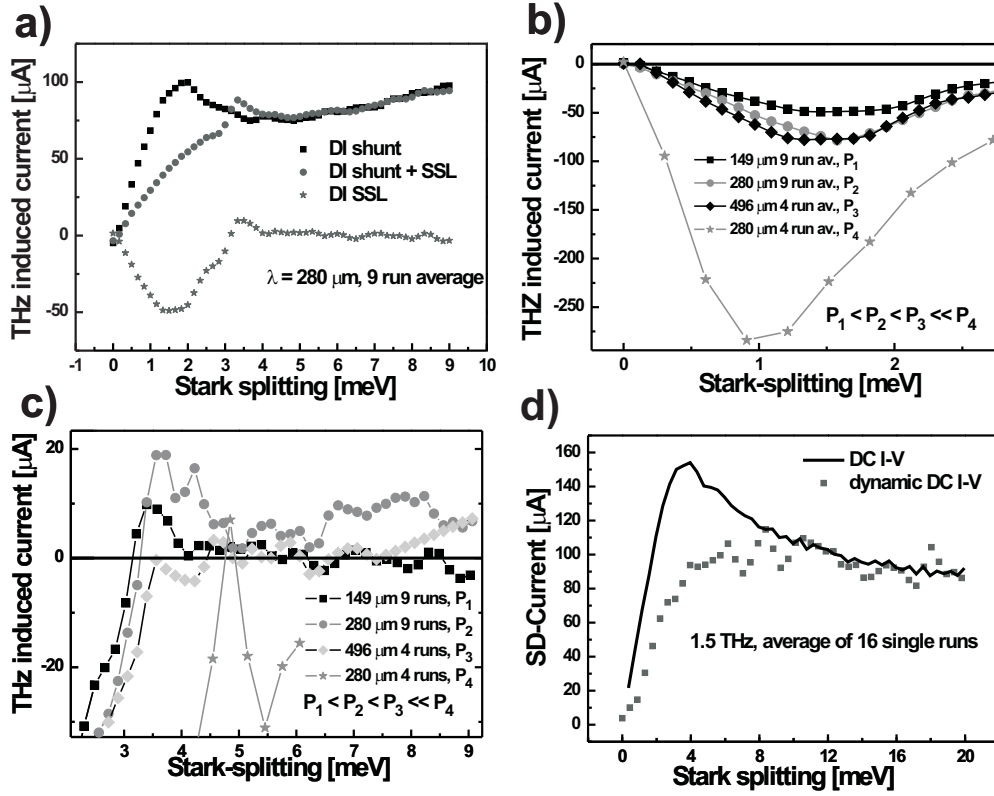


Figure 7.8: (a) THz field induced DC current for the shunt, the surface superlattice, and the combined system of a shunted surface superlattice structure. Panels (b) and (c) show the same as (a) for different excitation wavelengths and powers (P_1, \dots, P_4). In graphs (b) and (c) the small and large SD-bias intervals are, respectively, magnified. The number following the excitation wavelength indicates the number of independent runs which have been averaged to arrive at the shown data. (d) Static and dynamic DC current-voltage characteristics of a surface superlattice irradiated with the FEL at 1.5 THz.

the NDC peak is suppressed but it stays at its original SD-bias position. In the quasi-static case on the other hand, the maximum current reduction occurs at the SD-bias for which the current-voltage trace exhibits its largest curvature. This difference in the suppression of the NDC peak allows one to, in principle, distinguish between quasi-static and dynamic excitation. However, the very complicated bias distribution in the shunted surface SL structure makes it impossible to decide whether the observed maximum current change occurs right at the NDC peak position or not. Moreover, the unchanged transport through the surface SL beyond a Stark splitting of 3 meV indicates that the radiation power applied to the SL-shunt system depends strongly on the SD-bias so that ν in equation 7.13 might not be constant over the whole Stark splitting range. Thus, the DC transport changes in the small SD-bias regime are consistent with the theoretical predictions, but they do not allow to draw definite conclusions about the electric field

distribution inside the device.

While it is difficult to pinpoint the origin of the lack of transport changes induced by the high-frequency field in the high SD-bias regime, figures 7.9(a) and (b) suggest a direct connection to the high-frequency properties of the shunt SL. Graph (a) shows the radiation field induced current changes for three different devices. While those for the 1.2 THz and 5 GHz data are identical, the other two samples follow an earlier design and have a much larger n+-layer series resistance, which leads to an effective stretching of the SD-bias axis and makes them unsuitable for a study of photon assisted transport in surface SLs.⁷ However, we are only interested in the shunt properties here. All traces shown in figure 7.9(a) were measured at very strong excitation powers. The radiation field induced current is much stronger for the GHz excitation than for the THz excitation of an identical sample. Moreover, all traces taken at THz frequencies in figure 7.9(a) show

⁷Essentially, the SD-biases needed to observe photon-assisted transport are of the order of the gate bias. Such large SD-voltages lead, as discussed in section 5.6, to a quenching of the two-dimensional transport channel.

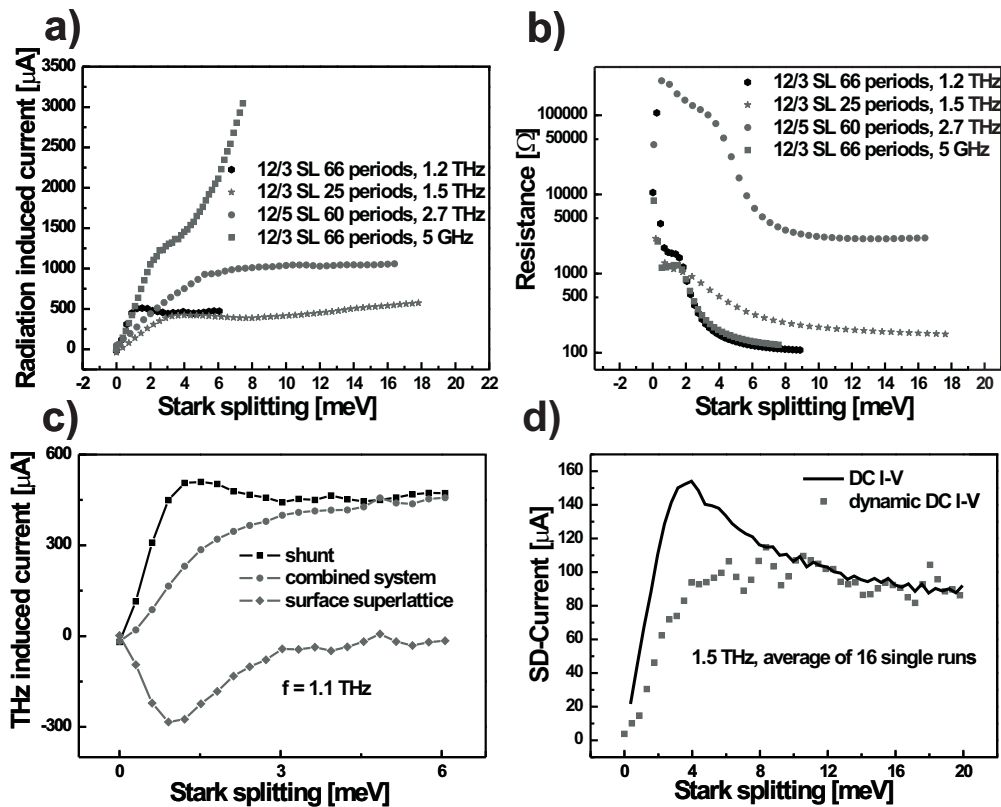


Figure 7.9: (a), (b) Radiation induced current and static resistance for different shunt structures. (c) THz field induced current changes of the shunt, the surface superlattice and the combined system of a shunted surface superlattice structure. (d) Static and dynamic DC current-voltage characteristics of a surface superlattice irradiated at 1.5 THz.

a saturation of the radiation induced current beyond a certain SD-bias. This saturation behavior seems to be directly correlated to the DC resistance of the shunt channel shown in graph (b). This resistance is high for all samples at small SD-bias which indicates a finite injection barrier into the SL. At high SD-voltages the resistance becomes very small, in part due to the relatively large area of the shunt channel.

It is interesting to note that the THz induced current in figure 7.9(a) saturates approximately at those Stark splittings beyond which the shunt resistance has decreased by about an order of magnitude. From this it might be concluded that for increasing SD-bias either a smaller and smaller part of the high-frequency field is dropped across the SL-shunt system or that the shunt resistance for the high-frequency field has become so small that the high-frequency field does not reach the two-dimensional channel any longer. In both cases, only the static DC surface SL current remains to be measured. And this is what was found experimentally in figures 7.9(c) and (d).

The real part of the high-frequency resistance of the shunt, assuming a resistor in parallel to a capacitor, is given by

$$\text{Re}(Z_{\text{shunt}})(\Omega, R) = \frac{R}{1 + R^2\Omega^2C^2}, \quad (7.15)$$

where R and C are the resistance and the capacitance of the shunt. A calculation of the capacitance from the sample geometry leads to a large value of about 40 pF for C . Thus, in the THz regime, the first term in the denominator of expression (7.15) can be neglected. In this limit, a decreasing resistance R actually leads to an increasing high-frequency resistance. This seems to contradict the observations of the experiment. However, both the resistance and the capacitance should depend on the SD-bias so that the real part of $Z_{\text{shunt}}(\Omega)$ might still actually decrease.

It is very difficult to get any conclusive answers from the experimental data. It appears that the high-frequency properties of the shunt make it very hard to study dynamic surface SL transport in the SL-shunt system. At the same time, it cannot completely be ruled out that the lack of photon assisted transport in the surface SL is caused by electric field inhomogeneities. A decision one way or the other requires additional experimental input. However, even when the problem lies with the shunt, the question arises whether the high-frequency properties of the shunt represent a main obstacle for the realization of a Bloch oscillator. An attempt of an answer will be given in the next section which deals with a general discussion of the gain properties of surface SL structures.

7.8 Gain considerations

Generally, the calculation of the gain of a SL structure can be quite demanding. However, the results of quantum-mechanical models [WDF03] showed⁸ that the semiclassical expression derived in [KSS72] is a very good approximation for (electron) temperatures

⁸In the comparison to the semiclassical prediction a single relaxation time was assumed.

above 100 K and even underestimates the gain for lower temperatures. Making use of the parameters τ_i , τ_e , and T_e found from the fully two-dimensional transport simulation in section 5.15, the gain for the corresponding surface SL structures can be calculated according to equation 2.17. The resulting gain for T_e values of 4.2 K and 200 K is shown in figure 7.10(a). Without the heating of the electron system there would be considerable gain in the surface SLs. However, the strong dominance of the elastic scattering processes leads to a reduction of these high values, just as it causes a suppression of the DC transport and of the photon assisted transport peaks. In order to reach higher gain values, devices with much larger miniband widths are needed so that the suppression, which depends on the ratio $\Delta/k_B T_e$, is less dramatic. Nevertheless, surface SL structures seem to possess one general advantage over conventional SLs. The relaxation times are generally much longer. This results, if all other parameters are fixed, in higher gain values as shown in figure 7.10(b).⁹ The larger the value $\omega_B \tau$ at fixed SD-bias is, the larger is the possible gain. Actually, in order for the gain minimum below the Bloch frequency to appear, $\omega_B \tau$ has to reach a minimum value. Otherwise the largest gain is found at very low frequencies.

For the above calculation the shunt has been ignored. Since it is in parallel to the surface SL, the conductivities of both channels must be added up in order to determine the total conductivity of the SL-shunt system. However, the gain in the shunted surface SL system is not strongly affected by the shunt. This is on one hand due to the very low electron density in the shunt, which results in a conductivity that is more than two orders of magnitude smaller than the surface SL one. On the other hand, the shunt is a SL with

⁹For the calculations τ_e was assumed to be infinite.

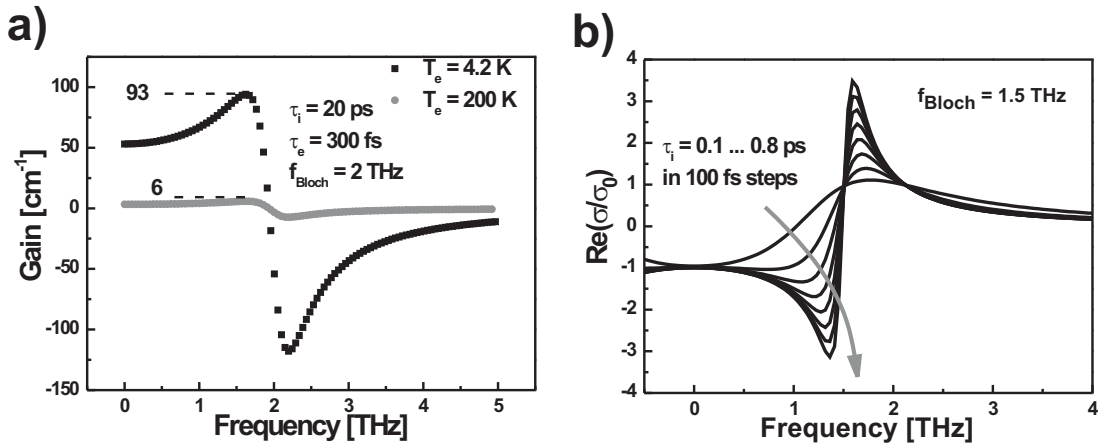


Figure 7.10: (a) Gain calculation for surface superlattices assuming two different effective electron temperatures. (b) Theoretical gain calculations for a fixed Bloch frequency and continuously increasing relaxation times ($\tau_e = \infty$).

an almost homogeneous electric field distribution so that it exhibits gain itself [SKLA04], albeit a very small one.

While the changes to the total conductivity induced by the shunt can be neglected, there is more concern about the fact that the shunt acts as a parallel capacitor. As seen in the last section, a very large capacity in parallel with a resistor reduces the real part of the total resistance strongly at THz frequencies. This is also true for the negative resistor represented by the surface SL. Then, if the resulting reduction is too strong, always present positive series resistances can compensate the negative resistance (gain) in the surface SL system. The effective gain in the structure will therefore critically depend on the device geometry and the absolute value of the gain in the surface SL. Especially, the exact form of the THz waveguide will play a crucial role in the development of a possible Bloch oscillator.

7.9 Conclusion

The absorption experiments on shunted surface SLs presented in this chapter were performed in order to answer the question whether it is possible to realize an active Bloch oscillator based on this device concept. However, the measurement results are inconclusive.

For low-frequency GHz excitation the observed changes in the DC transport through the surface SLs qualitatively agree well with the corresponding theoretical predictions. However, a quantitative evaluation of the data proves very difficult since the external field also strongly changes the shunt transport, which always leads to significant rearrangements in the voltage and current distributions inside the shunted surface superlattice system.

During THz excitation, the low SD-bias regions of the surface SL current-voltage characteristics also show the theoretically expected transport changes. However, beyond a certain, frequency-independent SD-bias the current through the surface superlattice stays unchanged. On one hand this might happen when the external field either does not reach the surface superlattice or becomes strongly weakened in the high SD-bias regime. On the other hand, electric field inhomogeneities can also not be completely ruled out as the origin for the missing photon-assisted transport. It will require additional experimental information to decide on this problem.

Unfortunately, without photon-assisted transport it is not possible to experimentally determine the gain in the surface superlattices. Theoretically, this gain proves to be dramatically reduced from a substantial value due to the strong dominance of elastic scattering. In order to achieve higher gain values, surface superlattices with much larger miniband width must be designed.

Finally, although the shunt does not strongly affect the overall gain in a shunted surface superlattice structure, the question of how the large capacitance of the shunt influences

the gain properties of the whole system needs to be addressed in further experimental and theoretical investigations.

Chapter 8

Magnetotransport in a two-dimensional electron system with a strong, short-period modulation

8.1 Introduction

Many equilibrium properties of metals have been shown to exhibit an oscillatory behavior when a magnetic field is applied to the sample. One of the earliest such experimental observations was made by Shubnikov and de Haas [SdH30], who found an oscillatory resistivity for bismuth when they performed a magnetic field sweep. While a similar effect is difficult to observe in many other metals, semiconductors and semimetals show even stronger Shubnikov-de Haas (SdH) oscillations. For high mobility two-dimensional electron systems in silicon inversion layer structures and GaAs modulation doped systems SdH oscillations are especially pronounced. Due to the observation of the integer and fractional Quantum Hall effects (a good introduction can be found in [Yos02]), the study of high-mobility, two-dimensional electron systems in strong magnetic fields has received immense attention.

In 1989 the first resistivity oscillations on a periodically modulated two-dimensional electron system were reported [WvKPW89]. Additional oscillations in the conductivity components of the system, the so-called Weiss oscillations, were found. Since then a lot of experimental and theoretical attention [WvKPW89, GWvK89, ZG90, BAM⁺90, BMD⁺90, BDM⁺91, WRM⁺91, WRM⁺93] has been given to such devices. The modulation potential is introduced by lithographic methods or by holographic illumination [TSYS84]. However, for both approaches the modulation period has an inherent lower limit. Minimum modulation periods of 50 – 100 nm are possible with electron beam lithography. For the illumination approach, the wavelength of the employed laser light limits modulation periods to about 300 – 400 nm. Moreover, the modulation strength

is relatively weak since the electron system is buried underneath a cap layer so that the modulation is only felt from a distance of about 100–500 nm. These experimental limitations of a long period (compared to the Fermi wavelength) and weak modulation strength (compared to the Fermi energy), have led to a strong focus of the theoretical work onto this regime.

With the introduction of the Cleaved-Edge-Overgrowth (CEO) method in 1990 [PWS⁺90] and the realization of the first surface superlattice [SPB⁺91] all these experimental limitations were removed. Since then it is possible to realize in principle arbitrary modulation periods with atomic precision. Also, the distance between the modulation structure and the two-dimensional electron system can be chosen arbitrarily. Thus, both very weak and very strong modulation potentials can be realized. Nevertheless, the first two publications [SPB⁺91, MRT⁺00] about two-dimensional electron systems with a strong, short-period modulation did not report any effects of the modulation on the two-dimensional electron system. There is a very reasonable explanation for these observations, which is discussed in the following sections. The third magnetotransport study [VSD02] of surface superlattices with a strong, short-period modulation potential finally showed a strong influence of the modulation on the transport properties. The relevant samples are actually those with which the investigation of the high electric field transport presented in the previous chapters was started. The observed effects could be fitted reasonably well with the results from a quantum mechanical model. However, a clear correspondence between the measured resistance and the calculated conductivity could not be established. During the course of this work, a reinvestigation of the problem, aiming at a reproduction of the observed results, showed large differences although the sample structures were nearly identical. Among these differences was the observation that samples without cleaved-edge well (and without intrinsic buffer between contact and superlattice) showed no magnetotransport oscillations (at least below 6 T) which is in stark contrast to the earlier measurements, where such oscillations could be observed already at fields well below 0.5 T. Moreover, the data presented in the next sections is analyzed with a resistance formula according to which the results of the earlier study cannot be attributed to the magnetoresistance (MR) of a two-dimensional electron system with a strong, short-period modulation. This resistance formula has been confirmed by four-point resistance measurements [Ler04] in Hall bar geometry. The Hall bar was fabricated on a two-dimensional electron gas that was grown on the cleaved-edge of a SL structure. The reason for the differences between the earlier and newer measurements is believed to be found in the intrinsic buffer layers between contact and sample.¹ Their thickness of

¹The presence of this intrinsic buffer layer in the two-dimensional electron systems with a short-period modulation is not mentioned (although it is present in the growth protocols as seen in figure 5.1) in [DLW⁺00, Deu01, FRW⁺04, FDW⁺04] as seemingly negligible compared to the superlattice section which is much wider and has a much larger resistance. And for all high electric field studies this is correct and the two-dimensional electron system along the intrinsic buffer is simply an extension of the contacts. However, for magnetotransport measurements the situation is different since the unmodulated two-dimensional electron system along the buffer layer has a much higher mobility than the one along

100 nm is wide enough so that a two-dimensional electron system is formed along their extension. Since, however, the cyclotron radius is for larger densities of the same order of magnitude, size effects can be expected. This might explain the delayed onset of the MR oscillations [DLW⁺00]. The latter are only possible when the cyclotron radius is smaller than about 50 nm (half the buffer layer extension).

In addition to the realization of samples with a strong, short-period modulation, the CEO method was also used to create electron systems with modulations of intermediate period lengths (about 50 nm) and of relatively weak strength. The resulting structure is a textbook example for a free (two-dimensional) electron gas subject to a weak periodic potential. The theoretically predicted opening of small gaps at the Fermi surface of the system could be beautifully linked to the experimentally observed MR oscillations [DWR⁺01]. Recently, such oscillations have also been observed for a two-dimensional electron system subject to a weak periodic modulation in both dimensions [GCS⁺05]. In this system, convincing evidence for the fractal Hofstadter butterfly energy spectrum has also been presented [GSU⁺04].

Besides the CEO approach, short period modulations have also been achieved by the growth of the two-dimensional electron gas on vicinal GaAs (001) [FS88, MTS89, TTS90] and GaAs (111)B surfaces [NIS98, SNY⁺99]. In this approach, atomic steps are formed on the substrate by the deposition of AlAs or n-AlGaAs under special growth conditions. These steps are periodic with a period of about 10 – 20 nm. The two-dimensional electron system is then grown on top of these steps. However, the resulting modulation is estimated to be weak since the electron system resides relatively far from the steps.

The samples used for the measurements presented in the next sections are of the final design described in chapter 5 and possess no intrinsic buffer layer between contact and superlattice. The quantum mechanical model with which the experimental data is analyzed was presented by Karel Výborný and co-workers [VSD02] with the aim of describing the results of the earlier experimental study [Deu01, VSD02]. The author is greatly indebted to Karel for his close cooperation and for providing computer programs for the calculation of the energy spectra and the density of states for the presented system.

8.2 Semiclassical description

The semiclassical theory of magnetic field-induced oscillations of material properties was developed in the middle of the last century for the description of such phenomena in metals. One of the earliest observations [SdH30] was made on bismuth. Shubnikov and de Haas found magnetic field-dependent oscillations of the electrical resistivity in this metal. This effect, now referred to as the Shubnikov-de Haas effect, is extremely small in most metals while other quantities oscillate much stronger. However, in semiconductors and

the superlattice. This might also explain why the fractional quantum Hall effect could be observed in these samples [Deu01, SDW⁺01, SDE⁺02] albeit without a signature of the strong modulation.

semimetals the SdH oscillations are much more pronounced. This is mainly due to the lower electron density in these materials compared to metals. Even stronger SdH oscillations are found in two-dimensional electron systems and they are nowadays a standard characterization tool for these structures.

The semiclassical model used to describe the oscillations of material properties in dependence on the magnetic field is based on a simple physical picture. It assumes that the closed k -space orbits (or energy values) which electrons follow when a magnetic field is applied are quantized. In the semiclassical approach this is derived from the Bohr-Sommerfeld quantization rule (cf. [Sho84, chapter 2.2.2]) and it corresponds to the Landau quantization resulting from the corresponding quantum mechanical hamiltonian. The orbit (or energy) quantization depends on the magnetic field strength. Furthermore, the material properties at equilibrium and in linear response are strongly dominated by the properties of the electrons at the Fermi surface. When the magnetic field is increased, the area of the orbits increases. They are successively shifted through the Fermi surface. It is this successive and periodic (with the inverse magnetic field) passing of the electron orbits through the Fermi surface that leads to the oscillating material properties in a varying magnetic field. Actually, it is not straight forward to calculate the observed oscillations in the resistivity of a metal from these assumptions. However, a qualitative connection can be established by the argument [Pip65] that the probability of scattering is proportional to the number of states into which an electron can be scattered. Thus the scattering time and with it the resistivity oscillate in accordance with the density of states (DOS),² which can be more easily calculated from the semiclassical model.

Just as in the case of high electric fields, the starting point for the semiclassical theory is the dispersion $E(k_x, k_y)$ given by

$$E(k_x, k_y) = \frac{\hbar^2 k_y^2}{2m} + \frac{\Delta}{2}(1 - \cos(k_x d)) , \quad (8.1)$$

where d is again the periodicity of the SL (modulation) potential and Δ is the width of the lowest miniband. From this the DOS can be computed directly using the expression [AM76, chapter 8]

$$D(E) = \int_{A(E)} \frac{1}{2\pi^2 |\nabla E(k_x, k_y)|} , \quad (8.2)$$

where $A(E)$ is the line segment of the k -space dispersion $E(k_x, k_y)$ at energy E . The result, in units of the DOS of a free two-dimensional electron system $D_0 = m/\pi\hbar^2$, is

$$D(E)/D_0 = \begin{cases} \frac{2}{\pi} \sqrt{\frac{m_\Delta}{m}} \sqrt{\frac{\Delta}{E}} K\left(\sqrt{\frac{\Delta}{E}}\right) & \Delta < E \\ \frac{2}{\pi} \sqrt{\frac{m_\Delta}{m}} K\left(\sqrt{\frac{E}{\Delta}}\right) & 0 < E < \Delta \end{cases} , \quad (8.3)$$

where K is the complete elliptic integral $K(m) = \int_0^{\pi/2} \frac{d\phi}{\sqrt{1-m^2 \sin^2 \phi}}$, with $K(0) = \frac{\pi}{2}$ and $K(1) = \infty$. Moreover, $m_\Delta = 2\hbar^2/\Delta d^2$ has been introduced as the effective mass along the

²However, the complete relation between resistivity and density of states is often very complicated.

miniband at $k = 0$. Both the DOS and the electron density are plotted versus energy in figure 8.1. The DOS shows a logarithmic divergence at $E = \Delta$. This van Hove singularity leads to a slight distortion in the otherwise close to linear increase in the electron density at $E \approx \Delta$. For energies within the first miniband ($0 < E < \Delta$) the DOS is larger than in a conventional two-dimensional electron system. Once the energy lies far in the gap above the miniband, the DOS decreases like one over the square root of energy ($K(m)$ is finite in the limit $m \rightarrow 0$) similar to a one-dimensional system. When the Fermi energy moves from the top of the miniband into the gap, a transition from a two-dimensional to a one-dimensional system takes place. For finite magnetic fields, finite temperature, and finite eigenstate lifetimes the logarithmic divergence in figure 8.1 will be smeared out and the relationship between density and Fermi energy will be very close to linear in the range plotted in figure 8.1.

According to the semiclassical electron transport description, the velocity and momentum change are given by

$$\vec{v}(\vec{k}) = \frac{1}{\hbar} \frac{\partial E(\vec{k})}{\partial \vec{k}} \quad (8.4)$$

$$\hbar \dot{\vec{k}} = \vec{F} = e\vec{v} \times \vec{B}, \quad (8.5)$$

when the Lorentz force \vec{F} due to a magnetic field \vec{B} acts on the system. From these

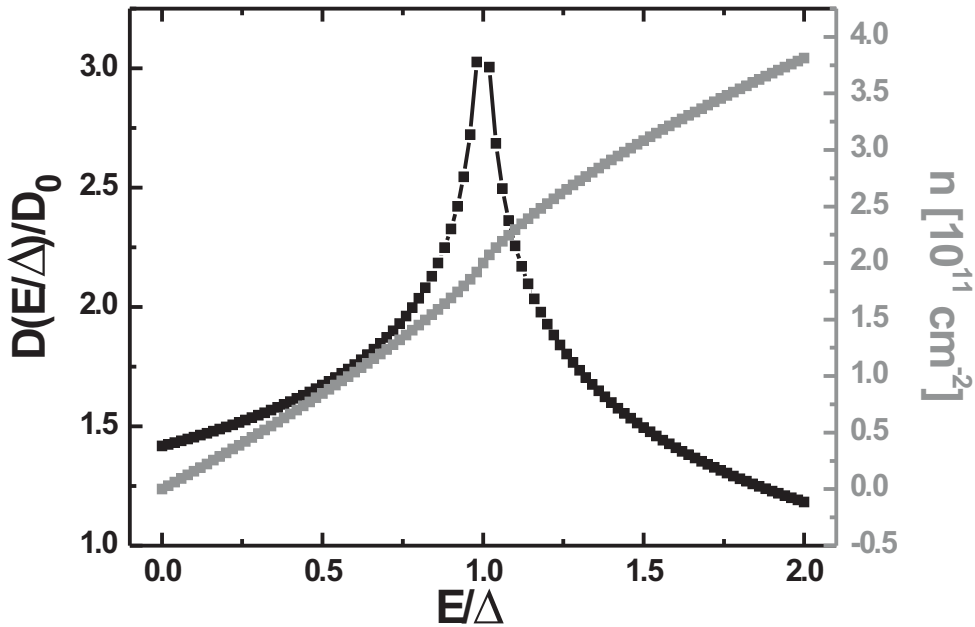


Figure 8.1: Density of states and electron density of a surface superlattice for Fermi energies ranging from the bottom of a miniband of width $\Delta = 4$ meV to twice the top of this miniband.

equations it follows immediately that electrons move in k -space along orbits which lie in a plane perpendicular to the magnetic field direction and which stay at constant energies. The Bohr-Sommerfeld quantization leads to the Onsager relation [Sho84, Chapter 2.2.2], which states an area (and thereby energy) quantization of the form

$$a(E) = \left(r + \frac{1}{2} \right) \frac{2\pi eB}{\hbar} \quad (8.6)$$

for the allowed energies E . In this expression, a is the area enclosed by a (closed) k -space electron orbit and r is an integer. From the Onsager relation an energy difference

$$\Delta E = \hbar\omega_c = \frac{\hbar eB}{m(E)} \quad (8.7)$$

between two neighbouring allowed areas is found. In this expression an effective cyclotron mass $m(E)$ has been introduced according to

$$m(E) = \frac{\hbar^2}{2\pi} \frac{\partial a(E)}{\partial E}. \quad (8.8)$$

This cyclotron mass can be directly expressed in terms of the DOS of the system,

$$m(E) = D(E)\pi\hbar^2. \quad (8.9)$$

This resembles the free electron result with a more general cyclotron mass. As figure 8.1 shows, the cyclotron mass $m(E)$ is not constant in our system but divergences at the top of the miniband. However, as mentioned before, this divergence will be smeared out, and measurements showed that at $E = 5.5$ meV the effective mass increases by less than 15 percent for a 7.7 meV wide miniband [MRT⁺00]. Therefore, the energy level spacing in the low magnetic field regime of the modulated system will still be very close to equidistant.

Oscillations in the resistivity come about when the energy level spectrum is pushed through the Fermi energy for increasing magnetic field. Whenever an allowed orbit area $a(E)$ is equal to the area of the orbit at the Fermi energy $a(E_F)$, many properties of the system will take on extremal values compared to when no $a(E)$ matches $a(E_F)$.

For the resistivity, the argument is again based on the DOS. When a small magnetic field is turned on, the DOS will closely resemble the one shown in figure 8.1, however, with periodic wiggles on top of the $B = 0$ value as shown in figure 8.2. When the Fermi energy moves through these periodic wiggles (or the other way around), the scattering rate oscillates in accordance with the DOS³ and thus the resistivity shows periodic oscillations.

The periodicity is given by the magnetic field difference between the situations were two neighbouring areas take on the value $a(E_F)$. It can be written as

$$\Delta \left(\frac{1}{B} \right) = \frac{2\pi e}{\hbar a(E_F)}. \quad (8.10)$$

³It will be seen later that this assumption is quite reasonable.

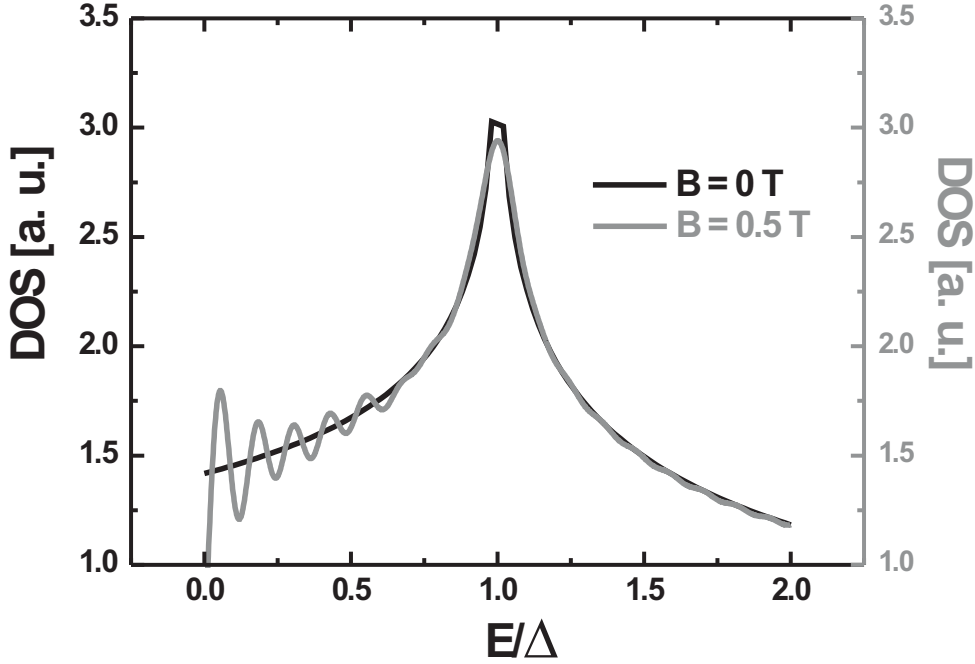


Figure 8.2: Density of states of a surface superlattice for magnetic fields of 0 and 0.5 T. The finite magnetic field leads to oscillations in the density of states, which are reflected in the scattering time and therefore the resistivity of the system.

The oscillations that appear due to the magnetic field are only observable if the wiggles in the DOS are not smeared out by strong scattering. Therefore, the system needs to have a high enough mobility so that

$$\omega_c \tau > 1. \quad (8.11)$$

This requirement states that the electron must be able to perform one closed cycle along its orbit before it is scattered. Requesting an energy level separation $\hbar\omega_c$ larger than the broadening due to scattering \hbar/τ leads to the same condition. Thereby τ is the scattering time which corresponds to the broadening of the oscillations in the DOS.

For magnetic fields too small to satisfy condition (8.11), the conductivity is given by the classical Drude result [AM76, chapter 1]

$$\bar{\sigma} = \frac{\sigma_0}{1 + \omega_c^2 \tau^2} \begin{pmatrix} 1 & -\omega_c \tau \\ \omega_c \tau & 1 \end{pmatrix}, \quad (8.12)$$

where $\sigma_0 = ne^2\tau/m$ is the Drude conductivity for an electron system with density n and with an effective electron mass m .

When the magnetic field fulfills condition (8.11) oscillations in the resistivity are observed. The amplitude of these oscillations is strongly influenced by the temperature of

the surrounding bath and by the strength of the scattering of the electrons. A finite temperature leads to a spread in the Fermi energy of the system so that the oscillations effectively have to be averaged over a finite region of Fermi energies. In this process, the oscillation amplitude acquires an additional reduction factor R_T , given by [Sho84, section 2.7.3.1]

$$R_T = \frac{2\pi^2 k_B T / \hbar \omega_c}{\sinh(2\pi^2 k_B T / \hbar \omega_c)} . \quad (8.13)$$

Likewise, the finite lifetime of an electron orbit due to scattering leads to a broadening of the quantized energy levels. This introduces an additional reduction factor R_D of the form⁴

$$R_D = e^{-\pi/\omega_c \tau} . \quad (8.14)$$

The study of the dependence of the resistivity oscillation amplitude on temperature allows the determination of the effective mass $m(E)$ according to (8.13). Once $m(E)$ is known, the magnetic field dependence of the amplitude can be used to determine the lifetime τ .

The semiclassical approach is based on the assumption of a large number of filled quantized states. Due to the low densities in two-dimensional semiconductor heterostructures this condition is only met in the small magnetic field limit $B \lesssim 1$ T.

The discussion is so far completely based on the quantization of the closed orbits of electrons on the constant energy surface of the system. However, as figure 8.3 shows, once the Fermi energy lies above the top of the miniband, the orbits at the Fermi energy are no longer closed. For these open orbits the area quantization is no longer valid. A detailed treatment of transport with open orbits [LAK56, LAK57, LP59, LP60] shows that the resistivity increases quadratically with the magnetic field in this situation. Thus, once the Fermi energy in the surface SL system is shifted into the first minigap, the resistivity oscillations are expected to vanish, being replaced by a quadratic increase in the resistivity.

In summary, the semiclassical theory gives the following predictions for the MR⁵ of the surface superlattice system: When the Fermi energy lies in the first miniband, the resistivity is constant as long as $\omega_c \tau < 1$ and it starts to exhibit periodic oscillations for magnetic fields that comply with $\omega_c \tau > 1$. Once the Fermi energy is pushed into the first minigap, the orbits at the Fermi energy are open and no oscillations occur. Instead, the resistivity is expected to increase quadratically.

The situation for open orbits is actually more complicated than described so far. The interpretation of studies of the de Haas-van Alphen effect (magnetic field dependent oscillations in the magnetization) in magnesium actually requires closed orbits which do

⁴Often R_D is expressed in the form $R_D = e^{-2\pi^2 k_B x / \hbar \omega_c}$. In this form, x has the meaning of a temperature, which is easily seen from a comparison to the argument of the sinh-factor of expression (8.13). Therefore, x is referred to as the Dingle temperature and is a temperature equivalent measure for the scattering in the system.

⁵The summarized effects actually apply to ρ_{xx} instead of the measured MR. However, it is shown shortly that these quantities are directly proportional in the presented surface SLs.

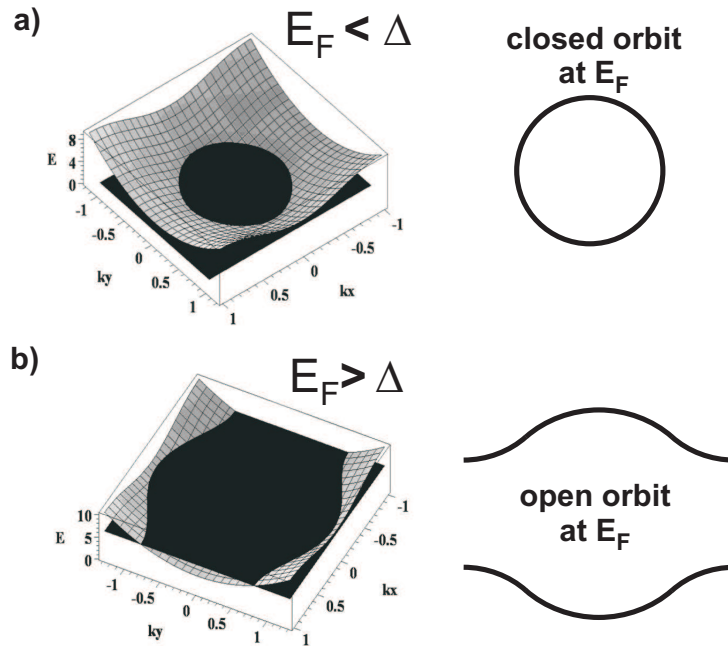


Figure 8.3: Full two-dimensional bandstructure of a surface superlattice. The Fermi level is shown by the black plane for the situation of being smaller (a) and larger (b) then the miniband width. The right sides of (a) and (b) show the resulting Fermi contours.

not exist on the Fermi surface of this element. The explanation for this inconsistency has been given in terms of magnetic breakdown [CF61, Blo62]. Magnetic breakdown states that for sufficiently strong magnetic fields electrons can tunnel from an orbit on one part of the Fermi surface to an orbit on another part which is separated by an energy gap E_g from the initial orbit. A similar situation can occur in the surface SL. Figure 8.4 shows the electron orbits at a number of energies inside and beyond the first miniband. All contours at $E < \Delta$ are closed as expected while those at $E > \Delta$ are open. However, when the magnetic field becomes large enough, electrons can tunnel between one arc of the open orbit into its mirror image so that they again follow a closed orbit. For these closed orbits the quantization according to the Onsager relation holds and leads again to oscillations in the resistivity. Therefore, once the system is in the regime of open orbits, the quadratic increase in the resistivity will last only up to a certain breakdown field B_0 before oscillations set in again. For metals the probability P of magnetic breakdown is expressed as

$$P = e^{-B_0/B} , \quad (8.15)$$

with the breakdown field approximately given by [Sho84, Chapter 7.2]

$$B_0 \sim \frac{B}{\hbar\omega_c} \frac{E_g^2}{E_F} . \quad (8.16)$$

Resistivity oscillations are expected for $B > B_0$. It is not immediately clear whether this

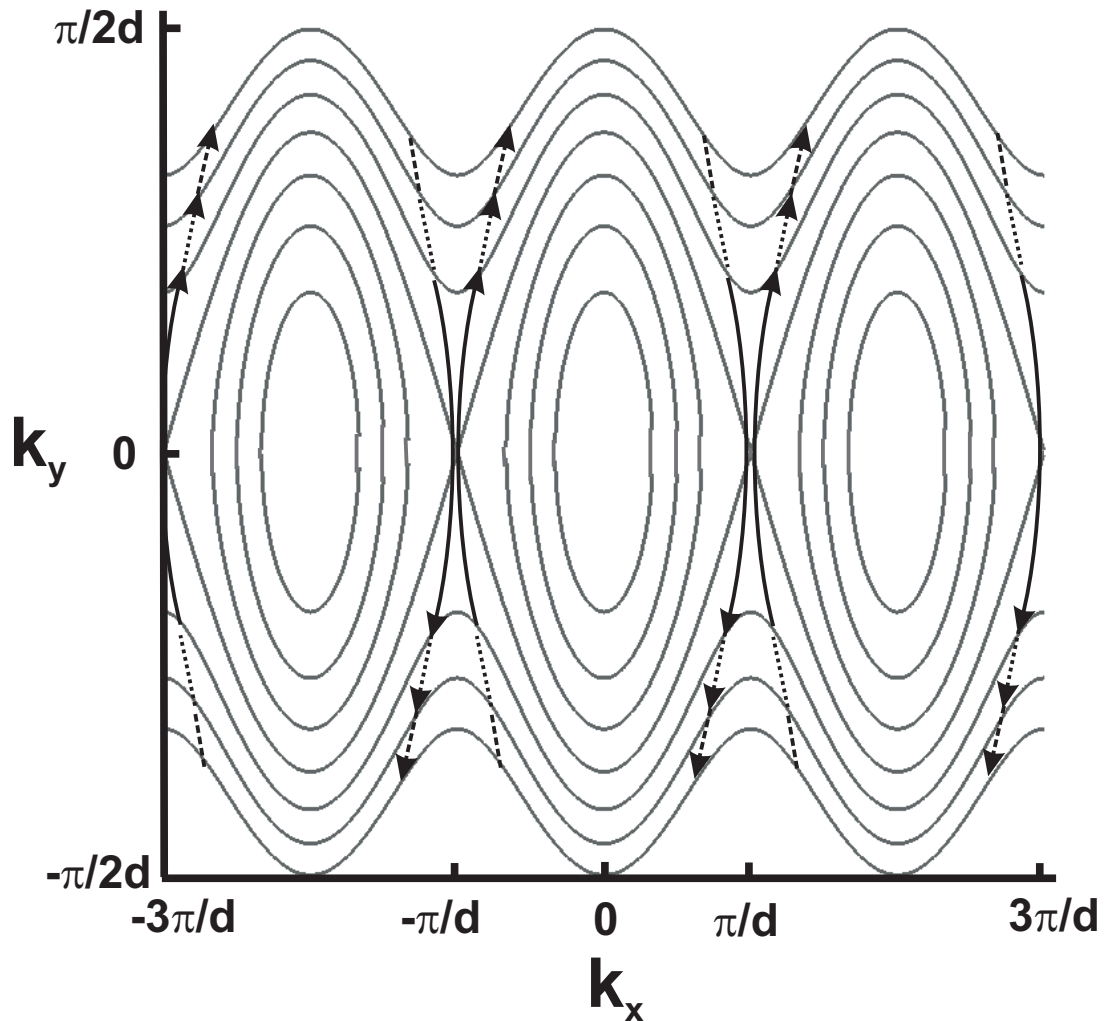


Figure 8.4: Fermi contours for energies ranging from 1 to 7 meV in 1 meV steps for a miniband of 4 meV width in the extended zone scheme. For energies smaller than the miniband width the orbits at the Fermi energy are closed (the four inner loops). Once the energies lie above the miniband (three outer trajectories), the Fermi contours extend infinitely along the k_x direction and are localized along the k_y axis. Since the real space trajectory is rotated by 90 degrees, electrons in real space are actually localized along the x direction and extend infinitely in the y direction. The localization leads to a quadratic increase of the resistivity along the x direction. When the magnetic field values become larger than some critical B_0 , electrons do not have to follow the open orbits but rather can tunnel, as indicated by the arrows, between the two branches of the same part of the Fermi contour. The resulting closed orbits are subject to the area quantization and an oscillatory resistivity results. A clockwise motion of the electrons is assumed.

formula can also be applied to the surface SL system. Unlike all other instances in which magnetic breakdown has been discussed so far,⁶ the modulation potential in the current structure is very strong. This results in an energy gap which is much larger than the Fermi energy and the cyclotron energy.

8.3 About contact geometries

Before a first interpretation of the experimental data is attempted, a relationship between the measured quantity (resistance) and the theoretically determined one (conductivity) needs to be established. The preferred geometry for magnetotransport measurements on planar two-dimensional electron systems is the Hall bar geometry as shown in figure 8.5(a). The sample is long and narrow and has extra contact pads (2,3,5,6) so that the longitudinal and the Hall voltage can be determined at pads different from those (1,4) at which the current through the sample is applied. It is assumed that there is no current

⁶Besides the context of the Fermiology of metals, magnetic breakdown has also been discussed for two-dimensional electron systems with weak periodic modulation [BDM⁺91, DWR⁺01, GCS⁺05] and also extensively for magnetotransport in organic superconductors [SST90, MSB⁺95, HCS⁺96, FZ98, FBGZ98].

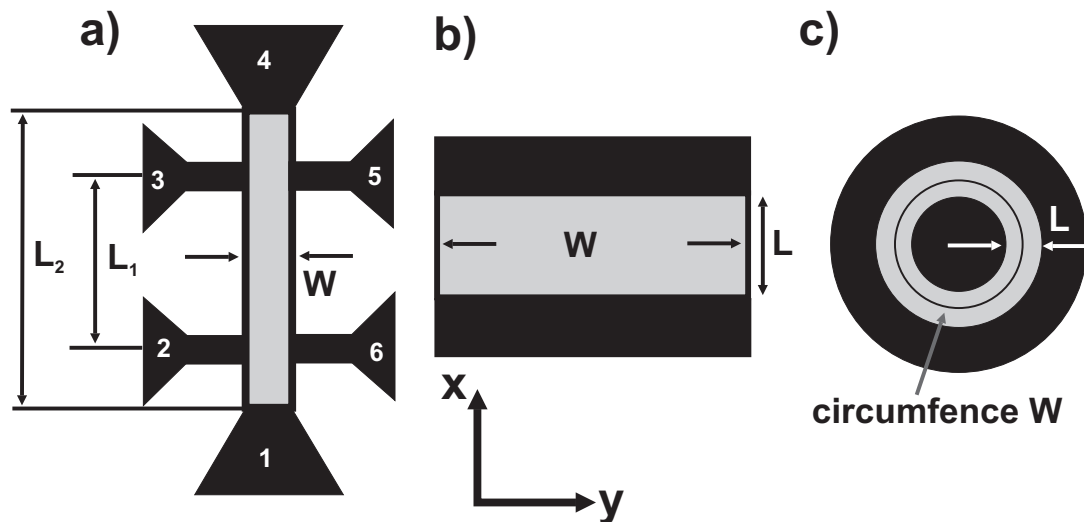


Figure 8.5: Comparison of three different experimental geometries for magnetoresistance measurements. Grey areas show the electron systems and black ones the contact pads. In (a) the Hall bar geometry is shown which is a long and narrow strip with a number of different contacts so that longitudinal and Hall voltage can be determined separately in a four-point measurement. In graph (b) the geometry of the surface SL is shown. It has the opposite limit of a wide and short electron gas area. Panel (c) shows the Corbino disc, which also satisfies the condition $W \gg L$, just like the surface superlattice. However, here the electrons can move infinitely in the lateral direction (i.e. along the circumference) whereas the surface superlattice eventually has barriers at the edges (left and right).

flow along the narrow direction. The relation between current density \vec{j} and electric field \vec{F} is then given by

$$\begin{pmatrix} j_x \\ 0 \end{pmatrix} = \begin{pmatrix} \sigma_{xx} & \sigma_{xy} \\ -\sigma_{xy} & \sigma_{yy} \end{pmatrix} \begin{pmatrix} F_x \\ F_y \end{pmatrix}. \quad (8.17)$$

From this equation the resistances

$$R_{23} = \frac{V_{23}}{I} = \frac{F_x L_1}{j_x W} = \frac{L_1}{W} \frac{\sigma_{yy}}{\sigma_{xy}^2 + \sigma_{xx}\sigma_{yy}} \quad (8.18)$$

$$R_{26} = \frac{V_{26}}{I} = \frac{F_y W}{j_x W} = \frac{\sigma_{xy}}{\sigma_{xy}^2 + \sigma_{xx}\sigma_{yy}} \quad (8.19)$$

$$R_{14} = \frac{V_{14}}{I} = \frac{F_x L_2 + F_y W}{j_x W} = \frac{\frac{L_2}{W}\sigma_{yy} + \sigma_{xy}}{\sigma_{xy}^2 + \sigma_{xx}\sigma_{yy}} \quad (8.20)$$

$$, \quad (8.21)$$

are calculated, which are, respectively, the four-point longitudinal resistance, the Hall resistance, and the two-point resistance. When the Fermi energy in the Quantum Hall regime lies between two Landau levels, then $\sigma_{xx} = \sigma_{yy} = 0$ and the four-point longitudinal resistance vanishes. The Hall resistance and the two-point resistance take on the geometry independent value of $1/\sigma_{xy}$ in this limit. This result is typical for two-point measurements which do not allow a separation between longitudinal and Hall resistance.

In contrast to the Hall bar geometry, the CEO sample structure, as shown in figure 8.5(b), has extensions in the opposite limit of $W \gg L$. Hence it seems reasonable to assume that now the electric field has only a component along the x direction. Then, the relation between current density \vec{j} and electric field \vec{F} is given by

$$\begin{pmatrix} j_x \\ j_y \end{pmatrix} = \begin{pmatrix} \sigma_{xx} & \sigma_{xy} \\ -\sigma_{xy} & \sigma_{yy} \end{pmatrix} \begin{pmatrix} F_x \\ 0 \end{pmatrix}. \quad (8.22)$$

From this, a two-point resistance of the form

$$R = \frac{U}{I} = \frac{F_x L}{j_x W + j_y L} = \frac{1}{\frac{W}{L}\sigma_{xx} + \sigma_{xy}} \quad (8.23)$$

is found. In the Quantum Hall limit, this expression again results in a resistance given by the geometry independent value of $1/\sigma_{xy}$. It is not quite obvious that the current is taken as the sum of the current densities along j_x and j_y . In this respect the geometry is very similar to the Corbino geometry (cf. figure 8.5(c)). The Corbino disc also has $W \gg L$ and the electric field is assumed to be completely radial. For this geometry the two-point resistance is completely determined by σ_{xx} [All88] and there is no Hall voltage drop in the measurement. For large magnetic fields perpendicular to the disc, the electrons flow perpendicular to magnetic and electric field ($\vec{F} \times \vec{B}$ -drift) and the measured resistance becomes infinite. In the CEO sample, however, this drift is terminated at the boundaries of the sample and the electrons will there cross the sample with skipping

orbits and contribute the term $j_y L$ to the current. Thus, the total current for large magnetic fields is the sum $j_x W + j_y L$. The validity of expression (8.23) has been tested experimentally [Ler04] by structuring a Hall bar on the cleavage plane of a CEO sample which then allowed the direct measurement of R , σ_{xx} , and σ_{xy} for known values of L and W . A comparison of formula (8.23) to the experimental data showed good agreement for magnetic fields above 1 T. Thus, the two-point resistance for $L \gg W$ is found by adding up voltages and for $W \gg L$ by adding up currents. In the semiclassical limit ($B \lesssim 1$ T), the σ_{xy} term can be neglected and the measured resistance R is directly proportional to $1/\sigma_{xx}$, which agrees with the assumptions made in the above discussions.

8.4 Experimental data in the semiclassical regime

The following data was taken on a final design surface superlattice with 12 nm wells, 3 nm barriers, a 5 nm CEW, and a gate barrier of 500 nm thickness. For linear response experiments the electric field across the surface SL is so small that pinch-off effects are of no concern. The data was taken in standard lock-in technique where a constant current is sent through the sample while the voltage across the device is recorded. The excitation current was set to 100 nA which limits the dissipated heat in the sample to less than 200 pW during a magnetic field sweep. The base temperature of the setup was about 350 mK.

Figure 8.6 shows the measured two-point resistance for a gate voltage of 1.5 V. In the magnetic field region between 0 and 0.4 T the resistance actually decreases. Beyond 0.4 T the resistance rises up strongly before it starts to saturate for magnetic fields larger than 4 T. It will be shown shortly that the 1.5 V gate bias is close to the threshold voltage beyond which electrons start to accumulate in the surface superlattice channel. For the resulting small electron density at this gate bias the electrons are strongly localized in the disorder potential of the system and the mobility is very low. It seems more reasonable to look at this situation as having a set of well separated parallel quantum wires. The electrons in each wire have a low mobility due to disorder and the probability to tunnel into a neighbouring wire is extremely small. This results in a very large resistance even at $B = 0$ T. The resistance decrease for small magnetic fields occurs for many gate voltages and will be the topic of the next section. Larger magnetic fields localize the electrons even stronger and lead to a quickly increasing resistance parallel to the set of quantum wires.

The situation changes when a higher gate voltage of 4 V is applied. The corresponding MR is shown in figure 8.7(a). While again a resistance decrease for magnetic fields below 0.4 T is observed, there occurs no dramatic resistance increase for higher fields. Instead, resistance oscillations appear which show an increasing amplitude with increasing magnetic field. A close examination shows that these oscillations already start at a B value of about 0.35 T. It is also noted that the zero field resistance has decreased by more than

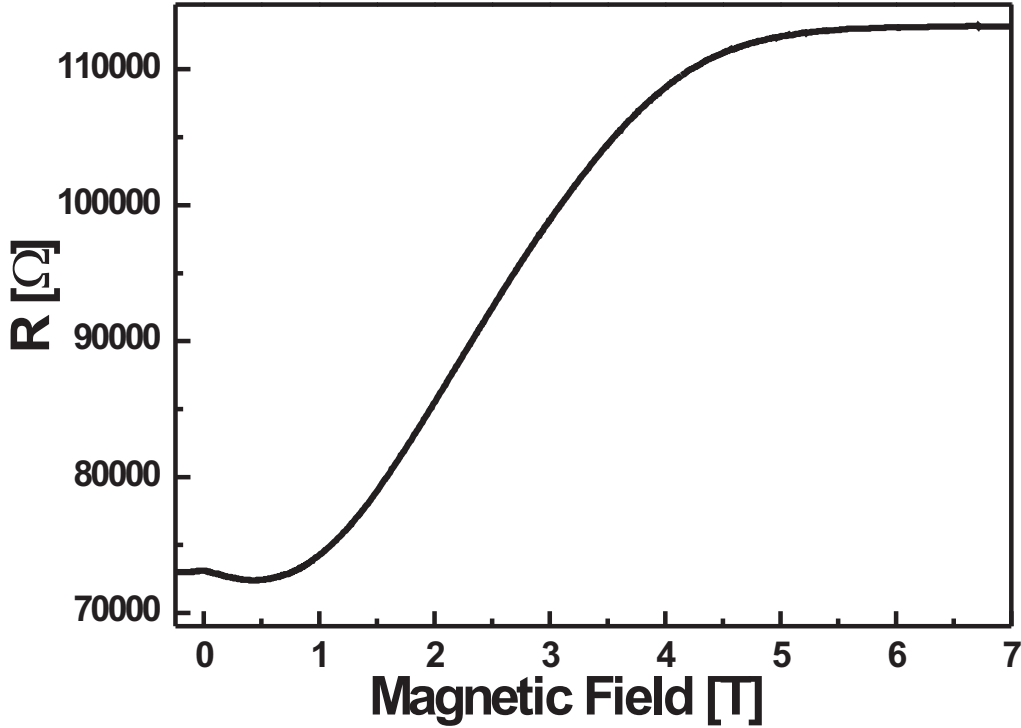


Figure 8.6: Magnetoresistance at 1.5 V gate voltage. The corresponding density is very small and the electrons in the system are strongly localized by the disorder potential. The low mobility of the carriers leads to a strong resistance increase with magnetic field.

two orders of magnitude. Now, the system resembles a two-dimensional electron gas with a mobility high enough so that resistance oscillations due to orbit quantization occur. The early onset of these oscillations indicates that the electrons at the Fermi surface follow closed orbits. When condition (8.11) is rewritten in the form

$$\mu \gg \frac{1}{B}, \quad (8.24)$$

a lower limit of about $30000 \text{ cm}^2/\text{Vs}$ can be deduced for the electron mobility μ . In order to compare the measured system properties to the bandstructure results of figure 3.6 in chapter 3, the density at each particular gate voltage must be determined. Following the semiclassical approach, the frequency of the oscillations with the inverse magnetic field can be evaluated through a Fourier transformation as shown in figure 8.7(b). Theoretically the frequency f is given as the inverse of the periodicity (8.10)

$$f = \frac{\hbar a(E_F)}{2\pi e}, \quad (8.25)$$

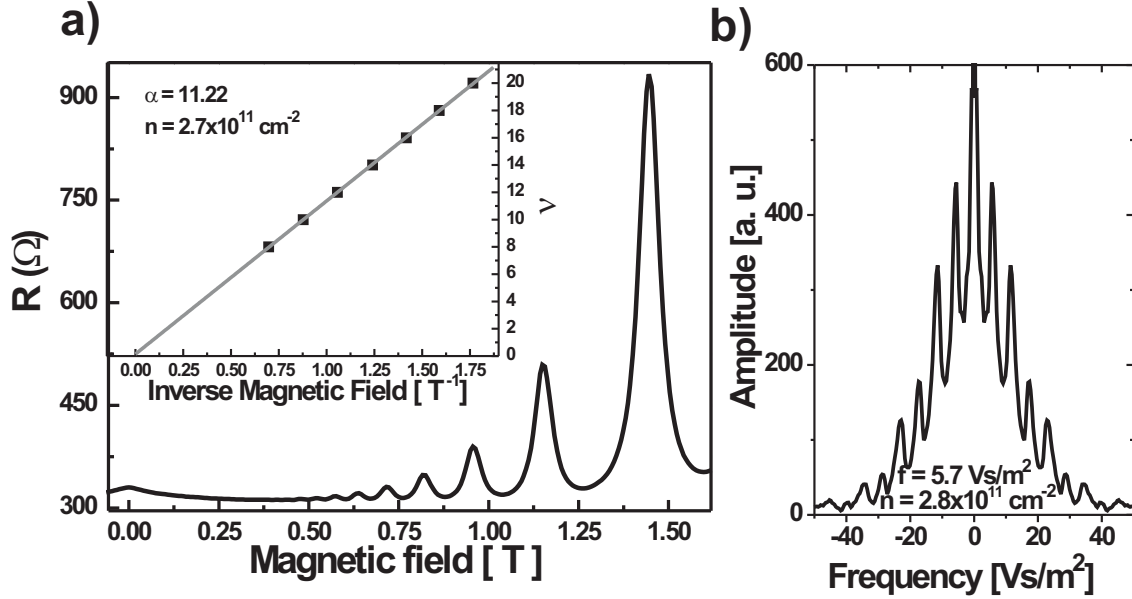


Figure 8.7: (a) Magnetoresistance at 4 V gate voltage. At this higher density the mobility has increased strongly and resistance oscillations are visible. The corresponding density of $2.8 \times 10^{11} \text{ cm}^{-2}$ can be deduced from a Landau plot as shown in the inset or from a Fourier transformation of the resistance to inverse magnetic field plot, depicted in (b).

which depends on the area of the electron orbit at the Fermi energy. The density n is found by summing up all states up to the Fermi energy. Making use of the relation (8.9) between DOS $D(E)$ and cyclotron mass $m(E)$ one finds

$$n = \int_0^{E_F} D(E) dE = \int_0^{E_F} \frac{m(E)}{\pi \hbar^2} dE = \frac{1}{2\pi^2} \int_0^{E_F} \frac{\partial a}{\partial E} dE = \frac{1}{2\pi^2} a(E_F), \quad (8.26)$$

where the general expression (8.8) for the cyclotron mass was inserted. From (8.25) and (8.26) a relation of the form

$$n = \frac{2e}{h} f \quad (8.27)$$

is found between electron density n and the frequency f of the resistance oscillations. The Fourier transform in figure 8.7(b) gives a frequency of 5.7 Vs/m^2 , which results in a density of $2.8 \times 10^{11} \text{ cm}^{-2}$. Alternatively, a so called Landau plot can be produced to find the electron density. Such a plot is shown in the inset of figure 8.7(a). It is assumed that at each maximum⁷ a fixed number of quantized energy levels are completely filled. If

⁷Actually, it is not known whether a maximum in the resistance or a minimum in the resistance corresponds to a complete filling of all occupied quantized states. However, the slope of the Landau plot, which determines the density, depends only on the magnetic field difference between the identical filling of two neighbouring quantized energy levels. Thus, it does not matter whether the system goes from n completely filled to $n - 1$ completely filled levels or from $n + 0.5$ to $n - 0.5$ filled levels.

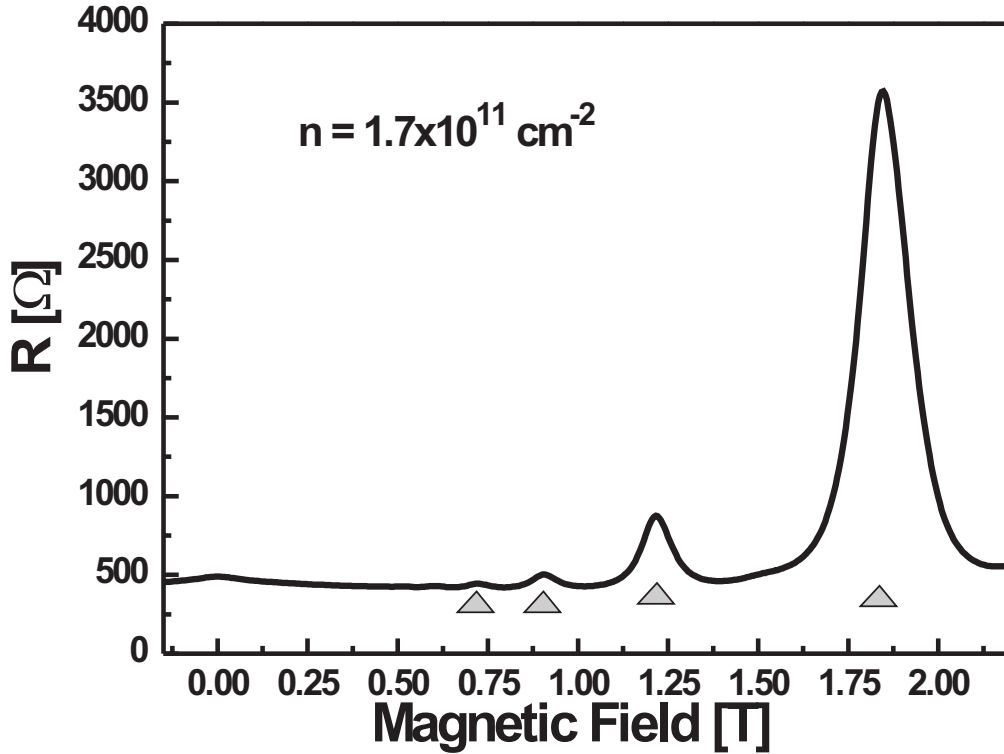


Figure 8.8: Magnetoresistance at 3 V gate voltage. Since for the corresponding density of $1.7 \times 10^{11} \text{ cm}^{-2}$ the Fermi energy is below the top of the miniband, the resistance oscillations are similar to those of an unmodulated two-dimensional electron gas. The gray arrows indicate the oscillations used to determine the density.

this number, the filling factor ν , is plotted versus the inverse magnetic field, it should lie along a straight line and the slope of this line determines the density. In order to establish which filling factor belongs to which peak, the condition that the filling factor goes to zero for vanishing inverse magnetic field is enforced. From the slope α of 11.22 Vs/m^2 a density of

$$n = \frac{e}{h}\alpha = 2.7 \times 10^{11} \text{ cm}^{-2} \quad (8.28)$$

is found. Thereby, use of the definition of the filling factor as the ratio between the electron density n and the degeneracy eB/h of each quantized state was made. Semiclassically this degeneracy is found by multiplying the k -space region between two neighbouring quantized orbits $\Delta a = 2\pi eB/h$ with the k -space density of states equal to $1/2\pi^2$. During the construction of the Landau plot each quantized orbit was counted twice due to the two possible, different spin alignments. Therefore, the slope of the Landau plot is twice

the frequency determined from the Fourier transform.

From figure 3.6 it is found that the position of the Fermi energy for a density of $2.7 \times 10^{11} \text{ cm}^{-2}$ is very close to the top of the miniband. For a gate voltage of 3 V the Fermi energy should then be somewhat below the top of the miniband. The corresponding MR is shown in figure 8.8. The increased zero B field resistance and a later onset of the oscillatory behavior indicate a lower mobility of the electron system. This is consistent with an expected mobility increase for two-dimensional electron systems when a larger density leads to stronger screening and therefore weaker scattering. From the period of the oscillations a density of $1.7 \times 10^{11} \text{ cm}^{-2}$ is deduced.

So far, the observed resistance oscillations seem to have shown no influence from the

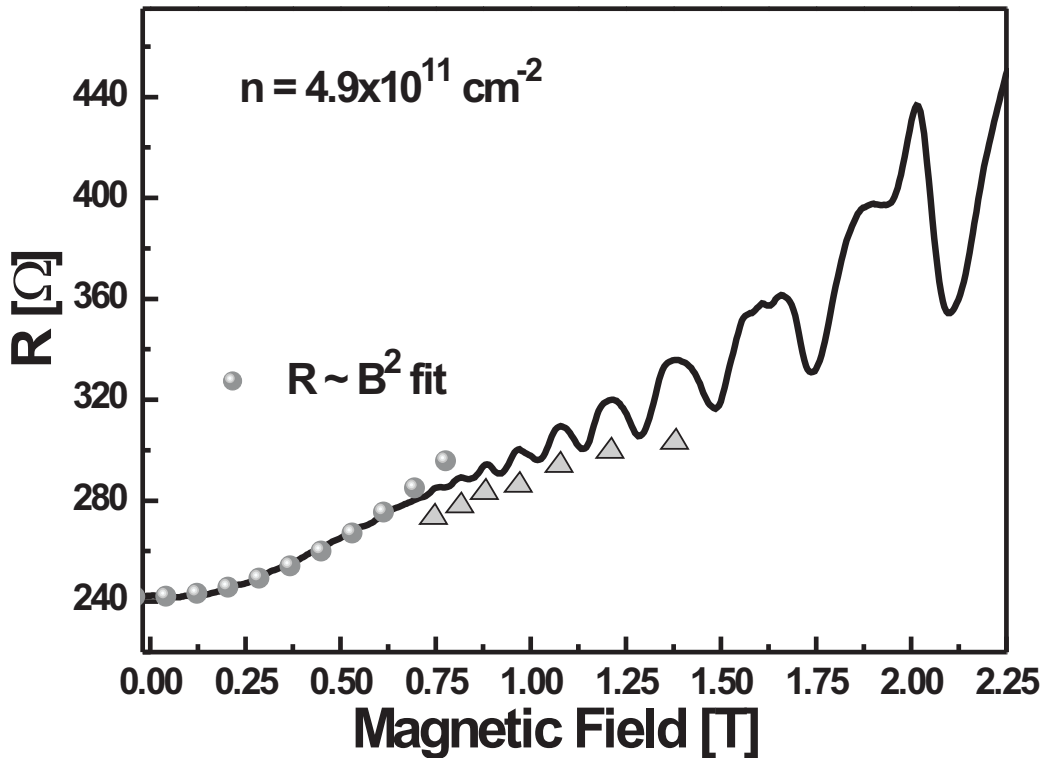


Figure 8.9: Magnetoresistance at 6 V gate voltage. For the corresponding density of $4.9 \times 10^{11} \text{ cm}^{-2}$ the Fermi energy lies considerably above the top of the miniband. This leads to a delayed onset of the resistance oscillations due to magnetic breakdown and to the appearance of double peak structures above 1.5 T. The gray arrows indicate the oscillations used to determine the density. The gray circles are a quadratic fit to the low magnetic field region.

periodic modulation of the two-dimensional electron system. This is in agreement with the earlier assessment that for energies within the miniband electrons can move along closed orbits which lead to the resistance oscillations which are shown in the last two figures. In order to observe transport changes due to the modulation potential, the Fermi level must be shifted deep into the gap above the miniband. This situation is shown in figure 8.9 where a gate voltage of 6 V is applied. A number of differences compared to the so far studied resistance traces are visible. First of all, it is noticed that the resistance decrease for small magnetic fields is absent. Also, the onset of the resistance oscillations is pushed up to about 0.7 T although an increased density should have further increased the mobility. This in turn should have led to a magnetic field value below 0.35 T for the onset of resistance oscillations. When the magnetic field becomes larger than 1.5 T, the

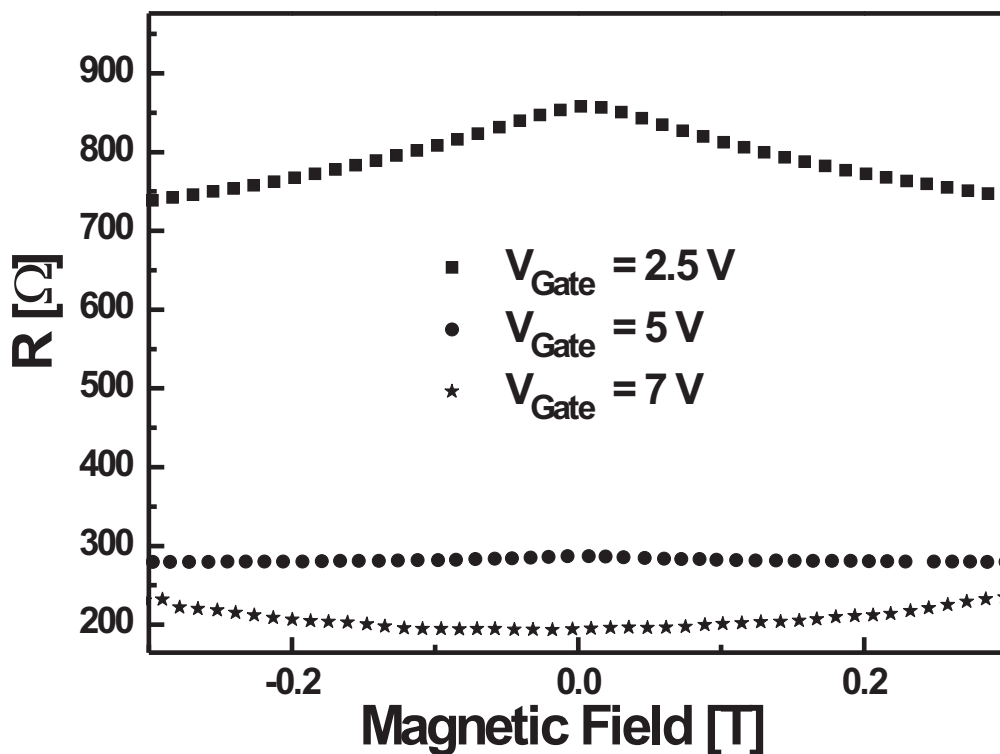


Figure 8.10: Magnetoresistance traces in a small interval around $B = 0$ T are shown at three different gate voltages. For Fermi energies well inside the miniband ($V_{\text{Gate}} = 2.5$ V) a strong negative magnetoresistance is observed. With increasing density the Fermi level rises above the miniband and the negative magnetoresistance becomes smaller ($V_{\text{Gate}} = 5$ V) and eventually vanishes ($V_{\text{Gate}} = 7$ V).

oscillations appear to take on a double peak structure which was not observable for smaller densities (cf. figure 8.8). From the oscillations below⁸ 1.5 T a density of $4.9 \times 10^{11} \text{ cm}^{-2}$ is found. The corresponding Fermi energy lies deep in the gap above the miniband (cf. figure 3.6).

The vanishing of the resistance decrease below 0.4 T is interesting and appears to be directly connected to whether the electrons move along closed or open orbits. The delayed onset for the resistance oscillations is actually expected from the earlier discussion. Since the electrons follow open orbits, the resistance should increase quadratically and oscillations are only expected to occur when there is an appreciable magnetic breakdown probability. The gray dots in figure 8.9 show a quadratic fit to the experimental data at low magnetic fields and confirm that the resistance indeed increases as expected for open orbits. The appearing double peak structure cannot be explained by semiclassical

⁸For the double peak structure it is unclear which peak should be chosen for the density evaluation.

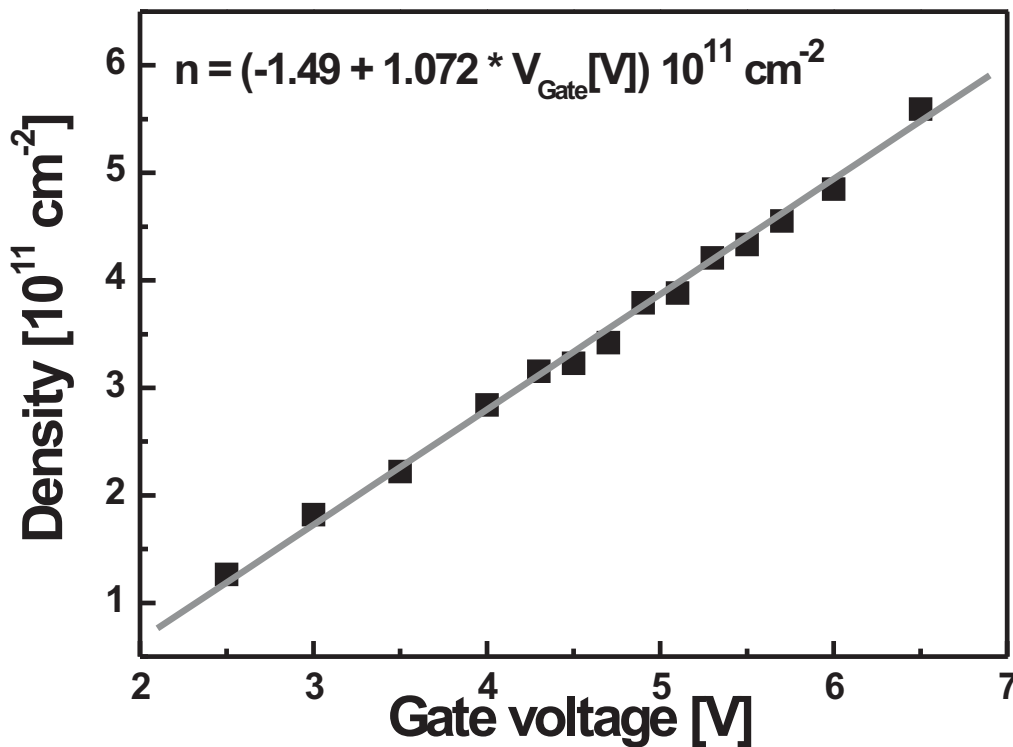


Figure 8.11: Density determined from magnetoresistance oscillations versus a number of applied gate voltages. The gray line is a linear fit to the data.

arguments. Its interpretation requires the application of a full quantum mechanical model. Such a discussion is presented in section 8.6.

In summary, the major changes observed when the Fermi level moves from inside the miniband into the gap above are a delayed onset of the resistance oscillations, the appearance of double peak structures and the suppression of the negative MR at small B values. The latter fact is again shown in figure 8.10 for three different gate voltages. It will be discussed in the next section in the framework of a quantum interference phenomenon referred to as weak localization. Weak localization is observed in relatively low mobility semiconductor structures at low temperatures. Since it depends on electrons being able to follow a closed real space orbit, its vanishing might be directly connected to the density dependent change from closed to open k-space orbits.

Figure 8.11 shows the densities extracted for a large number of applied gate voltages. The linear fit shows a voltage intercept (deduced from the fitted function in the graph) at 1.49 V for an empty surface SL channel. For gate voltages below this value the miniband lies far above the Fermi level of the system.⁹ When the gate is modeled as a plate capacitor, where the dielectric consists of AlGaAs with 32 percent Al ($\epsilon=11.5$), then a density-gate voltage relation of the form

$$n = \frac{CV}{eA} = \frac{\epsilon\epsilon_0}{ed}V = 1.27 \times 10^{11} \text{ cm}^{-2} V_{\text{Gate}}[\text{V}] \quad (8.29)$$

is found. Thereby, C is the capacitance of the gate, A is the active area of the gate, d is the thickness of the gate barrier and ϵ_0 is the dielectric constant. The resulting slope is close to the experimental value. Due to the GaAs in the well and in the cap of the AlGaAs barrier, ϵ is actually a little smaller and d a little larger so that theory and experiment come even closer. Also, the aluminum concentration might be slightly different from the assumed value. Nevertheless, the capacitor model nicely confirms the densities extracted from the resistance oscillations.

8.5 Weak localization

In the following discussion no attempt at a detailed and conclusive account of the weak localization phenomenon is made. The main aim is to establish a possible connection to the concept of closed and open k-space trajectories as discussed for the resistivity oscillations. Excellent introductions to this topic can be found in [Dat03, AL88, Ber84]. When a particle propagates between two points as shown in figure 8.12(a), it can do so along a number of different paths. Classically the path that the particle will take is determined by the condition that the action integral becomes extremal [Sch03, Chapter 2.6]. Quantum mechanically, however, the probabilities of all possible paths connecting point B to point A have to be summed up in order to calculate the probability of finding the particle at point B. Since these paths have different lengths, the phase of the particle

⁹This level is determined by the contact layers of the structure.

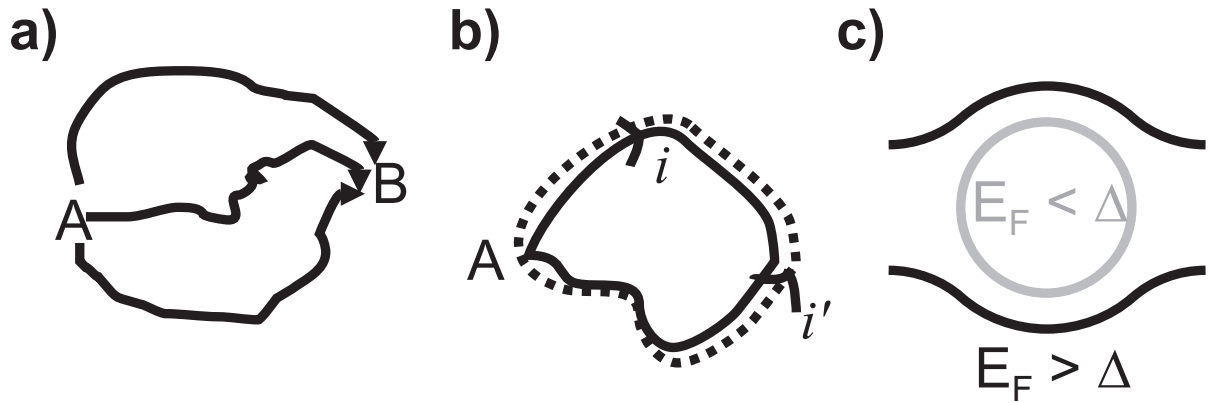


Figure 8.12: (a) Different paths connecting point A and B. (b) A pair of time-reversed paths connecting the same point A. (c) The Fermi contour of a surface superlattice system for Fermi energies within the first miniband (closed) and above this miniband (open).

wave will be different for the various possibilities. Therefore, one can approximate the probability of the particle being at point B by the sum over all the individual path probabilities. Interference terms between the different paths average to zero. However, the situation is different when the probability of the particle to return to point A is considered, which corresponds to the particle following a closed real space orbit (cf. figure 8.12(b)). Now, to every path i there exists a time reversed path i' of exactly the same length. These two paths will interfere constructively and lead to a doubled probability of finding the particle back at its starting point A. This enhancement of the back scattering of the particle, which is referred to as weak localization, effectively leads to a reduction of the diffusion constant and therefore to a smaller conductivity or, equally, larger resistivity.

When a magnetic field is applied, the particle wave picks up an additional phase $\Delta\phi$ along its path from one point to another. For a closed path this phase is proportional to the magnetic flux through the real space orbit area S_a ,

$$\Delta\phi \sim BS_a. \quad (8.30)$$

For the time-reversed path the phase is of opposite sign. Therefore, the interference of both paths will depend oscillatory on the magnetic field value. Since the areas of all possible real space orbits are different, these orbits will also have different phase oscillation periods. Thus, on average, the coherent back scattering probability decreases monotonically with the magnetic field. A suppressed coherent back scattering leads to a larger conductivity and therefore a reduced resistivity. It is this negative MR that is measured in the experiment.

In order to observe the enhanced back scattering in form of a constructive interference between path and time-reversed path, the phase information of the particle wave must not be lost along the path. Since such a loss of phase coherence is brought about

by inelastic scattering,¹⁰ it is required that the inelastic scattering rate is much smaller than that of elastic scattering events. Therefore, weak localization is observed in relatively low-mobility systems (due to strong elastic scattering) at low temperatures (long inelastic lifetimes due to a very low number of phonons). In surface SL systems, the strong elastic scattering is provided by the SL interfaces. It is interesting to note that in all formerly studied two-dimensional electron systems with a strong, short-period modulation, realized by cleaved-edge overgrowth, no weak localization was observed¹¹ [SPB⁺91, MRT⁺00, DLW⁺00, Deu01].

From this short introduction it follows that there are two possible explanations for the disappearance of the weak localization in the high density regime of the surface SL system. One of these is based on the assumption that the increased density leads to a very strong increase in the transport mobility. Then, the particle wave could have lost its phase coherence before it returns to its origin and no coherent back scattering occurs. The other explanation assumes that an electron at the Fermi level can only proceed along a closed real space orbit when it moves along states which have both positive and negative k_y values. While this is readily achieved when the Fermi energy lies below the top of the miniband, it requires scattering between the two different parts of the Fermi contour once the Fermi energy moves into the gap above the miniband (cf. figure 8.12(c)). The probability for such scattering events will decrease rapidly once the Fermi energy is significantly beyond the top of the miniband since the scattering then involves a larger and larger momentum change. Thus, with the change from a closed to an open Fermi contour, weak localization would be continuously suppressed. If this explanation were confirmed, it would provide further evidence for the validity of the band structure which was used as input for the discussion about Bloch oscillations. An experimental indication that the disappearance of the weak localization is indeed due to the change from closed to open k-space orbits is provided by the fact that the MR for a sample with a 1.6 nm CEW, shown in figure 8.13, also exhibits the same suppression for large densities. The electrons in this sample have a much lower mobility for all densities than a sample with a 5 nm CEW due to the much smaller distance to the modulation potential. It seems unlikely that the 1.6 nm CEW sample has a higher mobility at high densities than the 5 nm CEW one at low densities. Therefore, the observed suppression of weak localization is more likely due to the crossover from closed to open orbits than due to an increased transport mobility.

¹⁰In this context the term inelastic does not only involve electron-phonon interactions as discussed in the high electric field measurements of the preceding chapters. The term inelastic rather refers to all scattering processes involving fluctuating scatterers like phonons, electrons or impurities with internal degrees of freedom. In contrast, rigid scatterers (impurities without internal degrees of freedom, interfaces) will not affect the definite phase relationship between different trajectories.

¹¹It is unlikely that the growth conditions play a major role in this since the estimated mobilities for all samples are in the range between 50000 – 100000 cm²/Vs, which is a typical value for two-dimensional semiconductor structures in which weak localization has been observed.

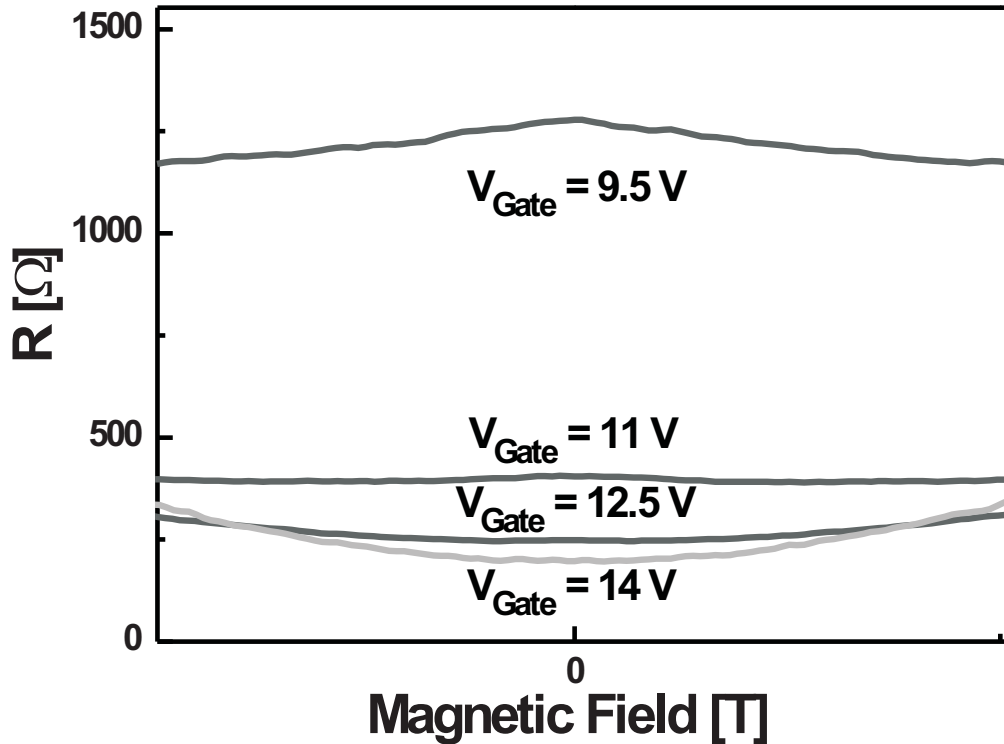


Figure 8.13: Magnetoconductance traces in a small interval around $B = 0$ T for a sample with a 1.6 nm wide cleaved-edge well, shown at four different gate voltages. For Fermi energies well inside the miniband ($V_{\text{Gate}} = 9.5$ V) a strong negative magnetoresistance is observed. With increasing density the Fermi level rises above the miniband and the negative magnetoresistance becomes smaller ($V_{\text{Gate}} = 11$ V, $V_{\text{Gate}} = 12.5$ V) and eventually vanishes ($V_{\text{Gate}} = 14$ V). The crossover from closed to open k -space orbits occurs approximately at about $V_{\text{Gate}} = 10$ V.

8.6 Quantum mechanical description

So far, an interpretation of the MR data of the surface SL structures in terms of oscillations in the DOS has been given. These oscillations appear when the Bohr-Sommerfeld quantization rule is applied to the semiclassical electron orbits in a magnetic field. In the high magnetic field regime, when only a small number of quantized energy levels are occupied, the semiclassical arguments become invalid. Basically, the cyclotron energy is no longer small compared to the Fermi energy. In this regime, the corresponding quantum-mechanical problem must be solved directly. This will be done in the following discussion.

First, the problem is formulated in the framework of the tight-binding approximation.¹² Then, the resulting equation is solved numerically to find the eigenenergies of the system. From these eigenvalues the DOS is computed and a relation between the DOS and the conductivity tensor is established by the solution of the Kubo formula.

Assume that the modulation potential $V(x)$ is given along the x -axis with a periodicity d . In this geometry, in which the motion along the y -axis is unperturbed, the Landau gauge $\mathbf{A} = (0, Bx, 0)$ is employed since the momentum $\hbar k = -i\hbar \frac{\partial}{\partial y} + eBx$ along the y -direction is then a good quantum number. The corresponding eigenfunctions are plane waves along the wires of the surface superlattice. According to these assumptions, the hamiltonian of the system can be written as

$$\hat{H} = \frac{1}{2m}(\mathbf{p} + e\mathbf{A})^2 + V(x) = \frac{\hbar^2}{2m} \left(-i \frac{\partial}{\partial y} + \frac{eBx}{\hbar} \right)^2 + \frac{p_x^2}{2m} + V(x) . \quad (8.31)$$

Since the translational invariance along the y -direction has been preserved, the wavefunction $\Psi(x, y)$ in the corresponding Schrödinger equation $\hat{H}\Psi(x, y) = E\Psi(x, y)$ can be written as a product state with a plane wave along the y axis,

$$\Psi(x, y) = \frac{1}{\sqrt{2\pi}} \exp(iky) \psi(x) . \quad (8.32)$$

The spectrum of the resulting Hamiltonian

$$\hat{H} = \frac{\hbar^2}{2m} \left(k + \frac{eBx}{\hbar} \right)^2 + \frac{p_x^2}{2m} + V(x) \quad (8.33)$$

is periodic in x since the magnetic field induces only a shift of the k -space origin. Therefore, only k values which comply with $|k| < eBd/2\hbar$ have to be considered. In order to make further progress, $\psi(x)$ is expanded in terms of the ground state $\phi(x - jd)$ of an electron in the j -th potential well,

$$\psi(x) = \sum_j a_j^\beta(k) \phi(x - jd) , \quad (8.34)$$

with $\phi(x - jd)$ being centered at the position jd . β labels the different discrete eigenstates (Landau levels) which occur for each k . The resulting problem is then solved in the tight-binding approximation. In this limit, the vector potential $A_y = Bx$ is replaced with the center position value $A_y = Bjd$ and all other x dependent parts are contained in the tight-binding condition

$$\langle \phi(x - jd) | H_x | \phi(x - qd) \rangle = t \delta_{j, q \pm 1} , \quad (8.35)$$

¹²The high electric field study in the preceding chapters was also based on this approximation and the results found there justify its application here.

where the $\phi(x - jd)$ were assumed to form an orthonormal basis with $\langle \phi(x - jd) | \phi(x - qd) \rangle = \delta_{j,q}$ and t is negative.¹³ The matrix representation of the tight-binding hamiltonian

$$\hat{H}_{jq} = \frac{\hbar^2}{2m} \left(k + \frac{eBjd}{\hbar} \right)^2 \delta_{jq} + t\delta_{j,q\pm 1} \quad (8.36)$$

converts the problem of finding the energy eigenvalues $E^\beta(k)$ of the original hamiltonian to the numerical solution of the set of equations

$$\sum_q \hat{H}_{jq} a_q^\beta(k) = E^\beta(k) a_j^\beta(k) , \quad (8.37)$$

with one such equation for every j . The solutions of the set of equations (8.37) are, for $|k| < deB/2\hbar = K/2$, mathematically identical to those for the Mathieu problem, given by the differential equation

$$-\frac{\hbar^2}{2m} \frac{\partial}{\partial y} \xi(y) - 2|t| \cos(Ky) \xi(y) = E \xi(y) , \quad (8.38)$$

when it is solved with the ansatz

$$\xi(y) = \sum_j a_j^\beta(k) e^{i(k+jK)y} . \quad (8.39)$$

This is easily seen when $\cos(Ky)$ is written as $\cos(Ky) = \frac{1}{2} (e^{iKy} + e^{-iKy})$. Then, a multiplication of the Mathieu problem by $e^{-i(k+qK)y}$ followed by an integration over y leads directly to equation (8.37).

Thus, the eigenstates of the two-dimensional electron system with a strong, short-period modulation in the tight-binding approximation are identical to those of the Mathieu problem. Although the numerical calculation is similar, additional qualitative information can be extracted from this identity. The Mathieu problem corresponds to the one-dimensional Schrödinger equation for a particle subjected to the periodic potential $W(y) = -2|t| \cos(Ky)$. The connection between $W(y)$ and the periodic potential $V(x)$ of the superlattice lies in the hopping or overlap parameter $|t| = \Delta/4$. Although the assumption of an infinite extension of the system along the y -axis is implicitly assumed in the correspondence argument with the Mathieu equation, only k -values according to $|k| < deB/2\hbar$ need to be considered due to the periodicity of the potential $W(y)$.

The spectrum of the Mathieu problem depends on the three energy scales given by the periodic potential $W(y)$ (in terms of $|t|$), the effective cyclotron energy $\hbar\omega_c$ (see below) and the energy E . Assume first that the cyclotron energy is small compared to the other two energies. Then, when energies close to the bottom of the miniband ($E \approx -2|t|$) are

¹³In this section the zero energy level is set at $E = -\Delta/2 = -2|t|$ in order to comply with the solutions from the provided computer programs which were programmed assuming this energy definition.

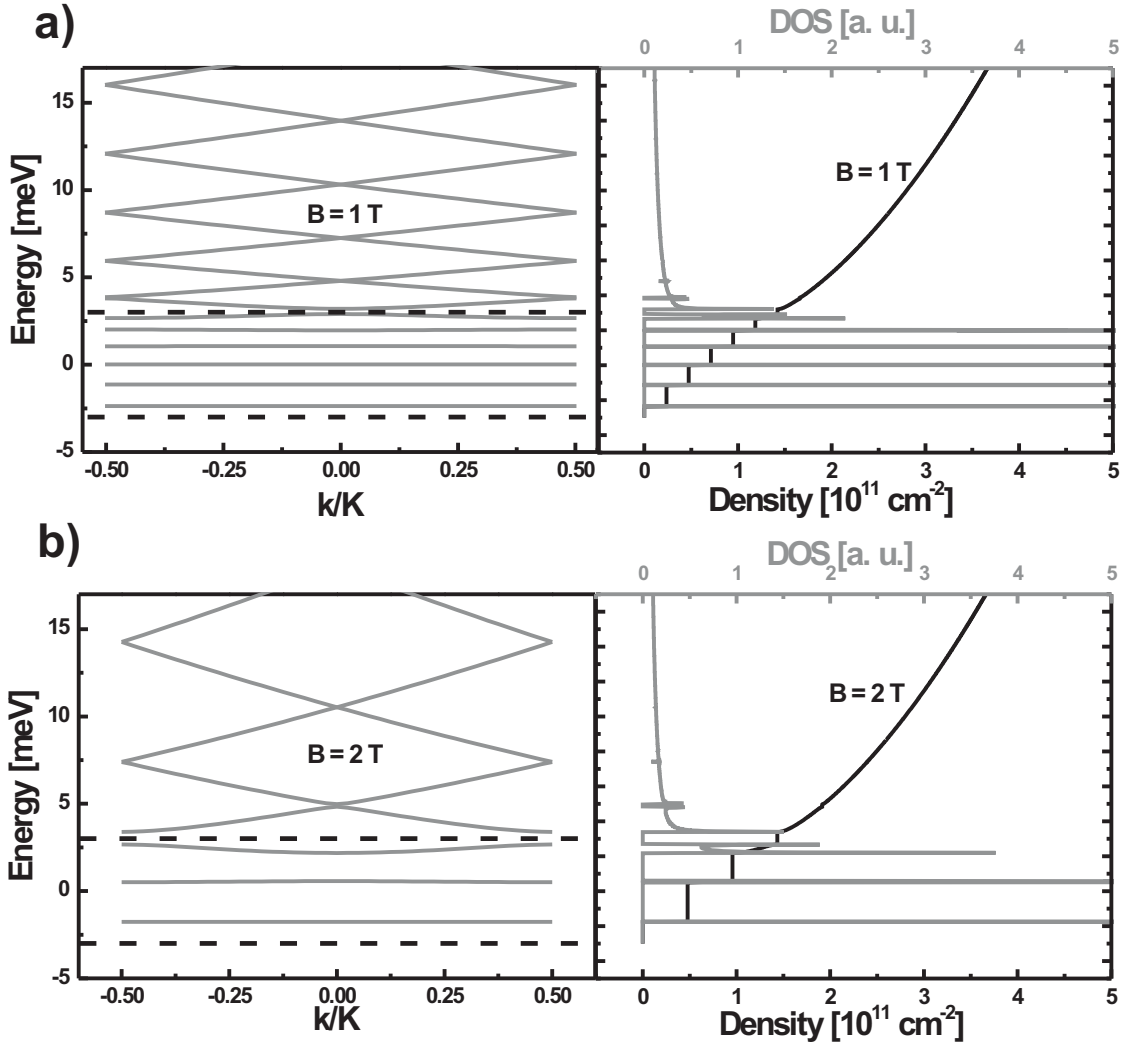


Figure 8.14: Energy eigenstates and corresponding density of states, and density for a two-dimensional electron system subject to a strong, short-period modulation, calculated within the tight-binding approximation. The lowest miniband is assumed to have a width of 6 meV and extends from -3 meV to $+3$ meV. In (a) the magnetic field was assumed to be 1 T and in (b) it was 2 T.

studied, it is convenient to expand the potential $W(y)$ around $y = 0$. An electron then essentially moves in a harmonic oscillator potential of the form

$$W(y) \approx 2|t| \left(-1 + \frac{1}{2} \left(\frac{deBy}{\hbar} \right)^2 \right). \quad (8.40)$$

The eigenstates of this problem are equidistantly spaced energy values with a separation $\hbar\omega_c$. This is found by equating $W(y)$ to the harmonic oscillator potential $\frac{1}{2}m\omega_c^2 y^2$, where

$\omega_c = eB/\sqrt{m_x m_y}$ is identified with the cyclotron energy for effective masses of $2\hbar^2/\Delta d^2$ and m along the x and y axis, respectively. Thus, in this limit the Landau level quantization is recovered, which is in agreement with the assessment that the system behaves like a free two-dimensional electron system (with changed effective mass) when the energy lies deep within the miniband. In contrast, for very large energies E the periodic potential $W(y)$ is only a small perturbation. Thus, the spectrum should resemble that of a free one-dimensional particle, however, with small gaps at the magnetic Brillouin zone center¹⁴ $k = 0$ and at the magnetic Brillouin zone boundaries $k = \pm deB/2\hbar$.¹⁵ The separation between the two-dimensional and one-dimensional character of the system is found at energies close to the top of the miniband.

The left part of figure 8.14(a) shows the corresponding numerical analysis at $B = 1$ T. Indeed, for energies much smaller than the strength of $W(y)$ (which is equal to a position far below the top of the miniband) the eigenenergies are constant and equidistant along the magnetic Brillouin zone $|k| < deB/2\hbar$. For energies much larger than $W(y)$ (or, equally, far above the miniband) the spectrum resembles that of a free electron with small (they cannot be resolved graphically) gaps at the magnetic Brillouin zone boundaries. The corresponding DOS, shown in the right part of figure 8.14(a), equally reflects the transition from a 2D to a 1D system when the energy is increased. For small energies the peaks of the individual Landau levels appear. For large energies the typical $1/\sqrt{E}$ -shape of the DOS for a free one-dimensional system is recovered. The transition clearly occurs at energies close to $E = 2|t|$ (the top of the miniband).

When the magnetic field is increased to $B = 2$ T, the situation is similar. As figure 8.14(b) shows, there are still Landau level like states at low energies, whereas the spectrum of a free electron is found for large energies. However, there are fewer eigenstates that show no dispersion (which are flat) and the gaps between the eigenstates have increased in strength (although the small gaps at the zone boundaries and at the zone center can still not be resolved graphically).

The situations for large magnetic fields of $B = 5$ T and $B = 12$ T are shown in figures 8.15(a) and (b). Even the lowest eigenstate has developed an inner dispersion since its energy is no longer small compared to the potential $W(y)$. The eigenstates at large energies look even more like the free-electron parabola. The gaps in the high energy regime have increased to a value so that they can now be resolved graphically. Nevertheless, these gaps are smaller than the cyclotron gaps in a free two-dimensional electron system with identical parameters. The widths of the Landau bands now greatly exceed the energetic broadening introduced by disorder and, therefore, the Landau bands take up large parts of the DOS gaps that would be there for an unmodulated system. The DOS of the broad Landau bands shows the one-dimensional $1/\sqrt{E}$ behavior, however, with strong peaks at the edges of the bands where the dispersion is flat. These peaks will appear in the resistance measurements once the Landau bands exceed a certain minimum width. Later

¹⁴There is no such gap for the lowest band.

¹⁵A detailed description of the origin of those well known gaps can be found in [AM76, Chapter 9].

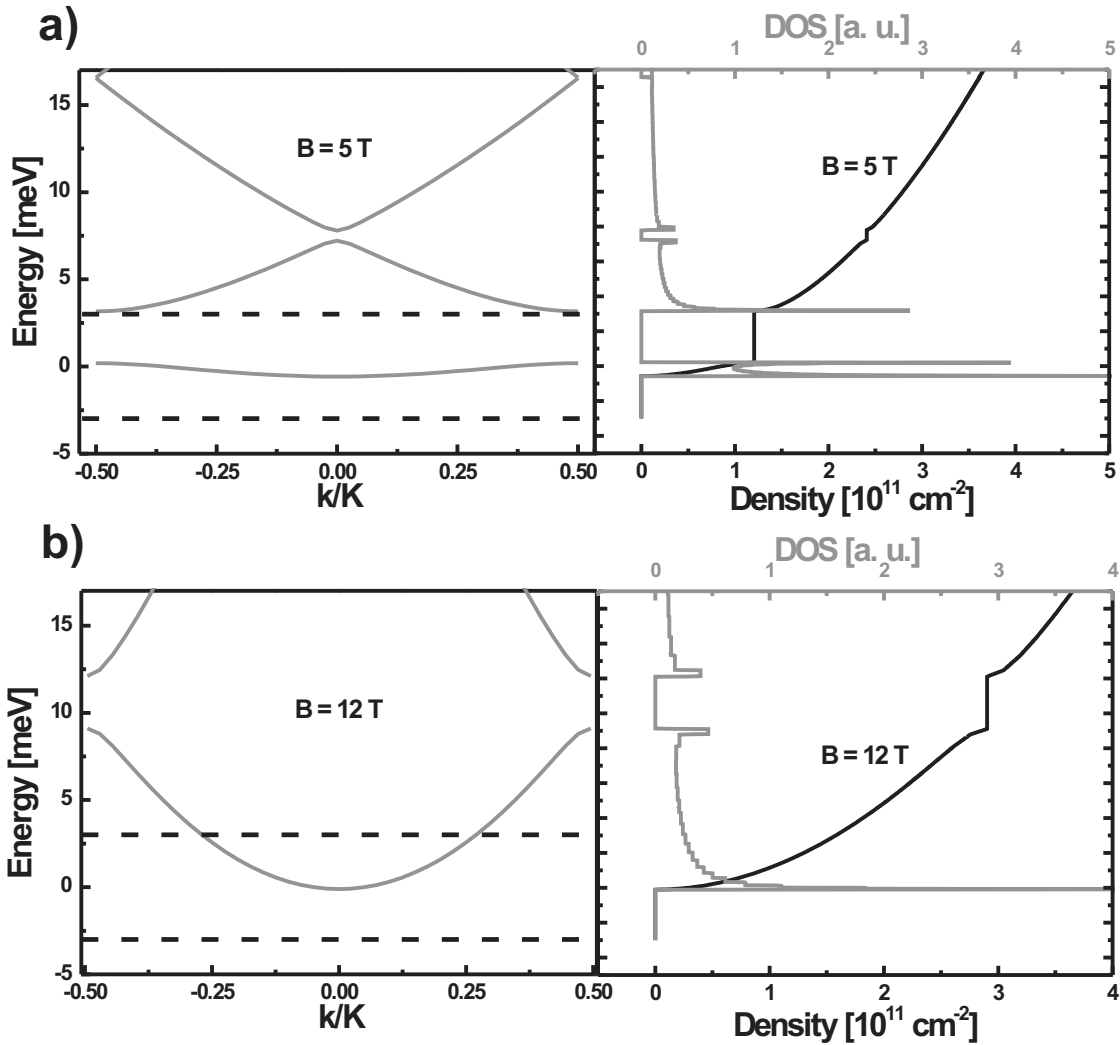


Figure 8.15: Energy eigenstates and corresponding density of states, and density for a two-dimensional electron system subject to a strong, short-period modulation, calculated within the tight-binding approximation. The lowest miniband is assumed to have a width of 6 meV and extends from -3 meV to $+3$ meV. In (a) the magnetic field was assumed to be 5 T and in (b) it was 12 T.

on, they will be referred to as the edge or side peaks in the DOS of a Landau band.

Assuming a direct reflection of the DOS in the resistance measurements, a number of features should appear in the experimental data. Sitting at a fixed small magnetic field, conventional SdH oscillations should be observed as long as the Fermi energy is smaller than the miniband width. Once the Fermi energy moves into the gap above the miniband, these oscillations should disappear since the tiny gaps in the spectrum will be completely smeared out by the disorder-induced energetic broadening. In the intermediate magnetic

field regime (about 3 – 5 T) the oscillations at small Fermi energies should still resemble the SdH oscillations since the energetic broadening will mask the DOS side peaks due to the small inner dispersion of the Landau levels. At Fermi energies above the top of the miniband, however, a substantial change in the oscillations can be expected. The widths of the Landau levels increases strongly and the DOS peaks at the edges of these broad bands should eventually be resolved in the measurement. Moreover, in the small gaps ($\sigma_{xx} = 0$) between the free-electron-like states the resistance should approach the plateau values of the Quantum Hall regime (cf. equation (8.23)). However, the widths of these gaps shrinks again when the Fermi energy moves deeper into the gap above the miniband and the contributions from the Hall resistance should then disappear. This vanishing of the cyclotron gap at very large Fermi energies (compared to the miniband width) is one fundamental change introduced by the strong, short-period modulation. At very large magnetic fields all observed oscillation peaks should be rather broad and the cyclotron gap should survive the longest since the corresponding gaps in the DOS are the largest. Before a comparison of the experimental data with the DOS presented in figures 8.14 and 8.15 is possible, however, relations between the conductivity tensor elements and the DOS of the system have to be established. They are given by

$$\sigma_{xx} = \frac{4\pi\Gamma}{d} \frac{e^2}{h} D(E) \sum_{\beta' \neq \beta} (\langle \psi(k, \beta') | x | \psi(k, \beta) \rangle)^2 \quad (8.41)$$

$$\sigma_{xy} = e \frac{\partial n(E)}{\partial B} + \frac{4\pi\hbar e B}{dm} \frac{e^2}{h} D(E) \sum_{\beta' \neq \beta} (\langle \psi(k, \beta') | x | \psi(k, \beta) \rangle)^2 \quad (8.42)$$

and are solutions to the Kubo formula [Str82], a result of the quantum linear response theory. Γ is a measure for the strength of the scattering in the system and the $\psi(k, \beta)$ are the wavefunctions defined in expression (8.34).

Equation (8.41) states that the longitudinal conductivity is directly proportional to the DOS. Numerical evaluation of the formula showed that the matrix elements do not significantly change this behavior. The direct proportionality of σ_{xx} to Γ states that the longitudinal conductivity vanishes without scattering.

The Hall conductivity σ_{xy} consists of two terms. The first one ensures the Hall quantization when the Fermi energy lies in a gap between Landau levels ($\sigma_{xx} = 0$). This can be seen by writing the density in terms of the filling factor ν (where spin-split states are counted)

$$n = \nu \frac{eB}{h} . \quad (8.43)$$

In this form the expression $e \frac{\partial n(E)}{\partial B}$ results in the Hall conductivity $\nu e^2/h$ at constant filling. The second term of σ_{xy} is again proportional to the DOS and looks very similar to the expression for σ_{xx} , but it does not depend on Γ . Recalling equation (8.23)

$$R = \frac{U}{I} = \frac{F_x L}{j_x W + j_y L} = \frac{1}{\frac{W}{L} \sigma_{xx} + \sigma_{xy}} , \quad (8.44)$$

which connects the measured resistance to the individual contributions of the conductivity matrix, the resistance is dominated by σ_{xx} as long as the Fermi energy is not very close to or inside a gap between eigenstates. The reason for this is the geometric contribution of W/L which strongly enhances the σ_{xx} part of the resistance. Only when σ_{xx} vanishes (inside a gap) or becomes very small (very close to a gap), the contribution from σ_{xy} becomes important. Thus, once gaps in the DOS are experimentally resolved, the measured resistance should tend towards the quantized Hall resistance values. Otherwise, the resistance essentially looks like the scaled inverse of the DOS. A maximum in the DOS leads to a large conductivity and therefore to a small resistance value (especially for this short and wide geometry). It is noted here that the experimental results for the MR of a two-dimensional electron system with a strong, short-period modulation (measured in the same geometry) reported in [Deu01, VSD02] do not seem to concur with the above resistance equation. Resistance values far above the Hall resistance (up to more than 100 k Ω) are found in between Hall plateaus with quantized resistance. These large resistance values suggest that the system is in an insulating state between two gaps of the DOS. This is, however, a clear contradiction to what should be expected. When the Fermi energy is inside a Landau band (between two DOS gaps), the system should be conducting and should show a very small resistance due to the wide and short sample geometry.

In the following, the experimental data already presented in the semiclassical discussion is analyzed with respect to the quantum model developed in this section. Figure 8.16 shows the measured magnetoresistance up to $B = 13$ T for gate voltages of 3.5 V, 5 V, and 7 V, which, respectively, correspond to $E_F < \Delta$, $E_F \approx \Delta$ and $E_F \gg \Delta$.

The oscillations observed in the resistance data for 3.5 V gate voltage look similar to those of a free two-dimensional electron system. The mobility in the sample is large enough so that the spin-split states¹⁶ with $\nu = 1, 3, 5$ are resolved, as indicated in the figure and its inset. The maxima at small magnetic fields (no real gap between Landau levels due to disorder broadening) are due to minima in the DOS when the Fermi energy lies between two broadened Landau levels. At larger magnetic fields the maxima contain large contributions from the Hall resistance, since the gaps between Landau levels are almost fully developed. Nevertheless, these gaps are narrower than those typical for a two-dimensional electron gas of equal mobility. The latter usually show very wide plateaus in the gaps between Landau levels. The small width of the maxima observed at

¹⁶Spin split states in two-dimensional GaAs heterostructures are only observed due to a strong increase of the effective g-factor through electron-electron interaction. Essentially, the exchange energy term dominates the total energy when two spin-split Landau levels are half filled. Therefore, the states at which the electrons completely fill one of the two levels (having the same spin) are much further separated energetically than it would be the case for bare Zeeman splitting. If the mobility is then large enough, or better the Landau level disorder broadening small enough, the spin-split states are resolved in the MR data. The additional exchange energy contribution is usually written in a formally similar way to the Zeeman energy term, through the introduction of an additional g-factor. Then, the total spin dependent energy can be expressed in terms of an effective Zeeman energy, however, with an enhanced effective g-factor.

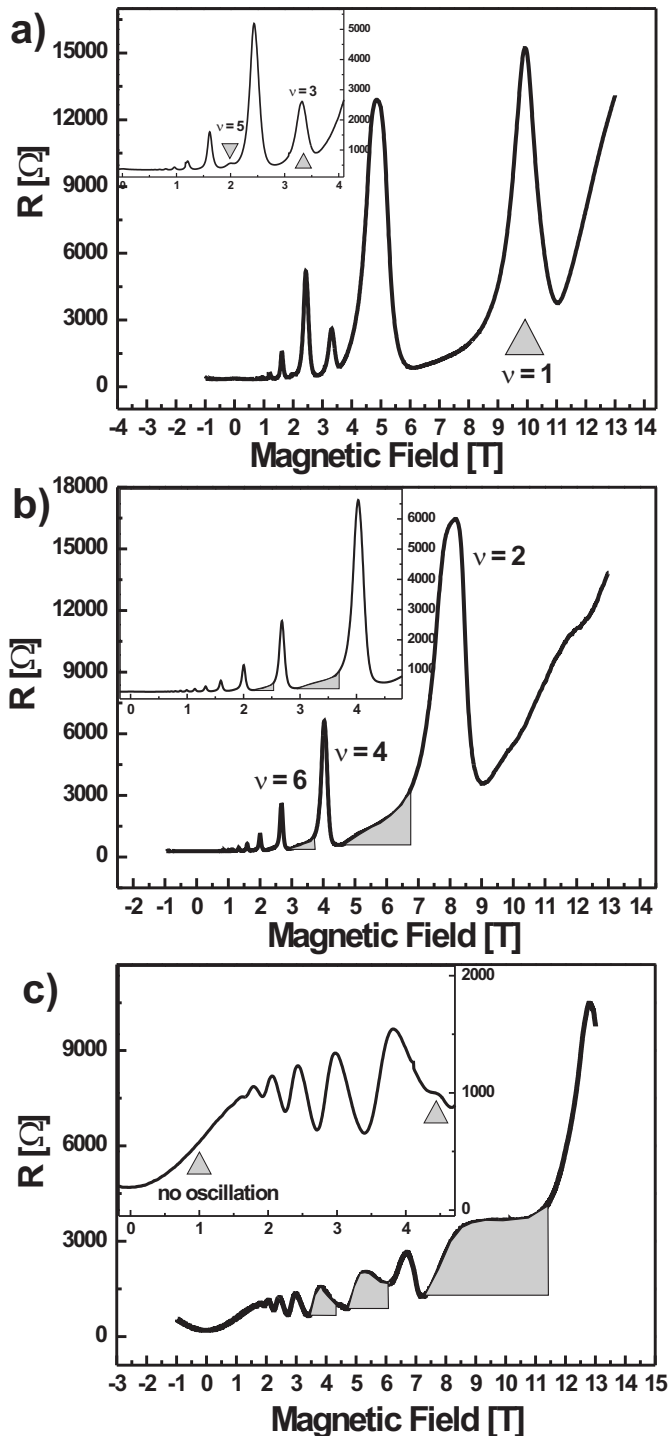


Figure 8.16:

Magnetoresistance data at gate voltages of 3.5 V, (a), 5 V, (b), and 7 V, (c). The corresponding insets show a magnification of the resistance at lower magnetic fields. The gray arrows in figure (a) and its inset indicate the positions of filling factors 1, 3, and 5. In figure (b) and its inset, and in figure (c) the gray shaded areas indicate magnetic field regions in which the resistance changes due to the modulation broadening of the Landau levels. In the inset of figure (c) the right gray arrow points at the remainder of a Hall plateau, which lies in a DOS gap that has almost completely vanished due to the strongly increased width of the Landau bands. The left gray arrow in the same inset indicates that at $B = 1$ T there are no resistance oscillations, even though clear oscillations are seen in the smaller gate voltage data. Semiclassically this suppression is due to widely separated open orbits at the Fermi energy. In the quantum mechanical model, the broadening of the Landau levels has smeared out all oscillations in the DOS.

high magnetic fields indicates a broadening of the Landau levels due to the periodic SL potential.

The data at 5 V gate voltage, plotted in figure 8.16(b) differs significantly from that

at 3.5 V. As the labeling of the oscillations indicates, the spin-split states at odd filling factors have vanished. It will be seen later that this vanishing of the spin-split states appears to occur rather abruptly when the Fermi energy moves above the top of the mini-band. More importantly, though, the oscillation peaks become asymmetric and develop a shoulder at their left side, indicated by the gray shaded areas in the figure and its inset. This shoulder is caused by the modulation broadened Landau bands. At a gate voltage of 7 V the broadening into Landau bands becomes even more pronounced as seen in figure 8.16(c). Now, not only the DOS side peak at the lower B -side of a Landau band is resolved but also those at the higher magnetic field value. These two peaks in the DOS with a minimum in between appear as an additional maximum in the resistance data (at $B = 3.8$ T, 5.3 T, and 9.5 T). In addition to the appearance of these additional maxima, also the peaks associated with the gaps between the Landau bands have become

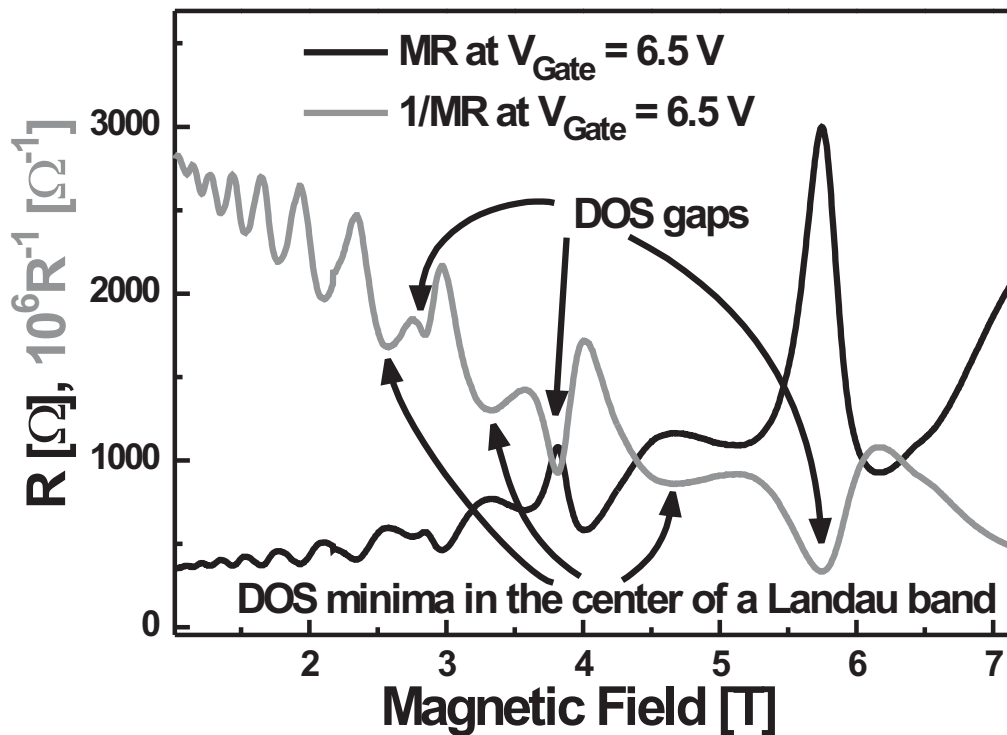


Figure 8.17: Magnetoresistance and scaled inverse magnetoresistance at a gate voltage of 6.5 V. Outside the energy regions in which the DOS vanishes (marked as DOS gaps by arrows), the inverse magnetoresistance represents a rescaled version of the DOS. In between the DOS gaps the DOS side peaks at the edges of the broadened Landau bands can be clearly observed. The minima in between these peaks lie close to the center of the Landau band (also marked by arrows).

much smaller (or vanished completely) when compared to the 5 V gate voltage data at similar magnetic fields. In the inset of 8.16(c) the gray triangle at about $B = 4.5$ T marks the remains of what would be a Hall plateau in an unmodulated system. In figure 8.16(b) these gaps are still open and clearly marked by large peaks. For high energies (compared to the miniband width) the two-dimensional electron system with a strong, short-period modulation turns into a one-dimensional system without a cyclotron gap. While the cyclotron gap disappears at high B values, there are no resistance oscillations at all below a field of about 1.5 T. In this regime the cyclotron gap is also suppressed by the modulation. Additionally, the disorder induced broadening smears out all remaining oscillations in the DOS. Semiclassically this was referred to as the regime of open orbits at magnetic fields that are too small to induce magnetic breakdown.

In figure 8.17 the MR and its inverse are plotted for a gate voltage of 6.5 V. The gray line essentially corresponds directly to the DOS. At the minima labeled as DOS gaps the DOS should actually vanish. However, a finite value is seen due to the contribution from the Hall conductivity. Next to the minimas at the DOS gaps there are additional minima surrounded by two maxima which correspond directly to the DOS resulting from a broad Landau band. This means that at this high gate voltage the maxima in the resistance (except for those resulting from the left overs of the cyclotron gap) correspond approximately to half filling of a Landau band whereas at low densities the maxima are between broadened Landau levels and therefore indicate a complete filling of a Landau level.

When the resistance data is plotted versus the inverse filling factor it is possible to directly follow the evolution of the oscillation extrema when the Fermi energy is increased from inside the miniband into the above lying gap. A magnification of the region showing filling factors 2-6 is shown in figure 8.18. For clarity, the traces have been offset vertically by a resistance of 4 k Ω . The three lowest lying traces correspond to Fermi energies within the miniband. From the fourth trace at a gate voltage of 4 V a density of 2.78×10^{11} cm $^{-2}$ is deduced. A comparison with figure 3.6 shows that the Fermi energy for this density lies right at the top of the miniband. All traces for gate biases larger than 4 V correspond to Fermi energies that lie beyond the top of the miniband. The most dramatic change can be observed at filling factor 3. As long as the Fermi energy is in the miniband, the corresponding spin-split maximum seems to become more pronounced with increasing density. This indicates that an increasing mobility leads to a smaller disorder broadening so that the exchange-enhanced energy separation of the spin-split states becomes better resolved in the measurement. However, as soon as the Fermi energy moves into the gap, filling factor 3 ceases to exist. The fact that the peak vanishes very abruptly indicates that the corresponding gap in the DOS is small and therefore closed very fast by the broadening of the Landau levels into Landau bands. For larger Fermi energies the broadened Landau bands appear at the position at which filling factor 3 would be expected.

The spin-split peaks disappear quickly when the Fermi energy moves into the gap. In comparison, the cyclotron gaps in the DOS show an increasing resistance up to a gate

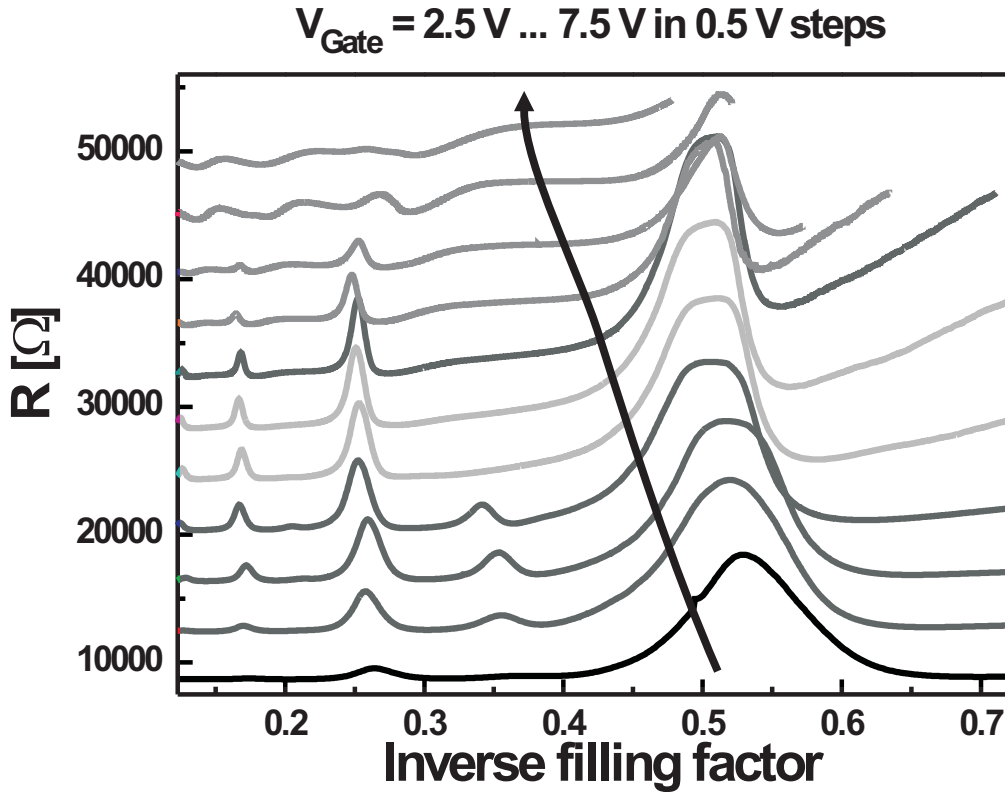


Figure 8.18: Magnetoresistance data for a large number of different applied gate biases. For each trace the magnetic field has been rescaled into the corresponding inverse filling factor, according to $\nu^{-1} = (n\hbar/eB)^{-1}$. For clarity the traces have been offset vertically by a resistance of 4 k Ω .

voltage of 5.5 V. Beyond the corresponding density of $4.4 \times 10^{11} \text{ cm}^{-2}$ the resistance peak height decreases and at the highest densities all gaps have vanished, except at $\nu = 2$. This peak still appears in the measurement, however, also strongly diminished.

In order to verify the validity of these conclusions, it is instructive to compare them with the MR data of samples with different CEW widths. In figure 8.19 and 8.20 the MR for samples with 1.6 nm and 10 nm wide CEWs is shown. The magnetic field has been rescaled to an inverse filling factor after the density was deduced from the resistance oscillations. The dependence of the density on the gate voltage is found to be

$$n = (-5.85 \times 10^{10} + 2.66 \times 10^{10} V_{\text{Gate}}[\text{V}]) \text{ cm}^{-2} \quad \text{CEW} = 1.6 \text{ nm} \quad (8.45)$$

$$n = (-1.03 \times 10^{11} + 2.99 \times 10^{10} V_{\text{Gate}}[\text{V}]) \text{ cm}^{-2} \quad \text{CEW} = 10 \text{ nm} . \quad (8.46)$$

From these densities it can be deduced that the Fermi energy in the sample with the 1.6 nm CEW should move into the minigap for gate voltages larger than about 10 V. For

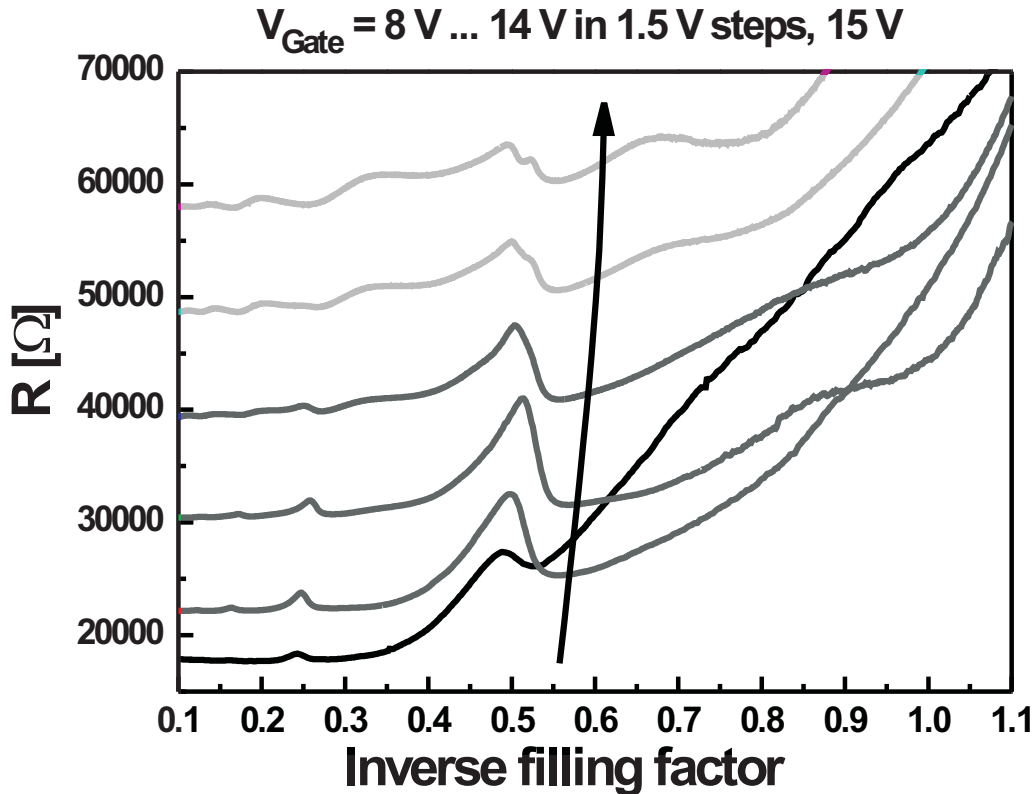


Figure 8.19: Magnetoresistance data for a sample with a 1.6 nm wide cleaved-edge well. The magnetic field has been rescaled into an inverse filling factor and traces for increasing gate bias are offset by a resistance of 5 k Ω .

the sample with the 10 nm CEW the modulation is so small and therefore the miniband width so large that the Fermi energy is within the miniband even for the highest density¹⁷ of about $3.5 \times 10^{11} \text{ cm}^{-2}$.

The structure of the resistance data presented in figures 8.19 and 8.20 is completely consistent with what was found for the initial sample in figure 8.18. In the data of the 1.6 nm CEW sample (cf. figure 8.19) again the vanishing of the cyclotron gaps at high Fermi energies is observed. The most dramatic change of this kind can be observed at filling factor 4. The maximum at low gate voltages corresponds to the Hall resistance contribution when the Fermi energy lies in the corresponding gap of the DOS. However, for high gate voltages the peak actually turns into a minimum. This minimum results when two edge peaks of broadened Landau bands overlap to form a single DOS peak

¹⁷Both samples have a gate barrier thickness of 2000 nm which reduces the maximum attainable densities in the structure compared to the 5 nm CEW sample with a 500 nm thick gate barrier.

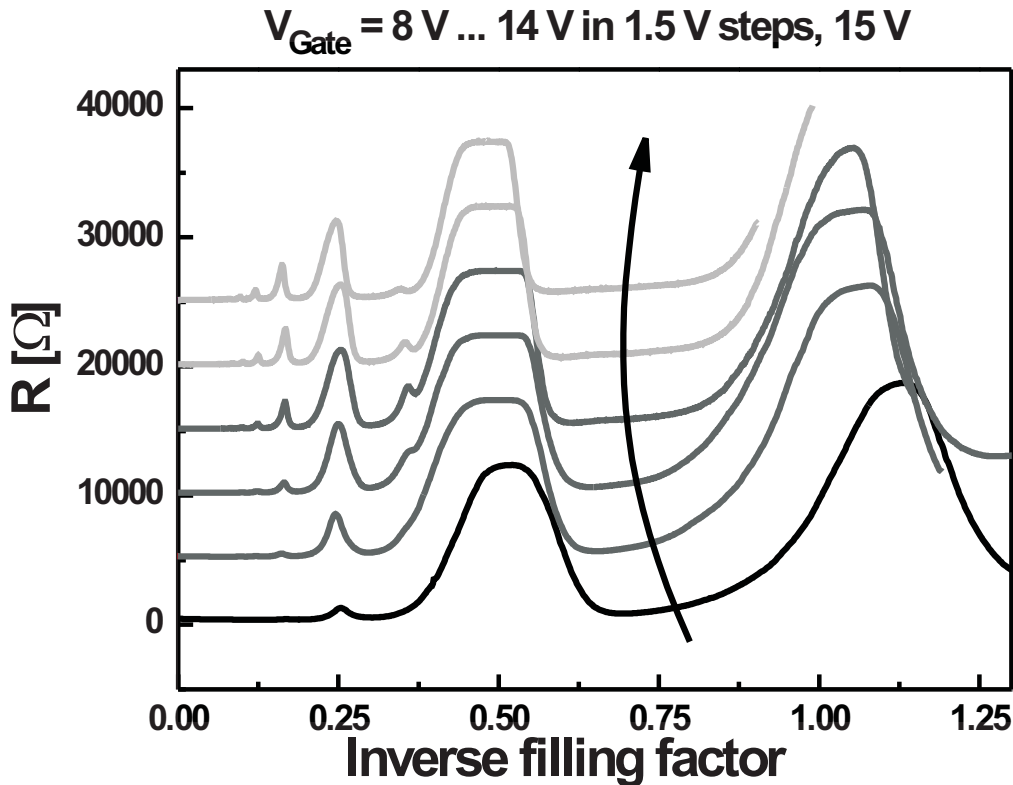


Figure 8.20: Magnetoresistance data for a sample with a 10 nm wide cleaved-edge well. The magnetic field has been rescaled into an inverse filling factor and traces for increasing gate bias are offset by a resistance of 5 k Ω .

(resistance minimum). While the peak at filling factor 2, which corresponds to the widest DOS gap, is not completely suppressed, it is still significantly reduced at large gate biases. The vanishing of the DOS gaps is accompanied by the broadening of the Landau bands which eventually become broad enough so that the double peak structure of each band is resolved. This is clearly seen in the development of peaks at $1/\nu = 0.2, 0.33$ with increasing density.¹⁸ In addition a delayed onset of the resistance oscillations is observed (not shown in the figure).

The resistance data of the 10 nm CEW sample shows the behavior of a free two-dimensional electron system. Due to an improved mobility in the regime $E_F < \Delta$, the DOS gaps are better resolved and filling factor 2 shows the expected Hall plateau value. Also, filling factors 1 and 3 are seen which indicates that when the mobility is high enough and the Fermi energy is inside the miniband (thin Landau bands) spin-split states can be

¹⁸Although these values actually correspond to filling factors 5 and 3, the data of the 5 nm CEW sample showed that they are not connected to spin splitting.

observed in the resistance oscillations.

Thus, the strong, short-period modulation introduces the following major changes into the MR of a two-dimensional electron system:¹⁹

When the Fermi energy moves from inside the miniband into the above lying gap, the modulated two-dimensional electron gas undergoes a transition into a quasi one-dimensional system. This transition manifests itself through the vanishing of the spin²⁰ and cyclotron gaps, through the delayed onset of the resistance oscillations, and probably also through the suppression of weak localization. The vanishing of the gaps and the delayed onset of oscillations are directly related to the broadening of the Landau levels into wide bands, which then tend to fill out the DOS gaps of a free system and also lead to additional resistance peaks when they are broad enough so that the resulting edge peaks in the DOS can be resolved. As long as the Fermi energy is inside the miniband the system behaves like a free two-dimensional electron system.

8.7 Some Loose Ends

1. Features not contained in the quantum mechanical model:

The discussion in the last section showed that the predictions of the quantum mechanical model correspond very well to the measured experimental data. Nevertheless, there are some parts which will need further experimental and theoretical investigation. The most prominent issue that needs additional theoretical treatment is the spin degree of freedom. The experiment suggests that the spin gap is closed very early when the Fermi level moves into the gap above the miniband. In the presented quantum-mechanical model the spin degree of freedom was not considered separately. The presence of the modulation makes the incorporation of the electron-electron interactions into a theoretical model a non-trivial matter. However, a first step in form of a Hartree-Fock approximation [MG95] might prove to be manageable.

In addition to the spin problem, a closer look at the experimental data shows that filling factor 2 in figure 8.18 and filling factor 1 in figure 8.20 appear shifted from their expected positions at low densities. Some of this shift can be accounted for by inaccuracies in the determination of the density that was used to rescale the magnetic field into an inverse filling factor. Moreover, one could speculate about a slight density increase when electrons preferably occupy the regions close to the GaAs sections of the SL. Then, for larger gate voltages the electron system is stronger localized in the CEW and this effect might quickly disappear. However, this is currently only speculation and it seems not immediately clear how this could be incorporated in a

¹⁹The form in which these changes are observed depends on the contact geometry used for the measurement.

²⁰It is not clear whether the enhanced g-factor is additionally suppressed or not.

theoretical model.

2. Mobility considerations:

Next to these open questions, there is the problem of determining the electron mobility in the presented structures. Unfortunately, there is no way to accurately extract this (these) value(s). In order to calculate the transport mobility, one needs to know the resistance at $B = 0$ T. However, due to the fact that there is an unknown series resistance contribution from the current path in the contact layers and due to the weak localization phenomenon, it is impossible to exactly determine the desired resistance value. In figure 8.21(a) the gate voltage, corrected for its $n = 0$ offset value V_0 , is plotted versus the estimated²¹ value of the resistance at $B = 0$ T minus a series resistance of 125Ω . In principle there might be a linear relationship between these values according to

$$V_{\text{Gate}} - V_0 = \frac{\alpha}{R(B=0) - R_0}. \quad (8.47)$$

However, the slope α contains the (inverse) mobility which is expected to increase for larger densities. Thus it is not too surprising that the deviations from a constant α are biggest for larger gate biases. Moreover, the choice of $R_0 = 125 \Omega$ is probably

²¹The values are basically extrapolations from the shape of the resistance trace at magnetic fields at which the weak localization contribution is absent. This procedure should lead to very crude guesses with a large error.

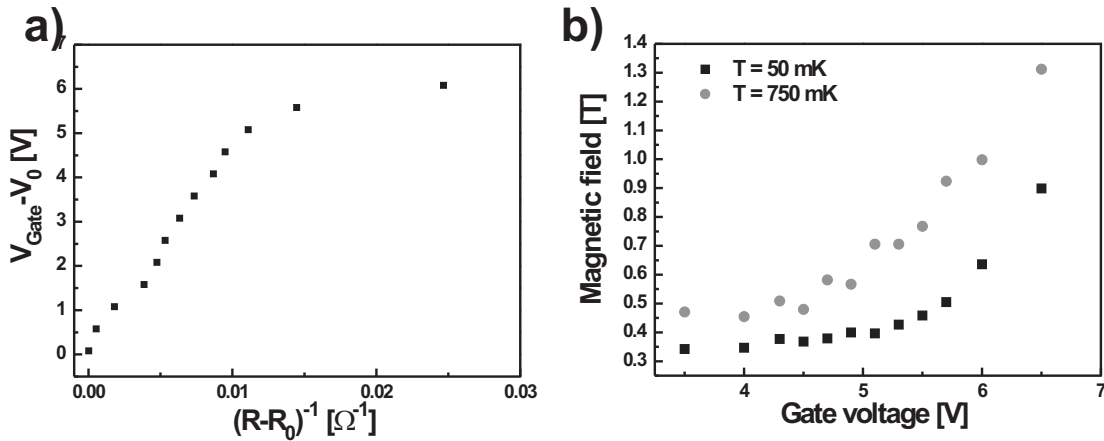


Figure 8.21: (a) Gate voltage versus the estimated resistance at $B = 0$ T. The gate voltage has been corrected for V_0 which is the bias at which the two-dimensional electron channel begins to be filled. The resistance has been corrected for an assumed series resistance of $R_0 = 125 \Omega$. (b) Magnetic field B_0 beyond which resistance oscillations start to appear versus the applied gate bias.

too low and should be closer to 160Ω , which leads to even larger deviations at large densities. The $R(B = 0)$ value of 165Ω at a gate voltage of 7 V sets an upper limit to the series resistance in the contact layers. Moreover, mobilities²² of more than $30000 \text{ cm}^2/\text{Vs}$ indicate a 2DES resistance of less than 20Ω for the two-dimensional electron system. Thus, a series resistance value of about 150Ω , as used in the interpretation of the current-voltage characteristics of the preceding chapters, seems quite reasonable.

Semiclassically, it is possible to determine the quantum lifetime τ_q from the oscillation amplitudes at low magnetic fields. If these amplitudes are corrected for temperature effects, then the slope of the so called Dingle plot [Sho84, Chapter 8] directly leads to τ_q . However, for the samples presented here, there is some difficulty in this procedure. For small gate biases the resistance oscillations at small magnetic fields contain a contribution from the remainder of the weak localization signal. And for large gate voltages there are no oscillations at small magnetic fields due to the broadening of the Landau levels into overlapping bands. Moreover, the effective mass is density dependent. Thus, a correction for temperature effects is not trivial, even though the introduced error would be acceptable due to the relative low mobility of the structures. If one attempts a Dingle plot despite these problems, a constant slope containing τ_q is indeed observed. However, this slope stays constant for a wide range of assumed series resistances R_0 and effective masses m . If the plot is forced to intercept at the value 4 for infinite magnetic field (cf. [CSF89, Col91]) then a value of $\tau_q = 0.5 \text{ ps}$ is found. This corresponds to a mobility of about $6500 \text{ cm}^2/\text{Vs}$. Since τ_q is usually much smaller than the transport mobility [Col91] a value of $50000 \text{ cm}^2/\text{Vs}$ could be estimated for the transport mobility at densities of about $2.5 \times 10^{11} \text{ cm}^{-2}$. However, the then resulting value for R_0 leads to a much lower transport mobility, directly contradicting the results from the Dingle plot. Therefore, the procedure seems to simply be impossible to apply in this situation or the forced intercept of 4 for infinite magnetic field is only valid for the free two-dimensional electron system and not for the studied modulated system.

3. Magnetic breakdown:

The terminology of magnetic breakdown was developed in order to incorporate experimentally observed oscillations due to the tunneling of electrons between different branches of the same Fermi surface. The observation of resistance oscillations in the strongly modulated two-dimensional electron system even when the Fermi energy is above the miniband can semiclassically be explained by a similar assumption. However, the expressions derived for the magnetic breakdown field B_0 , which separates the oscillations from the region without them, are difficult to apply in this situation. The energy gap that is associated with the miniband formation is an order of magnitude larger than both the Fermi energy and the cyclotron energy in contrast

²²Estimated from the onset of SdHs.

to the situation in metals. Moreover, experimental data in metals can be very well fitted using B_0 values which differ by as much as 100 percent [Sho84, Chapter 7]. In figure 8.21(b) B_0 is plotted versus the applied gate voltage for the 5 nm CEW sample at temperatures of 50 mK and 750 mK.²³ From this data it appears that the onset of the SdH oscillations becomes delayed for gate voltages above about 4 V. This is in excellent agreement with the crossover between closed and open orbits at about the same gate bias. However, the semiclassical expressions for B_0 do not contain any temperature dependence and it is not immediately clear how it should be introduced.

In the quantum mechanical model the delayed onset results from the broadening of the Landau levels into Landau bands, which leads in combination with the disorder broadening to a non-oscillatory DOS. In this context the temperature change is directly reflected in a smaller or larger disorder broadening of the Landau bands so that oscillations in the DOS and therefore in the resistance occur already at smaller magnetic fields for lower temperatures. Nevertheless, a derivation of the dependence of B_0 on the gate voltage, assuming realistic sample parameters, requires ample additional calculations which will not be attempted here.

8.8 Conclusions

In the preceding sections the magnetotransport of a surface superlattice in linear response to an applied electric field was studied. From bandstructure considerations typical Shubnikov-de Haas oscillations were expected for Fermi energies lying within the lowest miniband. This was confirmed by the experimental results. Once the Fermi energy moves into the gap above the miniband, the orbit of an electron at the Fermi energy becomes open and semiclassically no further resistance oscillations are expected. Experimentally, only a delayed onset of the resistance oscillations is found. This can be incorporated into the semiclassical model by the ad hoc introduction of the magnetic breakdown concept which allows for the possibility that electrons tunnel between the two branches of the formerly closed Fermi contour. However, at intermediate magnetic fields double peak structures appear in the resistance oscillations which the semiclassical model can no longer account for. A comparison with a quantum-mechanical model shows that the increase in Fermi energy leads to a transition from a two-dimensional to a quasi one-dimensional electron system. While the eigenstates for small energies are very close to the Landau levels of the free two-dimensional electron system, a strong broadening of the eigenstates into wide Landau bands occurs at Fermi energies in the gap above the miniband. This broadening leads to a successive closing of first the spin gaps and then of the cyclotron gaps in the density of states. In the resistance data this can be clearly seen by the vanishing of the

²³The B_0 values below $V_{\text{Gate}} = 3.5$ V are not shown since they are larger than the minimum values due to worse mobilities at lower densities.

Quantum Hall peaks that result when the resistance in a density of state gap takes on the quantized Hall resistance values. Next to the reduced Hall peaks, a new peak structure appears which corresponds to a minimum in the density of states centered between two large maxima that mark the density of states side peaks at the edges of the Landau bands. The excellent correspondence between the resistance data and the calculated density of states also gives strong support for the applied resistance formula which states that in a wide and short sample the perpendicular electric field vanishes and that the current is found by summing up the longitudinal and perpendicular contributions. Moreover, the presented magnetoresistance data shows, for the first time in such a structure, the phenomenon of weak localization. Since the system is strongly anisotropic and the interfaces provide strong elastic scattering, such a correction to the zero field resistance should actually be expected.

The presented analysis is an excellent starting point for the study of two-dimensional electron systems with arbitrary modulations. Such a study should help to provide further information under which conditions a two-dimensional electron system is metallic or insulating.

Chapter 9

Summary

The aim of this work was to investigate the possibility of the realization of an active Bloch oscillator with surface superlattice structures produced by cleaved-edge overgrowth. Even though this ambitious goal was not completely reached, the presented results and discussions widely extend the understanding about electron transport in surface superlattices. The developed sample structures should proof to be an important step towards a possible Bloch oscillator which seems within reach at this point.

The main results can be summarized in the following observations:

1. Both simulations and measurements indicate that surface superlattices show an increased resistance towards the formation of electric field domains. Therefore, it should be possible to realize unshunted surface superlattices at high densities and, according to the theoretical results, of arbitrary length with a field distribution that is almost homogeneous. Such structures are the basis of an active Bloch oscillator.
2. The initially observed negative differential conductivity in gated surface superlattices can be explained by resonant tunneling in combination with the pinch-off of the active transport channel. Through the introduction of very thick gate barriers this problem could be circumvented and the non-linear transport effects of the underlying superlattice structure could be observed without obstruction. When the electron system is established by modulation doping, any remaining influence of the equipotential gate plane on the transport characteristics can be eliminated (even though the density control is thereby lost).
3. It was shown that the great flexibility of the cleaved-edge overgrowth method offers the unique possibility to realize shunted surface superlattice structures with widely tunable electron densities. The resulting devices offer the possibility to separate the transport contributions from shunt and surface superlattice. Therefore, the combination of the electric field stabilizing shunt with the gate structure allowed, for the first time, the direct observation of the negative differential resistance due to stable, electrically excited Bloch oscillations. The direct proportionality between

drift velocity and measured current in these structures beautifully confirms the earliest theoretical predictions about superlattice structures. Moreover, the shunted surface superlattices are also the first high-density superlattice structures that do not suffer from electric field domain formation. They allow experimental studies in a parameter space that was formerly inaccessible. The validity of the interpretation that the negative differential resistance is due to Bloch oscillations can be shown by transport studies in magnetic fields and by the investigation of the density dependence of the superlattice transport. The presented data should stimulate new approaches towards high-density superlattice systems without electric field domains. One of these structures might eventually be turned into an active superlattice THz oscillator based on the Bloch gain.

4. As just mentioned, the shunted surface superlattice design offers the possibility to study electron transport in a new parameter space. One such example, studied in detail in this work, is the investigation of the interplay between electric field- and magnetic field-induced localization in superlattices. The presented experimental results are in excellent agreement with the predictions of the semiclassical model already applied by Esaki and Tsu in the first theoretical superlattice treatment. The theoretically predicted change in the drift velocity of the system can be directly seen in the current through the surface superlattice. Even the effective mass for motion lateral to the triangular gate induced confinement could be deduced from the data. Due to the high mobility in the plane of the two-dimensional electron system, experimental measurements on a superlattice system in which the electrons undergo Landau quantization along the superlattice axis could for the first time be performed. The corresponding results need a theoretical description beyond the semiclassical theory.
5. The most important information for a potential realization of a Bloch oscillator with the help of surface superlattice structures can be acquired from transport studies in the presence of an external high-frequency field. However, the corresponding experimental results proved to be inconclusive. On one hand, the DC current response for low frequencies in the GHz regime was close to the theoretical predictions. On the other hand, however, the DC current under irradiation with THz frequencies only showed significant changes in the small SD-bias regime. Most prominently, no photon assisted transport could be observed at larger Stark splittings. Such a direct observation would have allowed an experimental estimate of the magnitude of the Bloch gain in these structures. It is not clear why photon assisted transport was not detected in the measurements. Further investigations in this area should be performed with surface superlattices that have much larger miniband widths than those in the present structures, in order to be able to exclude saturation effects due to the heating of the electron system by the external electric fields. Such further studies should be complemented by theoretical investigations addressing both the need for

the incorporation of a THz waveguide into the structure and the influence of the sample capacitance on the high-frequency transport in surface superlattices. The outcome of this combined effort should give the final answer about whether or not a Bloch oscillator can be realized in form of a two-dimensional surface superlattice.

6. Besides the investigation of surface superlattice transport in the strong non-equilibrium regime, also the linear response transport studies in an external magnetic field produced exciting new results. For the first time, the experimental data could be conclusively linked to the quantum mechanical predictions for a two-dimensional electron system with a strong, short-period modulation. The modulation separates the transport behavior into two regimes that can be independently addressed by setting the Fermi energy either inside the superlattice miniband or in the gap above it. As long as the Fermi energy resides inside the miniband, the observed magnetoresistance oscillations resemble those of a free two-dimensional electron system. When the Fermi level lies above the miniband, the Landau levels broaden into Landau bands and both the spin and cyclotron gaps in the density of states collapse. This is directly observable in the experiment through a vanishing of the Hall resistance peaks which mark the positions of these gaps. In addition to the closed gaps, the density of states of the broad Landau bands leads to additional oscillations which are also clearly observed in the data.

The broadening of the Landau levels also leads to a delayed onset of the magnetoresistance oscillations. This delayed onset is expected semiclassically since the electron trajectories at the Fermi energy change from closed to open orbits when the Fermi energy moves into the gap. Moreover, for the first time, weak localization was observed in surface superlattice devices based on cleaved-edge overgrowth. Since the sample structure is strongly anisotropic and since it provides strong elastic scattering by the static superlattice interfaces, weak localization is actually expected to appear. According to the experimental data, the change from closed to open Fermi energy orbits also leads to a suppression of the weak localization. Such a dependence seems reasonable as weak localization is due to an enhanced probability of finding an electron back at its starting point after tracing a closed real space orbit.

The excellent overall correspondence between experimental data and theoretical predictions also lends strong support to the presented resistance formula for a short and wide sample geometry. This equation should provide a reliable starting point for magnetotransport studies on other cleaved-edge overgrowth based structures.

The combination of all these results clears the way for a number of additional interesting investigations. On top of this list is the realization of a Bloch oscillator. It is the author's opinion that cleaved-edge overgrowth based surface superlattices offer such a great design flexibility that it should eventually (if at all) be possible to build a tunable THz oscillator from these structures.

Besides this ambitious goal, the samples designed in this work should also prove to be an excellent starting point both for the study of two-dimensional electron systems of arbitrary modulation and for the realization of modulated quantum wires.

The cleaved-edge overgrowth method offers the possibility to tune the (one-dimensional) modulation period and strength in an unprecedented way. It is straight forward to proceed systematically from the system with a strong, short-period modulation to structures with aperiodic modulation. The corresponding experimental results should provide important information about transport in two-dimensional electron systems in arbitrary disorder potentials. Especially questions about metallic and insulating phases could be addressed systematically.

When a second cleaved-edge overgrowth step is added onto the surface superlattice structures, it becomes possible to realize modulated quantum wires. In the extreme limit of very wide modulation barriers, a set of well separated quantum dots can be produced in which the dot size can be tuned with atomic precision. Such a system might prove to be of strong interest in the field of quantum information processing. Especially the complete control of the size offers the great advantage of being able to address the dots separately, while the position control should be of help in the realization of entangled states.

Appendix A

Matlab program

The following program was used to perform the numerical integration of the equations (6.9) - (6.11) which describe the superlattice transport subject to a magnetic field perpendicular to the superlattice axis:

```
Main program
# define electric and magnetic field as global
global i ii
# open new figure
figure
# force plot of all traces in one figure
hold
# define an index counter
kk = 1
# sweep magnetic field from 0 to 13 Tesla
for ii = 0:1:13
# sweep electric field from 0 to  $5 \times F_C$  in 50 steps
for i = 0:50
# define some optional parameters for numerical solution of differential
# equations
IEBoptions = odeset('Refine',5,'MaxStep',1/10,'RelTol',1e-8,'AbsTol',[1e-8
1e-8],'MaxOrder',2);
# solve differential equation defined in function BsenkrechtI (see below)
[T,Y] = ode45(@BsenkrechtI,[0 5],[0 0],IEBoptions);
# define array containing the exponential in equation (6.11)
expvonT = exp(-T);
# define dt array for summing of equation (6.11)
T2 = circshift(T,1);
Tdiff = T - T2;
# extract velocity data from the numerical solution
```

```
Y(:,1) = [];  
# perform summation of equation (6.11)  
intwert = sin(Y.*15e-9).*expvonT.*Tdiff;  
v(i+1,kk) = sum(intwert);  
# end electric field sweep  
end  
# increase counter  
kk = kk+1  
# plot the velocity-field characteristic  
plot(v)  
# end magnetic field sweep  
end
```

Program defining the Matlab function BsenkrechtI:

```
# definition line  
function dy = BsenkrechtI(t,y)  
# make magnetic and electric field visible as global variables  
global i ii  
# define differential equation matrix  
dy = zeros(2,1);  
# equation (6.10)  
dy(1) = -ii*0.54e8*sin(y(2)*15e-9);  
# equation (6.9)  
dy(2) = i/10/15e-9 + ii*0.0192*y(1);
```

Appendix B

Folded phonons

The artificial periodicity of the superlattice does not only profoundly influence the electronic properties of the structure but also the long wavelength sound waves that can travel along the superlattice. The corresponding changes can roughly be described in the following way.¹

The acoustic phonon branches in the materials of wells and barriers travel at a different speed. In a simple approximation the superlattice can be described by an average speed of sound given by

$$\bar{v} = d \left(\frac{1}{\frac{d_w}{v_w} + \frac{d_b}{v_b}} \right). \quad (\text{B.1})$$

Then, in the reduced Brillouin zone of the SL, the acoustic branches are folded back at

¹For the interested reader, more detailed accounts can be found in [YC99, Chapter 9.3] and references therein.

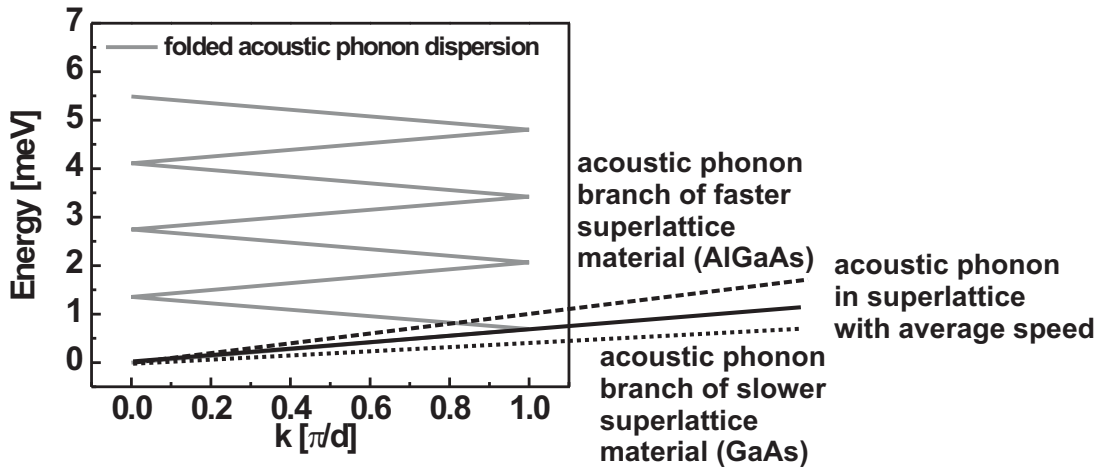


Figure B.1: Folded acoustic phonon branches of a superlattice. The folded phonons move with the average speed given by expression (B.1) which is determined by the sound velocities (slopes of the phonon dispersions) of the two superlattice materials.

the zone boundary $k = \frac{\pi}{d}$ as shown in figure B.1. In a more detailed theory there appear gaps at $k = 0$ and $k = \frac{\pi}{d}$ which are similar to the minigaps for the electronic structure. In the latter case the reason lies in the different band gaps of the superlattice materials. For the acoustic phonons the similar periodicity in the atomic mass of the superlattice crystals is responsible. The important point now is that the back folded acoustic phonon branches allow for equal k the dissipation of higher energies. Even at $k \approx 0$ there are acoustic phonons with finite energy. In general, the back folding of the acoustic branches allows electrons to dissipate energy more effectively. This could result in a higher effective scattering rate.

For the optic phonon modes no such back folding occurs. Due to their weak dispersion, these modes are confined in the individual superlattice layers [YC99, Chapter 9.3.3].

Bibliography

- [ACM⁺98] K. N. Alekseev, E. H. Cannon, J. C. McKinney, F. V. Kusmartsev, and D. K. Campbell. Spontaneous dc Current Generation in a Resistively Shunted Semiconductor Superlattice Driven by a Terahertz Field. *Phys. Rev. Lett.*, 80:2669, 1998.
- [AD00] G. P. Agrawal and N. K. Dutta. *Semiconductor Lasers*. Kluwer Academic Publishers, Dordrecht, 2nd edition, 2000.
- [AHSMM83] X. Aymerich-Humet, F. Serra-Mestres, and J. Millán. A generalized approximation of the Fermi-Dirac integrals. *J. Appl. Phys.*, 54:2850, 1983.
- [AL88] B. L. Al'tshuler and P. A. Lee. Disordered Electronic Systems. *Physics Today*, 41:36–45, 1988.
- [All88] R. S. Allgaier. Magneto-transport at high Hall angles: a comparison of the high-magnetic-field and high-mobility (quantum Hall effect) limits in the Hall bar and Corbino disc configurations. *Semicond. Sci. Technol.*, 3:306, 1988.
- [AM76] N. W. Ashcroft and N. D. Mermin. *Solid State Physics*. Thomson Learning Inc., United Kingdom, 1976.
- [API⁺05] K. N. Alekseev, P. Pietiläinen, J. Isohätälä, A. A. Zharov, and F. V. Kusmartsev. Chaos and rectification of electromagnetic wave in a lateral semiconductor superlattice. *Europhys. Lett.*, 2005. to be published.
- [ASP⁺93] F. Aristone, A. Sibille, J.F. Palmier, D.K. Maude, J.C. Portal, and F. Molot. Electronic perpendicular transport in GaAs-AlAs superlattices in a high magnetic field. *Physica B*, 184:246–249, 1993.
- [BAM⁺90] P. H. Beton, E. S. Alves, P. C. Main, L. Eaves, M. W. Dellow, M. Henini, O. H. Hughes, S. P. Beaumont, and C. D. W. Wilkinson. Magnetoresistance of a two-dimensional electron gas in a strong periodic potential. *Phys. Rev. B*, 42:9229, 1990.

- [BDM⁺91] P. H. Beton, M. W. Dellow, P. C. Main, E. S. Alves, L. Eaves, S. P. Beaumont, and C. D. W. Wilkinson. Magnetic breakdown of a two-dimensional electron gas in a periodic potential. *Phys. Rev. B*, 43:9980, 1991.
- [Ber84] G. Bergmann. Weak localization in thin films. *Phys. Rep.*, 107:1, 1984.
- [BF87a] G. Bernstein and D. K. Ferry. Negative differential conductivity in lateral surface superlattices. *J. Vac. Sci. Technol. B*, 5:964, 1987.
- [BF87b] G. Bernstein and D. K. Ferry. Observation of negative differential conductivity in a FET with structured gate. *Z. Phys. B - Condensed matter*, 67:449, 1987.
- [BI77] A. M. Belyantsev and A. A. Ignatov. High-frequency electromagnetic response of "classical" semiconductor-dielectric superlattices. *Solid State Commun.*, 24:817–819, 1977.
- [Blo28] F. Bloch. Über die Quantenmechanik der Elektronen in Kristallgittern. *Z. Phys.*, 52:555, 1928.
- [Blo62] E. I. Blount. Bloch Electrons in a Magnetic Field. *Phys. Rev.*, 126:1636, 1962.
- [BMD⁺90] P. H. Beton, P. C. Main, M. Davison, M. W. Dellow, R. P. Taylor, E. S. Alves, L. Eaves, S. P. Beaumont, and C. D. W. Wilkinson. Temperature dependence of magnetoresistance oscillations in a two-dimensional electron gas subjected to a periodic potential. *Phys. Rev. B*, 42:9689, 1990.
- [BT77] M. Büttiker and H. Thomas. Current instability and domain propagation due to Bragg scattering. *Phys. Rev. Lett.*, 38:78, 1977.
- [BT86] F. G. Bass and A. P. Tetervov. High-frequency phenomena in semiconductor superlattices. *Phys. Rep.*, 140:237, 1986.
- [CF61] M. H. Cohen and L. M. Falicov. Magnetic Breakdown in Crystals. *Phys. Rev. Lett.*, 7:231, 1961.
- [Col91] P. T. Coleridge. Small-angle scattering in two-dimensional electron gases. *Phys. Rev. B*, 44:3793, 1991.
- [CSF89] P. T. Coleridge, R. Stoner, and R. Fletcher. *Phys. Rev. B*, 39:1120, 1989.
- [Dat03] S. Datta. *Electronic Transport in Mesoscopic Systems*. Cambridge University Press, Cambridge, 2003.
- [Dav98] John H. Davies. *The physics of low-dimensional semiconductors*. Cambridge University Press, 1998.

- [DB90] I. Dharssi and P. N. Butcher. Interface roughness scattering in a superlattice. *J. Phys.: Condens. Matter*, 2:4629–4635, 1990.
- [Deu01] R. A. Deutschmann. *Two dimensional electron systems in atomically precise periodic potentials*. PhD thesis, Walter Schottky Institut, University of Technology Munich, 2001.
- [DGSA03] E. S. Daniel, B. K. Gilbert, J. S. Scott, and S. J. Allen. Simulations of electric field domain suppression in a superlattice oscillator device using a distributed circuit model. *IEEE Trans. Electron Devices*, 50(12):2434–2444, 2003.
- [DK86] D. H. Dunlap and V. M. Kenkre. Dynamic localization of a charged particle moving under the influence of an electric field. *Phys. Rev. B*, 34:3625, 1986.
- [dLKP31] R. de L. Kronig and W. G. Penney. Quantum Mechanics of Electrons in Crystal Lattices. *Proc. Roy. Soc. (London) A*, 130:499, 1931.
- [DLW⁺00] R. A. Deutschmann, A. Lorke, W. Wegscheider, M. Bichler, and G. Abstreiter. Breakdown of Shubnikov-de Haas oscillations in a short-period 1D lateral superlattice. *Physica E (Amsterdam)*, 6:561–564, 2000.
- [Döh84] G. H. Döhler. *n-i-p-i doping superlattice-semiconductors with tunable electronic properties*. The Physics of Submicron Structures. Plenum Press, New York, 1984.
- [DWR⁺00] R. A. Deutschmann, W. Wegscheider, M. Rother, M. Bichler, and G. Abstreiter. Negative differential resistance of a 2D electron gas in a 1D miniband. *Physica E (Amsterdam)*, 7:294–298, 2000.
- [DWR⁺01] R. A. Deutschmann, W. Wegscheider, M. Rother, M. Bichler, G. Abstreiter, C. Albrecht, and J. H. Smet. Quantum Interference in Artificial Band Structures. *Phys. Rev. Lett.*, 86:1857, 2001.
- [DZI98] E. P. Dodin, A. A. Zharov, and A. A. Ignatov. Lateral superlattices in a strong electromagnetic field: self-induced transparency, multistability, and frequency multiplication. *JETP*, 87:1226, 1998.
- [EC74] L. Esaki and L. L. Chang. New transport phenomenon in a semiconductor "superlattice". *Phys. Rev. Lett.*, 33:495, 1974.
- [Esa58] L. Esaki. New Phenomenon in Narrow Germanium p-n Junctions. *Phys. Rev.*, 109:603, 1958.
- [ET70] L. Esaki and R. Tsu. Superlattice and negative differential conductivity in semiconductors. *IBM J. Res. Dev.*, 14:61, 1970.

- [FBGZ98] J.-Y. Fortin, J. Bellissard, M. Gusmao, and T. Ziman. De Haas-van Alphen oscillations and magnetic breakdown: Semiclassical calculation of multi-band orbits. *Phys. Rev. B*, 57:1484, 1998.
- [FDW⁺04] T. Feil, R. A. Deutschmann, W. Wegscheider, M. Rother, D. Schuh, M. Bichler, G. Abstreiter, B. Rieder, and J. Keller. Transport in weakly and strongly modulated two-dimensional electron systems realized by cleaved-edge-overgrowth. *phys. stat. sol. (c)*, 1(8):2111–2130, 2004.
- [Fer91] R. Ferreira. Resonances in the hopping probability between flexible quantum dots: The case of superlattices under parallel electric and magnetic field. *Phys. Rev. B*, 43:R9336, 1991.
- [FLS⁺92] J. Feldmann, K. Leo, J. Shah, D. A. B. Miller, J. E. Cunningham, S. Schmitt-Rink, T. Meier, G. von Plessen, A. Schulze, and P. Thomas. Optical investigation of Bloch oscillations in a semiconductor superlattice. *Phys. Rev. B*, 46:R7252, 1992.
- [FRW⁺04] T. Feil, B. Rieder, W. Wegscheider, M. Bichler, G. Abstreiter, and J. Keller. Atomically precise modulated two-dimensional electron gas exhibiting stable negative differential resistance. *Physica E*, 22:733–736, 2004.
- [FS88] T. Fukui and H. Saito. $(\text{AlAs})_{1/2}(\text{GaAs})_{1/2}$ fractional layer superlattices grown on (001) vicinal GaAs substrates by metal-organic chemical vapor deposition. *J. Vac. Sci. Technol. B*, 6:1373, 1988.
- [FZ98] J.-Y. Fortin and T. Ziman. Frequency mixing of magnetic oscillations: Beyond the Falicov-Stachowiak theory. *Phys. Rev. Lett.*, 80:3117, 1998.
- [GBE⁺02] Z. S. Gribnikov, R. R. Bashirov, H. Eisele, V. V. Mitin, and G. I. Haddad. Electron dispersion relations with negative effective masses in quantum wells grown on the cleaved edge of a superlattice. *Physica E*, 12:276–280, 2002.
- [GCS⁺05] M. C. Geisler, S. Chowdhury, J. H. Smet, L. Hppel, V. Umansky, R. R. Gerhardts, and K. von Klitzing. Experimental evidence for predicted magneto-transport anomalies in rectangular superlattices. *Phys. Rev. B*, 72:045320, 2005.
- [Gra95] H. Grahn. *Semiconductor superlattices. Growth and electronic properties*. World Scientific Publishing Co., Singapore, 1995.
- [GSU⁺04] M. C. Geisler, J. H. Smet, V. Umansky, K. von Klitzing, B. Naundorf, R. Ketzmerick, and H. Schweizer. Detection of a Landau Band-Coupling-Induced Rearrangement of the Hofstadter Butterfly. *Phys. Rev. Lett.*, 92:256801, 2004.

- [Gue71] P. Gueret. Convective and Absolute Instabilities in Semiconductors Exhibiting Negative Differential Mobility. *Phys. Rev. Lett.*, 27:256, 1971.
- [Gun63] J. B. Gunn. Microwave Oscillations of Current in III-V Semiconductors. *Solid State Commun.*, 1:88, 1963.
- [Gun64] J. B. Gunn. Instabilities of Current in III-V Semiconductors. *IBM J. Res. Dev.*, 8:141, 1964.
- [GVB⁺03] Z. S. Gribnikov, N. Z. Vagidov, R. R. Bashirov, V. V. Mitin, and G. I. Haddad. Quantum real-space transfer in a heterostructure overgrown on the cleaved edge of a superlattice. *J. Appl. Phys.*, 93(10):330, 2003.
- [GWvK89] R. R. Gerhardts, D. Weiss, and K. v. Klitzing. Novel magnetoresistance oscillations in a periodically modulated two-dimensional electron gas. *Phys. Rev. Lett.*, 62:1173, 1989.
- [Hak67] B. W. Hakki. Amplification in Two-Valley Semiconductors. *J. Appl. Phys.*, 38(2):808–818, 1967.
- [HCS⁺96] N. Harrison, J. Caulfield, J. Singleton, P. Reinders, F. Herlach, W. Hayes, M. Kurmoo, and P. Day. Magnetic breakdown and quantum interference in the quasi two-dimensional superconductor κ -(BEDT-TTF)₂Cu(NCS)₂ in high magnetic fields. *J. Phys.: Condens. Matter*, 8:5415, 1996.
- [HGS⁺96] K. Hofbeck, J. Grenzer, E. Schomburg, A. A. Ignatov, K. F. Renk, D. G. Pavel'ev, Yu. Koschurinov, B. Melzer, S. Ivanov, S. Schaposchnikov, and P. S. Kop'ev. High-frequency self-sustained current oscillation in an Esaki-Tsu superlattice monitored via microwave emission. *Phys. Lett. A*, 218:349–353, 1996.
- [HHHS94] H. J. Hutchinson, A. W. Higgs, D. C. Herbert, and G. W. Smith. Observation of miniband transport in GaAs/Al_{0.33}Ga_{0.67}As superlattices. *J. Appl. Phys.*, 75:320–324, 1994.
- [IDS91] A. A. Ignatov, E. P. Dodin, and V. I. Shashkin. Transient Response Theory of Semiconductor Superlattices: Connection with Bloch Oscillations. *Mod. Phys. Lett. B*, 5(16):1087, 1991.
- [Ign80] A. A. Ignatov. Current fluctuations in semiconductors with a superlattice in a strong electric field. *Sov. Phys. Solid State*, 22(8):1362, 1980.
- [IPS85] A. A. Ignatov, V. I. Piskarev, and V. I. Shashkin. Instability (formation of domains) of an electric field in multilayer quantum structures. *Sov. Phys. Semicond.*, 19(12):1345, 1985.

- [IR76] A. A. Ignatov and Yu. A. Romanov. Nonlinear Electromagnetic Properties of Semiconductors with a Superlattice. *phys. stat. sol. (b)*, 73:327, 1976.
- [IRD93] A. A. Ignatov, K. F. Renk, and E. P. Dodin. Esaki-Tsu Superlattice Oscillator: Josephson-Like Dynamics of Carriers. *Phys. Rev. Lett.*, 70(13):1996, 1993.
- [IS83] A. A. Ignatov and V. I. Shashkin. A simplified approach to nonlinear HF response theory of superlattice materials. *Physics Letters A*, 94(3,4):169, 1983.
- [IS84] A. A. Ignatov and V. I. Shashkin. Diffusion coefficient of heated carriers, spectrum of space-charge waves, and characteristic instability frequencies of semiconductor superlattices. *Sov. Phys. Semicond.*, 18(4):449, 1984.
- [IS87] A. A. Ignatov and V. I. Shashkin. Bloch oscillations of electrons and instability of space-charge waves in semiconductor superlattices. *Sov. Phys. JETP*, 66(3):526, 1987.
- [KHP⁺97] J. Kastrup, R. Hey, K. H. Ploog, H. T. Grahn, L. L. Bonilla, M. Kindelahn, M. Moscoso, A. Wacker, and J. Galan. Electrically tunable GHz oscillations in doped GaAs-AlAs superlattices. *Phys. Rev. B*, 55:2476, 1997.
- [Kro66] H. Kroemer. Nonlinear Space-Charge Domain Dynamics in a Semiconductor with Negative Differential Mobility. *IEEE Transactions on Electron Devices*, 1:27, 1966.
- [Kro68] H. Kroemer. Negative conductance in semiconductors. *IEEE Spectrum*, 5:47–56, 1968.
- [Kro72] H. Kroemer. *Gunn effect - Bulk instabilities*, pages 20–98. Wiley, Chichester Sussex, UK, 1972.
- [Kro03] Herbert Kroemer. On the nature of the negative-conductivity resonance in a superlattice bloch oscillator. *Cond. Mat.*, 0007482(unpublished), 2003.
- [KS71] R. Kazarinov and R. Suris. Possibility of the amplification of electromagnetic waves in a semiconductor with a superlattice. *Sov. Phys. Semicond.*, 5:707, 1971.
- [KS72] R. Kazarinov and R. Suris. *Sov. Phys. Semicond.*, 6:120, 1972.
- [KSS72] S. A. Ktitorov, G. S. Simin, and V. Y. Sindalovski. Bragg Reflections and the High-Frequency Conductivity of an Electronic Solid-State Plasma. *Sov. Phys. Solid State*, 13:1872, 1972.

- [Kum68] K. Kumabe. Suppression of Gunn Oscillations by a Two-Dimensional Effect. *Proceeding of the IEEE*, page 2172, 1968.
- [KZA⁺95] B. J. Keay, S. Zeuner, S. J. Allen, K. D. Maranowski, A. C. Gossard, U. Bhattacharya, and M. J. M. Rodwell. Dynamic localization, absolute negative conductance, and stimulated, multiphonon emission in sequential resonant tunneling semiconductor superlattices. *Phys. Rev. Lett.*, 75:4102, 1995.
- [KZT⁺95] C. Kurdak, A. Zaslavsky, D. C. Tsui, M. B. Santos, and M. Shayegan. High field transport in an edge overgrown lateral superlattice. *Appl. Phys. Lett.*, 66:323, 1995.
- [LAK56] I. M. Lifshitz, M. I. Azbel, and M. I. Kaganov. On the theory of galvanomagnetic effects in metals. *Soviet Phys. JETP*, 3:143, 1956.
- [LAK57] I. M. Lifshitz, M. I. Azbel, and M. I. Kaganov. The theory of galvanomagnetic effects in metals. *Soviet Phys. JETP*, 4:41, 1957.
- [Leo98] K. Leo. Interband optical investigation of bloch oscillations in semiconductor superlattices. *Semicond. Sci. Technol.*, 13:249–263, 1998.
- [Leo03] K. Leo. *High-Field Transport in Semiconductor Superlattices*. Springer-Verlag Berlin Heidelberg New York, 2003.
- [Ler04] M. Lermer. private communication, 2004.
- [LP59] I. M. Lifshitz and V. G. Peschanskii. Galvanomagnetic characteristics of metals with open fermi surfaces. i. *Soviet Phys. JETP*, 8:875, 1959.
- [LP60] I. M. Lifshitz and V. G. Peschanskii. Galvanomagnetic characteristics of metals with open fermi surfaces. ii. *Soviet Phys. JETP*, 11:137, 1960.
- [LSL⁺98] V. G. Lyssenko, M. Sudzius, F. Löser, G. Valusis, T. Hasche, K. Leo, M. M. Dignam, and K. Köhler. Bloch oscillations in semiconductor superlattices. *Festkörperprobleme/Advances in Solid State Physics*, 38:225–249, 1998.
- [LVL⁺97] V. G. Lyssenko, G. Valusis, F. Löser, T. Hasche, K. Leo, M. M. Dignam, and K. Köhler. Direct measurement of the spatial displacement of bloch-oscillating electrons in semiconductor superlattices. *Phys. Rev. Lett.*, 79:301, 1997.
- [MARH88] E. E. Mendez, F. Agullo-Rueda, and J. M. Hong. Stark localization in GaAs-GaAlAs superlattices under an electric field. *Phys. Rev. Lett.*, 60:2426, 1988.

- [MG95] A. Manolescu and R. R. Gerhardt. Exchange-enhanced spin splitting in a two-dimensional electron system with lateral modulation. *Phys. Rev. B*, 51:1703, 1995.
- [MGvKP93] W. Müller, H. T. Grahn, K. von Klitzing, and K. Ploog. Resonant tunneling in crossed electric and magnetic fields in GaAs-AlAs superlattices. *Phys. Rev. B*, 48:11176, 1993.
- [MHEM01] N. Mori, C. Hamaguchi, L. Eaves, and P. C. Main. Monte Carlo simulation of miniband conduction in Landau-quantized superlattice. *Physica B*, 298:329–332, 2001.
- [ML94] D. Miller and B. Laikhtman. Theory of high-field-domain structures in superlattices. *Phys. Rev. B*, 50:18426, 1994.
- [ML95] D. Miller and B. Laikhtman. Semiclassical theory of the perpendicular magnetoresistance in superlattices. *Phys. Rev. B*, 55:12191, 1995.
- [Mov87] B. Movaghar. Theory of high-field transport in semiconductor superlattice structures. *Semicond. Sci. Technol.*, 2:185–206, 1987.
- [MPP⁺94] C. Minot, H. Le Person, J. F. Palmier, N. Sahri, F. Molloy, and R. Planel. Miniband conduction and electron heating in semiconductor superlattices through time-of-flight experiments. *Semicond. Sci. Technol.*, 9:789, 1994.
- [MRT⁺00] A. Majumdar, L.P. Rokhinson, D. C. Tsui, L. N. Pfeiffer, and K. W. West. Effective mass enhancement of two-dimensional electrons in a one-dimensional superlattice potential. *Appl. Phys. Lett.*, 76:3600, 2000.
- [MSB⁺95] F. A. Meyer, E. Steep, W. Biberacher, P. Christ, A. Lerf, A. G. M. Jansen, W. Joss, P. Wyder, and K. Andres. High-field de Haas-van Alphen studies of κ -(BEDT-TTF)₂Cu(NCS)₂. *Europhys. Lett.*, 32:681, 1995.
- [MTS89] J. Motohisa, M. Tanaka, and H. Sakaki. Anisotropic transport and non-parabolic miniband in a novel in-plane superlattice consisting of a grid-inserted selectively doped heterojunction. *Appl. Phys. Lett.*, 55:1214, 1989.
- [NIS98] Y. Nakamura, T. Inoshita, and H. Sakaki. Novel magnetoresistance oscillations in laterally modulated two-dimensional electrons with 20 nm periodicity formed on vicinal GaAs (111)B surfaces. *Physica E*, 2:944, 1998.
- [PA04] G. Platero and R. Aguado. Photon-assisted transport in semiconductor nanostructures. *Phys. Rep.*, 395:1–157, 2004.
- [Pip65] A. B. Pippard. *The dynamics of conduction electrons*. Documents on modern physics. Science Publishers, 1965.

- [PMF⁺04] A. Patanè, N. Mori, D. Fowler, L. Eaves, M. Henini, D. K. Maude, C. Hamaguchi, and R. Airey. Magnetic-Field-Induced Suppression of Electronic Conduction in a Superlattice. *Phys. Rev. Lett.*, 93:146801, 2004.
- [Pol81] V. M. Polyakovskii. Stark-cyclotron-phonon resonances in superlattice semiconductors. *Sov. Phys. Semicond.*, 15:1190, 1981.
- [PSE⁺92] J.F. Palmier, A. Sibille, G. Etemadi, A. Celeste, and J.C. Portal. Non-linear miniband conduction in crossed electric and magnetic fields. *Semicond. Sci. Technol.*, 7:B283–B286, 1992.
- [PSE⁺02] A. Patanè, D. Sherwood, L. Eaves, T. M. Fromhold, M. Henini, P. C. Main, and G. Hill. Tailoring the electronic properties of GaAs/AlAs superlattices by InAs layer insertions. *Appl. Phys. Lett.*, 81:661, 2002.
- [PWS⁺90] L. Pfeiffer, K. W. West, H. L. Stormer, J. P. Eisenstein, K. W. Baldwin, D. Gershoni, and J. Spector. Formation of a high-quality electron gas on cleaved GaAs. *Appl. Phys. Lett.*, 56:1697, 1990.
- [PWSB89] L. Pfeiffer, K. W. West, H. L. Stormer, and K. W. Baldwin. Electron mobilities exceeding 10^7 cm²/Vs in modulation doped GaAs. *Appl. Phys. Lett.*, 55:1888, 1989.
- [Rot99] M. Rother. *AQUILA - computer program for self-consistent calculation of semiconductor nanostructures*. Walter Schottky Institut, Technische Universität München, 1999.
- [SBG⁺98] E. Schomburg, T. Blomeier, J. Grenzer, K. Hofbeck, I. Lingott, S. Brandl, A. A. Ignatov, K. F. Renk, D. G. Pavel'ev, Yu. Koschurinov, B. Ya. Melzer, V. Ustinov, S. Ivanov, A. Zhukov, and P. S. Kop'ev. High-frequency current oscillation in doped GaAs/AlAs superlattices by traveling dipole domains. *Physica E*, 2:295–298, 1998.
- [SBH⁺98] E. Schomburg, T. Blomeier, K. Hofbeck, J. Grenzer, S. Brandl, I. Lingott, A. A. Ignatov, and K. F. Renk. Current oscillation in superlattices with different miniband widths. *Phys. Rev. B*, 58:4035, 1998.
- [Sch03] F. Scheck. *Theoretische Physik 1: Mechanik*. Springer, Berlin, 7th edition, 2003.
- [SDE⁺02] J. H. Smet, R. A. Deutschmann, F. Ertl, W. Wegscheider, G. Abstreiter, and K. von Klitzing. Gate-voltage control of spin interactions between electrons and nuclei in a semiconductor. *Nature*, 415:281, 2002.

- [SdH30] L. W. Schubnikov and W. J. de Haas. Die widerstandsänderung von wismuteinkristallen im magnetfeld bei der temperatur von flüssigem stickstoff. *Proc. Netherlands Roy. Acad. Sci.*, 33:130,163, 1930.
- [SDR03] E. Schomburg, N. V. Demarina, and K. F. Renk. Amplification of a terahertz field in a semiconductor superlattice via phase-locked k-space bunches of Bloch oscillating electrons. *Phys. Rev. B*, 155302, 2003.
- [SDW⁺01] J. H. Smet, R. A. Deutschmann, W. Wegscheider, G. Abstreiter, and K. von Klitzing. Ising ferromagnetism and domain morphology in the fractional quantum hall regime. *Phys. Rev. Lett.*, 86:2412, 2001.
- [Shi75] A. Y. Shik. Superlattices - periodic semiconductor structures. *Sov. Phys. Semicond.*, 8:1195, 1975.
- [Sho54] W. Shockley. Negative Resistance Arising from Transit Time in Semiconductor Diodes. *Bell System Tech. J.*, 33:799, 1954.
- [Sho84] D. Shoenberg. *Magnetic oscillations in metals*. Cambridge University Press, 1984.
- [SHOC03] Y. Shimada, K. Hirakawa, M. Odnoblioudov, and K. A. Chao. Terahertz Conductivity and Possible Bloch Gain in Semiconductor Superlattices. *Phys. Rev. Lett.*, 90:046806, 2003.
- [SKLA04] P. G. Savvidis, B. Kolasa, G. Lee, and S. J. Allen. Resonant Crossover of Terahertz Loss to the Gain of a Bloch Oscillating InAs/AlSb Superlattice. *Phys. Rev. Lett.*, 92:196802, 2004.
- [SN96] Nguyen Hong Shon and H. N. Nazareno. Hopping conduction in semiconductor superlattices in a quantized magnetic field. *Phys. Rev. B*, 53:7937, 1996.
- [SN97] Nguyen Hong Shon and H. N. Nazareno. Stark-cyclotron resonances in semiconductor superlattices. *Phys. Rev. B*, 55:6712, 1997.
- [SNY⁺99] H. Sakaki, Y. Nakamura, M. Yamauchi, T. Someya, H. Akiyama, and D. Kishimoto. 10 nm scale edge- and step-quantum wires and related structures: Progress in their design, epitaxial synthesis and physics. *Physica E*, 4:56, 1999.
- [SPB⁺91] H. L. Stormer, L. N. Pfeiffer, K. W. Baldwin, K. W. West, and J. Spector. Atomically precise superlattice potential imposed on a two-dimensional electron gas. *Appl. Phys. Lett.*, 58:726, 1991.

- [SPM⁺89] A. Sibille, J. F. Palmier, F. Mollot, H. Wang, and J. C. Esnault. Negative differential conductance in GaAs/AlAs superlattices. *Phys. Rev. B*, 39:6272, 1989.
- [SPMM89] A. Sibille, J. F. Palmier, C. Minot, and F. Mollot. High-field perpendicular conduction in GaAs/AlAs superlattices. *Appl. Phys. Lett.*, 54:165–167, 1989.
- [SPWM90] A. Sibille, J. F. Palmier, H. Wang, and F. Mollot. Observation of Esaki-Tsu negative differential velocity in GaAs/AlAs superlattices. *Phys. Rev. Lett.*, 64:52, 1990.
- [SS84] R. A. Suris and B. S. Shchamkhalova. Heating of electrons in superlattice semiconductors. *Sov. Phys. Semicond.*, 18:738, 1984.
- [SST90] T. Sasaki, H. Sato, and N. Toyota. Magnetic breakdown effect in the organic superconductor κ -(BEDT-TTF)₂Cu(NCS)₂. *Solid State Comm.*, 76:507, 1990.
- [Str82] P. Streda. Theory of quantised Hall conductivity in two dimensions. *J. Phys. C*, 15:L 717, 1982.
- [Sze81] S. M. Sze. *Physics of Semiconductor Devices*. John Wiley & Sons, New York, 2nd edition, 1981.
- [TD75] R. Tsu and G. Döhler. Hopping conduction in a "superlattice". *Phys. Rev. B*, 12:680, 1975.
- [TF85] J. R. Tucker and M. J. Feldman. *Rev. Mod. Phys.*, 57:1055, 1985.
- [TSYS84] K. Tsubaki, H. Sakaki, J. Yoshino, and Y. Sekiguchi. Spatially modulated photoconductivity at N-AlGaAs/GaAs heterojunctions and formation of persistent charge patterns with submicron dimensions. *Appl. Phys. Lett.*, 45:663, 1984.
- [TTS90] K. Tsubaki, Y. Tokura, and N. Susa. Density of states of an AlAs/GaAs fractional superlattice in a modulation-doped structure. *Appl. Phys. Lett.*, 57:2101, 1990.
- [UKW⁺96] K. Unterrainer, B. J. Keay, M. C. Wanke, S. J. Allen, D. Leonard, G. Medeiros-Ribeiro, U. Bhattacharya, and M. J. W. Rodwell. Inverse Bloch oscillator: Strong THz photocurrent resonances at the Bloch frequency. *Phys. Rev. Lett.*, 76:2973, 1996.

- [Unt00] K. Unterrainer. *Photon-Assisted Tunneling in Semiconductor Quantum Structures*. The Physics of Submicron Structures. Academic Press, New York, 2000.
- [VBB⁺88] P. Voisin, J. Bleuse, C. Bouche, S. Gaillard, C. Alibert, and A. Regreny. Observation of the Wannier-Stark quantization in a semiconductor superlattice. *Phys. Rev. Lett.*, 61:1639, 1988.
- [VSD02] K. Výborný, L. Smrčka, and R. A. Deutschmann. Magnetoresistance calculations for a two-dimensional electron gas with unilateral short-period strong modulation. *Phys. Rev. B*, 66:205318, 2002.
- [Wac98] A. Wacker. *Vertical transport and domain-formation in multiple quantum wells*, volume 4 of *Electronic materials series*, chapter 10, pages 321–352. Chapman&Hall, edited by E. Schöll, 1998.
- [Wac02a] A. Wacker. Gain in quantum cascade lasers and superlattices: A quantum transport theory. *Phys. Rev. B*, 66:085326, 2002.
- [Wac02b] A. Wacker. Semiconductor superlattices: A model system for nonlinear transport. *Physics Reports*, 357:1–111, 2002.
- [Wan60] G. H. Wannier. Wave functions and effective Hamiltonian for Bloch electrons in an electric field. *Phys. Rev.*, 117:432, 1960.
- [WBR⁺99] A. Wacker, S. Bose, C. Rauch, G. Strasser, and E. Gornik. Transmission through superlattices with interface roughness. *Superlatt. Microstruct.*, 25:43–46, 1999.
- [WDF03] H. Willenberg, G. H. Döhler, and J. Faist. Intersubband gain in a Bloch oscillator and Quantum cascade laser. *Phys. Rev. B*, 67:085315, 2003.
- [WMN⁺92] R. J. Warburton, J. G. Michels, R. J. Nicholas, J. J. Harris, and C. T. Foxon. Optically detected cyclotron resonances of GaAs quantum wells: Effective-mass measurements and offset effects. *Phys. Rev. B*, 46:13394, 1992.
- [WRM⁺91] D. Weiss, M. L. Roukes, A. Menschig, P. Grambow, K. v. Klitzing, and G. Weimann. Electron pinball and commensurate orbits in a periodic array of scatterers. *Phys. Rev. Lett.*, 66:2790, 1991.
- [WRM⁺93] D. Weiss, K. Richter, A. Menschig, R. Bergmann, H. Schweizer, K. von Klitzing, and G. Weimann. Quantized periodic orbits in large antidot arrays. *Phys. Rev. Lett.*, 70:4118, 1993.

- [WRS⁺93] C. Waschke, H. Roskos, R. Schwedler, K. Leo, H. Kurz, and K. Köhler. Coherent submillimeter-wave emission from Bloch oscillations in a semiconductor superlattice. *Phys. Rev. Lett.*, 70:3319, 1993.
- [WSG⁺97] S. Winnerl, E. Schomburg, J. Grenzer, H.-J. Regl, A. A. Ignatov, A. D. Semenov, K. F. Renk, D. G. Pavel'ev, Yu. Koschurinov, B. Melzer, V. Ustinov, S. Ivanov, S. Schaposchnikov, and P. S. Kop'ev. Quasistatic and dynamic interaction of high-frequency fields with miniband electrons in semiconductor superlattices. *Phys. Rev. B*, 56:10303, 1997.
- [WvKPW89] D. Weiss, K. v. Klitzing, K. Ploog, and G. Weimann. Magnetoresistance oscillations in a two-dimensional electron gas induced by a submicrometer periodic potential. *Europhys. Lett.*, 8:179, 1989.
- [YC99] P. Y. Yu and M. Cardona. *Fundamentals of Semiconductors*. Springer-Verlag, Berlin, 1999.
- [Yos02] D. Yoshioka. *The Quantum Hall Effect*. Springer-Verlag, Berlin, 2002.
- [Zen34] C. Zener. A Theory of the Electrical Breakdown of Solid Dielectrics. *Proc. Roy. Soc. (London) A*, 145:523, 1934.
- [ZG90] C. Zhang and R. R. Gerhardts. Theory of magnetotransport in two-dimensional electron systems with unidirectional periodic modulation. *Phys. Rev. B*, 41:12850, 1990.

Publications about selected parts of this thesis

- [FDW⁺04] T. Feil, R. A. Deutschmann, W. Wegscheider, M. Rother, D. Schuh, M. Bichler, G. Abstreiter, B. Rieder, and J. Keller. Transport in weakly and strongly modulated two-dimensional electron systems realized by cleaved-edge-overgrowth. *phys. stat. sol. (c)*, 1(8):21112130, 2004.
- [FRW⁺04] T. Feil, B. Rieder, W. Wegscheider, M. Bichler, G. Abstreiter, and J. Keller. Atomically precise modulated two-dimensional electron gas exhibiting stable negative differential resistance. *Physica E*, 22:733–736, 2004.
- [FTR⁺05] T. Feil, H.-P. Tranitz, M. Reinwald, W. Wegscheider, M. Bichler, D. Schuh, G. Abstreiter, and S. J. Allen. Negative differential conductance in cleaved edge overgrown surface superlattices. *Proc. of the 27th Int. Conference on the Physics of Semiconductors (ICPS2004)*, 2005.
- [FTRW05] T. Feil, H.-P. Tranitz, M. Reinwald, and W. Wegscheider. Electric field stabilization in a high-density surface superlattice. *Appl. Phys. Lett.*, 87:212112, 2005.
- [FTGW] T. Feil, H.-P. Tranitz, C. Gerl, and W. Wegscheider. Transport in a shunted surface superlattice with a perpendicular magnetic field. *Physica E*, In Press, Corrected Proof, Available online 31 January 2006.
- [FGW05] T. Feil, C. Gerl, and W. Wegscheider. Transport properties of a shunted surface superlattice in an external magnetic field. *Phys. Rev. B*, 73:125301, 2006.

Acknowledgments

It is the author's pleasure to acknowledge invaluable contributions from a large number of people that helped to make the project a success. In particular I would like to mention

- Prof. Dr. Werner Wegscheider; for entrusting me with this project and for providing a research environment in which I could freely follow my interests and realize my own ideas. Also for making all those overseas trips possible and for the occasional growth of an urgent new surface superlattice design.
- Prof. S. James Allen; without your interest and (financial) support the project would not have reached this point. Discussions with you made me truly understand the vital parts of superlattice physics. Thanks also for being a great host to someone you had never heard about and for making me understand what the word 'quadruplets' means. I wish we would have seen at least one PAT-peak.
- Dr. Karel Výborný; for a most pleasurable collaboration in the field of strongly modulated 2DEGs, for revisiting a finished project, and for proof-reading the magnetotransport chapter. Let me also thank you and Prof. Ludvíg Smrčka for the generous invitation to Prague and for staying late on a Friday night.
- Dr. Bernhard Rieder; for the numerous stimulating discussions about transport in superlattice structures. And also for your important contribution to electric field instabilities in surface superlattices.
- Max Bichler, Matthias Reinwald, Dr. Hans-Peter Tranitz, Christian Gerl and Dr. Dieter Schuh; for the timely growth of innumerable high-quality surface superlattice structures. There would be no project without your work. Special thanks goes to H.-P. Tranitz for growing 5 substrates and 15 different CEO-samples in less than four months.
- Gerald Ramian and David Enyeart; without your immense help the THz experiments at UCSB would not have been possible.
- Prof. Dr. Sergej Ganichev and his group; for giving me access to their THz lasers. Special thanks to Dr. Sergej Danilov for helping me with the setup of the absorption experiments.

- Alexander Maier; for the numerous helpful discussions and comments on GHz electronics.
- Peter Müller; for technical support and especially for helping me keep my sanity during insane times.
- Jing Xu; for keeping the FEL running at the most ridiculous times of the day (& night) and for sharing precious equipment. Also for putting up with me in the lab (Britney rocks).
- Dr. Stefan Birner; for the support with and free sharing of the nextnano tool.
- The magnetotransport group of Prof. Gerhard Abstreiter at the Technical University of Munich; for putting up with the Regensburg visitors when the MBE machine in Regensburg was still not running. Specially thanks to Dr. Matthew Grayson for many helpful discussions and for introducing me to Cleaved-Edge Overgrowth. Also to Frank Ertl and Michael Huber for numerous discussions about the transport properties of cleaved-edge overgrowth devices.
- The group of Prof. Dr. Dieter Weiss; for giving me access to their cleanroom facilities and for introducing me to the equipment. Special thanks to Markus Lermer for numerous discussions, for providing samples with finger-contacts, and for access to his Hall bar measurements on cleaved-edge overgrowth devices. Also thanks to Christian Mitzkus for the introduction to the dilution refrigerator setup and for sharing the leak detector.
- The group of Prof. Dr. Karl F. Renk; for sharing expensive GHz equipment and for providing access to their Dektak.
- Matthias Habl; for being an enjoyable roommate; for making me understand how liquid helium works and why it sometimes acts as fuel for rockets. Special thanks for taking the time to proof-read this thesis while being under pressure to finish your own.
- Thomas Herrle; for helpful discussions on THz waveguides and for proof-reading this thesis.
- The technicians in our group, the members of the Mechanikwerkstatt und of the Elektronikwerkstatt; your expertise in technical matters was the basis for many of the presented experiments. Thanks for providing an enjoyable and successful work environment. Special thanks to Walter Wendt for often doing the impossible.
- Renate Creuzburg and Annemarie Dinkel; for the friendly help with all matters bureaucratic.

- All PhD candidates and Diploma-students in our group; for the many enjoyable after lunch coffee breaks. Also for many interesting scientific and non-scientific discussions. Special thanks to Robert Schuster for being a dependable roommate all across the world.
- The Deutsche Forschungsgemeinschaft and the Bundesministerium für Bildung, Wissenschaft, Forschung und Technologie; for financial support through, respectively, SFB 348 and contract No. 01BM912.
- And last but not least, all the people who have supported me outside the physics world and whom I have cheated for a lot of quality time while brooding over I-V characteristics. I will try to make up for it.